TECHNISCHE UNIVERSITÄT MÜNCHEN
Lehrstuhl für Messsystem- und Sensortechnik

Adaptive Optics for the Mitigation of Atmospheric Effects in Laser Satellite-To-Ground Communications

Markus Knapek

Vollständiger Abdruck der von der Fakultät für Elektrotechnik und Informationstechnik der Technischen Universität München zur Erlangung des akademischen Grades eines

Doktor-Ingenieurs

genehmigten Dissertation.

Vorsitzender: Univ.-Prof. Dr. rer. nat. habil. B. Wolf
Prüfer der Dissertation: 1. Univ.-Prof. Dr.-Ing. habil. Dr. h.c. A. W. Koch
                           2. Prof. Chr. Dainty, Ph.D., National University
                              of Ireland, Galway

Abstract

Laser links have become a promising solution for bottle-necks in satellite-to-ground communication links (SGL). Investigations, however, show that atmospheric index-of-refraction turbulence has a significant impact especially on coherent and fiber-coupled communication schemes. This thesis investigates adaptive optics techniques for the correction of atmospherically distorted wavefronts. Atmospheric measurements in SGLs from two LEO satellites form the basis of this work. An analysis of conventional wavefront sensors widely used in astronomy disclosed performance limitations. Based on the findings self-referencing interferometers appear to be a promising solution for the difficult atmospheric conditions in these scenarios. Instantaneous phase-shifting interferometers and Fourier fringe analysis techniques are introduced as a new solution in this application. A lab implementation in the atmospheric testbed supports the obtained results.

Zusammenfassung

Laserverbindungen haben sich zu einer vielversprechenden Lösung für Engpässe in der Satelliten-Boden Kommunikation entwickelt. Atmosphärische Untersuchungen zeigen jedoch, dass atmosphärische Brechungsindexturbulenz einen signifikanten Einfluss auf Laserkommunikation hat. Diese Arbeit untersucht Techniken der adaptiven Optik zur Korrektur von atmosphärischen Wellenfrontverzerrungen. Grundlage dieser Arbeit bilden atmosphärische Messungen mit zwei LEO Satelliten. Eine Untersuchung von konventionellen Wellenfrontsensoren hauptsächlich aus der Astronomie zeigt Schwachpunkte dieser Sensoren auf. Basierend auf diesen Ergebnissen stellen selbst-referenzierende Interferometer eine vielversprechende Lösung dar. Instantane Phase-Shifting Interferometer und Fourier Fringe Analyse Techniken werden als neue Lösungen in dieser Applikation präsentiert. Erste Laboraufbauten im Atmosphärentestbett bestätigen die theoretischen Ergebnisse.

Table of Content

Acknowledgment

First of all I want to thank my colleagues in the Optical Communication Group at DLR for supporting me to put together this work with fruitful discussions and allowing me to concentrate on writing even during strenuous measurement campaigns, in which they could have well used my support. At this point I would also thank my boss and colleague Dr. Dirk Giggenbach for his support providing me the time for this work and his helpful suggestions.

Several people in the group have contributed to this work. Florian Moll designed and built the optical turbulence generator and the general setup of the testbed during his master thesis. Dr. Nicolas Perlot contributed software tools for the evaluation of DIMM and turbulence profiler. Joachim Horwath contributed with numerical simulations of the atmospheric conditions in the SGL scenarios with the DLR tool PILab, and he always was open for helpful discussion. Christian Fuchs contributed to the OGS with a new mount design and was responsible for the power measurements with the PIN diodes. Dr. Ramon Mata-Calvo contributed with the setup of the first interferometers and with many valuable programs for the real-time evaluation of Shack-Hartmann images and the Fourier Fringe Analysis technique. Several students, Andreas Gstöttner, Sebastian Kurz, Christina Morfopoulou, Karl Zettl, and Carlos Burnett, have taken part in the programming of the measurement instruments and the telescope mount software to perform the orbit satellite tracking.

Part of the work for this thesis was funded via the European Space Agency (ESA) by the German Space Agency in Bonn. The first generation of the optical ground station with the measurement instruments was built under an ESA contract. Especially I want to mention the colleagues in Bonn, Rolf Meyer and Michael Lutzer, and at ESTEC Dr. Zoran Sodnik with his helpful contributions.

A large number of experiments were conducted from the satellite TerraSAR-X with the Laser Communication Terminal (LCT) built by Tesat Spacecom AG. During these campaigns several colleagues at or close to Tesat supported the measurements, and I learned many things about optical communications and acquisition techniques. Here I want to mention and thank Dr. Bernhard Wandernoth, Dr. Uwe Sterr, Hartmut Kämpfner, Karin Saucke, and Mark Gregory.

In the context of the project TerraSAR-X I also want to mention Dr. Florian David, from whom I took over the project DLR TerraSAR-X. His organized ways allowed me a quick start in the management of this project.

Very successful and pleasant was the cooperation with the Japanese colleagues at the National Institute for Communications Technology NICT and the Japanese Space Agency JAXA, both in Tokyo. They allowed us to use their satellite OICETS for two measurement campaigns in 2006 and 2009, on which most of the measurement results in this work are based. I am especially grateful to Dr. Yoshihisa Takayama and Dr. Morio Toyoshima, who were very supportive and enabled the campaigns in a very trusting manner.

Prof. Chris Dainty at the National University of Ireland supported me with several very inspiring discussions significantly improving this thesis. I feel very grateful to him for his encouraging ways and the willingness to support this work despite the geographic distance.

I also want to thank Prof. Alexander Koch, who supported me to obtain my Ph.D. from the Technical University Munich, although the work was not performed at his department. He always backed me in a very straightforward way.

And finally I want to express my special gratefulness to my parents Karin and Herbert for their unconditional support, love, and also patience. They were the most important ingredient to this work.

The research for the presented thesis was performed during my work at the German Aerospace Center (DLR) at the Institute of Communications and Navigation.

Team of the DLR Optical Communication Group during a measurement campaign on Tenerife, 2005. Satellite-to-ground links from ARTEMIS with atmospheric measurements. (from left: Dr. Dirk Giggenbach, Brandon Wilkerson, Markus Knapek, Hennes Henniger, Bernhard Epple, Joachim Horwath, Dr. Nicolas Perlot)
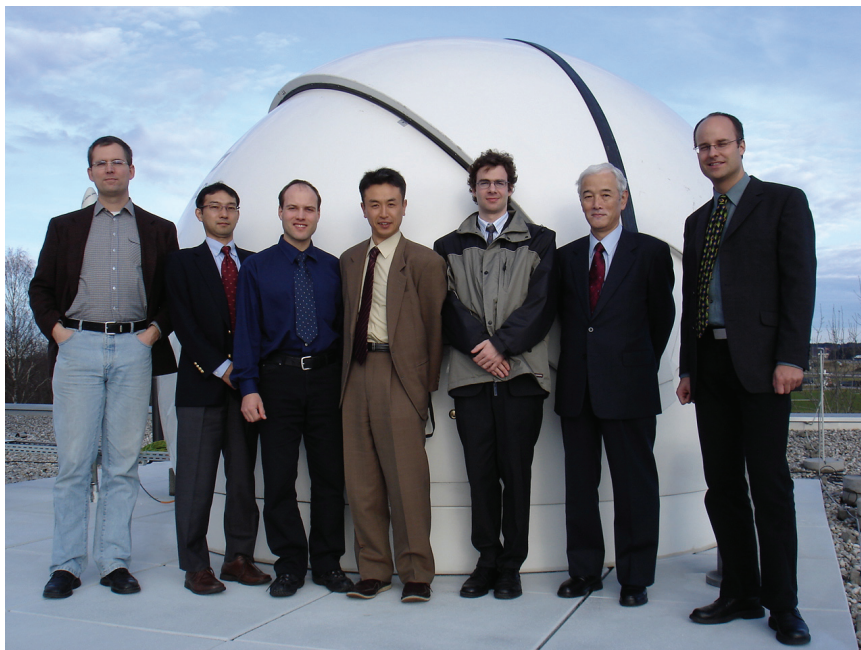
Visit of the Japanese colleagues of NICT/JAXA 2006 to Oberpfaffenhofen during the preparations of the measurement campaign with OICETS. (from left: Dr. Dirk Giggenbach, Dr. Takashi Jono, Joachim Horwath, Dr. Yoshihisa Takayama, Dr. Nicolas Perlot, Dr. Yoshisada Koyama, Markus Knapek)

1 Introduction

1.1 Free-Space Laser Communications and its Applications

The most prominent motivation for using optical communications for satellite links in spite of the risks of a relatively new technology is an increase of the transmittable data rate by several orders of magnitude. Already the state-of-the-art Laser Communication Terminal (LCT) developed by Tesat-Spacecom under a DLR space agency contract, currently in operation on the German remote-sensing satellite TerraSAR-X, offers a data rate of 5.6Gbps for inter-satellite links (ISL) over a distance of up to 6000km [LAN05]. Optical space qualified terminals of the next generation can be expected to achieve even higher data rates. Spectrum in the optical domain is practically unlimited, and on top optical links do not interfere with each other due to beam divergence angles of less then a 1/1000 degree. Spectrum allocation is not coordinated by the ITU, which is a significant advantage for optical links.

Inter-satellite links have been demonstrated in several semi-operational links since 2001; however, satellite-to-ground links (SGL) pose an additional challenge due to the impact of atmospheric turbulence on the communication link. The impact can be classified into three types:

- Intensity effects, so called scintillation, describe the fluctuations in the signal intensity due to focussing effects of atmospheric turbulence cells. The communication receivers have to be able to cope with the large dynamics of the received power. Larger receiver apertures, apart from the higher received power, allow spatial averaging of the received intensity and therefore offer a reduced variability of the signal power.

- Wavefront distortions (phase distortions) at the receiver are caused by optical path length differences due to fluctuations of the index-of-refraction in the atmosphere. A distorted wavefront especially impairs the performance of single-mode fiber-coupled receivers and coherent receivers, which superpose the received (distorted) wavefront with a local (undistorted) laser.

- Attenuation effects, as they are caused by clouds or atmospheric absorption and scattering, have a significant impact on the viability and design of optical communication links; however, this work is concerned with index-of-refraction turbulence and this category is not treated here.

Adaptive optics (AO) systems are proposed to correct the detrimental effects, especially phase distortions, of the atmosphere. This method is based on systems mainly applied in astronomy but is modified for the specific conditions of SGLs. Figure 1.1 shows the basic principle of an AO system for an optical communication link through the atmosphere. The transmitter sends out an undistorted wavefront, which is distorted by the atmosphere. On the receiver side a closed-loop control system with a wavefront sensor and correcting elements (deformable/tip-tilt mirror) attempts to correct the wavefront distortions, so that an optimal performance of the communication receiver is achieved. For a fiber-coupled receiver the performance is determined by the fiber-coupling efficiency and the strength of the fluctuations of the received power. For a coherent communication receiver the performance is given by the heterodyning efficiency.
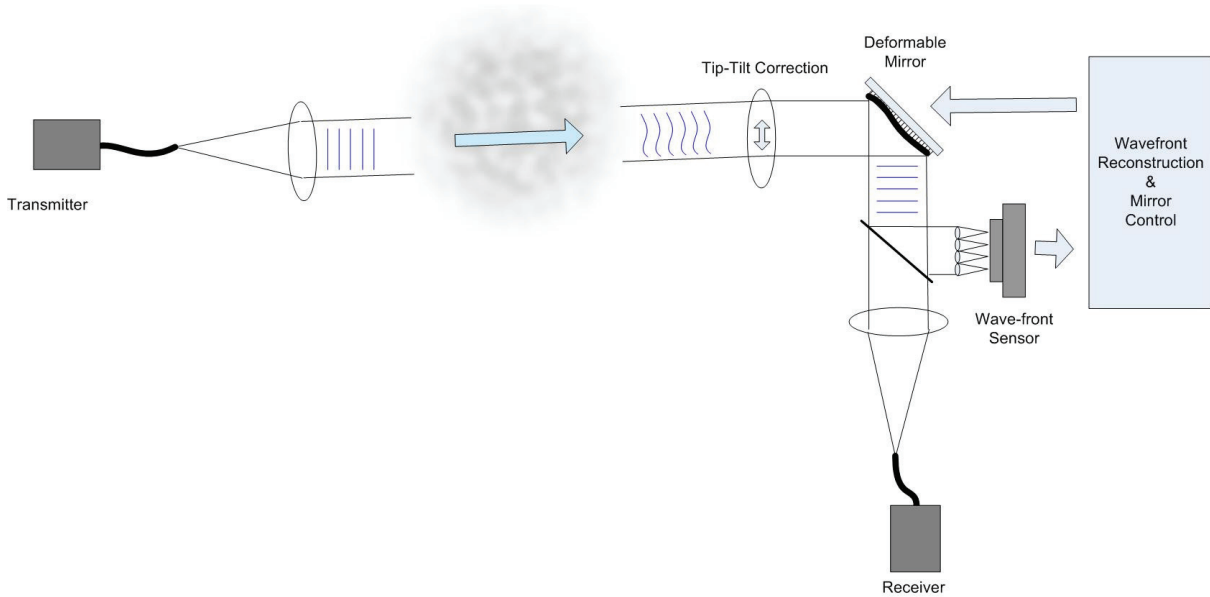
Figure 1.1: Principle of an adaptive optics system for a communication link through the atmosphere.

This work is primarily concerned with SGLs from low-earth orbit (LEO) and geostationary (GEO) satellites. LEO satellite SGLs are especially challenging due to the fast movement of the satellite across the sky. Typical SGLs last only around 10 minutes. Due to the satellite motion higher demands on the speed (wavefront corrector, sensor, and reconstruction) are placed upon an AO system; however, smaller aperture diameters are possible, as the link distances are quite short (<3000km). GEO SGLs are rather static and comparable to conditions in astronomy. Nevertheless, atmospheric conditions for SGL ground stations are expected to be worse than in astronomical applications, whose sites are usually operated at high altitudes with extremely good atmospheric conditions. SGL ground stations will be also operated at low altitudes with very difficult turbulence conditions.

Figure 1.2: Possible link scenarios for optical communication links involving satellites and high altitude platforms (HAP).

Other link scenarios like connections between satellites and high-altitude platforms (HAP) or airplanes have been discussed in the literature; however, these links operate in higher atmospheric layers with low air pressure. Consequently, atmospheric effects are quite weak. A similar situation is true for future inter-HAP links, which are expected to operate at a minimum altitude of 13km to avoid cloud blockage. Downlinks from a HAP to a ground station can be treated similarly to a GEO-ground link. They would be almost static, but the elevation angles could be very low. Figure 1.2 shows a summary of possible link scenarios.

1.2 History of Free-Space Laser Communications in Space

The investigation of space laser communication systems started in the United States already in the 1960s with first experiments to solve the demanding challenges of pointing, acquisition, and tracking problems, and to find suitable laser sources and communication detectors [KOE02]. Initially only gas lasers were available, but soon solid-state and semiconductor lasers were developed and replaced the gas lasers as a candidate for space applications.

In 1977 ESA started the development of space optical communication technologies with the investigation of high data-rate laser modulators for space applications [LUT97]. In the mid-1980s the organisation launched the ambitious SILEX (Semiconductor laser Inter-satellite Link Experiment) program to demonstrate a pre-operational optical link in space. In 2001 ESA could perform the world-first inter-satellite optical link between the European GEO satellite ARTEMIS and the French LEO satellite SPOT-4. Hundreds of successful links have been performed since then, relaying Earth observation data from SPOT-4 to ARTEMIS and via microwave to the ground [SOD06]. The SILEX communication system is an intensity modulation, direct detection (IM/DD) system with an asymmetric data rate of 50Mbps to ARTEMIS and 2Mbps in the other direction.

As part of the SILEX program ESA constructed an optical ground station (OGS) on the Canary Island Tenerife, which was completed in the late 1990's (Figure 1.3). The ESA OGS with its 1m telescope allowed to perform SGLs from ARTEMIS and to verify the performance of the optical communication terminal (OCT) on ARTEMIS.

Figure 1.3: The ESA optical ground station on Tenerife at an altitude of 2400m above the sea level.

In 2005 the Japanese Aerospace Exploration Agency (JAXA) launched the Optical Inter-Orbit Communications Engineering Test Satellite (OICETS), which is equipped with an OCT

compatible with the terminal on ARTEMIS. A first inter-satellite link between OICETS and ARTEMIS was established in December 2005. JAXA also performed SGL experiments from OICETS to their 1.5m OGS in Tokyo.

The French department of defence planned an optical link from an airplane to ARTEMIS. The first link experiments of the project Liaison Optique Laser Aéroportée (LOLA) were performed in October 2006 with a first communication link in December 2006.

In the 1990s very ambitious satellite communication networks with several hundred LEO satellites were envisaged in the Teledesic program. Each satellite in the network was planned to be equipped with six inter-satellite OCTs. The OCTs were to be developed by companies in Europe and the US; however, the work on this program was suspended in 2002. On the European side the development of the OCTs was led by the German Bosch-Telecom (today Tesat-Spacecom) and the Swiss Contraves (today Oerlikon Space).

The Deutsche Agentur für Raumfahrtangelegenheiten (DARA, today the space agency as a part of the German Aerospace Center DLR) supported the development of coherent OCTs in the German program SOLACOS (Solid-State Laser Communications in Space) in the 1990s. In 1996 ESA placed a contract to Contraves Space (today RUAG Aerospace) to develop a lightweight optical terminal for short-range inter-satellite links in the project SROIL.

SGL: Satellite-ground link, ISL: Inter-satellite link, TSX: TerraSAR-X, LCT: Laser Communication Terminal, LCTSX: LCT on TSX, OGS: Optical Ground Station
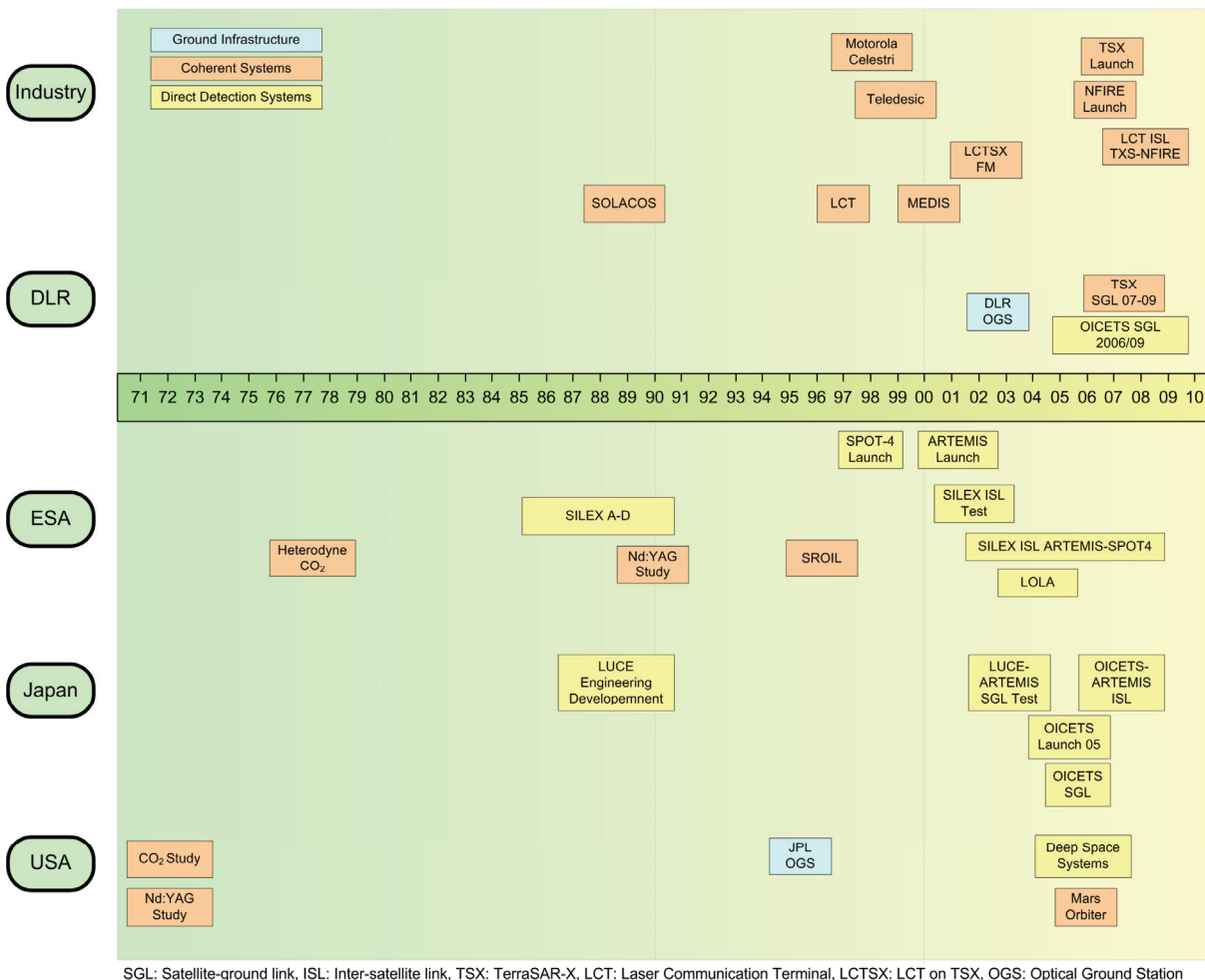
Figure 1.4: History of laser satellite communications of European research organizations and industry. Some facts of American and Japanese activities were added.

Although the efforts of SOLACOS and SROIL did not lead to the manufacturing of flight terminals, the experience and knowledge of the developments at that time went into a further development of OCTs at Tesat-Spacecom, which finally led to the development of the Laser Communication Terminal (LCT), a space qualified 5.6Gbps ISL terminal with coherent binary

phase-shift keying (BPSK) modulation scheme [LAN05]. The development was financed by the Bundesministerium für Wirtschaft und Technologie (BMWi) via the DLR space agency in the program DLR-LCT. The first two terminals of this type were launched on the American military LEO satellite NFIRE in April 2007 and the German TerraSAR-X in June 2007. In May 2008 first ISLs were successfully demonstrated at a distance of up to 5000km. Figure 1.5 shows an image of the LCT installed on TerraSAR-X.
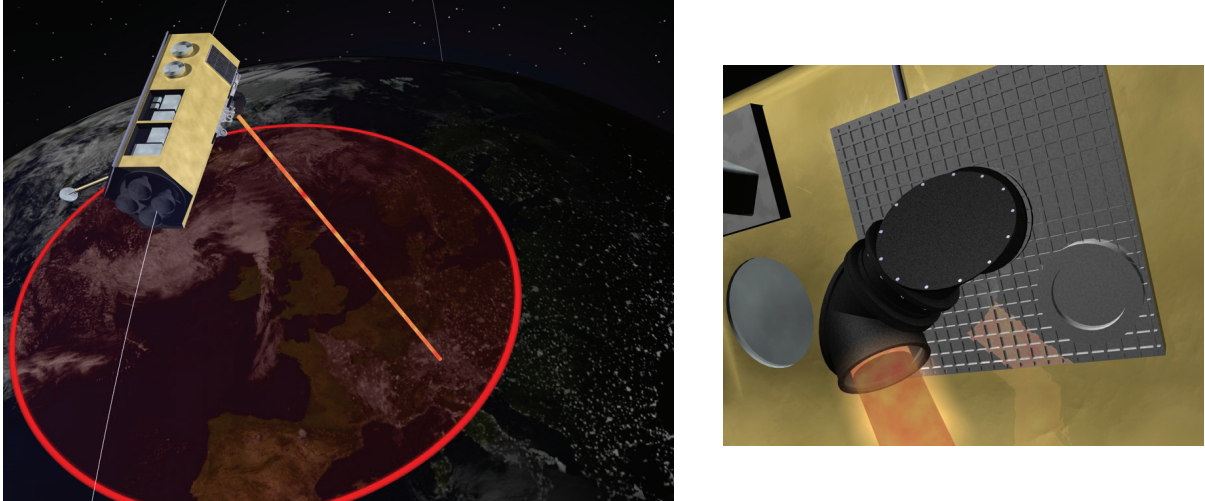
Figure 1.5: The Laser Communication Terminal on TerraSAR-X with the periscope-type coarse pointing device (Artist's Impression).

1.3 Research at the DLR Institute of Communications and Navigation

The German Aerospace Center (DLR) with the Optical Communication Group (OCG) at the Institute of Communications and Navigation started to study optical free-space communications for space applications in the late 1980's. Early theoretic work at the OCG went into the developments of the SOLACOS and later of the DLR-LCT program. The OCG initially contributed advanced techniques for phase-locked loops, modulation schemes, and error correction techniques. Later the group studied the effects of the atmosphere on optical communication links.

In 2004 ESA awarded a contract to the OCG to investigate the challenges of optical communication from a satellite to a ground station with a significant part of the link in the atmosphere. The project was intended to accompany the efforts of Tesat Spacecom in the development of the LCT for the LEO satellite TerraSAR-X.

The results of a detailed study were summarized in the Coherent Transmission Feasibility Analysis (CTFA) [DAV04], which studied the feasibility of SGLs with the LCT through the atmosphere and gave recommendations for its improvement.

In parallel the OCG started the development of an optical ground station (DLR OGS). The OGS includes a multitude of measurement instruments to study the atmospheric conditions in parallel to the communication link. The quality of the communication link is measured e.g. by the bit-error rate (BER) in the SGLs. Figure 1.6 shows the scheme of the optical measurement instruments (Atmospheric Transmission Monitor), which is further explained in Chapter 3. The OGS helped to expand and verify the practical knowledge of typical atmospheric conditions and their impact on the communication performance, i.e. heading towards a channel model for optical SGLs. Especially critical are communication links at very low elevation angles (<10 degrees), as turbulence conditions become severe. The scales of intensity and phase speckles decrease to the range of centimetres, which significantly impacts on the performance of communication links.
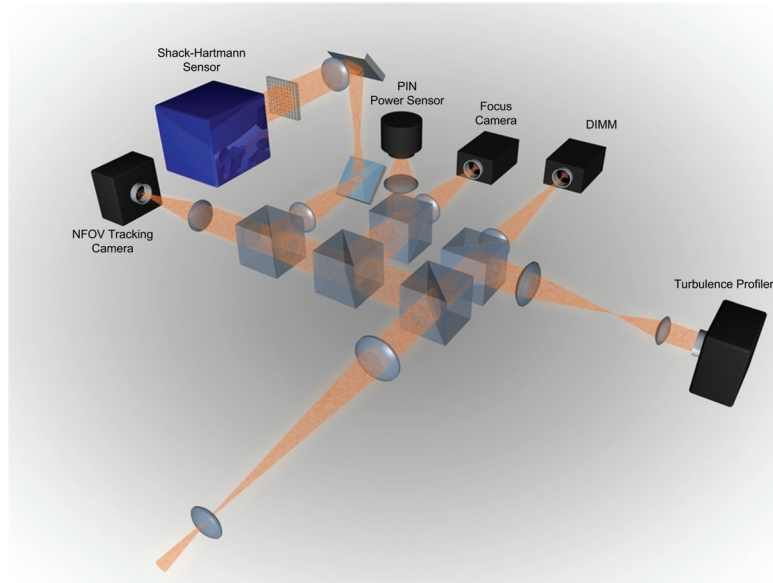
Figure 1.6: Atmospheric measurement (Atmospheric Transmission Monitor) instruments of the DLR OGS. Turbulence Profiler and a power sensor (PIN diode) measure the intensity distribution in the receiver aperture. Differential Image Motion Monitor (DIMM), Shack-Hartmann sensor, and focus camera allow an evaluation of the phase distortions. Details are given in Chapter 3.
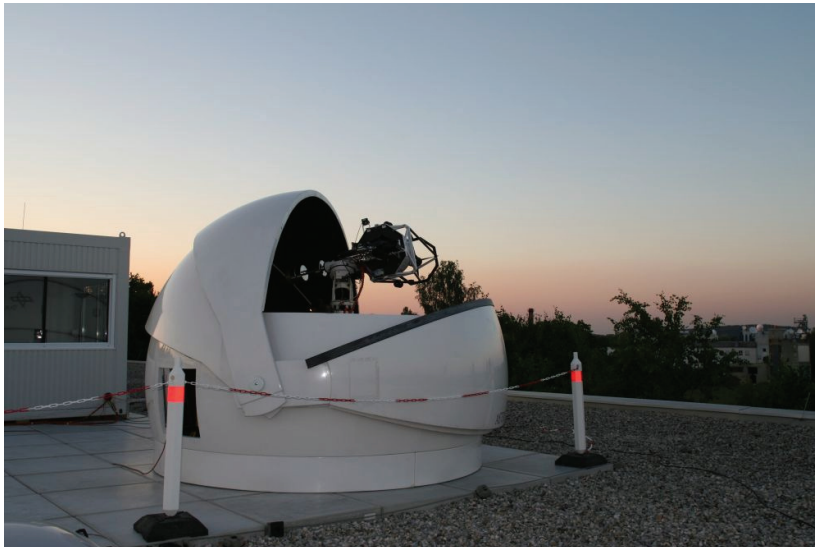
Figure 1.7: DLR Optical Ground Station at Oberpfaffenhofen near Munich.

In order to verify the results of the CTFA in experiments already before the LCT was launched on TerraSAR-X, a link between the Canary islands of La Palma and Tenerife over 142km was performed in 2005 [LAN06]. Both transmitter and receiver were located on mountains at about 2000m altitude on La Palma and Tenerife, respectively. First atmospheric measurements were gained under atmospheric conditions, which can be considered to be worst case. The experiment showed that coherent communication at the LCT's data rate of 5.6Gbps works through an extended volume of atmosphere, although challenges became apparent due to the high dynamics of the received signal power and the phase distortions of the received field.

In 2006 a first European SGL from the Japanese LEO satellite OICETS was performed to the DLR OGS in a close cooperation with the Japanese Aerospace Exploration Agency

(JAXA) and the National Institute of Information and Communications Technology (NICT) both in Tokyo. Figure 1.7 shows the DLR OGS during the experiments with OICETS. Figure 1.8 gives an impression of OICETS with the laser communication terminal during an SGL to Oberpfaffenhofen. Valuable data on the atmosphere was gained during these SGLs, including scintillation and phase distortion effects. Standard atmospheric parameters as scintillation index, temporal spectrum of the scintillation, and the atmospheric coherence length or Fried parameter r_0 were measured over various elevation angles as low as 3 degrees. In parallel to the atmospheric measurements a pseudo-random binary sequence was successfully received from the satellite at 50Mbps. Bit-error rates were measured, and conclusions could be drawn for the improvement of data receivers under atmospheric conditions especially to minimize the effects of intensity scintillation.

In June 2007 TerraSAR-X was launched with an LCT on board. First tests of SGLs were performed to the DLR OGS in Oberpfaffenhofen in September. A first link acquisition could be demonstrated, however, a stable link could not be established. The OCG suggested that the combination of atmospheric beam-wander in the uplink and a very narrow beam divergence were responsible for the failure of a stable link. In October 2007 the experiments were repeated to the astronomical site Calar Alto in southern Spain at an altitude of 2133m, which offers the advantage of less atmospheric turbulence. Experiments were continued until mid-November. A stable communication link could not be established, but successful acquisition and incoherent tracking could be demonstrated.

During the experiments with OICETS and TerraSAR-X, the OCG has gained valuable knowledge of the atmospheric effects and collected experience of how to design optical communication terminals for atmospheric links. The theoretic/ simulatory predictions and the atmospheric measurements form the foundation for the study of adaptive optics in optical SGLs presented in this work.
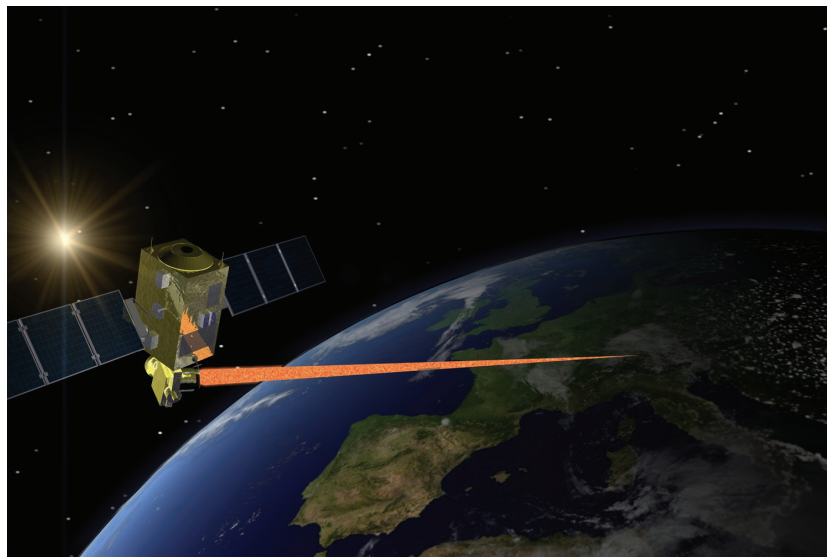
Figure 1.8: Optical SGL from the Japanese LEO satellite OICETS to the DLR OGS at Oberpfaffenhofen. (Artist's impression)

1.4 Thesis Outline

Topic of this work is the application of AO systems under the specific conditions found in satellite-to-ground optical communications. AO systems are well understood from astronomy and find wide application in this field; however, the deployment of AO systems for SGLs has to cope with different conditions compared to the application in astronomy. Typical LEO satellites are seen 90 percent of the line-of-sight time below an angle of 30 degrees elevation. This implies very long link paths through highly turbulent layers of the atmosphere, causing strong phase distortions and intensity fluctuations; in addition, the beam moves with high angular velocity through the atmosphere due to the satellite motion, which puts

challenging temporal requirements on the AO system to correct the fast phase changes. An issue for low elevation links, which operate in the so called strong fluctuation regime, are phase singularities. Singularities prevent the description of the phase front with a continuous phase function. This has an impact on wavefront sensing as well as on the phase correction. Measurement quality of typical astronomical wavefront sensors like the Shack-Hartmann sensor or the curvature sensor significantly deteriorates using standard reconstruction algorithms. Even for a perfect measurement of the wavefront, corrector elements, which frequently use a continuous membrane/faceplate, are not able to cope with singularities. Alternative approaches are studied in this work to minimize correction errors and optimize the communication performance.

Chapter 2 gives an overview of optical free-space communication systems including intensity modulated/ direct detection and coherent communication systems. State-of-the-art ground stations and flight-terminal systems are discussed.

Chapter 3 shows typical atmospheric conditions and their impact on optical SGLs. In a first section theoretic models of the atmospheric effects are presented including statistical distributions of the received phase and intensity. Standard atmospheric turbulence profiles and a brief overview of the theoretic treatment of the atmospheric impact on communication links are given.

Between 2006 and 2009 the OCG performed atmospheric measurements in SGLs mainly from the Japanese LEO satellite OICETS (and a few from TerraSAR-X) with the Atmospheric Transmission Monitor (ATM), which is part of the DLR OGS. Section 3.2 gives a short introduction to the measurement instruments of the ATM and the DLR OGS. Section 3.3 shows a summary of the measurement results, which represent the basis for the further analysis in Chapter 4 and 5.

Chapter 4 introduces basic AO concepts and gives a survey of relevant wavefront sensors, which have been discussed in the astronomical literature since the 1960s. Special emphasis will be given to the performance of the sensors under strong turbulence conditions also considering phase singularities. The wavefront sensors including the phase reconstruction will be evaluated for their processing speed. This chapter provides the foundations for the development of alternative AO concepts, which are optimized for the specific conditions in SGLs.

In Chapter 5 alternative concepts for AO systems are presented with a main emphasis on self-referencing interferometric wavefront sensors. Here common-path interferometers and point-diffraction interferometers with phase-shifting techniques are discussed. This chapter is a starting point for the implementation of an AO system for LEO SGLs.

In Chapter 6 first demonstrations of interferometric wavefront sensors in a lab environment are presented in the DLR atmospheric testbed.

The structure of the thesis is summarized in Figure 1.9 showing the relation between the four main chapters.

1.5 Statement of Work

This thesis was motivated by the SGL experiment campaigns with the satellites OICETS and TerraSAR-X. The DLR optical ground station with its atmospheric measurement instruments was developed by the optical communication group (OCG) at DLR under an ESA contract specifically for the SGLs from TerraSAR-X. The idea of the atmospheric measurement instruments appeared in the OCG around 2003. Dr. Dirk Giggenbach, Dr. Florian David, Dr. Nicolas Perlot, Joachim Horwath, Hennes Henniger, and I were the leading characters in this process.

Many contributions of the OCG have made this thesis possible. Florian Moll designed and built the optical turbulence generator and the general setup of the testbed during his master thesis. Dr. Ramon Mata-Calvo contributed with many valuable programs for the real-time evaluation of Shack-Hartmann images and the Fourier Fringe Analysis technique. Dr. Perlot contributed software tools for the evaluation of DIMM and turbulence profiler. Joachim Horwath contributed numerical simulations of the atmospheric conditions in the SGL

scenarios with the DLR tool PiLab. Several students have taken part in the programming of the measurement instruments and the telescope mount software to perform the orbit satellite tracking.

The main aspects of my own work in this PhD thesis are:

- Responsibility for the planning and construction of the DLR optical ground station. Development of large parts of the software.

- Development of the optical/mechanical design and setup of the atmospheric measurement instruments of the DLR ground station, which was used for the measurements of the atmospheric channel in SGL scenarios (Chapter 3).

- Development of a Shack-Hartmann sensor evaluation software (Matlab), which was used to obtain estimates of the atmospheric turbulence in the SGL scenarios.

- Literature survey of potential wavefront sensors suitable for the deployment in SGL scenarios. Evaluation of the wavefront sensors' performance (theory and simulations) under the relevant atmospheric conditions, including strong scintillation, phase distortions, phase singularities, and bandwidth requirements (Chapter 4). To my knowledge this has not been done in such a comprehensive manner before, although of course individual sensors had been characterized under strong turbulence conditions.

- Detailed theoretic and simulatory evaluation of interferometric sensors including several concrete system setups, which promise good performance in terms of robustness to strong scintillation and speed (Chapter 5). These methods are mainly known from optical shop testing. In this work special attention is given to strong phase distortions with intensity fluctuations caused by atmospheric turbulence and the increased bandwidth requirements caused by the satellite motion.

- Test and evaluation of the performance of a promising interferometric measurement method with one interferometer (Fourier Fringe Analysis, Section 5.3.1) in the DLR lab testbed (Chapter 6). Dr. Ramon Mata-Calvo and I jointly designed and setup the interferometric test system.

Due literature reference is given in all places, where I have used the work and results of other authors.

List of personal references with relation to the topic:

F. Fidler, M. Knapek, J. Horwath, and W. R. Leeb, "Optical communications for high altitude platforms," IEEE J. Sel. Top. Quantum Electron. (accepted 2010).

D. Giggenbach, J. Horwath, and M. Knapek, "Optical data downlinks from earth observation platforms," SPIE Free-Space Laser Communications XXI (San Jose, 2009).

J. Horwath, M. Knapek, B. Epple, and M. Brechtelsbauer, "Broadband backhaul communication for stratospheric platforms: results of the stratospheric optical payload experiment," SPIE Free-Space Laser Communications VI (San Diego, 2006).

T. Jono, Y. Takayama, K. Shiratamab, I. Maseb, B. Demelennec, Z. Sodnik, A. Bird, M. Toyoshima, H. Kunimori, D. Giggenbach, N. Perlot, M. Knapek, and K. Arai, "Overview of the inter-orbit and orbit-to-ground laser communication demonstration by OICETS," SPIE Free-Space Laser Communication Technologies XIX and Atmospheric Propagation of Electromagnetic Waves (2007).

M. Knapek, J. Horwath, N. Perlot, and B. Wilkerson, "The DLR ground station in the optical payload experiment (STROPEX) – Results of the atmospheric measurements instruments," SPIE Free-Space Laser Communications VI, (San Diego, 2006).

M. Knapek, "Conditions for adaptive optics in LEO satellite-to-ground links," 7th Workshop on Adaptive Optics for Industry and Medicine (Shatura, 2009, to be published 2010).

M. Knapek and R. Mackey, "Adaptive Optics" in *High Altitude Platforms and Their Applications,* Springer Verlag, Editor T. Tozer, Sub-Editor M. Knapek (to be published 2010).

F. Moll and M. Knapek, "Wavelength selection criteria and link availability due to cloud coverage statistics and attenuation affecting satellite, aerial, and downlink scenarios," SPIE - Free-Space Laser Communications VII **6709** (2007).

F. Moll, *Conception and Development of an Adaptive Optics Test-bed for Free-Space Optical Communication* (Master Thesis, Supervisor M. Knapek, A. Koch, Munich, 2009).

N. Perlot, M. Knapek, D. Giggenbach, J. Horwath, M. Brechtelsbauer, Y. Takayama, and T. Jono, "Results of the optical downlink experiment KIODO from OICETS satellite to optical ground station Oberpfaffenhofen (OGS-OP)," SPIE Photonics West, Free-Space Laser Communication Technologies XIX (San Jose, 2007).
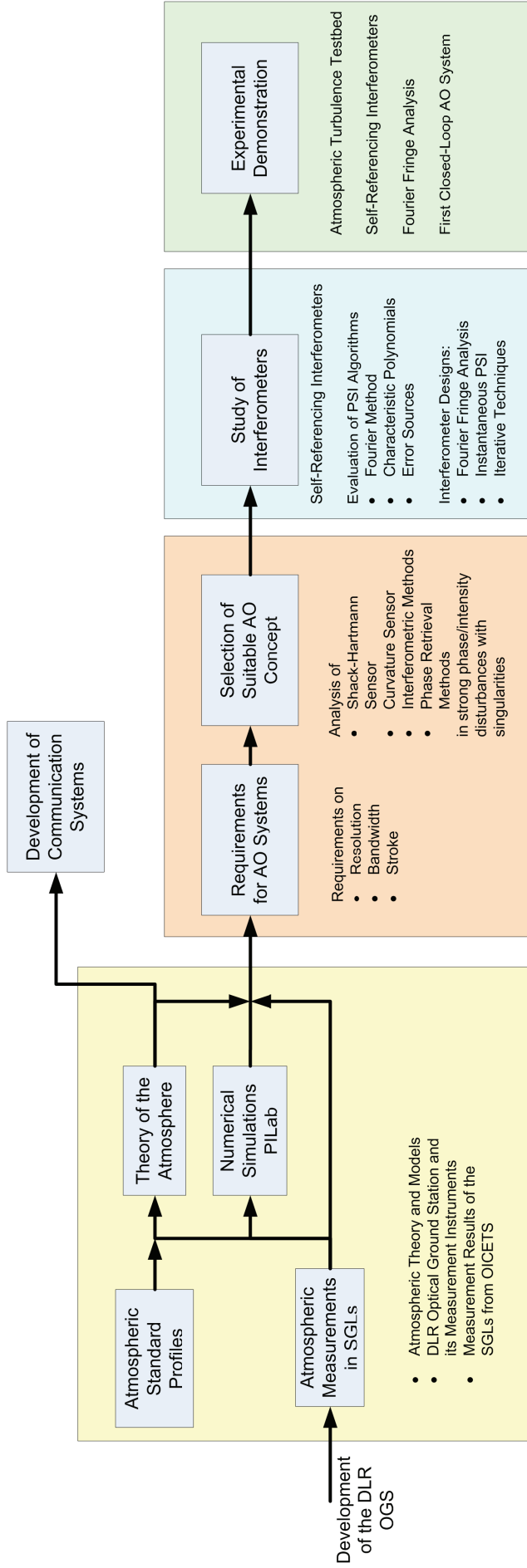
Figure 1.9: Summary and overview of the thesis with the four main parts: Atmospheric conditions, selection of a suitable wavefront-sensor concept for the atmospheric conditions in SGLs, analysis of interferometric sensors, and the experimental verification of an interferometric sensor in the atmospheric turbulence testbed.

2 Laser Communications and the Impact of the Atmosphere

Chapter 2 describes general aspects of satellite-to-ground communication links (SGL) including link durations and elevation angles, but also some general thoughts on coherent and direct-detection communication techniques.

2.1 Design of Optical Communication Systems in Satellite-To-Ground Links

This section gives an overview of currently existing optical communication terminals (OCT) and optical ground stations (OGS) to illustrate typical technical designs of these systems in SGLs.

2.1.1 Satellite Optical Communication Terminals

Figure 2.1 shows the Laser Communication Terminal (LCT) on TerraSAR-X. This terminal was built for inter-satellite links (ISL) between LEO satellites, i.e. for distances of 500-5000km. This system is the most advanced of the terminals up to date, providing 5.6Gbps communication rate. The modulation format is a coherent binary phase shift keying technique, which offers high sensitivity and a very good background-light rejection; however, the system was not designed for atmospheric SGLs. In principle coherent systems are sensitive to phase distortions but also suffer from scintillation like the direct-detection systems. So far the ground receivers were implemented small enough with a receiver diameter of 6.5cm to avoid wavefront distortions over the aperture, but scintillation had a very deteriorating effect on the communication. Larger telescope areas reducing the scintillation due to aperture averaging are only feasible with an active wavefront correction. A second terminal of the LCT series was installed on the American LEO satellite NFIRE.
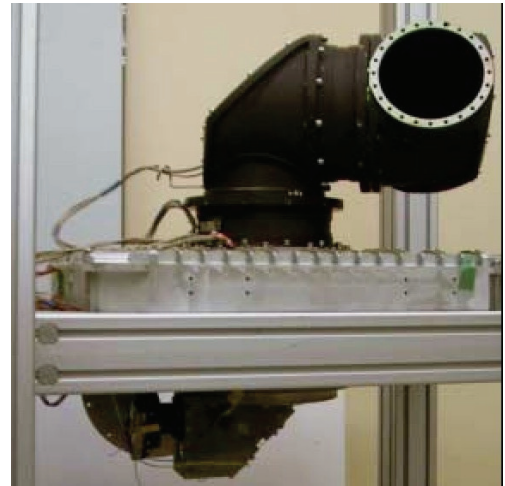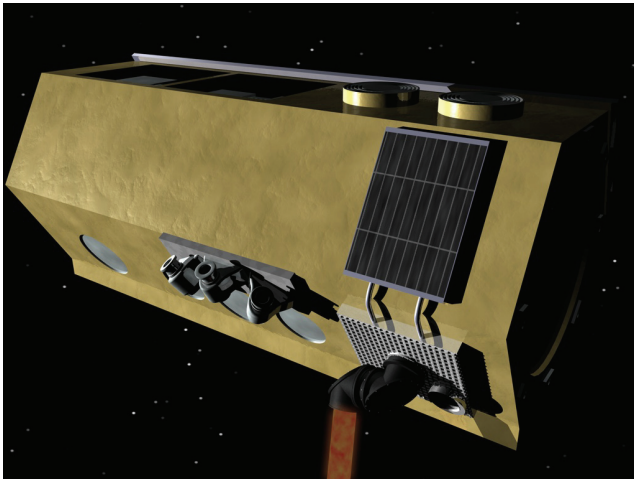
Figure 2.1: The Laser Communication Terminal LCT on the German LEO satellite TerraSAR-X. Left: Artist's impression of the LCT on TerraSAR-X; Right: The engineering model of the LCT in the system testbed at Tesat Spacecom.

Figure 2.2 depicts the 25cm aperture terminal PASTEL installed on the European geostationary communication satellite ARTEMIS. This system was already designed in the 1990s to demonstrate ISLs with the French LEO satellite SPOT-4. The 50Mbps laser link was intended to transmit remote-sensing date from SPOT-4 to ARTEMIS. The link to the ground was implemented by a conventional microwave link, although laser links from

ARTEMIS to the ground were successfully demonstrated (albeit only 2Mbps) to the 1m telescope of the ESA OGS on Tenerife.

Figure 2.2: The terminal PASTEL on the geostationary satellite ARTEMIS.

Figure 2.3 shows the 26cm aperture OCT LUCE on the Japanese LEO satellite OICETS. This system was designed to be compatible with the European ARTEMIS. Apart from the successful ISLs, LUCE was extensively used to demonstrate SGLs to ground stations in Japan, Europe, and the USA.

Table 2.1 summarizes the most important parameters of the presented satellite terminals to give a general idea of the design data of such systems.
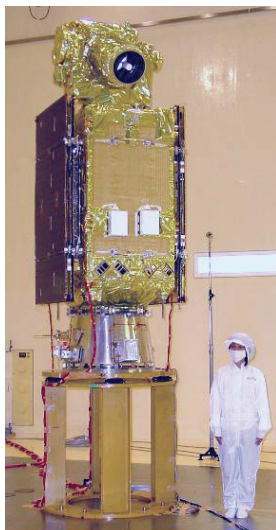
Figure 2.3: The OCT LUCE on the Japanese LEO satellite OICETS. Left: LUCE during the integration on OICETS; Right: LUCE in the laboratory.

Table 2.1: Satellite optical communication terminals [GIG09][PLA04][SOD06][PER07].

Satellite	Spot 4	ARTEMIS	OICETS	TerraSAR-X
Communication Terminal	OPALE	PASTEL	LUCE	LCT
Launch Date	24th March 1998	12nd July 2001	23rd Aug. 2005	15th June 2007
Satellite Type	LEO	GEO	LEO	LEO
Link Types	ISL LEO-GEO	ISL LEO-GEO, SGL	ISL LEO-GEO, SGL	ISL LEO-LEO, (SGL)
Channel Data Rate TX/RX	50/2Mbps	2/50Mbps	50/2Mbps	5.6/5.6Gbps
Orbit Altitude	850km	35800km	610km	514km
Distance in SGL	n.a.	~38000km	2540 .. 610km	1728 .. 514km
Min. Elevation with Tracking-Lock	n.a.	n.a.	3°	~10°
Modulation Format	IM/DD NRZ	IM/DD BPPM	IM/DD NRZ	homodyne BPSK
Communication TX-Power	60mW	37mW	100mW	0.7W
Wavelength TX/RX	847nm/819nm	819nm/847nm	847nm/819nm	1064nm/1064nm
Downlink Beam Divergence FWHM	<10µrad	<10µrad	5.5µrad	<10µrad
TX Aperture	125mm	200mm	260mm	135mm
RX Aperture	250mm	250mm	260mm	135mm
DLR OGS Uplink Beacon	n.a.	819nm	808nm	1064nm

2.1.2 Optical Ground Stations

This section presents some optical ground stations (OGS) as they are currently operated. The ESA OGS (Figure 2.4) is located on Tenerife at the astronomical site Izana. It has a 1m telescope, which was originally used for the demonstration of laser SGLs from ARTEMIS. Atmospheric conditions at the altitude of 2393m are very favorable. The station is only partly suitable for LEO SGLs, as mount and also the dome were designed for astronomical observations and GEO SGLs. The 1.5m NICT OGS (Figure 2.5) is located directly in the city

of Tokyo, only slightly above the sea-level, which brings rather poor atmospheric conditions. The ground terminal of Tesat Spacecom (Figure 2.6) intended as a counter terminal on the ground for the TerraSAR-X SGLs is mounted on a transportable container. It already was operated in Germany (Oberpfaffenhofen, Backnang), Spain (Calar Alto, Tenerife) and in the USA (Maui). Especially the locations outside Germany were chosen at extremely favorable sites above 2000m altitude to improve the SGL performance from TerraSAR-X. The DLR OGS is described in Section 3.2 with Figure 3.20. Table 2.2 summarizes parameters of those four OGSs to give an impression of typical ground stations as they are currently used.

Figure 2.4: ESA OGS on the Canary island Tenerife. Left: Building of the OGS; Right: The 1m telescope with the paraxial mount.
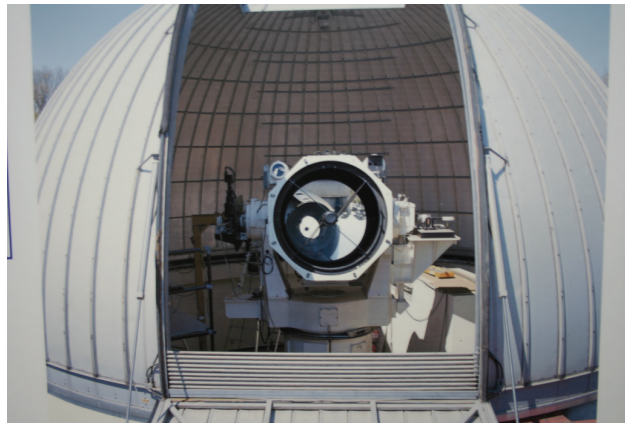
Figure 2.5: 1.5m telescope of the NICT OGS in Tokyo.

Figure 2.6: Laser Communication Terminal (LCT) with a 6.5cm aperture during the SGL experiments in Oberpfaffenhofen 2007.

Table 2.2: Ground stations for laser SGLs

Ground Station	DLR OGS	NICT OGS	ESA OGS	Tesat LCT (ground)
Location	Oberpfaffenhofen, Germany	Tokyo, Japan	Tenerife, Spain	Mobile Container
Height above Sea-Level	653m	122m	2393m	n.a.
Link Types	LEO	LEO	GEO, LEO	LEO
Satellites	OICETS TerraSAR-X Aircraft Downlinks @1550nm	OICETS TerraSAR-X	OICETS ARTEMIS TerraSAR-X	TerraSAR-X
RX Aperture	0.4m	0.2m or 1.5m	1m	0.065m
OGS Uplink Beacon[*]	2x8W@808nm, CW, 5mrad 2x5W@1064nm, Pulsed, 5mrad 2x5W@1550nm, CW	30W@808nm CW, 9mrad[†] 10mW@815nm, BPPM, 204μrad[‡] 5W@1064nm, CW	0.3W@847nm, CW 14W@1064nm, Pulsed, 1mrad	1W@1064nm, BPSK, 7μrad

[*] Divergence angle, full cone $1/e^2$
[†] NICT OGS beacon laser for the OICETS SGLs
[‡] NICT OGS communication laser with a 2PPM modulation at 2.048Mbps

2.2 Satellite Orbits in Laser Satellite-To-Ground Communication Links

In this thesis special emphasis is given LEO SGLs. LEO satellites move in about 10 minutes over the sky (horizon to horizon). The consequence of this is, that most of the time, the satellite is seen under low elevation angles and that the communication duration is rather short. Figure 2.7 shows an example pass of the Japanese satellite OICETS with a maximum elevation of around 70 degrees. The orbit is a near-polar orbit with around 98 degrees inclination and an orbit height of about 600km. Link duration for this pass is approximately 12.5 minutes. The range satellite-ground station is between 600km in the zenith to 2800km at the horizon. The laser beam moves with a small angular velocity close to the horizon due to the large link distance, but travels a long path through very turbulent parts of the atmosphere. At the zenith the angular velocity increases, but the beam has a much shorter fraction of the distance in the thick atmosphere at low altitudes.
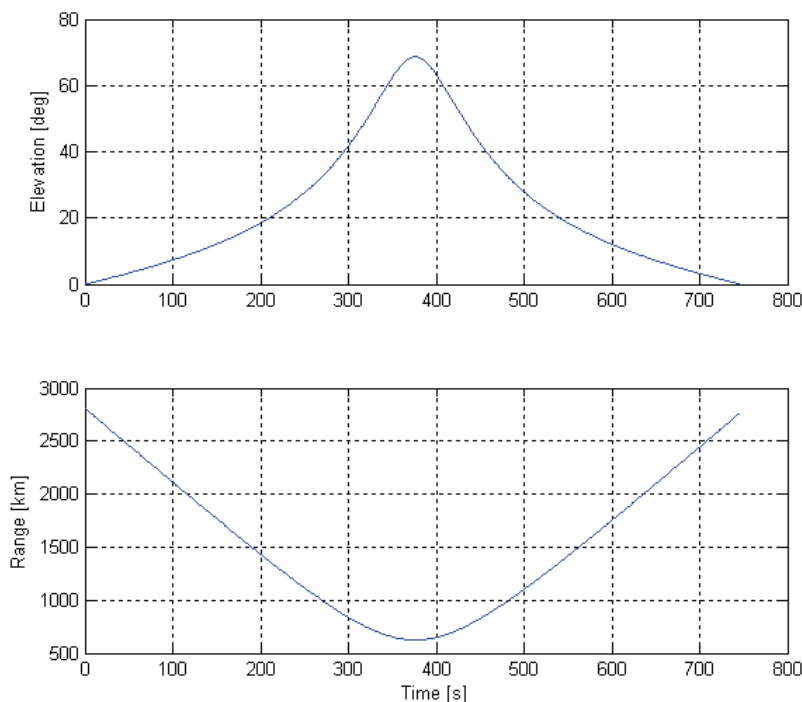
Figure 2.7: Typical LEO satellite pass, here as an example the Japanese satellite OICETS with a polar orbit (98deg inclination) and an orbit height of about 600km.

The German LEO satellite TerraSAR-X also has a similar orbit with 97.4 degrees inclination and around 508km orbit height. Its orbit is precisely tailored to an 11 day repeat cycle. This means, that the satellite repeats its track above the ground every 11 days. Its orbit is sun-synchronous, so that TerraSAR-X is always visible at the same time during sunrise or sunset. TerraSAR-X's orbit is illustrated in Figure 2.8. Figure 2.9 shows the elevation angles of TerraSAR-X for the ground station site Oberpfaffenhofen during the 11 day cycle (=264 hours). Satellite passes occur always in the morning or evening with 2-3 passes in a row, about 1.5 hours apart equaling one orbit. Between these packets of satellite passes, the satellite is not visible for 10-12 hours. It can be seen that most of the links have low elevation angles below 30 degrees elevation. Only 18 passes have maximum elevation angles of more than 30 degrees. This becomes even more obvious in Figure 2.10, which shows the share of the link time as a function of the elevation angle. The satellite is 90% of the overall link time visible below 30 degrees elevation. This illustrates the need for operational laser links at low elevation angles.
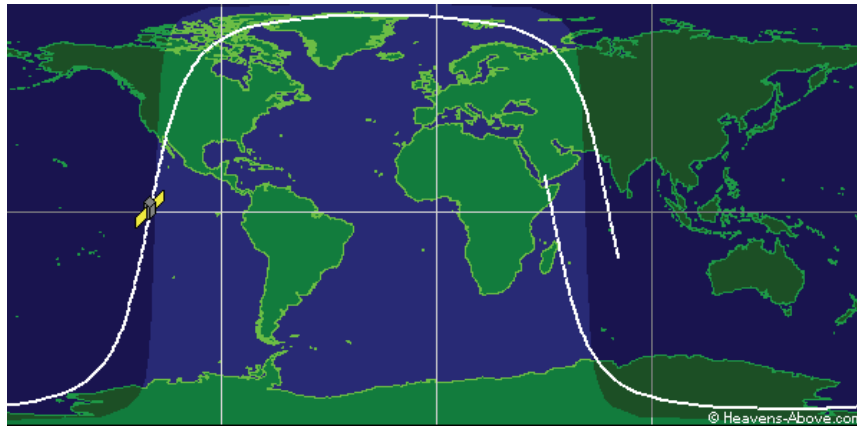
Figure 2.8: Ground track of the sun-synchronous, polar orbit of TerraSAR-X. The brighter regions are lit by the sun, the shaded areas are night time regions (from Heavens-Above.com).
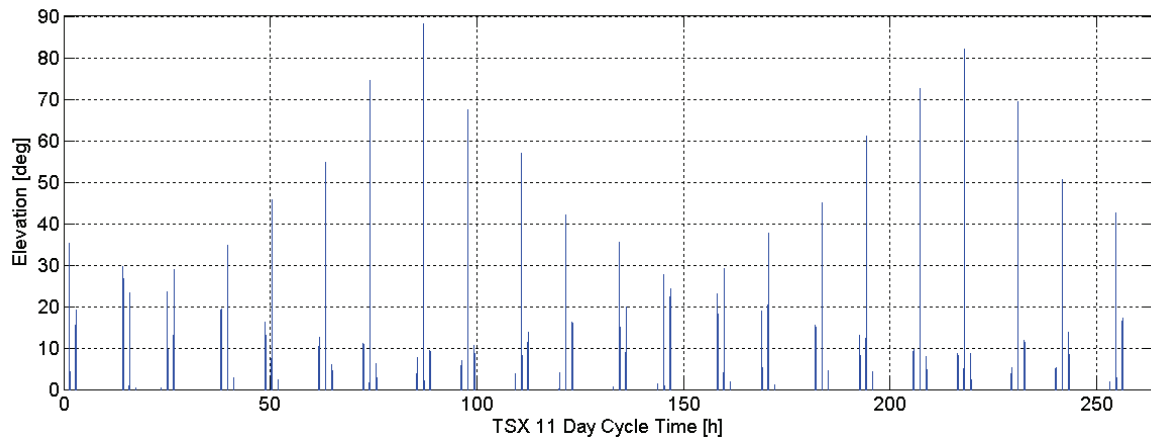
Figure 2.9: Elevation angles for the TerraSAR-X passes in the 11 days sun-synchronous orbit cycle. Each blue vertical line indicates a satellite pass.
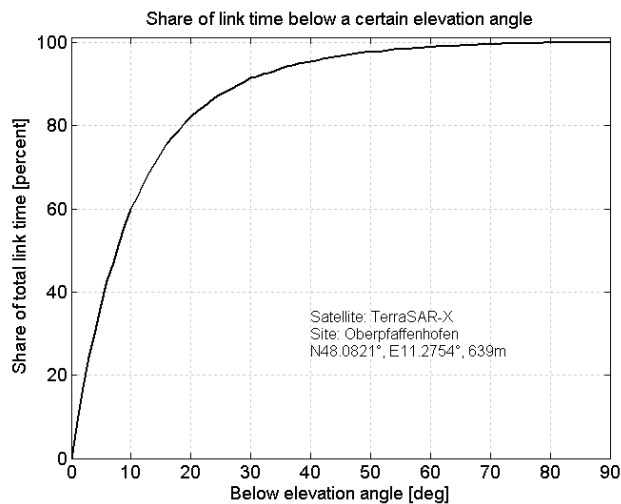
Figure 2.10: Share of the link time for TerraSAR-X SGLs. It can be seen, that 90% of the total link time is below 30deg elevation.

Figure 2.11 shows the elevation angle for several example passes of TerraSAR-X with different maximum elevation angles. The graph shows, that the link duration has only a weak dependence on the maximum elevation angle. A pass with 82 degrees maximum elevation

19

has a link duration of 11.5 minutes, whereas the low pass with only 10 degrees takes 9 minutes.
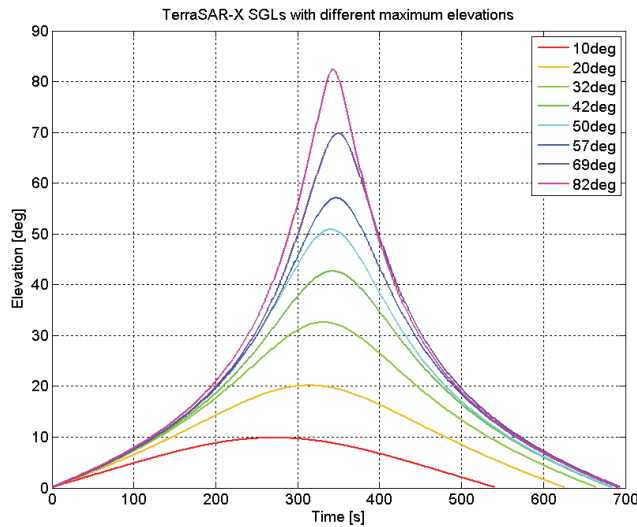
Figure 2.11: Elevation angle of different TerraSAR-X passes with different maximum elevation.

2.3 Direct-Detection and Coherent Optical Communication Systems

This section gives a short overview on communication systems as they are used in the SGL scenarios. Two principle types of communication systems can be distinguished: Non-coherent direct-detection systems with an intensity modulation (IM/DD) and coherent superposition receivers [GIG04][RYU04][MAJ08][DAV04b].

In the case of an IM/DD system, the transmitter modulates the laser-beam intensity to transmit the information to the receiver. In the simplest case this is done in a binary fashion with an on-off amplitude modulation. The receiver then recovers the information bits simply from the course of the detected power. This technique has been used for the communication terminals on ARTEMIS, SPOT-4, and OICETS.

In coherent systems the information can be modulated on the amplitude (amplitude-shift keying ASK), the frequency (frequency-shift keying FSK), the phase (phase-shift keying PSK), or the polarization of the transmission beam. The beam at the receiver is superposed with a controlled laser, the local oscillator (LO). If the local oscillator has precisely the same frequency as the received signal, the system is called homodyne, or otherwise heterodyne. The most sensitive method is binary PSK with a homodyne receiver (homodyne BPSK), i.e. the local oscillator is exactly controlled (phase-locked) to the frequency of the transmit laser. This technique has been implemented in the Laser Communication Terminals by Tesat Spacecom.

Different receiver types can be compared by the number of photons per bit (Ph/b) required for a certain bit-error rate [BAR90]. The theoretic limit for a homodyne BPSK system is 9Ph/b. A heterodyne BPSK system is a factor 2 less sensitive with 18Ph/b. IM/DD systems require theoretically 20Ph/b for "1" bits. Coherent communication systems have the advantage that real systems outside the laboratory get close to the theoretic limits. The performance of IM/DD systems is significantly worse. Realistic systems often require 400Ph/b. An extensive list on publications of optical receiver sensitivities was collected by Caplan in [MAJ08, pp. 212].

In addition, coherent communication systems have the advantage that they are very insensitive to background light, as the coherent superposition produces a very narrow filtering of the signal at the communication frequency. IM/DD systems can be only protected

from background light by optical interference filters, which typically have a transmission bandwidth of some nano-meter.

Both techniques are sensitive to intensity fluctuations of the input signal caused by atmospheric turbulence, however only the coherent receivers suffer from wavefront distortions.

Figure 2.12 shows the design of a basic IM/DD receiver. The signal is directly taken from a photo-diode via a trans-impedance amplifier. An advantage of IM/DD receivers is the simplicity. Coherent receivers are more complex due to the LO as shown in Figure 2.13. The phase-locked LO and the received signal are combined with a beam-splitter cube or a fused fiber coupler to produce the superposed signals.
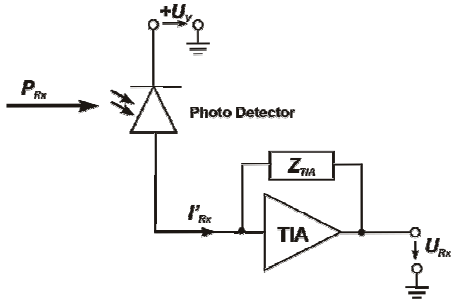
Figure 2.12: Direct detection receiver.
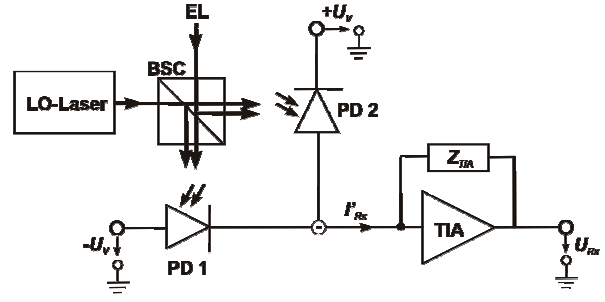
Figure 2.13: Balanced coherent receiver system using both outputs of the coupler. [GIG04]

Writing the signal and the local oscillator electric field

$$U_S = |U_S| \cdot e^{i\omega_S t + i\varphi_S(t)}$$

$$U_L = |U_L| \cdot e^{i\omega_L t - i\varphi_L}$$

with the frequencies ω_S, ω_L and the phase shifts $\varphi_S(t), \varphi_L$, the output signal is given by [RYU94]

$$
\begin{aligned}
I &= |U_L + U_S|^2 \\
&= I_L + I_S + 2\sqrt{I_L I_S} \cos\left[(\omega_S - \omega_L) t + \varphi_S(t) + \varphi_L \right]
\end{aligned}
\tag{2.1}
$$

The information of a PSK modulation is contained in $\varphi_S(t)$. The mixing process is governed by the square-law of the photo-diode. If the two frequencies are the same ($\omega_S - \omega_L = 0$) with an accurately phase-locked local oscillator, Eq. (2.1) becomes

$$I = I_L + I_S + 2\sqrt{I_L I_S} \cos\left[\varphi_S(t) + \varphi_L \right], \tag{2.2}$$

now describing a homodyne receiver. Assuming a balanced receiver as in Figure 2.13, using both arms of the beam splitter, the DC components disappear and the signal increases by a factor 2

$$I = 4\sqrt{I_L I_S} \cos\left[\varphi_S(t) + \varphi_L \right].$$

2.4 Coherent Receivers and Fiber Coupling

In the formulas of Section 2.3 a perfect match of the local oscillator wavefront and signal wavefront was assumed. In this section a more realistic approach with the heterodyne efficiency is discussed taking wavefront mismatches into account. Interesting to note is, that the same approach can be used to describe fiber coupling efficiency for a single-mode fiber. Details on efficiency calculation can be found for example in [COH75][WAG82][RUI01].

The incoming wavefront is described in the entrance pupil of the telescope by

$$P_\varphi(\vec{r}) = W_0(\vec{r}) \cdot A_0(\vec{r}) \cdot \exp(i\varphi(\vec{r})), \qquad (2.3)$$

where W_0 denotes the pupil/aperture transmittance function

$$W_0(\vec{r}) = \begin{cases} 1 & if \quad r < R \\ 0 & otherwise \end{cases}. \qquad (2.4)$$

$R = D/2$ gives the telescope aperture radius. $A_0(\vec{r})$ and $\varphi(\vec{r})$ respectively describe the amplitude and phase of the field. Central in the calculation of fiber coupling and heterodyne/homodyne efficiencies is the normalized overlap integral over the telescope aperture $A = \pi R^2$

$$\eta_{het} = \frac{\left| \iint_A P_\varphi(\vec{r}) M_0^*(\vec{r}) d^2r \right|^2}{\sqrt{\left[\iint_A |P_\varphi(\vec{r})|^2 d^2r \right] \left[\iint_\infty |M_0(\vec{r})|^2 d^2r \right]}}. \qquad (2.5)$$

Using Parseval's theorem (see Appendix A.1.3) Eq. (2.5) can be equally used in the focus plane. Here the integral area is given by the detector size with $A = \pi r_d^2$. The aperture transmittance function is in both cases implicitly contained in the integral over the circular area A.

In the case of a coherent homodyne/ heterodyne receiver $M_0(\vec{r})$ represents the reference field of the local laser, which takes the shape of a Gaussian profile. For single-mode fiber coupling $M_0(\vec{r})$ represents the mode distribution in the fiber, which can be also approximated by a Gaussian distribution. So even in the case of a perfectly plane signal wave from the counter terminal, i.e. without any atmospheric disturbances, the overlap integral has a maximum value of around 0.8 due to the mismatch of the plane signal wave and the Gaussian local oscillator or the Gaussian-type fiber mode.

In principle a Gaussian mode with the *1/e* waist radius is given by

$$M_0(\vec{r}) = A \exp\left(\frac{-r^2}{w_0^2} \right). \qquad (2.6)$$

For a single-mode fiber with step-index profile the mode radius w_0 in the fiber is well approximated by [NEU88]

$$w_0 = a\left(0.65 + 1.619 V_f^{-3/2} + 2.879 V_f^{-6} \right)$$

or in a different approximation by [THI04]

$$w_0 = \frac{a}{\sqrt{2 \cdot \log_{10}(V_f)}} .$$

(2.7)

V_f denotes the fiber normalized frequency and a the fiber core radius. The two approximations are compared in Figure 2.14. The V_f number, which is closely related to the number of guided modes in the fiber, is calculated by [SAL91]

$$V_f = \frac{2\pi a}{\lambda} \sqrt{n_{co}^2 - n_{cl}^2} ,$$

(2.8)

where the numerical aperture $NA = \sqrt{n_{co}^2 + n_{cl}^2}$ is given from the index of refraction in the core n_{co} and in the fiber cladding n_{cl}. A V_f number smaller than 2.405 describes a single-mode fiber.
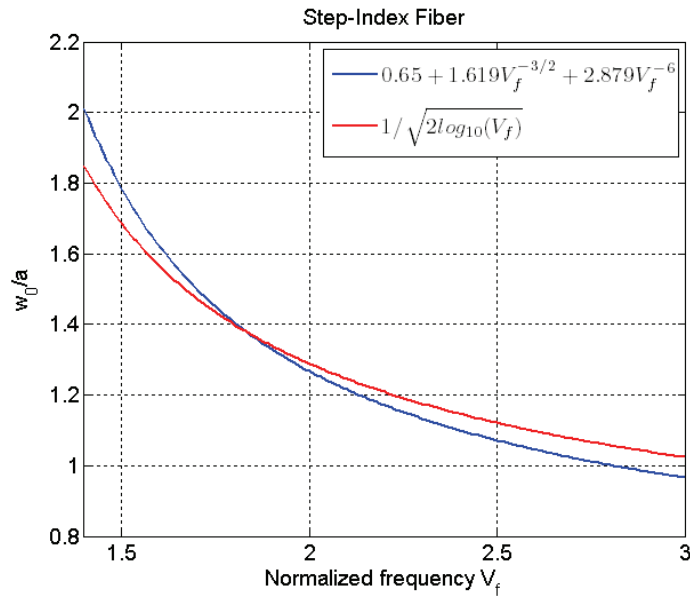
Figure 2.14: Ratio w_0/a for step-index fibers as a function of the normalized frequency V_f (2.8).

Cohen [COH75] derived in detail formulas for the overlap integral Eq. (2.5) for various distributions of the signal and local oscillator. The most relevant in the discussion of a coherent receiver or fiber-coupled receiver is a Gaussian local oscillator

$$U_L(r) \propto e^{-\frac{r^2}{w^2}}$$

(2.9)

and an Airy distribution of the signal wave imaged into the focus plane with a focal length f

$$U_S \propto \frac{J_1\left(\frac{\pi D_{Rx}}{\lambda f} r\right)}{\frac{\pi D_{Rx}}{\lambda f} r} .$$

(2.10)

Putting Eq. (2.9) and (2.10) into (2.5) and using the integration formula $\int_0^\infty \frac{J_1^2(x)}{x}dx = \frac{1}{2}$, the coupling efficiency η_{het} for a single-mode fiber with a mode diameter of w_0, the telescope diameter D_{Rx}, the focal length f, the detector radius r_d, and the wavelength λ results to

$$\eta_{het} = 2 \cdot \frac{\left[\frac{2}{w_0} \int_0^{r_d} J_1\left(\frac{\pi D_{Rx}}{\lambda f} r \right) e^{-\frac{r^2}{w_0^2}} dr \right]^2}{1 - e^{-2\frac{r_d^2}{w_0^2}}} . \tag{2.11}$$

The ratio between the Airy diameter to the first zero crossing and the mode diameter in the single-mode fiber has to fulfill

$$\frac{D_{Airy}}{2w_0} = 1.72 \tag{2.12}$$

to achieve maximum coupling efficiency. The Airy diameter to the first zero-crossing for an undisturbed plane wave is given by

$$D_{Airy} = 2.44 \cdot \frac{\lambda f}{D_{Rx}} . \tag{2.13}$$

The optimum focal length for a given aperture diameter and a given mode diameter in the fiber is then calculated by

$$\frac{w_0 D_{Rx}}{f\lambda} \approx 0.71 \text{ or } f \approx 1.408 \cdot \frac{\omega_0 \cdot D_{Rx}}{\lambda} . \tag{2.14}$$

With these parameters the optimum coupling efficiency respectively homodyne/heterodyne coupling efficiency is limited to

$$\eta_{het} \approx 0.81 . \tag{2.15}$$

This theoretic limit is caused by the mismatch of the plane incoming wave and the Gaussian mode of the single-mode fiber, or expressed in the focus plane, a mismatch of the Airy distribution caused by the circular aperture of the entrance pupil and the Gaussian mode of the single-mode fiber. An equivalent calculation can be given for heterodyne/homodyne efficiencies.

Figure 2.15 shows the fiber coupling efficiency for an example setup. Obviously the maximum efficiency is 0.81 at the point defined in Eq. (2.14), from which the correct F-number of the telescope can be derived. Figure 2.16 then shows the amplitude distributions for the Airy and Gaussian distribution in the case of the best match. A telescope aperture of D_{Rx}=0.4m was assumed yielding an optimum focal length of 1.18m.
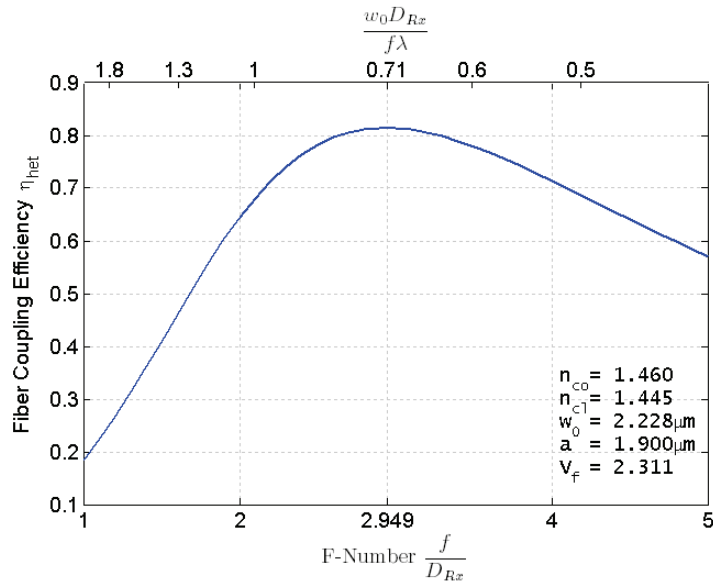
Figure 2.15: Fiber-coupling efficiency as a function of the telescope F-number. The assumed parameters of the single-mode fiber are shown in the right bottom corner of the graph. The top horizontal axis shows that Eq. (2.14) is fulfilled for a maximum efficiency.
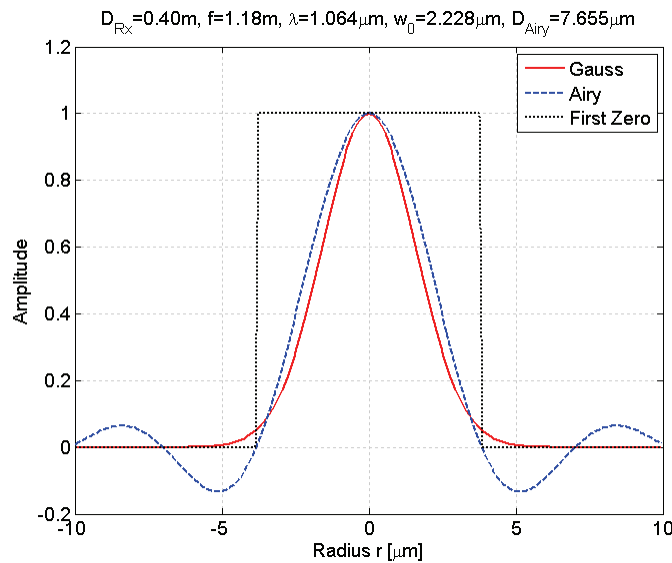
Figure 2.16: Best match of Airy and Gaussian (fiber) distribution according to Eq. (2.14) with the same fiber as in Figure 2.15. Coupling efficiency is $\eta_{het} = 0.81$. The rectangular area denotes the sensor area, which should be of the same size as the Airy distribution to the first zero.

The approximation of the Strehl ratio (see Section 4.1.3) in dependence of the phase variance σ_φ^2 of the received wave

$$S_1 \approx \exp\left(-\sigma_\varphi^2\right)$$

can be also used to estimate the normalized coupling efficiency $\eta_{het}\left(\sigma_\varphi^2\right)/\eta_{het,\max}$. According to Ruilier [RUI98] the Strehl ratio underestimates the coupling efficiency. He also showed, which of the Zernike modes have a particularly detrimental effect on the coupling efficiency.

25

2.5 Motivation for Adaptive Optics in Communication Scenarios

In the last decades several high-performance free-space laser communications systems have been developed, achieving very high data rates of several Gbps. The Laser Communication Terminal (LCT) on TerraSAR-X transmitted with 5.6Gbps with a coherent BPSK modulation scheme [LAN05]. In 2009 Ciaramella et al. [CIA09] presented a free-space laser communication based on single-mode fiber components for a transmission over 2x212m (transmitter and receiver were at the same side) with a wavelength division multiplex (WDM) transmission scheme. Each of the 32 WDM channels had a transmission rate of 40Gbps, resulting in a total rate of 1.28Tbps. Especially fiber-coupled systems with such data rates are only possible with the help of commercially available components from the fiber communication industry.

Both systems, the LCT and the 1.28Tbps system, require an undisturbed plane wave over the receiver aperture to guarantee reasonable heterodyne and fiber-coupling efficiencies. This can be achieved if the receiver aperture is smaller than the atmospheric coherence length. The LCT ground terminal had an aperture diameter of 6.5cm and the fiber-coupled system of 2.4cm. For larger apertures the phase distortions over the aperture become significant. Small apertures however mean, that the link budget quickly proves to be a limiting element and scintillation become very strong on longer paths through the atmosphere with very deep fades causing outages of the communication link. Scintillation can be only decreased with the averaging effect of a larger aperture.

Consequently, if coherent or fiber-coupled communication systems are used in long atmospheric communication scenarios, some means of correcting the disturbed incident wave has to be applied and thus enable the application of larger receiver apertures. The impact of the atmosphere becomes especially pressing for SGL scenarios at low elevation angles, where the atmospheric coherence length is very small and scintillation is very strong.

3 Atmospheric Models and Measurements

Chapter 3 gives an overview on atmospheric effects in laser satellite-to-ground communications. Section 3.1 presents theoretic concepts including atmospheric attenuation and cloud considerations, turbulence standard models, and atmospheric turbulence models based on the Rytov theory. Section 3.2 gives a short overview of the atmospheric measurement instruments of the DLR ground station, which were used in several measurement campaigns. The measurement results are presented in Section 3.3.

3.1 Laser Beam Transmission through the Atmosphere

There are three principle effects affecting the transmission of a laser beam through the atmosphere:

- Atmospheric attenuation due to absorption and scattering (Section 3.1.1)
- Attenuation/blockage of the link due to clouds (Section 3.1.2)
- Refractive-index effects due to atmospheric turbulence (Section 3.1.3 and 3.1.4).

Atmospheric turbulence of course is most important for phase distortions and scintillation effects concerning adaptive optics (AO), however attenuation and clouds are also briefly addressed here, as they play a crucial role for communication links.

3.1.1 Atmospheric Attenuation

Laser beam attenuation in the atmosphere is described by Beer's law [SMI93]:

$$T_{Beer} = \frac{I_L}{I_0} = e^{-\int_0^L \left\{ \sum \alpha_{ext}(\lambda, z) \right\} dz} \ .$$

(3.1)

It yields the transmission of a beam path through the atmosphere with the extinction coefficient α_{ext} and the path length L. α_{ext} has a strong dependence on the altitude above sea-level and changes with the wavelength λ. The transmission T_{Beer} gives the ratio between the output intensity I_L and the input intensity I_0. Beer's law usually is used to describe molecular absorption and scattering of the clear atmosphere, but it can also be applied for attenuation in clouds.

The atmospheric extinction coefficient is shown in Figure 3.1 as an example in the wavelength range from 500nm to 2000nm. It can be seen, that typical communication wavelengths like 1064nm or 1550nm have low extinction coefficients and represent suitable transmission windows for satellite-to-ground links (SGL).
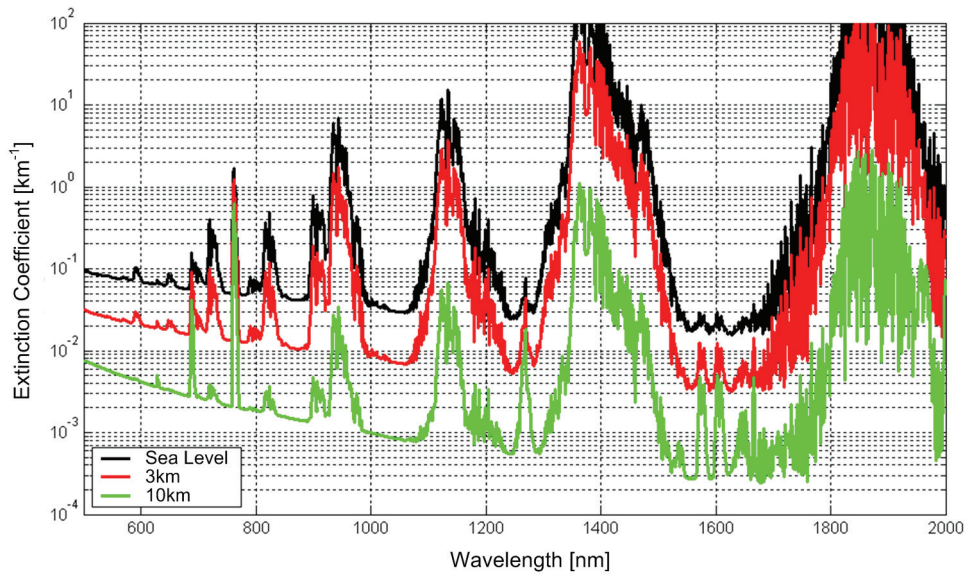
Figure 3.1: Extinction coefficient between 500 and 2000nm for three altitudes (sea-level, 3km, 10km) [DAV04].

Transmission windows in the optical domain are plotted in Figure 3.2, also showing other atmospheric transmission windows with low absorption values, numbered from 1 to 9. The limit for usable long wavelengths is given by the atmospheric window between 7.5µm and 15.0µm. Above this window laser communication through the atmosphere is prevented by water-vapor absorption.
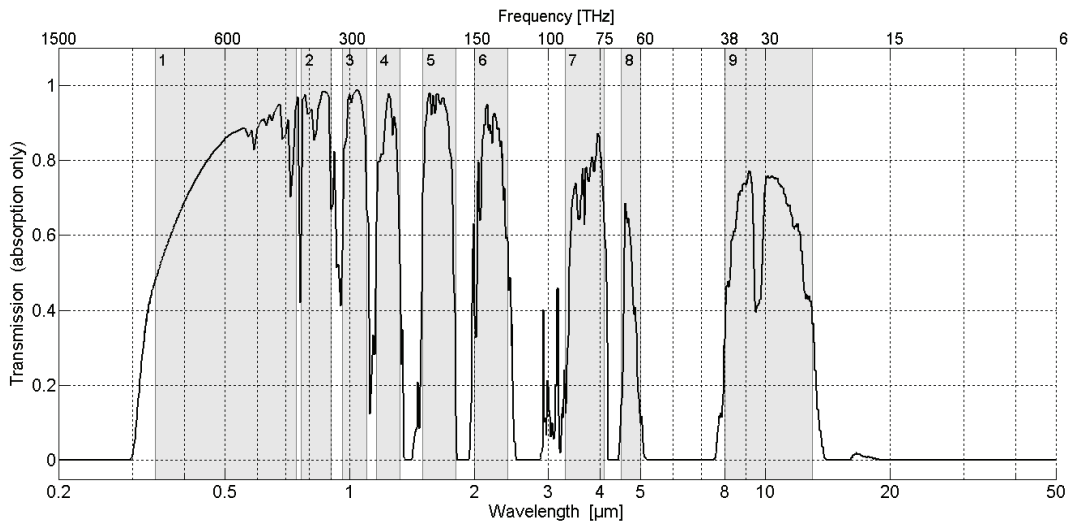
Figure 3.2: Transmission through the atmosphere in a vertical path e.g. for a satellite-to-ground link. Transmission windows are marked in gray [MOL07].

3.1.2 Clouds and Ground Station Diversity

Clouds pose a challenging issue for SGLs as they strongly influence the availability of the communication links. Already relatively thin clouds totally block laser beams. Thus, it is important to establish ground stations for SGLs at locations, where the probability of cloud coverage is low. Figure 3.3 shows the mean cloud coverage over Europe based on data from

the European Cloud Climatology (ECC) project. The images were taken by the AVHRR/3 (Advanced Very High Resolution Radiometer Version 3), which is a payload of the NOAA satellites.

Cloud coverage in southern regions of Europe is significantly lower than in the north. Thus, ground stations in Europe should be as far as possible located closer to the Mediterranean Sea, where the average availability of a single ground stations reaches 70%.
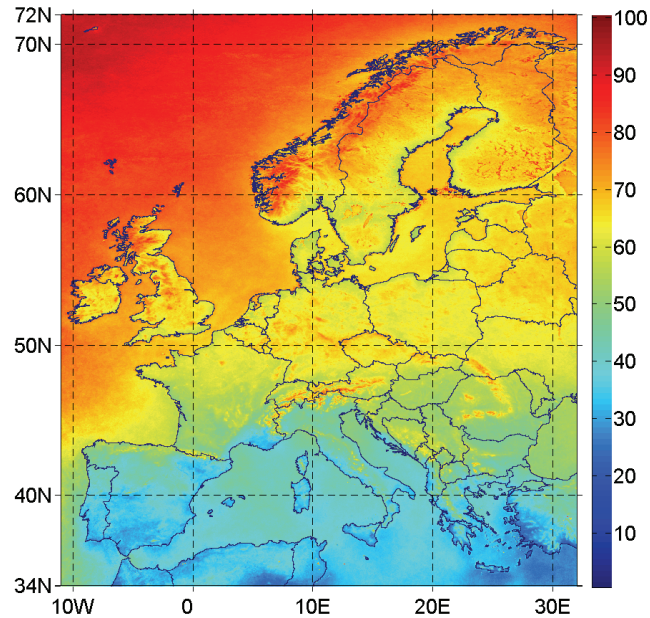
Figure 3.3: Mean cloud coverage (in percent) over Europe derived from the European Cloud Climatology (ECC) of the years 1990/1995/2000/2004/2005. The typical north-south decrease is clearly visible. Also the influence of mountains can be seen, e.g. the Alps and the Carpathians [MOL07].
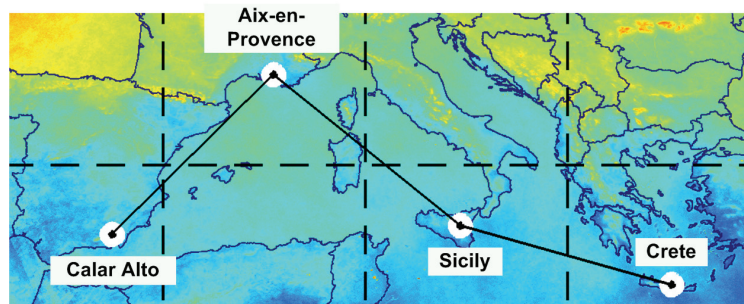
Figure 3.4: Example locations of ground stations in the south of Europe: Spain, France, Italy, and Greece. The stations are separated by a distance of at least 1000 km between each other to avoid strong correlation of the weather situation between the stations [MOL07].

The availability of a single ground station even at favorable location still appears not high enough for many applications. Several stations distributed over a larger area, e.g. Europe, can be employed to increase the combined availability of the whole network. This scheme is called ground station diversity. In this way the probability, that all ground stations are blocked at the same time by a cloud layer, decreases. An example of several ground stations in southern Europe is shown in Figure 3.4. The locations are: Calar Alto (Spain), Aix-en-Provence (France), Catania on Sicily (Italy), and Heraklion on Crete (Greece).

A single station in this region has an availability p_j of around 70%. Assuming statistical independence of the cloud coverage between two of these locations, the joint availability p_M of M stations can be calculated by

$$p_M = 1 - \prod_{j=1}^{M} \left(1 - p_j\right).$$

(3.2)

The more ground stations are included in the network, the higher the combined system availability becomes. Figure 3.5 shows the combined availability in dependence of the number of stations M and the single-station availability p_j. The availability of the example stations of Figure 3.4 can be approximately read from the uppermost curve ($p_j \approx 70\%$). Here only four ground stations are sufficient to achieve over 98% combined availability, i.e. less than 2% of the time all four stations are blocked by clouds at the same time.
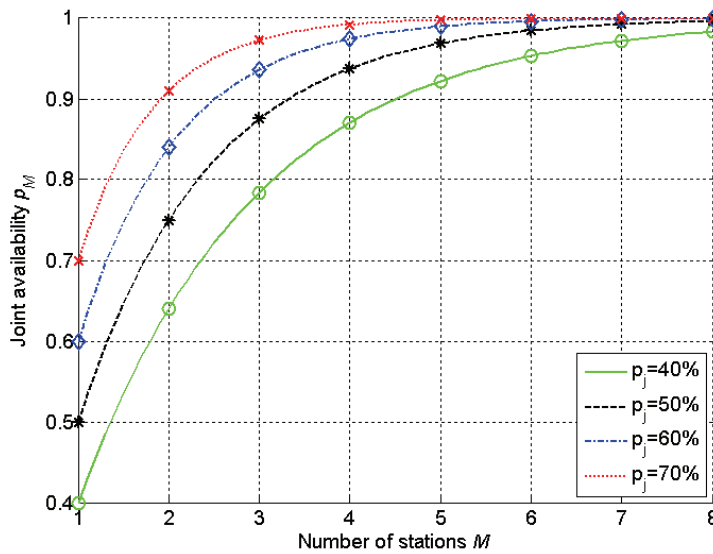
Figure 3.5: Combined availability of a ground network as a function of the number of stations.

3.1.3 Atmospheric Standard Models

The knowledge of typical atmospheric conditions is important for the assessment of atmospheric effects on communication links. In the following atmospheric models for the index-of-refraction turbulence $C_n^2(h)$ and atmospheric wind speeds $v_0(h)$ are presented, which will be used for the remainder of the work to evaluate analytic formulas and also to numerically simulate the effects of the atmosphere. The numerical field simulations in this work are based on the DLR proprietary tool PILab [HOR04][PER05].

3.1.3.1 C_n^2 Turbulence Profiles

The index-of-refraction structure parameter $C_n^2(h)$ describes the atmospheric turbulence strength over the height h above ground in a turbulence profile. There are strong variations of the $C_n^2(h)$ parameter with the atmospheric conditions, but also with location and time (day/night). Lower $C_n^2(h)$ turbulence levels can be expected for elevated locations and during the night. Average $C_n^2(h)$ profiles over the height have been developed from measurement results.

A widely used model profile is the generalized Hufnagel-Valley (HV) model. The $C_n^2(h)$ profile is given as a sum of exponential terms [HAR98]

$$C_n^2(h) = A \cdot \exp[-h/H_A] + B \cdot \exp[-h/H_B] + C \cdot (h/\mathrm{m})^{10} \cdot \exp[-h/H_C] + \\ + D \cdot \exp[-(h-H_D)^2/(2d^2)] \quad . \quad (3.3)$$

In this expression A is the coefficient for the surface (boundary layer) turbulence strength and H_A is the height for its $1/e$ decay. B and H_B similarly define the turbulence in the troposphere (up to about 10 km). C and H_C define a turbulence peak at the tropopause, and D and H_D define one or more isolated layers of turbulence, with d being the layer thickness. Parameters of the generalized HV model widely vary with the location. By far the largest $C_n^2(h)$ values are found close to the ground.

Throughout this work a specific parametrization of the Hufnagel-Valley model was used, commonly known as the HV$_{5/7}$ model. This model yields an atmospheric coherence length r_0=5cm and an isoplanatic angle of 7μrad for a wavelength λ=0.5μm. Figure 3.6 shows the HV$_{5/7}$ model calculated with the parameters in Table 3.1 and Eq. (3.3).

Table 3.1: Parameters of the standard Hufnagel-Valley HV$_{5/7}$ model.

	$A\left[\mathrm{m}^{-2/3}\right]$	H_A [m]	$B\left[\mathrm{m}^{-2/3}\right]$	H_B [m]	$C\left[\mathrm{m}^{-2/3}\right]$	H_C [m]	$D\left[\mathrm{m}^{-2/3}\right]$
HV$_{5/7}$	17x10^{-15}	100	27x10^{-17}	1500	3.59x10^{-53}	1000	0
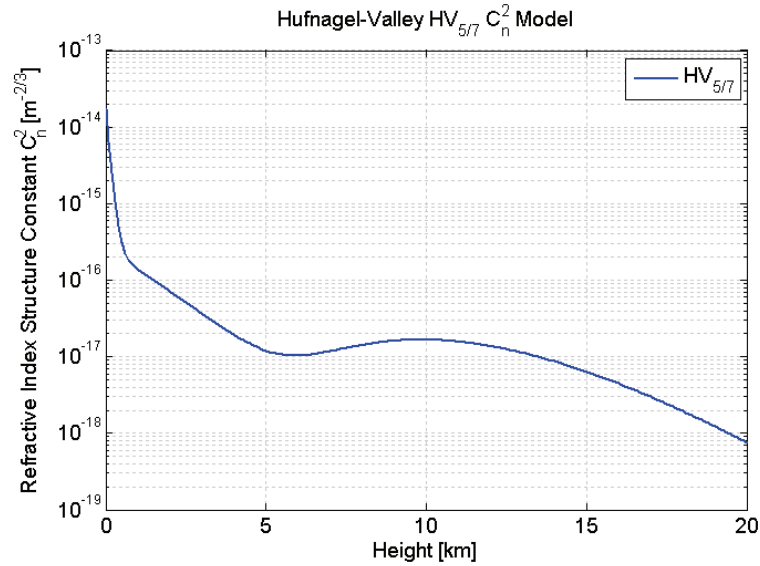
Figure 3.6: Refractive-index structure parameter $C_n^2(h)$ for a Hufnagel-Valley HV$_{5/7}$ turbulence model.

3.1.3.2 Wind Profiles and Satellite Motion

Another important factor influencing the atmospheric propagation channel is the beam motion with respect to the air masses and therefore the turbulence cells. We distinguish atmospheric wind (motion of air masses) and motion of the beam with respect to air masses due to motion of the communication terminals (e.g. satellite motion). The combination of both influences the expected bandwidth requirements for the communication and AO system with respect to the atmospheric turbulence.

Atmospheric wind can be modelled by the Bufton (also called Gaussian) model, which is given by [HAR98]

$$v_0(h) = v_G + v_T \cdot \exp\left[-\left(\frac{h - H_T}{L_T}\right)^2\right], \tag{3.4}$$

where h is the height above ground, v_G is the wind velocity at low altitudes, v_T is the wind velocity in the tropopause, H_T is the height and L_T the thickness of the tropopause layer. The peak wind speed at the tropopause varies greatly with location and season.

Throughout this work the Bufton wind model with Greenwood's parametrization [GRE77] is used for the evaluation of analytic formulas and numerical simulations. The parametrization is given in Table 3.2 and the resulting wind profile is shown in Figure 3.7.

Table 3.2: Greenwood parametrization [GRE77] for the Bufton wind model.

	v_G	v_T	H_T	L_T
Greenwood	8m/s	30m/s	9.4×10^3m	4.8×10^3m
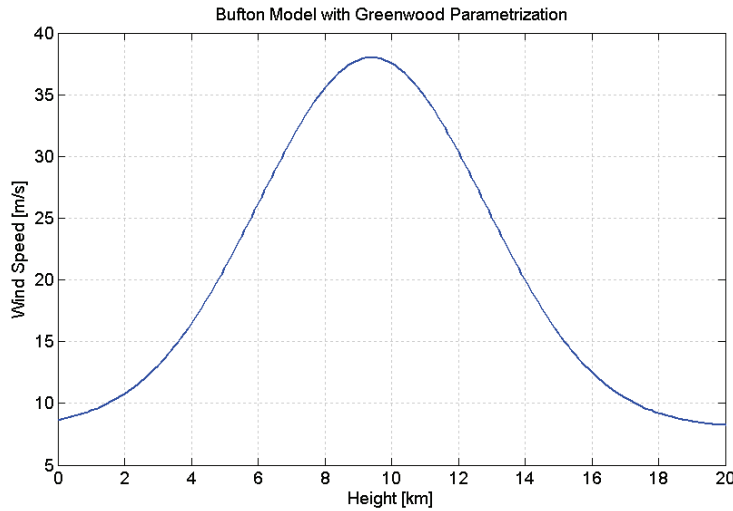
Figure 3.7: Wind speed profile according to the Bufton model for a Greenwood parametrization. The peak of the wind speed is at an altitude of 9.4km.

In the case of an SGL the combined transversal, relative velocity v_{B0} of the air masses across the beam can be calculated by

$$v_{B0}(z) = \left[v_0^2(z) \cdot \sin^2\left(\beta_g\right) + \left(v_0(z) \cdot \cos\left(\beta_g\right) \cdot \sin\left(\alpha_g\right) - \omega_{sat} z\right)^2\right]^{1/2}, \tag{3.5}$$

where $v_0(z)$ is the wind speed, e.g. given by Eq. (3.4), β_g is the telescope azimuth relative to the wind direction, α_g is the elevation angle, z is the distance from the telescope, and ω_{sat} is the slew rate (in radians/second) associated with the satellite motion with respect to the terminal on the ground. Eq. (3.5) neglects the curvature of the Earth in order to keep the calculations simple. The wind direction is assumed to be horizontal.

The slew rate for a satellite pass going through the Zenith, seen from the ground station, is given by

$$\omega_s = \frac{V_{sat}}{L} \cdot \frac{L^2 + H_{sat}^2 + 2R_e H_{sat}}{2L(H_{sat} + R_e)}, \qquad (3.6)$$

where V_{sat} is the satellite speed, H_{sat} is the satellite altitude, and R_e is the Earth radius. The distance ground-to-satellite L is calculated for the elevation angle α_g by

$$L = \sqrt{(H_{sat} + R_e)^2 - R_e^2 \cos^2(\alpha_g)} - R_e \sin(\alpha_g). \qquad (3.7)$$

For the analytic formulas and simulations in this work the following parameters were assumed approximating the orbit of the LEO satellite TerraSAR-X: V_{sat} = 7km/s, H_{sat} = 510km, R_e = 6370km. Similar parameters are valid for other LEO satellites. The resulting slew rate ω_{sat} of satellite is shown in Figure 3.8 as a function of the elevation angle α_g.
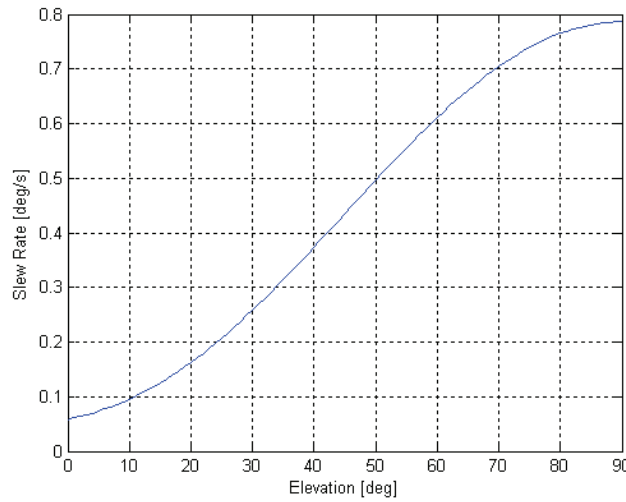
Figure 3.8: Slew rate (at the ground station) of the beam to track TerraSAR-X as a function of the elevation angle. A zenith pass was assumed, which leads to the largest slew rates.

Figure 3.9 shows the combined, relative atmospheric motion (across the beam) for the elevation angles $\alpha_g = 30\,\mathrm{deg}$ and $\alpha_g = 90\,\mathrm{deg}$. The left plot shows the cases, where the horizontal beam-motion component and atmospheric wind have equal and opposite directions ($\beta_g = 0\,\mathrm{deg}$ and $\beta_g = 180\,\mathrm{deg}$). The right plot shows the combined motion for a crosswind ($\beta_g = 90\,\mathrm{deg}$). The motion on the ground equals then the wind velocity (8m/s), as can be seen from Eq. (3.5).
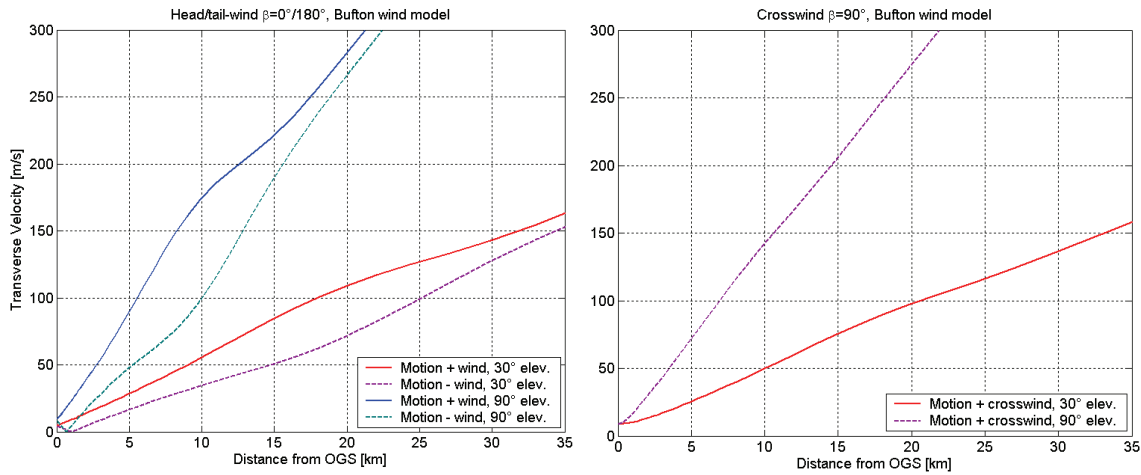
Figure 3.9: Relative motion of the turbulence cells across the beam resulting from beam motion and wind speed. Left: Velocity profiles for head and tail wind $\beta_g = 0/180\,\mathrm{deg}$**, indicated by Motion±Wind, at 30deg and 90deg elevation. Right: Velocity profiles for crosswinds at 30deg and 90deg elevation. The Bufton wind model was assumed for a link with TerraSAR-X.**

3.1.3.3 Spatial Power Spectra of Refractive-Index Fluctuations

Based on Kolmogorov's turbulence theory the structure of atmospheric turbulence can be understood with the idea of the energy cascade theory [e.g. AND05]. This describes the energy transfer from large turbulence cells on the order of the outer scale L_0 to smaller cells on the order of the inner scale l_0 (see Figure 3.10), where the turbulence cells/eddies disappear and their energy is dissipated as heat due to viscous forces. Typical outer scales are up to 100m at the surface layer. L_0 is assumed to grow linearly with height. The energy on the top of the cascade is injected by wind and eventually by solar radiation. The inner scale is on the order of several millimeters near ground and also increases with height. Eddies of scale size smaller than the outer scale are assumed to be statistically homogeneous and isotropic.
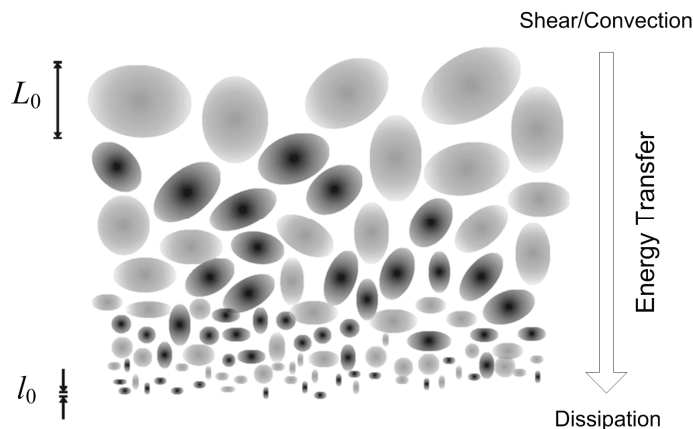
Figure 3.10: Energy transfer cascade based on the Kolmogorov theory.

The energy cascade describes in the first place the motion of air masses due to wind, but it can be transferred to temperature fluctuations and thus to refractive-index turbulence, which is most significant for optical wave propagation.

The refractive index in the atmosphere at a point $\vec{r}$ in space and at a certain time t is described by

$$n(\vec{r},t) = n_0 + n_1(\vec{r},t),\qquad(3.8)$$

where n_0 denotes the mean (constant) part of the refractive index and n_1 the variable, random deviation of the mean value. Fluctuations of the refractive index correspond to temperature and pressure fluctuations. Specifically in the near infrared the refractive index can be approximated by

$$n(\vec{r}) \approx 1 + 79 \cdot 10^{-6}\,\frac{P(\vec{r})}{T(\vec{r})}\cdot\frac{\mathrm{K}}{\mathrm{mbar}},\qquad(3.9)$$

which already implies, that there is only a very weak dependence of the refractive index on the wavelength. The pressure P is given here in millibar and the temperature T in kelvin.

The refractive index is related to the refractive-index structure function by

$$D_n(\rho) = \left\langle \left[n(\vec{r}) - n(\vec{r}+\vec{\rho}) \right] \right\rangle,\qquad(3.10)$$

where $\rho = |\vec{\rho}|$. The angular brackets denote an ensemble average. With an increasing separation distance ρ, the refractive index of two points become more and more independent, and thus the structure function $D_n(\rho)$ also increases. The dependence on only one parameter, the separation distance, includes the assumption of homogeneity and isotropy. The structure function exhibits two asymptotic behaviours

$$D_n(\rho) = \begin{cases} C_n^2 l_0^{-4/3}\rho^2, & 0 \le \rho \ll l_0 \\ C_n^2\rho^{2/3}, & l_0 \ll \rho \ll L_0 \end{cases}.\qquad(3.11)$$

The physical meaning of the refractive-index structure constant C_n^2 is a measure of the strength of refractive-index fluctuations. The structure function is related to the 3-dimensional refractive-index power spectrum $\Phi_n(\kappa)$ by

$$D_n(\rho) = 8\pi\int_0^\infty \kappa^2\Phi_n(\kappa)\left(1 - \frac{\sin(\kappa\rho)}{\kappa\rho}\right)d\kappa,\qquad(3.12)$$

where κ denotes a spatial frequency. $\Phi_n(\kappa)$ is widely used in the optical turbulence theory. One of the early models, which is often used for theoretical calculations due to its simplicity, is the Kolmogorov power-law spectrum

$$\Phi_n(\kappa) = 0.033 C_n^2 \kappa^{-11/3}, \qquad 1/L_0 \ll \kappa \ll 1/l_0\qquad(3.13)$$

which is valid only for the inertial subrange $1/L_0 \ll \kappa \ll 1/l_0$. Usually it is assumed that the outer scale tends to infinity ($L_0 = \infty$) and the inner scale is negligible small ($l_0 = 0$), however this may lead to divergent integrals in certain cases.

Other models provide more accurate descriptions taking inner and outer scale effects into account. Two representatives are the modified von Kármán spectrum [AND05]

$$\Phi_n\left(\kappa\right) = 0.033C_n^2 \frac{\exp\left(-\kappa^2/\kappa_m^2\right)}{\left(\kappa^2 + \kappa_0^2\right)^{11/6}}, \qquad 0 \le \kappa < \infty$$

$$\kappa_m = 5.92/l_0 \tag{3.14}$$

$$\kappa_0 = 2\pi/L_0$$

and the modified atmospheric spectrum [AND05]

$$\Phi_n\left(\kappa\right) = 0.033C_n^2 \left[1 + 1.802\left(\frac{\kappa}{\kappa_l}\right) - 0.254\left(\frac{\kappa}{\kappa_l}\right)^{7/6}\right] \frac{\exp\left(-\kappa^2/\kappa_l^2\right)}{\left(\kappa^2 + \kappa_0^2\right)^{11/6}}, \quad 0 \le \kappa < \infty$$

$$\kappa_l = 3.3/l_0 \tag{3.15}$$

$$\kappa_0 = 2\pi/L_0$$

which are both valid over all frequencies. Figure 3.11 compares the three spectrum laws presented. The frequencies κ_0 and κ_l corresponding to the inner scale l_0 and the outer scale L_0 are marked by vertical lines.

In the satellite-to-ground link scenarios the refractive-index constant depends on the height of the turbulence layer in the atmosphere and the parameters in Equations (3.13)-(3.15) are substituted by $C_n^2\left(h\right)$, $\Phi_n\left(\kappa, h\right)$, $l_0\left(h\right)$, $L_0\left(h\right)$.
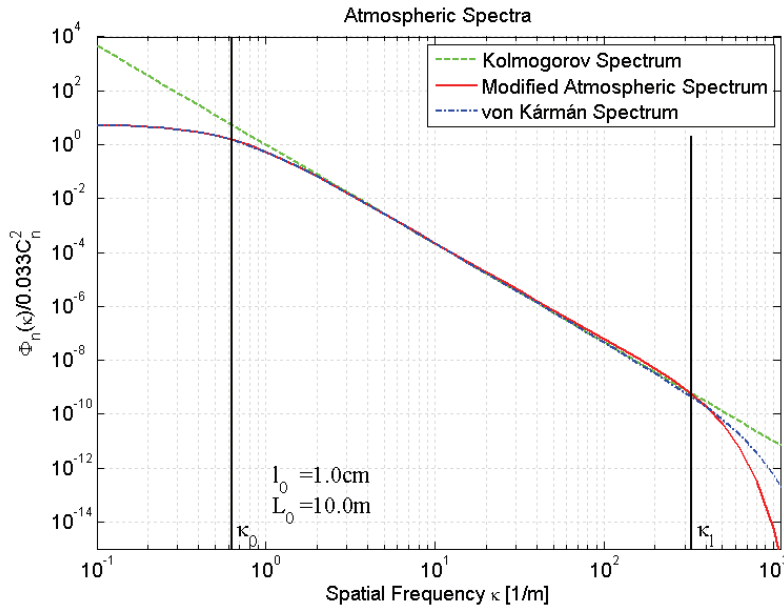
Figure 3.11: Atmospheric spectrum models of refractive-index fluctuations according to Equations (3.13), (3.14), (3.15).

3.1.4 Atmospheric Turbulence Effects on the Communication Beam

The atmospheric turbulence effects on the communication beam are summarized by

1. **Wavefront distortions:** Due to optical path-length differences increasing wavefront distortions appear and the beam becomes increasingly less (spatially) coherent with the propagation distance in the atmosphere.

2. **Redistribution of the intensity within the beam:** The distorted wavefront causes constructive and destructive interference effects, which disturb the beam's intensity distribution.
3. **Beam wander:** Turbulent cells larger than the beam radius cause the beam centroid to be redirected.
4. **Beam spreading:** Broadening of the beam radius and thus reduction of the average received intensity.

Especially significant for the development of AO systems are wavefront distortions (1) and scintillation effects (2, 3). Wavefront distortions, as they have an influence on the required mirror stroke and the speed requirements, have to be corrected with a suitable AO system. Scintillation effects significantly impact on the wavefront sensing, i.e. the sensors have to cope with the fact, that parts of the sensing area might not be illuminated sufficiently to produce meaningful results in this area.

The following sections present the current state of the theory describing weak and especially strong intensity/phase fluctuations in LEO satellite downlinks, although it is clear due to the complexity of the topic that a detailed derivation cannot be given in this work. Appropriate references to the literature are given.

3.1.4.1 Extended Rytov Theory for Weak&Strong Fluctuations

The classical theory of beam propagation in the turbulent atmosphere is only valid in the weak intensity fluctuation regime. The principles of weak-fluctuation theory can be found in [TAT67][AND05]. In the weak fluctuation regime, the classical approximations of the Rytov and the Born approximations are valid. The turbulence regime is usually classified according to the Rytov variance, which equals the scintillation index of a plane wave under weak fluctuation conditions. The Rytov variance is given by

$$\sigma_R^2 = 2.25 k^{7/6} \int_0^L C_n^2(z) \cdot z^{5/6} dz \,, \tag{3.16}$$

where z denotes the distance of the turbulence layer from the receiver on the ground. The Rytov variance is mainly influenced by high-altitude turbulence layers, which implies that scintillation needs a certain propagation distance to develop in contrast to phase distortions. At elevation angle above 30 degrees at the distances relevant for scintillation, the turbulence is already significantly reduced so that weak-fluctuation theory is applicable. Below 30 degrees weak fluctuation theory is not valid anymore. It overestimates (deems it worse) the scintillation index.

Weak fluctuations are commonly assumed for Rytov indices $\sigma_R^2 < 0.3$. Strong fluctuations are present for $\sigma_R^2 > 1$. In between the focusing regime is given. For very large σ_R^2 the level of scintillation decreases again. This is called saturation regime.

Several attempts have been made to produce a single theory for all fluctuation regimes. For the scintillation index Andrews et al. [AND00] presented such a model applying it to an SGL. This treatment assumes that the received intensity can be expressed as a product of two statistically independent variables $I = X \cdot Y$, where X describes effects of large-scale turbulence cells/eddies, and Y of small-scale cells. The scintillation index is then given by

$$\sigma_I^2 = \left\langle X^2 \right\rangle \left\langle Y^2 \right\rangle - 1 = \left(1 + \sigma_X^2\right)\left(1 + \sigma_Y^2\right) - 1 = \exp\left(\sigma_{\ln X}^2 + \sigma_{\ln Y}^2\right) - 1, \tag{3.17}$$

assuming an average received power of one, $\left\langle X \right\rangle = \left\langle Y \right\rangle = 1$. The large- respectively small-scale scintillation indices are denoted by σ_X^2, σ_Y^2 and the corresponding log-intensity scintillation indices by $\sigma_{\ln X}^2, \sigma_{\ln Y}^2$.

For the understanding of small scale and large scale, the significant scale sizes in respect to a propagating wave are

- Inner scale of turbulence l_0
- Spatial coherence radius of the optical wave $l_1 \sim \rho_0$
- First Fresnel zone $l_2 \sim \sqrt{L/k}$
- Beam radius w
- Scattering disk $l_3 \sim L/k\rho_0$
- Outer scale of turbulence L_0

From atmospheric turbulence theory it has been recognized that cells larger than the spatial coherence radius ρ_0 and smaller than the scattering disk $L/k\rho_0$ have little influence on scintillation under strong fluctuations [AND05]. Figure 3.12 illustrates this property for a horizontal link with constant C_n^2. At around 200m propagation distance the strong scintillation regime dominates and certain turbulence cell sizes are not effective anymore due to the loss of wavefront coherence. The excluded cell sizes are indicated by the shaded area.
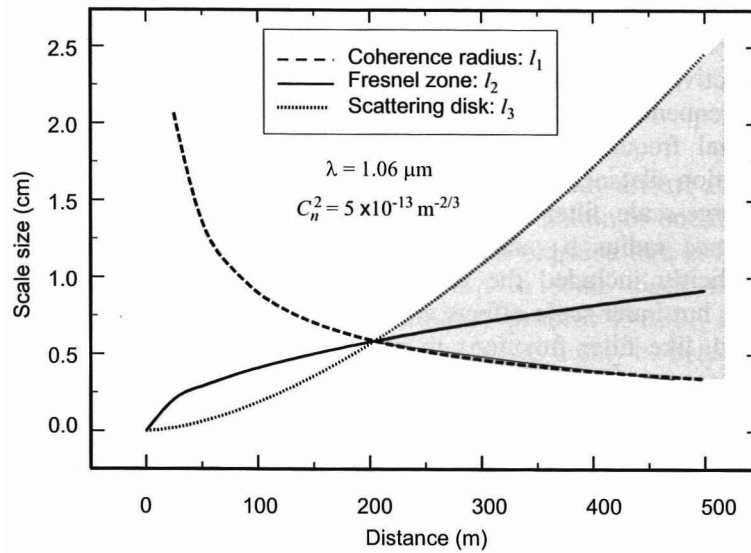
Figure 3.12: Relative turbulence scale sizes as a function of propagation distance. The point of intersection denotes the onset of strong fluctuations. The shaded area indicates the excluded scale sizes. (from [AND01])

A filtering technique is now applied to reflect the effective power-law spectrum, excluding ineffective cell sizes. This leads to the effective atmospheric spectrum (Kolmogorov spectrum)

$$\Phi_{n,e}(\kappa) = \Phi_n(\kappa) G_0(\kappa, l_0, L_0) = 0.033 C_n^2 \kappa^{-11/3} G_0(\kappa, l_0, L_0). \qquad (3.18)$$

$G_0(\kappa, l_0, L_0)$ is an amplitude spatial filter, which consists of a small- and a large-scale component G_X and G_Y

$$G_0(\kappa, l_0, L_0) \quad = G_X(\kappa, l_0, L_0) + G_Y(\kappa, l_0) \qquad (3.19)$$

with

$$
\begin{aligned}
G_X(\kappa, l_0, L_0) &= f(\kappa l_0) g(\kappa L_0) \exp\left(-\frac{\kappa^2}{\kappa_X^2}\right) \\
G_Y(\kappa, l_0, L_0) &= \frac{\kappa^{11/3}}{\left(\kappa^2 + \kappa_Y^2\right)^{11/6}}
\end{aligned}
$$

(3.20)

The functional forms of G_X and G_Y were chosen for mathematical tractability, but other equations might be just as suitable. The spatial cutoff frequencies κ_X and κ_Y define the filtering of the ineffective mid-range scale sizes under strong fluctuations. The cutoff frequencies can be estimated from the correlation width, scattering disk, and the Fresnel zone in the following way

$$
\frac{1}{\kappa_X} \sim \begin{cases} \sqrt{L/k}, & \sigma_R^2 \ll 1 \\ L/k\rho_0, & \sigma_R^2 \gg 1 \end{cases}
$$

(3.21)

$$
\frac{1}{\kappa_Y} \sim \begin{cases} \sqrt{L/k}, & \sigma_R^2 \ll 1 \\ \rho_0, & \sigma_R^2 \gg 1 \end{cases}
$$

(3.22)

The functions $f(\kappa l_0)$ and $g(\kappa L_0)$ contain the influence of inner and outer scales of the turbulence.

3.1.4.2 Intensity Scintillation Models

Based on the extended Rytov theory of the previous section, the scintillation index for all turbulence regimes, neglecting inner and outer scale effects ($l_0 \to 0, L_0 \to \infty$), can be estimated for a plane wave by [AND00]

$$
\sigma_I^2 = \exp\left[\frac{0.49\sigma_R^2}{\left(1+1.11\sigma_R^{12/5}\right)^{7/6}} + \frac{0.51\sigma_R^2}{\left(1+0.69\sigma_R^{12/5}\right)^{5/6}}\right] - 1,
$$

(3.23)

where the Rytov variance σ_R^2 is given by (3.16). Inner and outer scale effects [AND05] slightly modify the results, but do not contribute to the understanding of the order of magnitude of the scintillation effects in this discussion. Based on the results in horizontal links ($C_n^2 = const$) it can be expected that inner scale effects increase the maximum value of the scintillation index, as is also confirmed by the measurements (Section 3.3.2.1). Figure 3.13 shows the scintillation index for a satellite-to-ground link (downlink) as a function of the elevation angle. A Hufnagel-Valley HV$_{5/7}$ $C_n^2(h)$ profile (3.3) was assumed for a wavelength of λ=1064nm. The Rytov variance equals the scintillation index in the weak fluctuation regime and for a plane wave. A good match of the Rytov variance and the extended Rytov theory can be observed for elevation angles larger 30 degrees. Below 30 degrees the Rytov variance overestimates the scintillation effects. At very low elevation angle (<5 deg), the extended Rytov theory shows the expected saturation of the scintillation index due to multiple scattering. This is also observed in the measurements.
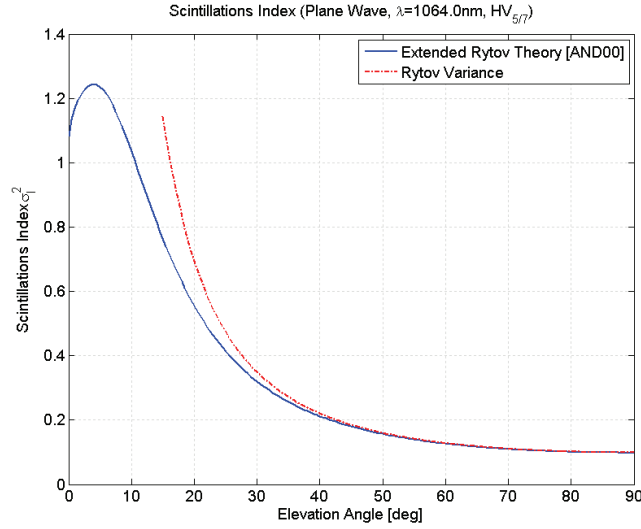
Figure 3.13: Scintillation index σ_I^2 for an SGL: Comparison of the extended Rytov theory Eq. (3.23), which is valid in the weak and strong fluctuation regime, with the Rytov variance (3.16), which is only valid in the weak fluctuation regime. An HV$_{5/7}$ (Section 3.1.3.1) atmospheric turbulence model was assumed.

Several probability density functions (PDF) $p(I)$ have been suggested to describe intensity scintillation covering weak and strong scintillation regimes. An overview was given by Perlot [PER06]. Examples are the *K-*, the *I-K* or the Gamma-Gamma distributions. In the context of this work only the Gamma-Gamma distribution, discussed in several publications by Andrews et al. [AND00][AND05], is presented in more detail, as it allows relating the distribution parameters to physical atmospheric parameters. The Gamma-Gamma distribution (named after the two Gamma functions) is given by

$$p(I) \quad = \frac{2\left(\alpha_1\beta_1\right)^{(\alpha_1+\beta_1)/2}}{\Gamma(\alpha_1)\Gamma(\beta_1)} I^{(\alpha_1+\beta_1)/2-1} K_{\alpha_1-\beta_1}\left(2\sqrt{\alpha_1\beta_1 I}\right), \; I > 0. \tag{3.24}$$

$K_p(x)$ denotes the modified Bessel function of the second kind and $\Gamma(x)$ the Gamma function [AND03]. The parameters α_I and β_I of the distribution can be related to the large- and small-scale scintillation indices by

$$\alpha_1 = \frac{1}{\sigma_X^2} = \frac{1}{\exp\left(\sigma_{\ln X}^2\right)-1}$$
$$\beta_1 = \frac{1}{\sigma_Y^2} = \frac{1}{\exp\left(\sigma_{\ln Y}^2\right)-1} \tag{3.25}$$

Again neglecting inner and outer scale effects the large- and small-scale log-intensity scintillation indices can be estimated by

$$\sigma_{\ln X}^2 = \frac{0.49\sigma_R^2}{\left(1+1.11\sigma_R^{12/5}\right)^{7/6}}$$
$$\sigma_{\ln Y}^2 = \frac{0.51\sigma_R^2}{\left(1+0.69\sigma_R^{12/5}\right)^{5/6}} \tag{3.26}$$

The combined scintillation index is calculated with Eq. (3.17). Table 3.3 summarizes the atmospheric parameters and the resulting Gamma-Gamma distribution parameters for several elevation angles. The resulting PDFs according to (3.24) are shown in Figure 3.14. At higher elevation angles the typical log-normal distributions can be observed almost assuming Gaussian shape at 90 degrees. At low elevation angles the distributions tend to a negative exponential shape.

Table 3.3: Scintillation parameters and parameters of the Gamma-Gamma distribution for several elevation angles.

Elevation [deg]	σ_R^2	σ_I^2	$\sigma_{\ln x}^2$	$\sigma_{\ln y}^2$	α_1	β_1
2.0	25.6	1.21	0.12	0.68	8.12	1.03
10.0	2.3	1.03	0.22	0.49	4.01	1.59
20.0	0.7	0.56	0.18	0.26	5.04	3.36
30.0	0.3	0.32	0.12	0.15	7.55	6.03
90.0	0.1	0.10	0.05	0.05	21.72	19.95
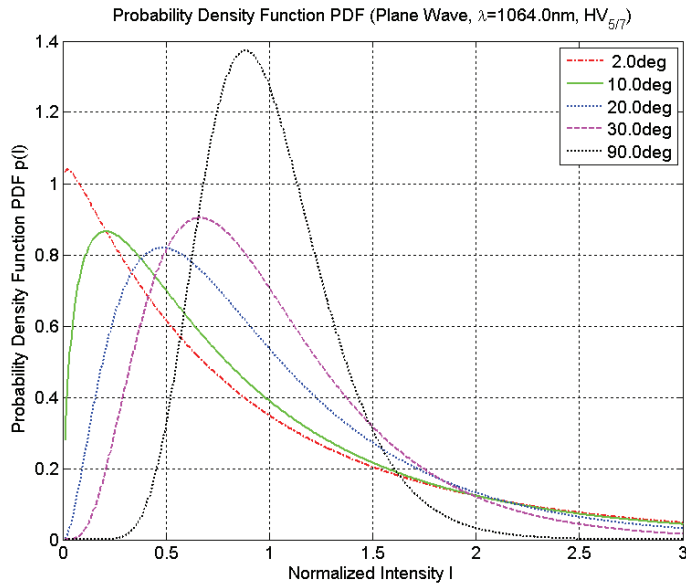
Figure 3.14: Probability Density Function (PDF) of the received intensity at the ground station calculated from Eq. (3.24). Each curve shows one elevation angle. The simulation is based on a HV$_{5/7}$ turbulence model (3.3) at the wavelength λ=1064nm. The intensity values are normalized to one.

The Cumulative Distribution Function (CDF) $P\left(I \leq I_T\right)$ can be simply derived from the PDF by its definition

$$P\left(I \leq I_T\right) = \int_0^{I_T} p\left(I\right) dI \,, \tag{3.27}$$

where I_T denotes the threshold intensity. For elevation angle below 20 degrees the received intensities reach down to zero, marking complete fades.
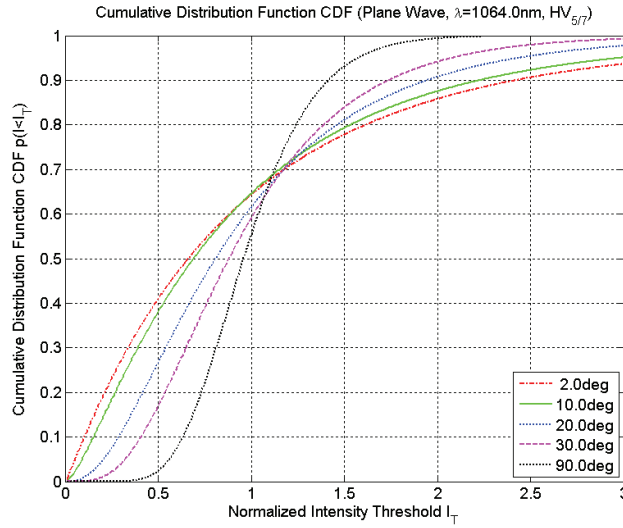
Figure 3.15: Cumulative Distribution Function (CDF) of the received intensity at the ground station calculated from Eq. (3.24) and the definition of the CDF (3.27). Each curve shows one elevation angle.

3.1.4.3   Phase Fluctuation Models

A PDF of the phase for a point source propagating through the turbulent atmosphere is assumed to be Gaussian [FAN61]. The phase variance of this Gaussian distribution can be calculated based on the formulas by Noll [NOL76], who gave the remaining phase variance in dependence of the degree of phase correction (See Section 4.1.2), i.e. the number of corrected Zernike modes. The variance over an aperture with diameter D is given excluding piston errors by

$$\sigma_1^2 = 1.0299 \cdot \left(\frac{D}{r_0}\right)^{5/3} \tag{3.28}$$

and excluding piston and tilt in x/y direction by

$$\sigma_3^2 = 0.134 \cdot \left(\frac{D}{r_0}\right)^{5/3}. \tag{3.29}$$

The second formula is of interest, as most AO systems use a separate tip/tilt correction to relax the requirements on the deformable mirror. The atmospheric coherence length or Fried parameter r_0 for a plane wave is given by

$$r_0 = \left(\frac{\lambda}{2\pi}\right)^{6/5} \left[0.423 \int_{z=0}^{L} C_n^2(z)dz\right]^{-3/5}. \tag{3.30}$$

Figure 3.16 shows the phase variance for different aperture diameters D as a function of the elevation angle. A significant increase of the phase disturbances towards low elevation angles and also an increase with the aperture size can be observed. The phase standard deviation is reduced by a separate tip/tilt correction by about a factor $\sigma_1 / \sigma_3 = \sqrt{1.0299 / 0.134} \approx 2.77$.
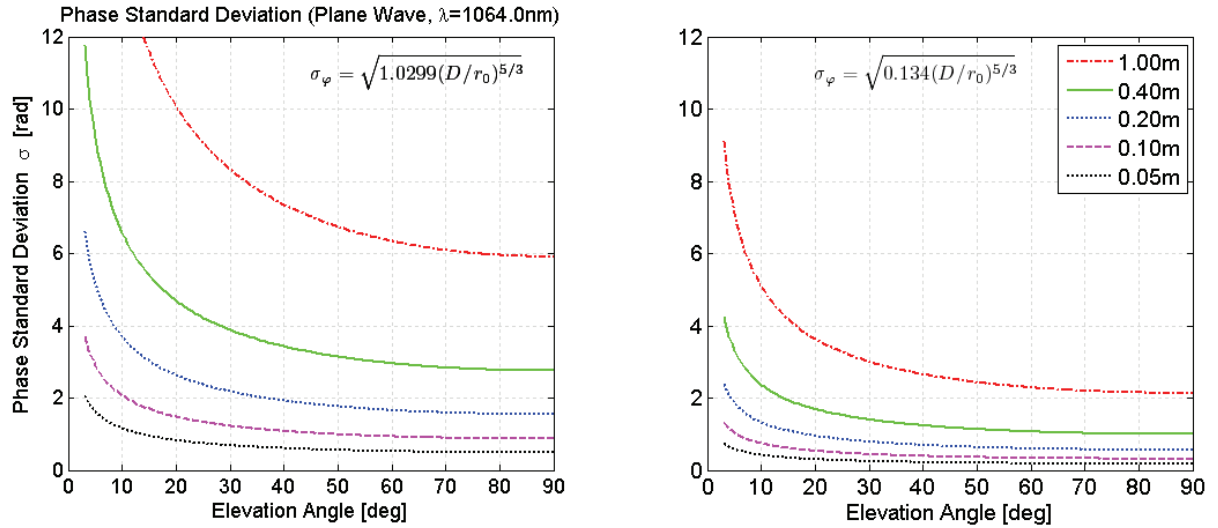
Figure 3.16: Phase standard deviation σ_φ for various aperture diameters D as a function of the elevation angle; left: only piston errors excluded; right: piston and tip/tilt excluded. The atmospheric coherence length was calculated with (3.30) with a HV$_{5/7}$ turbulence model (3.3) at the wavelength λ=1064nm.

The phase PDFs assuming a Gaussian distribution with zero mean

$$p(\varphi) = \frac{1}{\sqrt{2\pi\sigma_\varphi^2}} \exp\left(-\frac{\varphi^2}{2\sigma_\varphi^2}\right) \tag{3.31}$$

are shown in Figure 3.17 without tip/tilt correction (3.28) and in Figure 3.18 with tip/tilt correction (3.29), each for 5deg and 90deg elevation and different aperture diameters. Small receiver apertures (e.g. $D < 5cm$) imply a significantly reduced width of the phase PDF, eliminating the need of an AO system, but they also imply less received power with significantly higher intensity scintillation, as the aperture averaging effect is not present. In most communication systems and scenarios this cannot be tolerated.
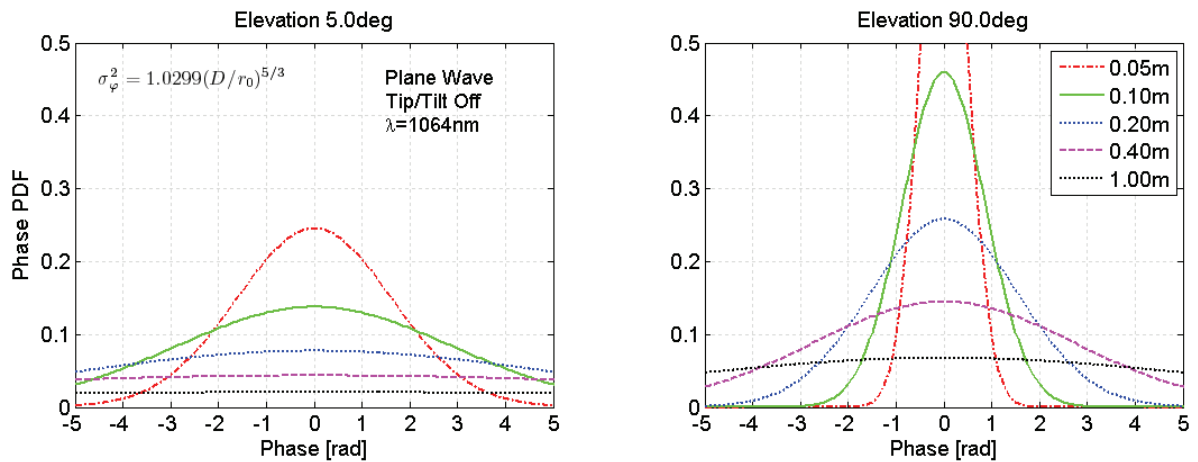
Figure 3.17: Phase PDF without tip/tilt correction (3.28) for various aperture diameters D; left: 5 degrees elevation; right: 90 degrees elevation.
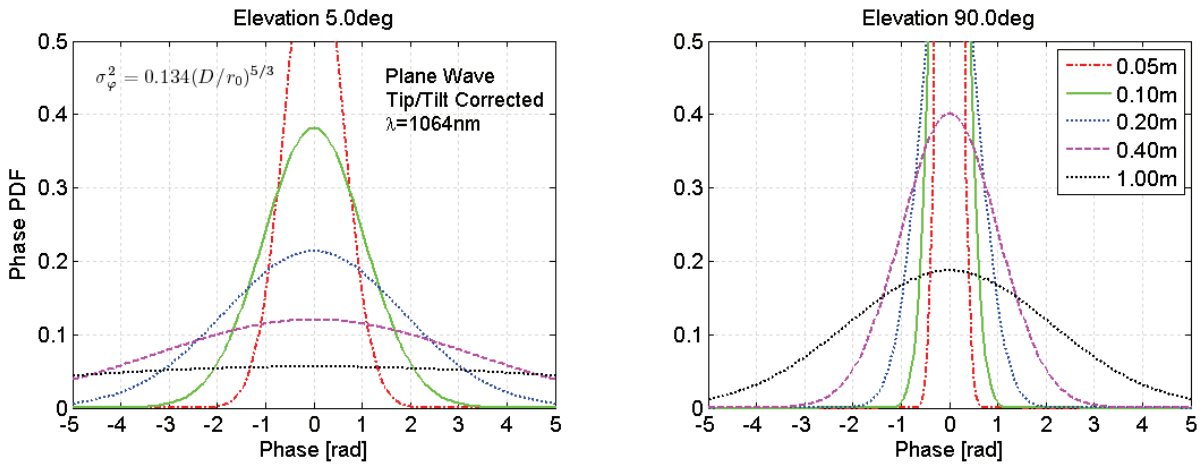
Figure 3.18: Phase PDF with tip/tilt correction (3.29) for various aperture diameter D; left: 5 degrees elevation; right: 90 degrees elevation.

3.2 Atmospheric Measurements in the Satellite-To-Ground Links

Atmospheric measurement instruments for the satellite-to-ground links to the DLR optical ground station (OGS) were developed between 2004 and 2009 in the framework of an ESA contract (see Chapter 1). This combination of several measurement instruments was called Atmospheric Transmission Monitor (ATM), as the laser source is located in space and the measurements are performed in the transmission through the atmosphere.
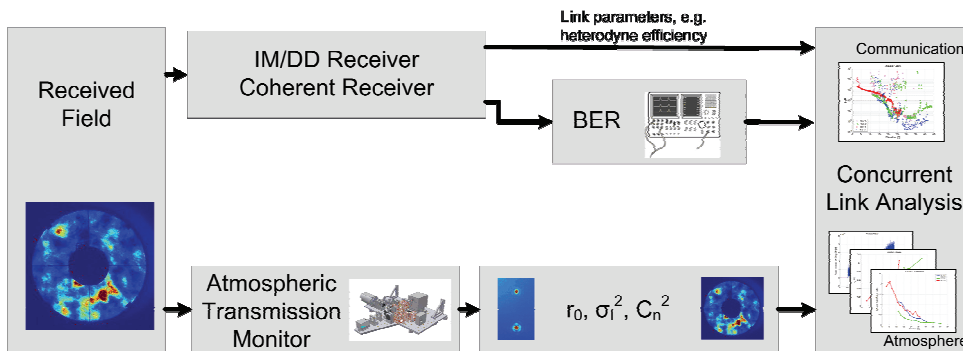
Figure 3.19: Concept of the Atmospheric Transmission Monitor (ATM).

The fundamental idea of the ATM is to measure the atmospheric conditions in parallel with the quality of the data transmission. This idea is summarized in Figure 3.19. The measurement instruments of the ATM estimate the phase and the intensity distribution over the receiving aperture of the incoming beam from the satellite. From the distributions several statistical atmospheric parameters as the Fried parameter r_0, the scintillation index σ_I^2, or the $C_n^2(h)$ profile (under weak turbulence conditions) can be estimated. At the same time a data receiver detects the communication signal and calculates the bit-error rate (BER) of the transmission. The combination of atmospheric measurements and BER allows conclusions about the atmospheric impact on the data transmission at various elevation angles, and thus, a channel model can be derived.

The instruments and sensors of the ATM are summarized in Table 3.4. Brief overviews on the instruments are given in the following sections but are not the main focus of this work. Further details can be found in the referred publications.

Table 3.4: ATM measurement instruments of the optical ground station, including the sensors and the expected results.

Instrument	Camera§/Sensor**	Results
Turbulence Profiler	Basler A102f (Si CCD, 1392x1040px, 6.45µm, 15fps)	High-resolution intensity distribution in the aperture, $C_n^2(h)$ profile over the beam path, scintillation index σ_i, intensity correlation length ρ_i.
Differential Image Motion Monitor	Basler A602f (Si CMOS, 656x491px, 9.9µm, 100fps)	Fried parameter r_0.
Shack-Hartmann Wavefront Sensor	Xenics Cheetah CL (InGaAs CMOS, 640x512px, 20µm, 440fps) or Basler A504k (Si CMOS, 1280x1024px, 12µm, 500fps)	High-resolution wavefront measurement, Fried parameter r_0.
Focus Camera	Basler A622f (Si CMOS, 1280x1024px, 6.7µm, 25fps)	Focus intensity distribution (Point Spread Function PSF), Fried parameter r_0, focus speckle-pattern analysis.
Power Sensor (external 5cm telescope aperture)	Thorlabs PDA400 (InGaAs PIN-Diode, 3.6x3.6mm, 20kS/s)	PIN diode with a 5cm aperture co-aligned to the main telescope; received power with high sampling rate (20kS/s).
Power Sensor (40cm telescope aperture)	Thorlabs PDA55 (Si PIN-Diode, 3.6x3.6mm, 20kS/s)	Received power with the 40cm main telescope with high sampling rate (20kS/s).
Tracking Cameras (WFOV&NFOV)	Basler A102f (CCD, 1392x1040px, 6.45µm, 15fps) Basler A602f (CMOS, 656x491px, 9.9µm, 100fps)	Wide/narrow field-of-view (WFOV/NFOV) camera for the pointing, acquisition, and tracking (PAT) system; estimate of the tracking errors.

§ The following parameters are given for cameras: Manufacturer and camera designation, material: silicon (Si)/ indium gallium arsenide (InGaAs), sensor type (CCD/CMOS), pixel resolution (px), pixel size, full-image frame rate (frames per second fps).
** The following parameters are given for PIN diodes: Manufacturer and diode designation, material: silicon (Si)/ indium gallium arsenide (InGaAs), sensor size, used sampling rate for this sensor (kilo-samples/second kS/s).

Figure 3.20 shows the DLR optical ground station (OGS) at the site Oberpfaffenhofen. The main instrument is a 40cm Cassegrain telescope. On the back side of the telescope a plate with the measurement instruments (ATM) and the narrow field-of-view camera is attached. Two co-aligned beacon lasers are fixed to opposite sides of the telescope frame. The spatial separation of the beacons reduces scintillation of the two beams at the satellite receiver and tracking system, as they pass different volumes of the atmosphere. Additionally there are a PIN diode with a 5cm telescope (scintillation measurements) and the wide field-of-view (WFOV) tracking camera. Each sensor is connected to an own data recording system to maximize the sampling rate. Data evaluation is performed off-line after the experiments. Figure 3.21 and Figure 3.22 show detailed views of the ATM instrument plate, which is attached to the back of the main telescope.
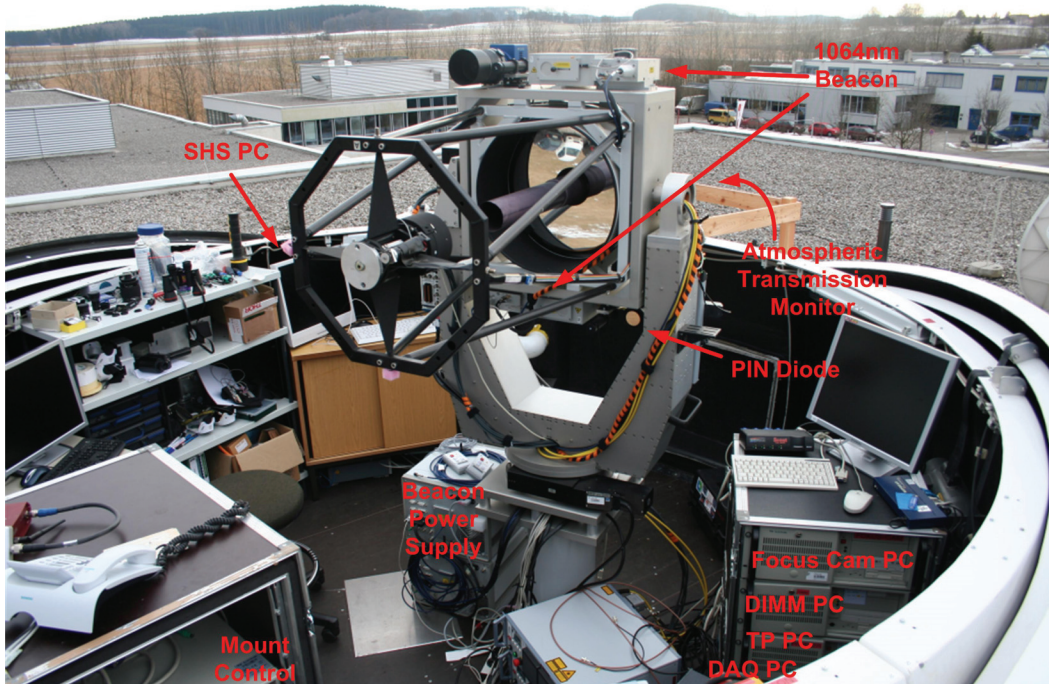
Figure 3.20: The DLR OGS in Oberpfaffenhofen. The plate of the ATM is located behind the telescope.
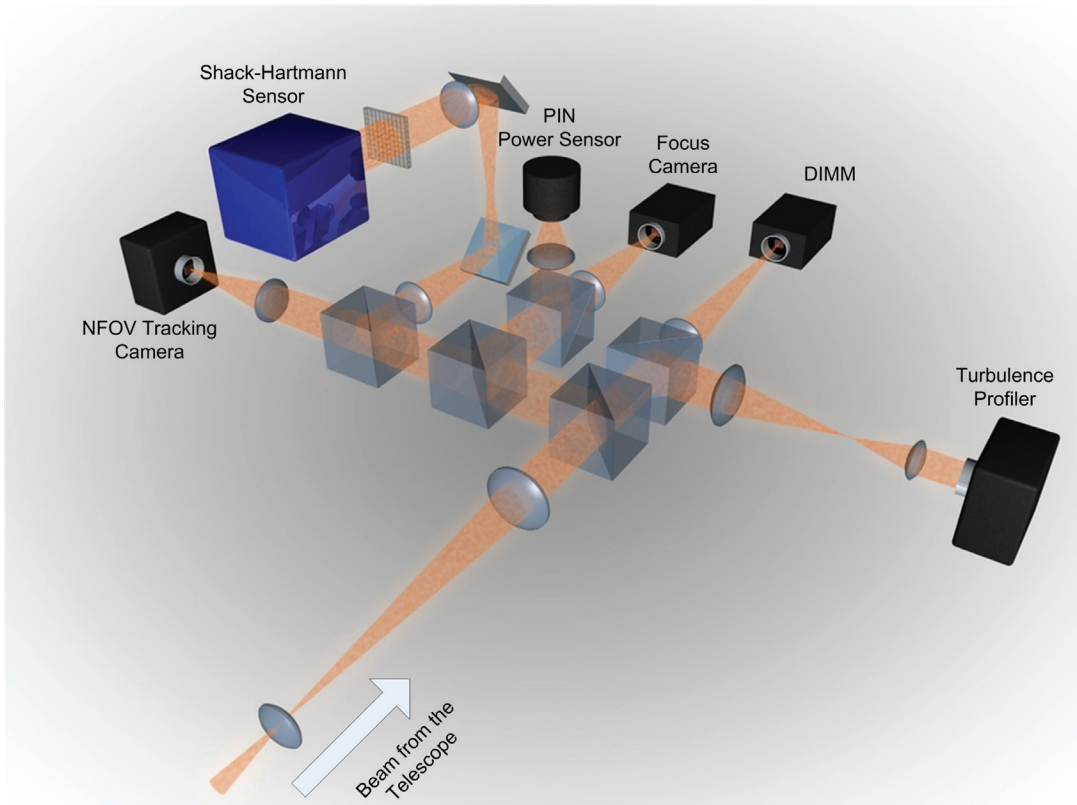
Figure 3.21: Layout of the ATM. The incoming beam is collimated and distributed to the NFOV tracking camera, the SHS, a power sensor (PIN diode), focus camera, DIMM, and Turbulence Profiler.
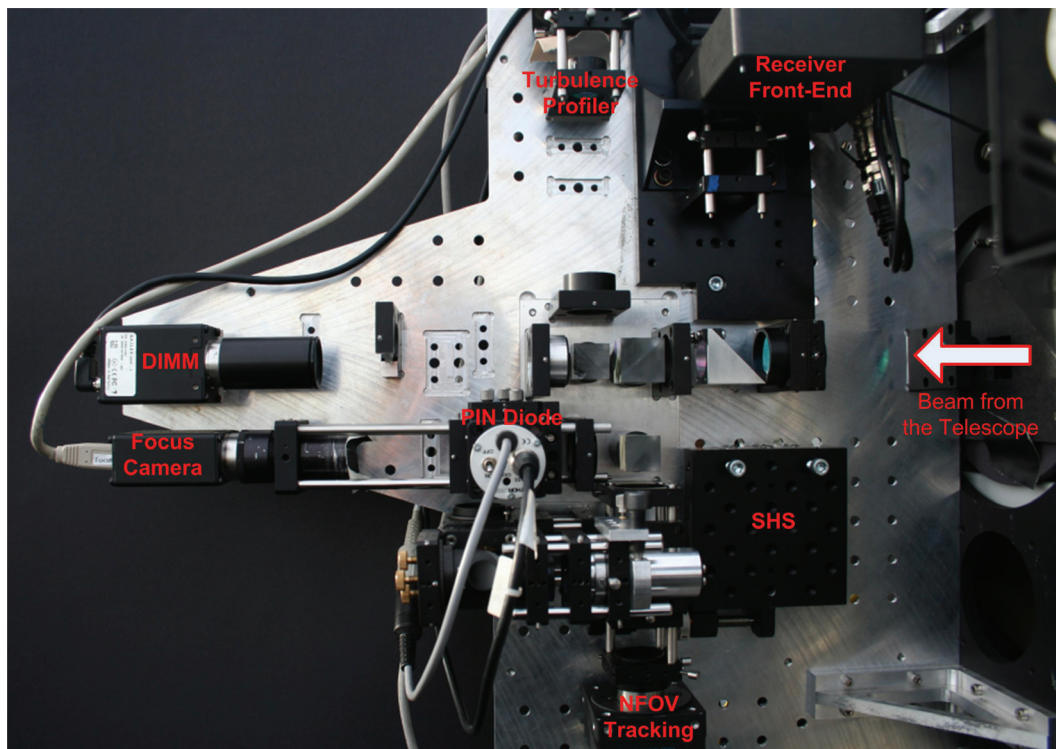
Figure 3.22: Photo of the ATM.

The DLR OGS during a pass of the Japanese LEO satellite OICETS is shown in Figure 3.23. The two co-aligned beacon lasers on the left and right of the telescope produce a strong glow in the atmosphere and form an imaginary focus in the distance. The beacon lasers serve the acquisition and tracking system on the satellite to acquire and keep the link during the pass, i.e. keep the satellite terminal pointed to the ground station with micro-radian accuracy.

Figure 3.23: DLR OGS seen from an installed web-cam during the OICETS satellites passes 26th June 2009 at 2:53AM local time. The two co-aligned beacon lasers on opposite sides of the telescope, which illuminate the satellite for the link acquisition and tracking, can be nicely seen. Also the glow of the fiber feed is visible.

3.2.1 Differential Image Motion Monitor (DIMM)

The Differential Image Motion Monitor (DIMM) was developed by astronomers to estimate the Fried parameter r_0 at observatory sites [SAR90][TOK02b]. Usually referred to as the atmospheric coherence diameter for a plane wave, r_0 can also characterize the coherence of other kinds of waves.

The DIMM principle is depicted in Figure 3.24. The angle-of-arrival of the incoming wave is measured in two small apertures (diameter D_{sub}) separated by a distance d. The waves from the two apertures are focused by a lens, and one of the paths propagates through an optical wedge to separate the two focus spots on the camera chip. The variance of the differential focus-spot motion is taken to estimate the r_0 parameter. As a source in space the laser on the satellite is used.

The advantage of considering the difference of the focus-spot displacements is the cancellation of tracking errors. This characteristic is especially important for dynamic scenarios, where the ground station will always have residual tracking errors. In this way the DIMM gives an unbiased estimate of the image degradation due to the atmosphere alone. Details on the DIMM for the OGS-OP can be found in [KNA06]. An example for the two focus spots, which move relative to each other, can be seen in Figure 3.25.
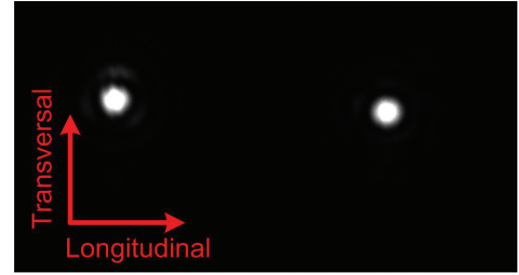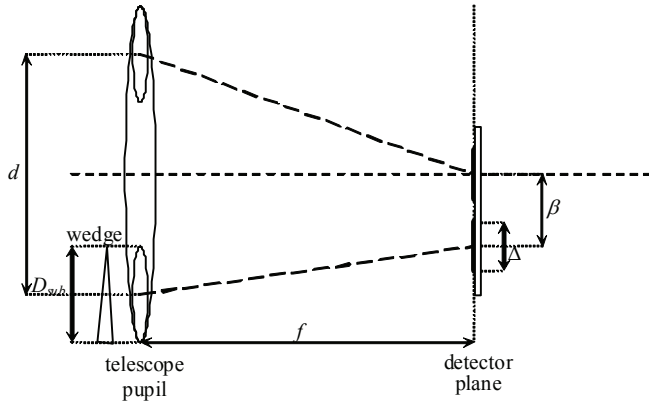
Figure 3.24: Principle of the DIMM sensor. Two focus spots are generated by a lens and a wedge in one of the two paths. The variance of the relative spot motion allows the estimation of the Fried parameter.

Figure 3.25: Typical frame of a DIMM, where the two focus-spots move relatively to each other.

The Fried parameter in longitudinal direction $r_{0,l}$ and in transversal direction $r_{0,t}$ in dependence of the wavelength λ and the variance of the transversal/longitudinal differential spot motion $\sigma_{d,l/t}$ is calculated by

$$r_{0,l} = \left(\frac{K_l \lambda^2 D_{Sub}^{-1/3}}{\sigma_{d,l}^2} \right)^{3/5} \tag{3.32}$$

$$r_{0,t} = \left(\frac{K_t \lambda^2 D_{Sub}^{-1/3}}{\sigma_{d,t}^2} \right)^{3/5} \tag{3.33}$$

with

$$K_l = 0.358 \left(1 - 0.541 \left(\frac{d}{D_{Sub}} \right)^{-1/3} \right) \tag{3.34}$$

$$K_t = 0.358 \left(1 - 0.810 \left(\frac{d}{D_{Sub}} \right)^{-1/3} \right) \tag{3.35}$$

A combined r_0 is estimated by an average of the transversal and longitudinal r_0 values.

3.2.2 Turbulence Profiler

The ATM turbulence $C_n^2(h)$ profiler is based on scintillation measurements from a single source (in contrast to SCIDAR profilers, which require two sources). Despite its relative simplicity due to the use of a single source, the ATM profiler is intended to measure the atmospheric turbulence profiles in the SGL scenarios. Some astronomers have designed single-star profilers intended to sense the vertical atmosphere of astronomical sights with a plane wave from a bright star [TOK00][CAC87]. For those particular astronomical applications, the type of source is predefined and the turbulence profile roughly follows the well-known $C_n^2(h)$ models also given in Section 3.1.3.1.

Turbulence profilers work only under weak-fluctuation conditions (vertical paths or short horizontal paths) as the underlying theory does not allow the profile restoration in the strong

turbulence regime. The single star profiler is based on the relation between the turbulence profile $C_n^2(h)$ and the intensity spatial covariance function $B(\rho)$ in the receiving aperture. Because this correspondence relies on an ill-conditioned transformation, the profiles can be restored with only limited resolution, i.e. the relation between covariance function and profile is rather weak.

A typical image of the intensity distribution at the entrance pupil of the telescope (plane of the spider and central obscuration) in an SGL is shown in Figure 3.26. Further details on the DLR OGS profiler can be found in [KNA06].
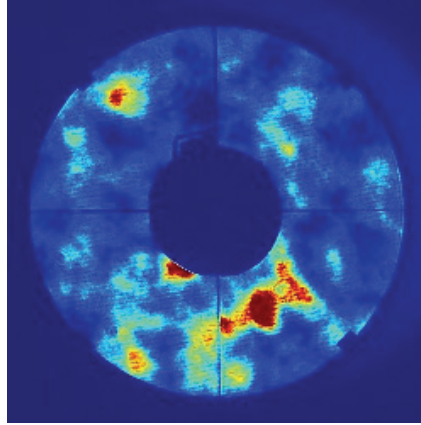
Figure 3.26: Typical intensity distribution in the 40cm telescope aperture with spider and central obscuration.

The spatial covariance function of the intensity distribution in the telescope aperture directly contains the following information:

-   Scintillation index $\sigma_I^2 = \dfrac{\langle I^2 \rangle - \langle I \rangle^2}{\langle I \rangle^2}$, which determines the strength of the intensity fluctuations and thus the depth of the fades.
-   The spatial correlation of the intensity, which gives the mean size of the intensity speckles in the receiver plane.

For the reconstruction of the turbulence profile along the propagation path, the relation

$$B(\rho) = \sum_{i=1}^{N} \Delta z_i \cdot C_n^2(z_i) \cdot W(z_i, \rho) \qquad (3.36)$$

between the intensity spatial covariance function $B(\rho)$ in the telescope aperture and the $C_n^2(h)$ profile has to be inverted. The intensity spatial covariance depends on the location of turbulence layers along the propagation path. The weighting function $W(h, \rho)$ describing the relation between the covariance function $B(\rho)$ and the profile $C_n^2(h)$ are known from scintillation theory under weak fluctuations [TOK00][CAC87]. Considerations on the profile restoration are given in [TOK02a].

3.2.3 Shack-Hartmann Wavefront Sensor

The Shack-Hartmann wavefront sensor (SHS) of the DLR OGS was designed to measure the phase of the incoming beam with high resolution and sampling rate. Each focus spot covers an area of 12x12mm in the entrance pupil of the telescope. The intensity distribution

can be either read from the SHS with high temporal resolution (440fps) or with high spatial resolution from the Turbulence Profiler (~30fps). Figure 3.27 shows the optical setup of the SHS.
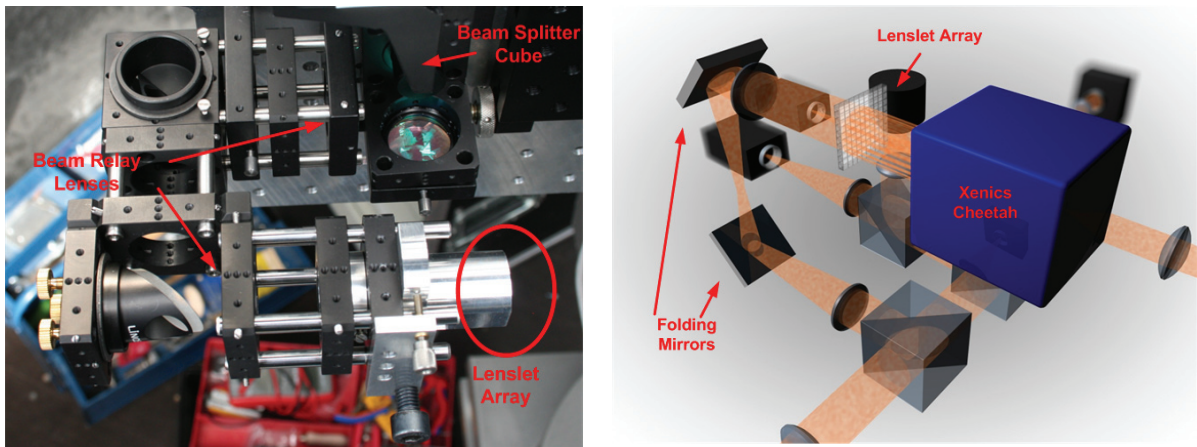
Figure 3.27: Left: Shack-Hartmann sensor's optical setup with the relay lenses and the mount for the lenslet array; Right: Schematics of the Shack-Hartmann sensor, also showing the lenslet array.

Wavefront reconstruction is the process of restoring the phase values with respect to a reference plane from the slopes measured by the focus spot positions of the SHS lenslet array. The general principle is explained in many publications, e.g. [HAR98]. Figure 3.28 on the left shows a typical image obtained from the SHS camera. On the right side the reconstructed wavefront is depicted. Specific aspects of the wavefront reconstruction in the SGL scenarios are presented in Section 4.4.1.
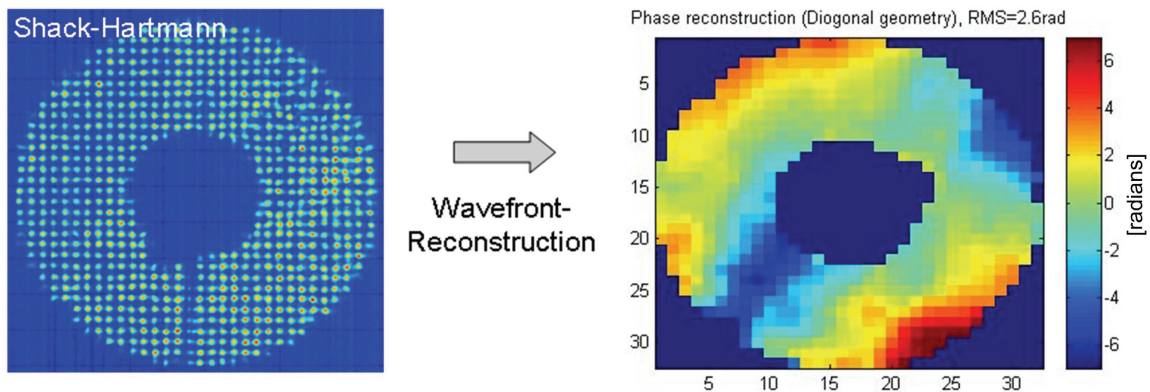
Figure 3.28: Left: Shack-Hartmann sensor image recorded with the Cheetah CL for a link distance of 400m at 1064nm. Artifacts of the spider, the central obscuration and the secondary-mirror drive can be seen. Right: Reconstructed wavefront.

3.2.4 Focus Camera

The atmospheric coherence length r_0 can be estimated from several instruments, the DIMM , the SHS, and the focal spot (PSF) camera. The estimation of r_0 from the focal spot images is based on Glindemann [GLI97]

$$r_0 = 0.98 \cdot \frac{\lambda \cdot f}{D_{FWHM}},$$ (3.37)

where f is the effective focal length and D_{FWHM} the full-width half maximum of the long-term spot in the focal plane. Figure 3.29 shows a typical image of the focal spot recorded during an SGL from the Japanese satellite OICETS.
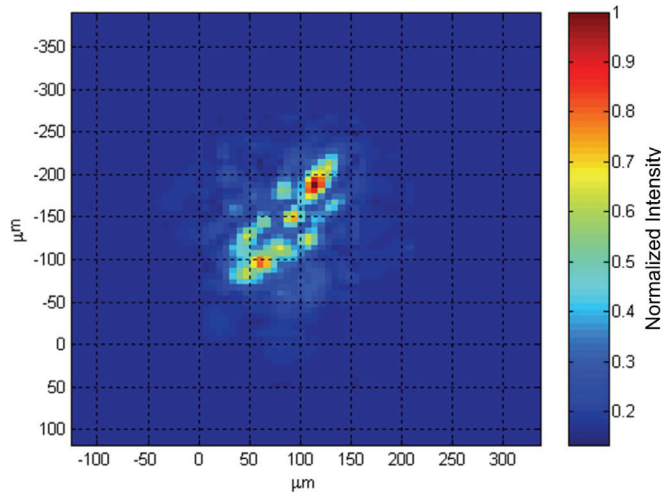
Figure 3.29: Focal spot image recorded during an SGL experiments from the Japanese satellite OICETS.

3.2.5 Scintillation Measurements

The ATM contains two PIN diodes to measure the received power values with a sampling rate of 20kHz. One PIN diode uses the full 40cm aperture and the other is attached to the main telescope frame with a 5cm aperture. The large bandwidth is required to resolve scintillation effects of the atmosphere.

Figure 3.30 shows a sample graph of the optical power received at the OGS during the OICETS SGLs. The mean received power increases with the elevation angle, as the link distance decreases. The variation of the intensity shows the scintillation strength. Several short breaks of the signal can be seen, which are caused by a problem of the coarse pointing unit on the satellite.
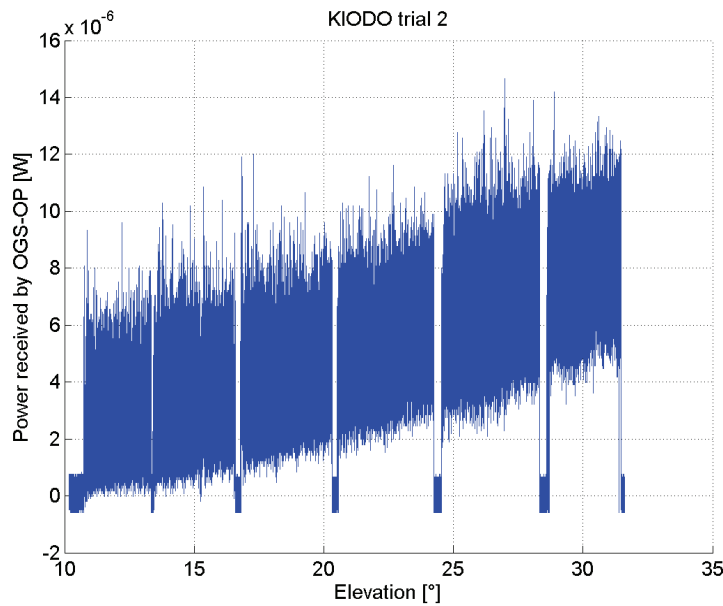
Figure 3.30: Sample power measurement during the OICETS SGLs 2007. The short signal breaks were caused by a problem of the coarse pointing unit of the satellite.

3.3 Atmospheric Measurement Results

The following measurement results were recorded with the instruments of the DLR optical ground station during SGLs from the Japanese satellite OICETS. Some of the results were already published in [PER07] with stronger emphasis on the performance of the measurements itself.

3.3.1 Phase Fluctuations

3.3.1.1 Atmospheric Coherence Length r_0

Figure 3.31 (left) shows the atmospheric coherence length r_0 during the SGLs from the Japanese LEO satellite OICETS as a function of the elevation angle. r_0 increases (improves) with the elevation, as expected. Each curve shows a different SGL experiment (trial number (day) 2, 3, 4, 7). Variability between the r_0 estimates for different downlinks (on different days) can be noticed. The experiments took place shortly after mid-night local time. The Japanese space agency JAXA avoided direct illumination of the satellite by the sun, which resulted in the maximum elevation angles between 30 and 40 degrees. The communication wavelength of OICETS is 847nm in the downlink.

The Fried parameter r_0 can be estimated based on the Rytov theory for a plane wave and the turbulence profile $C_n^2(z)$ along the optical path from Eq. (3.30). Figure 3.31 (right) shows r_0 values from analytic calculations at the typical communication wavelength λ=847, 1064, and 1550nm for a standard $C_n^2(h)$ Hufnagel-Valley model $HV_{5/7}$ (see Section 3.1.3.1). The values of the 847nm curve nicely match with the OICETS downlink measurements. It can be seen that longer wavelengths suffer less from the effects of the atmosphere.
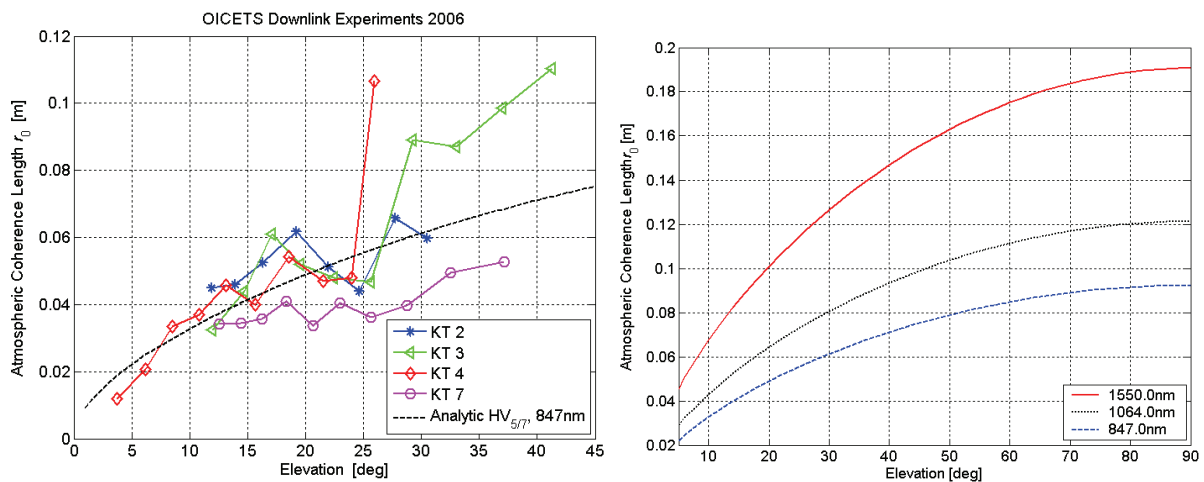
Figure 3.31: Atmospheric coherence length r_0; Left: Measurement of r_0 during the OICETS SGL experiments 2006 at 847nm; Right: Analytic r_0 values for λ=847, 1064, and 1550nm based on Eq. (3.30) and a $HV_{5/7}$ turbulence profile.

3.3.1.2 Phase Probability Density Function

Figure 3.32 and Figure 3.33 show phase probability density functions (PDF) from phase measurements recorded with the Shack-Hartmann sensor during the SGLs from OICETS during the second measurement campaign 2009. Figure 3.32 gives the unwrapped phase. A standard reconstruction algorithm was used, so that the phase values for elevation angles below 20 degrees elevation might be underestimated due to branch points (see Section 4.4.1.1); however, a comparison with theory and standard models supported the qualitative validity of the results. Figure 3.33 shows the same results for a wrapped phase, i.e. $-\pi < \varphi \leq +\pi$. For low elevation angles the phase distribution tends to a uniform distribution.
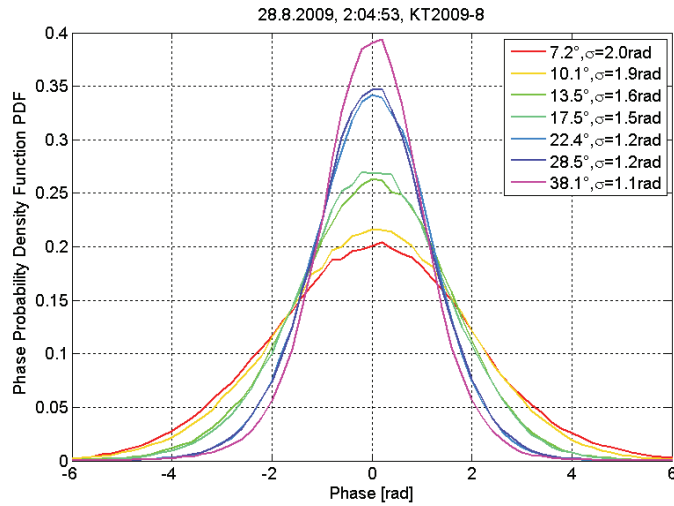
Figure 3.32: Unwrapped phase Probability Density Function (PDF) recorded by the Shack-Hartmann sensor during the SGLs from OICETS 2009, trial day 8. Several elevation angles are shown. Averaging time for the evaluation was 10.7s (100 frames).
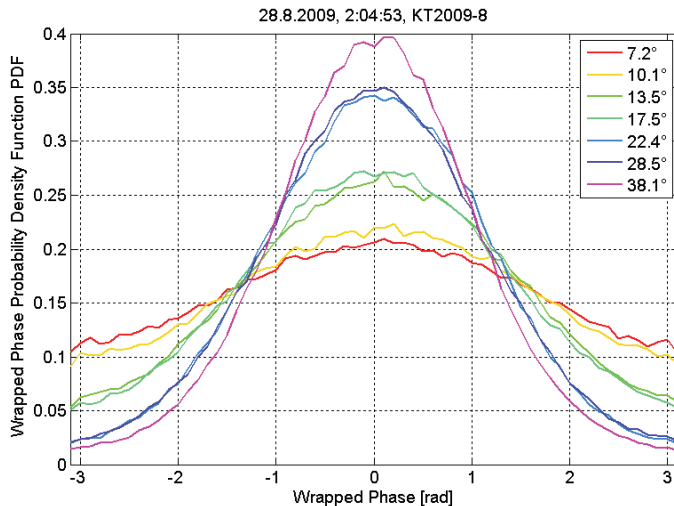
Figure 3.33: Probability Density Function (PDF) of the wrapped phase (range $-\pi < \varphi \leq +\pi$) recorded by the Shack-Hartmann sensor during the SGLs from OICETS 2009, trial day 8. Several elevation angles are shown. Averaging time for the evaluation was 10.7s (100 frames).

3.3.2 Intensity/Power Scintillation

3.3.2.1 Scintillation Index

The scintillation index is obtained in the measurements from the turbulence profiler, which gives the intensity distribution over the receiver aperture (e.g. Figure 3.26). Figure 3.34 shows the intensity (left) and power (right) scintillation index for the OICETS downlink experiments 2006. The scintillation index is defined by

$$\sigma_I^2 = \frac{\langle I^2 \rangle - \langle I \rangle^2}{\langle I \rangle^2}.$$

(3.38)

The measurements for the experiment days vary greatly (KT7 is about 5 times higher than KT3). Higher elevation angles have significantly lower scintillation levels. The power scintillation index for the full 40cm telescope aperture is about a factor 5 lower than the intensity scintillation index due to the aperture averaging effect [PER06].
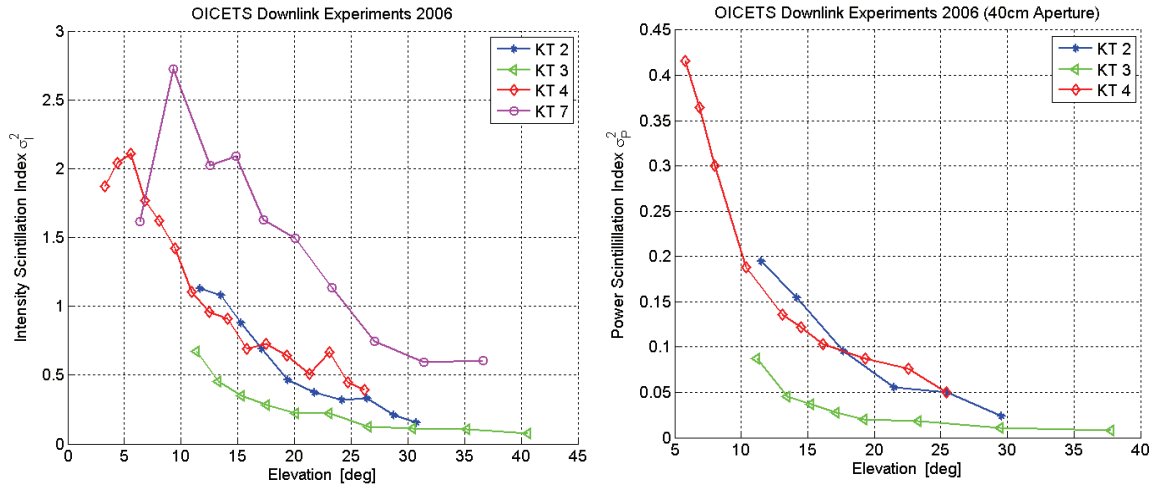
Figure 3.34: Left: Intensity scintillation index σ_I^2 as a function of the elevation. Right: Power scintillation index σ_P^2 for the full 40cm aperture with a central obscuration of about 12cm (OICETS SGL experiments 2006).

Figure 3.35 shows the intensity/power scintillation index for simulated fields for SGLs at various elevation angles. Each curve shows the scintillation index for a certain aperture diameter D. This clear shows the aperture averaging factor reducing the scintillation with growing aperture diameter.
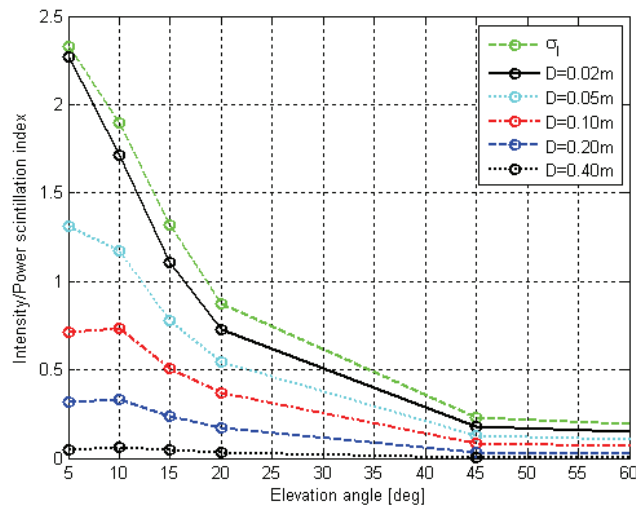
Figure 3.35: Intensity/power scintillation index for different aperture diameters over the elevation angle showing the aperture averaging effect (PILab simulation with a HV$_{5/7}$ model at $\lambda = 1064\text{nm}$).

3.3.2.2 Intensity/Power Probability Density Function

Figure 3.36 shows the normalized power PDF measured with the Shack-Hartmann sensor. Each lenslet of the sensor corresponds to a 1.3cm diameter aperture in the telescope entrance pupil, and thus the power PDF comes pretty close to an intensity PDF. The shape

55

at higher elevations tends towards a Gaussian distribution around one implying few power drops to zero. Towards lower elevation angles, the shape becomes log-normal distributed, and then more and more similar to a negative-exponential distribution.
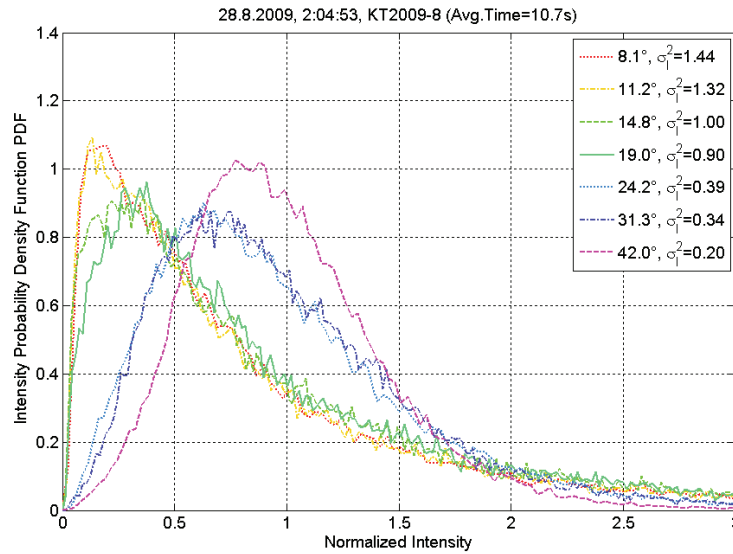
Figure 3.36: Probability Density Function (PDF) of the power recorded with the Shack-Hartmann sensor during the SGLs from OICETS 2009, trial day 8. Several elevation angles are shown. Averaging time for the evaluation was 10.7s (100 frames).

The intensity and power PDFs in the SGL scenarios were also simulated with PILab to compare them with the measurements and to extrapolate the results to other elevation angles. A standard $HV_{5/7}$ model (Section 3.1.3) at 1064nm was assumed for the simulations. Figure 3.37 shows the normalized intensity PDF at different elevation angles, again with the expected Gaussian, log-normal, and negative exponential shapes. Figure 3.38 gives normalized power PDFs. Each graph is given for a certain aperture diameter (D=0.5cm, 5cm, 20cm). For small apertures, the received mean power over the aperture exhibits large variations and contains drops down to zero power for low elevation angles, which indicates strong fades for the communication system. Also the dynamics of the received power levels is larger for small apertures.
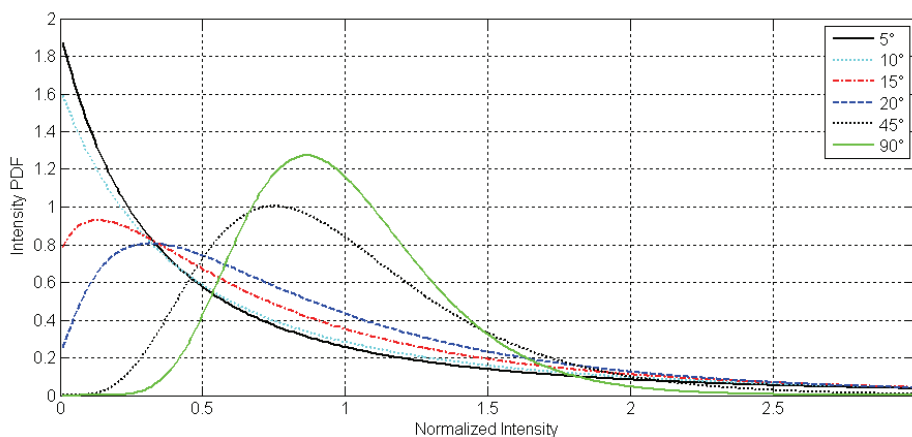
Figure 3.37: Probability density function (PDF) of the (normalized) received intensity D at different elevation angles (PiLab simulation with a standard $HV_{5/7}$ model at $\lambda = 1064\text{nm}$).
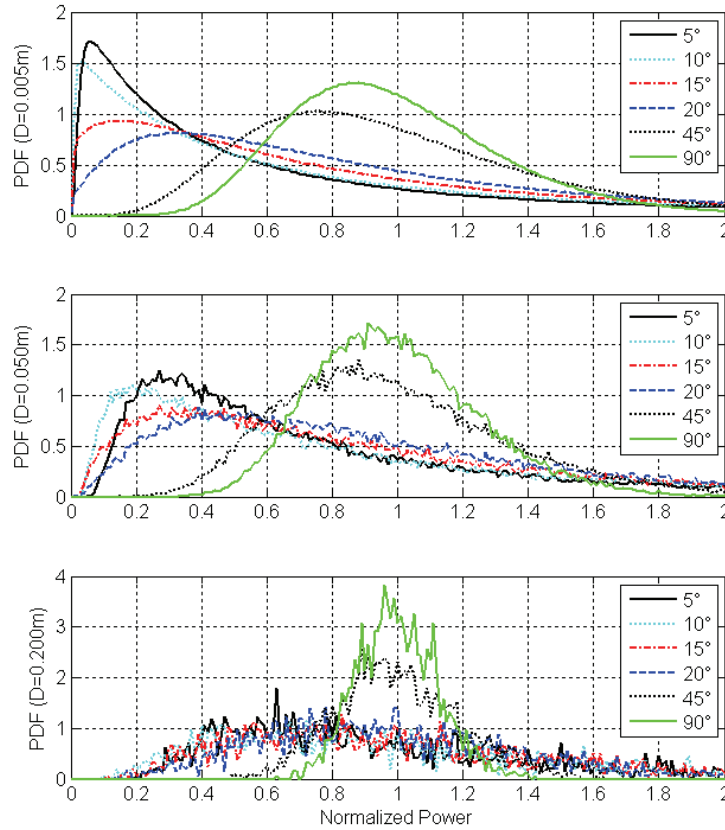
Figure 3.38: Probability density function (PDF) of the (normalized) received power for different aperture diameters D (0.5cm, 5cm, 20cm) at different elevation angles (PiLab simulation with a standard HV$_{5/7}$ model at $\lambda = 1064$nm).

3.3.2.3 Intensity Correlation Length

The intensity correlation length is obtained in the measurements from the turbulence profiler. It can be interpreted as the mean intensity-speckle size in the telescope aperture. It is derived from the normalized spatial covariance function $b_I(\rho)$ of the intensity distribution [AND01]

$$b_I(\rho) = \frac{B_I(\rho)}{B_I(0)},$$

(3.39)

where $B_I(\rho)$ denotes the covariance function. The intensity correlation length is defined for the 1/e point of the normalized covariance function.

The intensity correlation length measured during the OICETS downlink experiments 2006 is shown in Figure 3.39. Typically values range between 4 and 8cm. Maximum values are reached at 10-15 degrees elevation. At lower elevation angles it decreases due to saturation as predicted from theory.

Interesting to note is the different behaviour of the phase atmospheric coherence length r_0 and the intensity coherence length. r_0 continues to increase at higher elevation angles, whereas the intensity correlation length saturates to about 4cm.
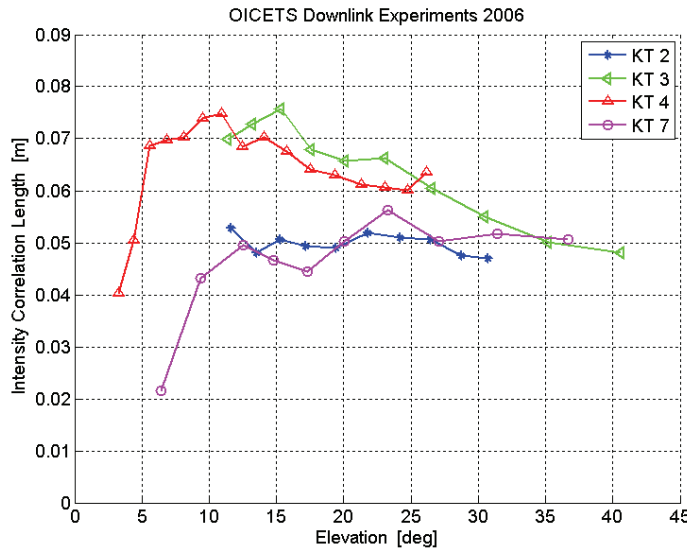
Figure 3.39 Intensity correlation length (1/e point of the normalized covariance function) as a function of elevation (OICETS SGL experiments 2006).

3.3.3 Bit-Error Rate Measurements

Figure 3.40 shows the bit-error rate (BER) measurements for the OICETS SGL experiments 2006. This is not important for the understanding of AO in the SGL scenarios, but the information is given for completeness in the discussion of AO for communication links. The data from OICETS was transmitted at 847nm with 50Mbps intensity modulation with a direct detection scheme. At low elevation angles, the BER is high due to the low signal level and strong scintillation. To higher elevation angles the BER improves as the satellite-to-ground distance decreases. An interesting effect in the experiments was the saturation of the BER above 30 degrees elevation. This was explained with the non-optimal adjustment of the threshold levels in the receiver front-end and a problem on the satellite with the laser driver causing a non-optimal signal shape. Interesting to note is that data could be received at elevation angles as low as 3 degrees in spite of the extreme atmospheric conditions.
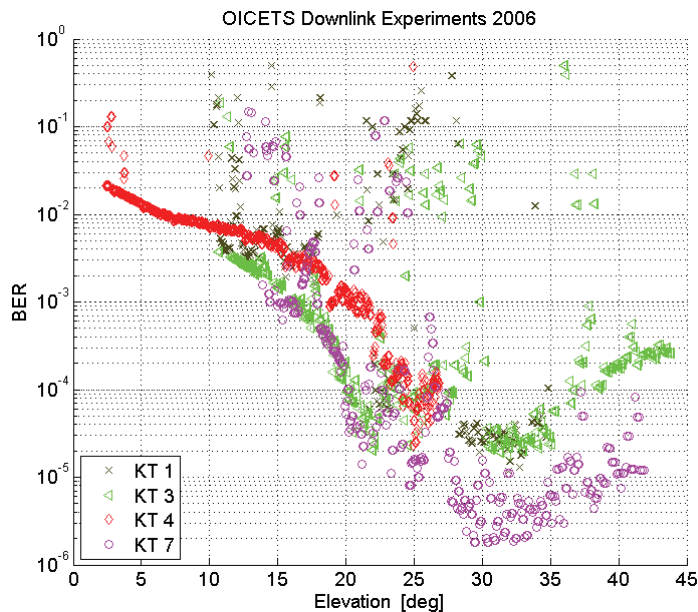
Figure 3.40: Bit-error rate measurements as a function of the elevation angle during OICETS SGL experiments 2006.

3.4 Discussion

The presented measurement results illustrated the atmospheric conditions expected in an SGL scenario. Especially LEO satellites are most of the time seen under very low elevation angles (<10 degrees), as has been shown in Chapter 2. As a consequence optical communication links have to cope with severe atmospheric conditions. Typical r_0 values become as low as 1-2cm, and also the intensity correlation length drops to a few centimeters. This implies that the AO system has to be designed with a high resolution for the wavefront sensor and the corrector. Assuming a telescope diameter of 40cm, as the telescope of the DLR OGS, the ratio D/r_0 becomes 20-40.

In addition, very strong scintillation appear on the link with frequent occurrences of low-intensity regions. This has to be taken into consideration for the selection and development of suitable wavefront sensors. The low-intensity regions also contain zero-intensity points, which cause the appearance of phase singularities. This has a significant impact on widely used wavefront sensors as the Shack-Hartmann sensor and will be further discussed in Chapter 4.4.1.

Another issue is that the atmospheric effects during a LEO satellite pass have a large dynamic range over the elevation angle. Already the received power varies by over a factor 30, as the link distance ranges from around 600km in the zenith to 3000km at the horizon. The receiver system including the AO has to be designed with this dynamic range in mind. Not only too low intensities but also high intensities with sensor saturation can disturb the performance.

4 Adaptive Optics for Laser Satellite-To-Ground Communication

This chapter gives an overview of adaptive optics (AO) in the context of laser satellite-to-ground link (SGL) communications. This scenario is characterized by very strong scintillation and wavefront distortions, which increasingly become worse the lower the elevation angles are. Additionally, the fast transversal movement of the communication beam through the atmosphere due to the satellite motion causes very fast fluctuations of the intensity and the phase.

Section 4.1 introduces the typical components of an AO system and presents general concepts widely used in adaptive optics like Zernike polynomials and Strehl ratio. Section 4.2 discusses the general requirements on an AO system based on the atmospheric characteristics presented in Chapter 3. Section 4.3 introduces the concept of phase singularities, which also appear in the SGL scenarios at low elevation angles and which can severely disturb wavefront sensing and the correction of the wavefront. Section 4.4 discusses the performance of various wavefront sensor types in strong turbulence conditions. And finally Section 4.5 briefly introduces non-conventional methods of adaptive receiver systems, which can be counted to AO systems in a broader sense, but which do not fit into the conventional concepts of AO systems.

Based on the finding in this chapter, the rich class of self-referencing interferometers appears to be promising to be further investigated for wavefront sensing in SGL scenarios. A detailed discussion of self-referencing interferometers and their application in SGL communications is given in Chapter 5.

4.1 Adaptive Optics Systems

Adaptive optics is a technique that is used to correct dynamic aberrations in an optical system in real time. The concept has been particularly developed in the field of astronomy, where it was originally proposed for correcting aberrations introduced after propagation of stellar light through the atmosphere. Introductions to AO and the history of its development can be found in the works of Hardy [HAR98], Roddier [ROD99], or Tyson [TYS98].

The basic principle of an AO system in a laser communication application is shown schematically in Figure 4.1. An incoming wavefront from a laser source that is corrugated after propagation through the atmosphere is collected at the receiver and reflected from a deformable mirror. The mirror is shaped to flatten the wavefront aberration using feedback from a wavefront sensor to give a corrected point-spread function at a detector, ideally close to that of a diffraction limited system. Usually such systems contain an additional element to correct angle-of-arrival errors, i.e. the Zernike modes 2 and 3, to relieve the deformable mirror, which is typically limited in its maximum stroke, from these modes. Here the element appears as a shiftable lens but is often a mirror on piezo actuators.

In this schematic we have only considered the correction of the received light, but in principle the correction that is applied to an incoming wave can also be applied to an outgoing wave, i.e. to pre-compensate the aberrations that will be introduced by the atmosphere as the beam propagates, and thus increase the collected energy at a distant receiver. Pre-compensation is possible in the case, where the incoming and outgoing beams travel through approximately the same volume of atmosphere. This might not be true for dynamic scenarios, where the incoming and outgoing beams have to be separated by a point-ahead angle to achieve a link, taking runtime and the platform motion into account. A critical parameter is the isoplanatic angle of the atmosphere, i.e. the angular range in which the atmosphere has approximately the same properties [HAR98].

The predominant development of AO has been for the use in astronomical applications at ground based observatories, therefore many of the components that are conventionally used in AO systems have a strong focus on low light levels, incoherent light sources, only

moderate phase distortions and weak intensity fluctuations. The requirements for AO systems in the field of optical communications however differ from the requirements in astronomy. AO systems seem to be most suitable for the deployment on the ground (less on flight platforms), considering the complexity of these systems and taking into account, that most of the atmospheric phase distortions are generated close to the ground.

In the following sections we review the benefits of AO systems for the use in satellite-to-ground communication scenarios. Estimates for the spatial (resolution) and temporal (bandwidth) requirements of such AO systems will be discussed. Different types of wavefront sensors are introduced and examined in the light of the special requirements of the scenario.
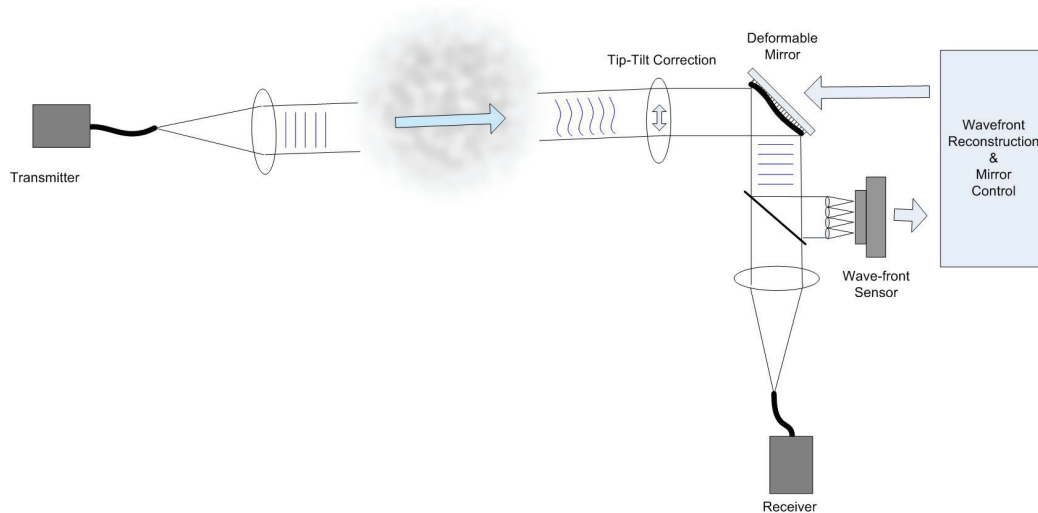
Figure 4.1: Schematic of a general AO system for a laser communication link, including a deformable mirror, a wavefront sensor with control system, and the receiver element.

4.1.1 Adaptive Optics Components

The main components of an AO system are the correcting element to straighten the distorted wavefront, the wavefront sensor used to measure the residual wavefront error and the control computer, which is used to update the wavefront corrector with feedback from the wavefront sensor signal in real time.

The wavefront corrector in most AO systems is typically a deformable mirror (DM), where a reflecting surface or membrane is moved by a number of actuators. A DM can be characterized by the surface type (continuous or segmented), the actuation type (piezoelectric, electrostatic, magnetic), the stroke (i.e. the maximum surface deformation and the maximum inter-actuator stroke), the number and arrangement of the actuators and the response time of the mirror. A comparison of a selection of commercially available mirrors in terms of spatial correction can be found in [DAL05, DEV08]. Two deformable mirrors with their actuator layout are depicted in Figure 4.2.
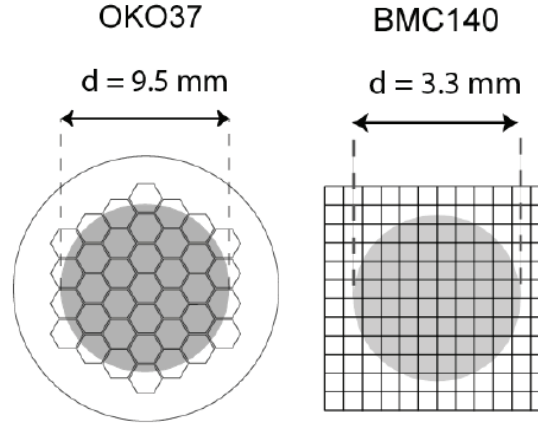
Figure 4.2: Actuator layout of two deformable mirrors (left: BMC140 from Boston Micromachines, 140 actuators, segmented/continuous; right: OKO37 from Flexible Optical, 37 actuators, continuous) with the typical optical pupil superimposed (from [DEV08]).

4.1.2 Modal Representation of the Wavefront Phase by Zernike Polynomials

Zernike polynomials are used to represent a wavefront over a circular aperture. Originally the polynomials were used to describe aberrations of optical systems. Therefore the lower order polynomials give aberrations like tilt (j=2,3), defocus (j=4), astigmatism (j=5,6), and coma (j=7,8). Piston (j=1) is usually neglected for AO systems, as it does not influence the wavefront correction. An introduction to Zernike polynomials can be found in [HAR98, BOR99, ROD99, NOL76]. The following formulas and the numbering for the polynomials are based on Noll's work [NOL76].

The wavefront phase φ (in radians) is represented by the Zernike polynomials $Z_j(\rho,\psi)$ in polar coordinates $\bar{\rho} = (\rho,\psi)$ by

$$\varphi(\rho,\psi) = \sum_{j=1}^{\infty} a_j Z_j(\rho,\psi) \ , \tag{4.1}$$

where the radius coordinate ρ *(0<ρ<1)* is normalized to the aperture radius R. The Zernike polynomials are chosen so that they fulfill the modal orthogonality property

$$\frac{1}{\pi} \int_0^1 \int_0^{2\pi} Z_i(\rho,\psi) Z_j(\rho,\psi) \rho \cdot d\rho \cdot d\psi = \delta_{ij} \ , \tag{4.2}$$

where δ_{ij} is the Kronecker delta

$$\delta_{ij} = \begin{cases} 1, & \text{if } i = j \\ 0, & \text{if } i \neq j \end{cases} \tag{4.3}$$

and the integration is performed in polar coordinates over the circular aperture. The factor π before the integral gives the area of the aperture with radius 1. Multiplying Eq. (4.1) on both sides with Z_i

$$Z_i(\rho,\psi) \cdot \varphi(\rho,\psi) = \sum_{j=0}^{\infty} a_j Z_i(\rho,\psi) \cdot Z_j(\rho,\psi) \ , \tag{4.4}$$

integrating over the circular aperture and using property (4.2), the Zernike coefficients a_j for a specific wavefront can be calculated by

$$a_j = \frac{1}{\pi} \int_0^1 \int_0^{2\pi} \varphi(\rho, \psi) Z_j(\rho, \psi) \rho \cdot d\rho \cdot d\psi \qquad (4.5)$$

The functions of the Zernike polynomials Z_i can be found e.g. in [NOL76]. Figure 4.3 shows the first Zernike polynomials. Noll also presented, besides the Zernike polynomials, the Fourier transform and the derivative of the polynomials.
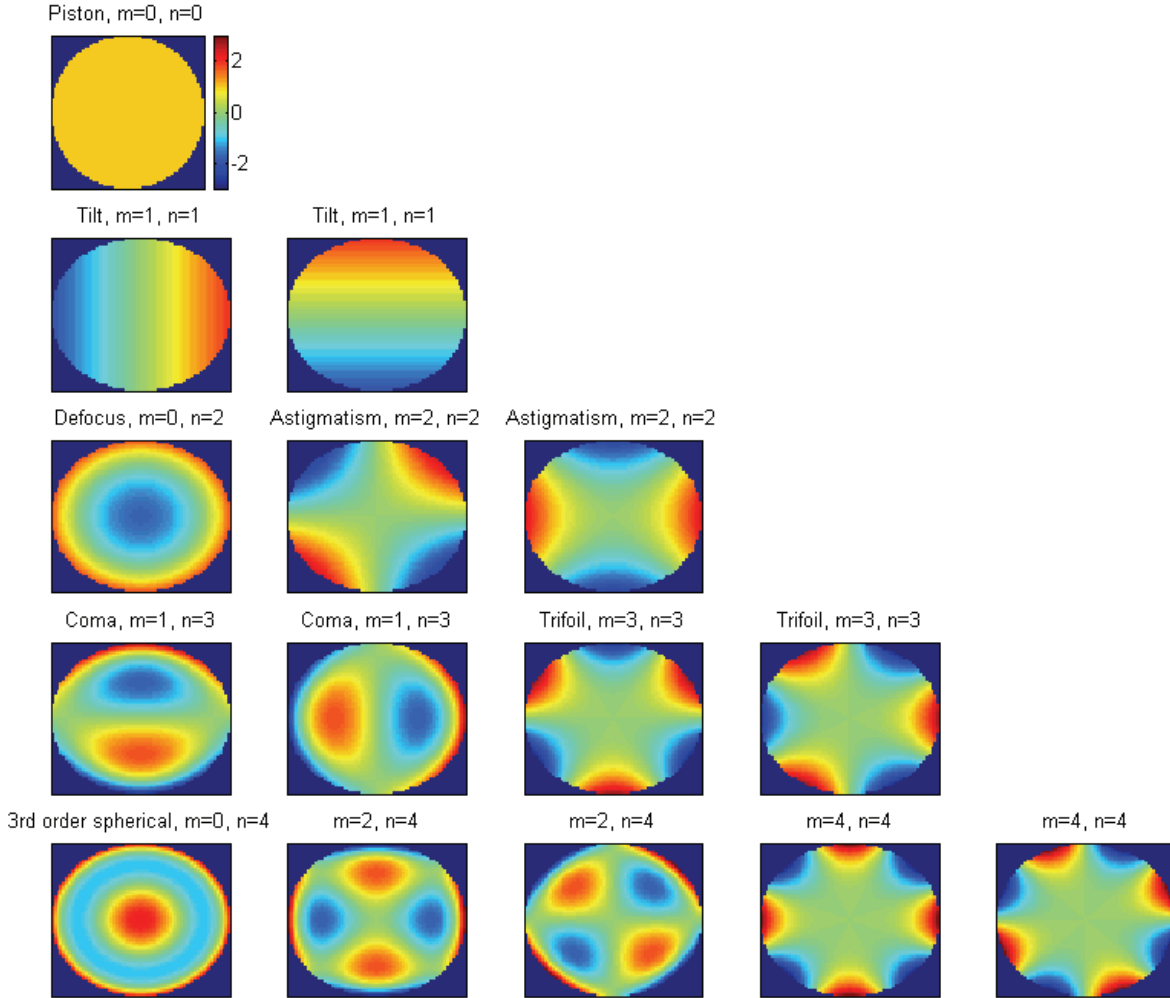
Figure 4.3: First Zernike polynomials. The azimuthal degree *m*, the radial degree *n*, and the aberration name are given above the images.

Mahajan [MAH81] and Dai [DAI07] extended the Zernike polynomials from circular to annular shaped apertures, i.e. with a central obscuration. A similar expression to Eq. (4.1) is given taking the obscuration ration $\varepsilon_a = \frac{D_{Aperture}}{D_{Obscuration}}$ into account

$$\varphi(\rho, \psi, \varepsilon_a) = \sum_{j=0}^{\infty} a_j(\varepsilon_a) \cdot Z_j(\rho, \psi, \varepsilon_a) . \qquad (4.6)$$

Again the orthogonality property is fulfilled, this time over the annulus, being expressed in the integral over the annulus

$$\frac{1}{\pi\left(1-\varepsilon_a^2\right)} \int_{\varepsilon_a}^{1} \int_{0}^{2\pi} Z_i\left(\rho,\psi,\varepsilon_a\right) Z_j\left(\rho,\psi,\varepsilon_a\right) \rho \cdot d\rho \cdot d\psi = \delta_{ij}. \tag{4.7}$$

The annular coefficients are calculated by

$$a_j\left(\varepsilon_a\right) = \frac{1}{\pi\left(1-\varepsilon_a^2\right)} \int_{\varepsilon_a}^{1} \int_{0}^{2\pi} \varphi\left(\rho,\psi,\varepsilon_a\right) Z_j\left(\rho,\psi,\varepsilon_a\right) \rho \cdot d\rho \cdot d\psi \tag{4.8}$$

The derivation of the annular Zernike polynomials in a recursive formula based on the conventional Zernike polynomials can be found in [DAI07]. Figure 4.4 shows the first annular Zernike polynomials with a central obscuration $\varepsilon_a = 1/3$.
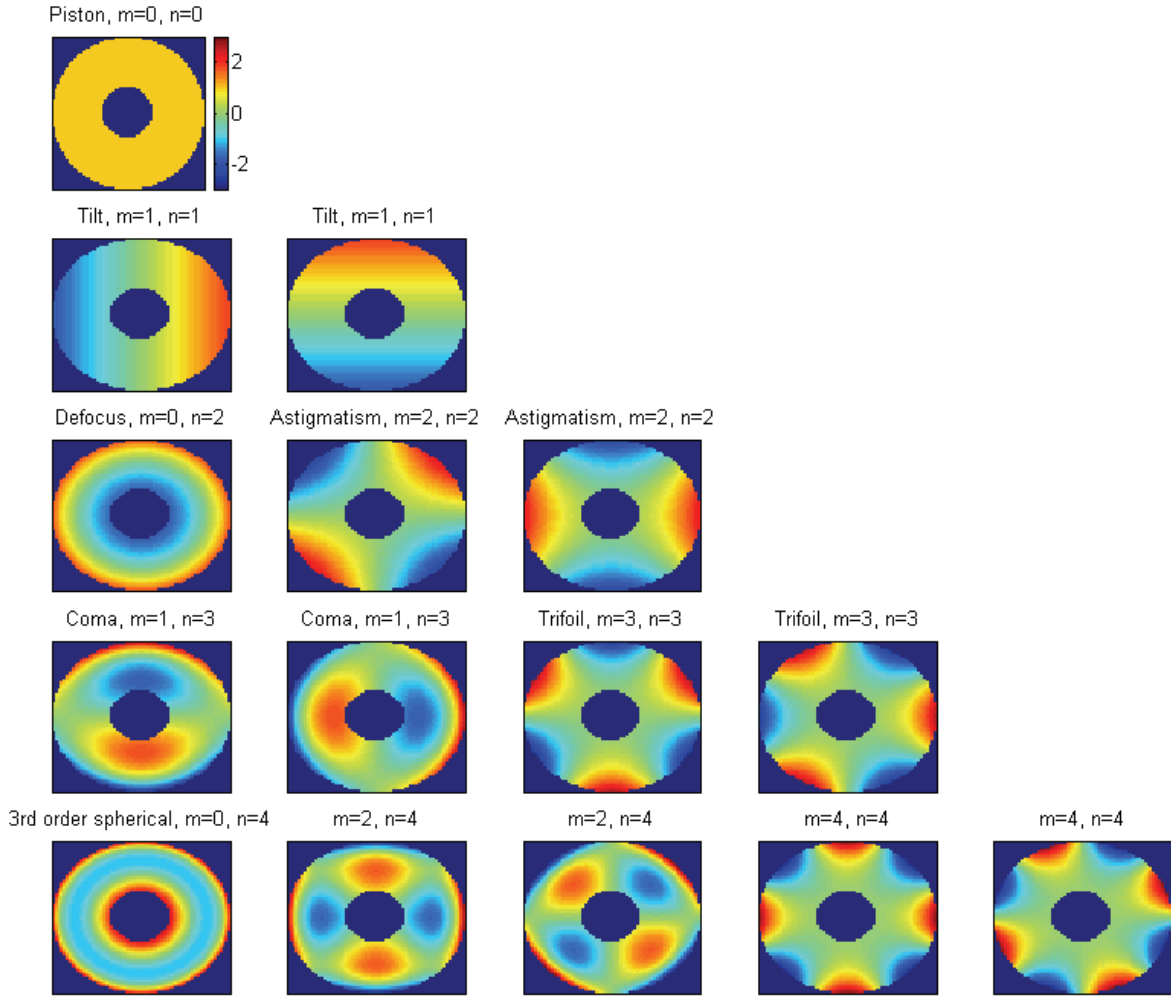
Figure 4.4: First annular Zernike polynomials based on the publication of Dai and Majahan. The azimuthal degree *m*, the radial degree *n*, and the aberration name are given above the images.

A topic of interest in the literature was the statistical analysis of phase distortions based on the Kolmogorov turbulence spectrum in terms of Zernike polynomials. Wang and Markey [WAN78] gave, based on the work of Fried [FRI65] and Noll [NOL76], an expression for the correlation $\left\langle a_j^* a_{j'} \right\rangle$ between two Zernike polynomials Z_j and $Z_{j'}$ with the coefficients a_j and $a_{j'}$. Based on this the variance of a coefficient a_i with the radial degree n is given by

$$\sigma_{a_i}^2 = \left\langle a_i^2 \right\rangle = 0.152 \left(\frac{D}{r_0}\right)^{5/3} (n+1) \frac{\Gamma\left(\frac{14}{3}\right)\Gamma\left(n-\frac{5}{6}\right)}{\Gamma\left(\frac{17}{6}\right)^2 \Gamma\left(n+\frac{23}{6}\right)} , \qquad (4.9)$$

where Γ denotes the Gamma function. Figure 4.5 shows the magnitude of the variance for the first 20 coefficients, omitting the factor $\left(\frac{D}{r_0}\right)^{5/3}$ in Eq. (4.9). It can be clearly seen that the most significant impact on the wavefront comes from the first two Zernike polynomials ($j=2,3$), i.e. tip and tilt.
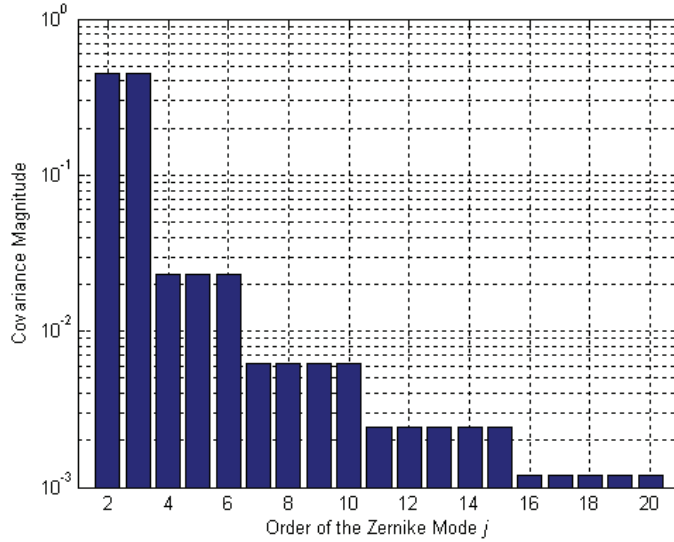
Figure 4.5: Variance of the Zernike coefficients $\left\langle a_j^* a_j \right\rangle$ for a Kolmogorov spectrum.

A correcting element like a deformable mirror reduces the wavefront error by inversely applying the estimated wavefront φ_c. The mean square residual wavefront error can then be written as

$$\sigma^2 = \frac{1}{\pi} \iint_{Aperture} \left[\varphi(\rho,\psi) - \varphi_c(\rho,\psi)\right]^2 \rho \, d\rho \, d\psi \qquad (4.10)$$

The factor ρ is included for the integration in polar coordinates and σ^2 is given in radians square. The relation to the wavefront error expressed in meters instead of radians and assuming a wavelength λ is given by $\sigma_W = \frac{\lambda}{2\pi} \cdot \sigma$. For a modal Zernike approximation up to order N the resulting wavefront is given by

$$\varphi_c(\rho,\psi) = \sum_{j=1}^{N} a_j Z_j(\rho,\psi). \qquad (4.11)$$

Substituting Eq. (4.11) into (4.10) and changing the order of integration and summation gives the residual mean square phase error σ_N^2 for a modal correction up to order N

$$\sigma_N^2 = \frac{1}{\pi} \iint\limits_{Aperture} \rho \cdot \varphi(\bar{\rho})^2 d\bar{\rho} - \frac{2}{\pi} \sum_{j=1}^{N} a_j \iint\limits_{Aperture} \rho \cdot \varphi(\bar{\rho}) Z_j(\bar{\rho}) d\bar{\rho} +$$
$$+ \frac{1}{\pi} \sum_{i,j=1}^{N} a_i a_j \iint\limits_{Aperture} \rho \cdot Z_i(\bar{\rho}) Z_j(\bar{\rho}) d\bar{\rho} \qquad (4.12)$$

With relation (4.5) to substitute the integral in the second term with πa_j and the orthogonality condition (4.2) to perform the integration in the last term, we get

$$\sigma_N^2 = \frac{1}{\pi} \iint\limits_{Aperture} \rho \varphi(\bar{\rho})^2 d\bar{\rho} - \sum_{i=1}^{N} a_i^2 . \qquad (4.13)$$

Eq. (4.12) and (4.13) yield the mean square residual error for one specific phase distribution. This relation can be modified to calculate the ensemble average, i.e. the average over time.

$$\sigma_N^2 = \left\langle \varphi^2 \right\rangle - \sum_{i=1}^{N} \left\langle a_i^2 \right\rangle \qquad (4.14)$$

Noll provided explicit formulas for the mean residual phase error σ_N^2 based on a Kolmogorov turbulence spectrum. These expressions are based on Eq. (4.9). The value for the piston term $j=1$ is infinite, but the piston-corrected phase variance can be calculated by the sum

$$\sigma_1^2 = \sum_{i=2}^{\infty} \left\langle a_i^2 \right\rangle \qquad (4.15)$$

which yields in accordance with Noll

$$\sigma_1^2 = 1.03 \cdot \left(\frac{D}{r_0} \right)^{5/3} . \qquad (4.16)$$

Table 4.1 shows the first 8 expressions for the for the mean square residual error for partial modal corrections.

Table 4.1: Residual mean square phase error for selected orders of modal correction.

Residual Error	Corrected terms
$\sigma_1^2 = 1.0299 \cdot \left(\frac{D}{r_0}\right)^{5/3}$	Piston
$\sigma_2^2 = 0.582 \cdot \left(\frac{D}{r_0}\right)^{5/3}$ $\sigma_3^2 = 0.134 \cdot \left(\frac{D}{r_0}\right)^{5/3}$	Piston, tilt
$\sigma_4^2 = 0.111 \cdot \left(\frac{D}{r_0}\right)^{5/3}$	Piston, tilt, defocus
$\sigma_5^2 = 0.0880 \cdot \left(\frac{D}{r_0}\right)^{5/3}$ $\sigma_6^2 = 0.0648 \cdot \left(\frac{D}{r_0}\right)^{5/3}$	Piston, tilt, defocus, astigmatism
$\sigma_7^2 = 0.0587 \cdot \left(\frac{D}{r_0}\right)^{5/3}$ $\sigma_8^2 = 0.0525 \cdot \left(\frac{D}{r_0}\right)^{5/3}$	Piston, tilts, astigmatism, coma
$\sigma_N^2 \approx 0.2944 \cdot N^{-\sqrt{3}/2} \cdot \left(\frac{D}{r_0}\right)^{5/3}$	Approximation of the residual square phase error for larger values of N

4.1.3 Wavefront Residual Error and Strehl Ratio

A widely used measure for wavefront distortions and therefore for the quality of a formed focus spot is the Strehl ratio S. The Strehl ratio gives the ratio between the maximum intensity of an aberrated beam over the maximum intensity of an unaberrated beam, i.e. an Airy distribution. Therefore $S=1$ indicates an ideal focus spot. The range of S lies between zero and one. Several approximations for the relation between the wavefront error variance and the Strehl ratio have been given in the literature. Mahajan [MAH83] gave a comparison between several approximations. A widely used approximation is (σ in radians)

$$S_1 \approx \exp\left(-\sigma^2\right). \tag{4.17}$$

Maréchal gave the approximation

$$S_2 \approx \left(1 - \frac{\sigma^2}{2}\right)^2, \tag{4.18}$$

which is closely related to a formula given by Born and Wolf [BOR99]

$$S_3 \approx 1 - \sigma^2 \tag{4.19}$$

and can be easily derived from S_2 by neglecting the fourth order term σ^4. S_2 and S_3 are both related to S_1 by the Taylor expansion $\exp\left(-\sigma^2\right) = 1 - \sigma^2 + \frac{1}{2}\sigma^4 - \ldots$ Mahajan showed that the error of all three approximations stays below 10% for Strehl ratios greater 0.6 or a wavefront standard deviation smaller 0.6 radians applied to primary aberrations across the pupil. Approximation S_1 yields slightly better values. Both S_2 and S_3 underestimate the Strehl ratio. Figure 4.6 shows a comparison of the three algorithms.
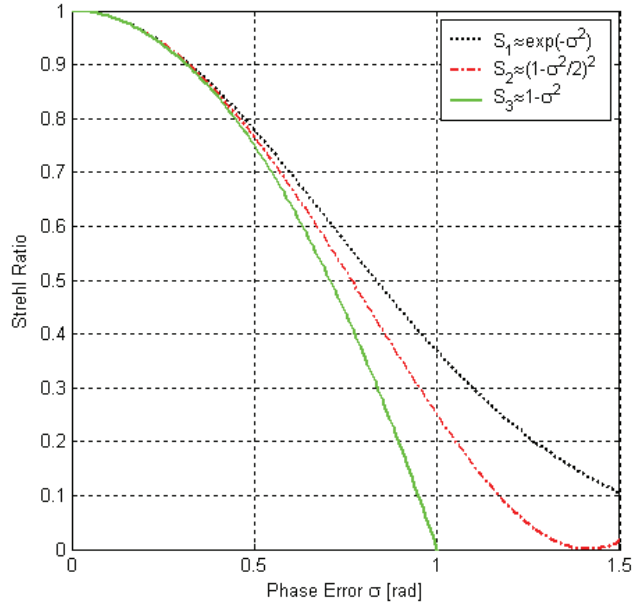
Figure 4.6: Comparison of the approximations for the relationship between wavefront error and Strehl ratio. S_1 and S_2 typically underestimate the Strehl ratio.

4.2 General Requirements for Adaptive Optics Systems in Satellite-To-Ground Links

This section analyzes the particular demands on an AO system for satellite-to-ground links (SGL). This will be the basis for the analysis of wavefront sensors and their performance characteristics under these specific conditions. From the experiments and measurements described in Chapter 3, it can be said that AO systems in these scenarios have to work under the following conditions [KNA09]:

- Very strong phase distortions and intensity fluctuations (scintillation) due to the long path through the atmosphere especially at low elevation angles.

- Challenging temporal requirements due to the transversal motion of the beam through the atmosphere.

- Phase singularities, which impair the performance of wavefront sensors and might inhibit the use of continuous deformable mirrors.

- Deployment of the ground stations at preferably non-astronomical sites at low altitudes to allow a wide spread of stations, however at the cost of difficult atmospheric turbulence conditions.

4.2.1 Wavefront Variance and Tip-Tilt over the Telescope Aperture

In a first step the expected variance of the wavefront and therefore the required stroke of a deformable mirror (DM) and the range of a tip-tilt correction for certain atmospheric conditions is estimated. The central atmospheric parameter for this estimation is the Fried parameter r_0.

Usually an AO system corrects the tip/tilt modes and the higher order modes with separate correctors. The reason for this is that typical DMs have a limited stroke, which is not sufficient to correct all modes. This seems to be especially reasonable as the tip/tilt modes produce the strongest phase distortions. The peak-to-peak stroke across the aperture can be estimated to 5 times [TYS00] the standard deviation of the values given in Table 4.1. Thus, the maximum required DM stroke with a tip/tilt corrected phase would be calculated by

$$Stroke\,[rad] = \frac{5}{2} \cdot \sqrt{\sigma_3^2} = \frac{5}{2} \cdot 0.366 \left(\frac{D}{r_0} \right)^{5/6}. \qquad (4.20)$$

The factor ½ is included as the mirror has to move only half the distance of the wavefront distortion due to the reflection. The stroke in meters is then calculated by

$$Stroke[meters] = Stroke[rad] \cdot \frac{\lambda}{2\pi} \qquad (4.21)$$

The variance of the atmospheric tilt σ_θ over the aperture D of the telescope primary mirror and at the wavelength λ can be estimated by [TYS00]

$$\sigma_\theta^2 = 0.184 \left(\frac{D}{r_0} \right)^{5/3} \left(\frac{\lambda}{D} \right)^2. \qquad (4.22)$$

The maximum atmospheric tilt α_θ that a tip-tilt correction mirror should be able to remove is estimated by

$$\alpha_\theta = \pm 2.5 \sigma_\theta. \qquad (4.23)$$

Because of the telescope magnification the total stroke of the tilt mirror calculates to

$$Stroke_\theta = \frac{1}{2} \alpha_\theta \left(\frac{D}{D_{\text{tilt-mirror}}} \right), \qquad (4.24)$$

where $D_{\text{tilt-mirror}}$ denotes the beam diameter at the tilt mirror. The magnification of the telescope system is given by $m = \frac{D}{D_{tilt-mirror}}$. As the tilt motion of the mirror results in twice the angular tilt of the beam, a factor ½ is included.

Taking the Fried parameter for a plane wave (Section 3.1.4.3)

$$r_0 = \left(\frac{\lambda}{2\pi} \right)^{6/5} \left[0.423 \int_{z=0}^{L} C_n^2(z) dz \right]^{-3/5} \qquad (4.25)$$

and inserting it into Eq. (4.22) results in

$$\sigma_\theta^2 = 0.184 \cdot D^{-1/3} \cdot \lambda^2 \cdot r_0^{-5/3} = 3.073 \cdot D^{-1/3} \int_{z=0}^{L} C_n^2(z) dz. \qquad (4.26)$$

It is interesting to note that the tilt variance is independent of the wavelength.

4.2.2 Zonal Analysis – Resolution

The achievable Strehl ratio S of an AO system depends on the actuator spacing r_c of the DM, the Fried parameter r_0 and the constant κ_{DM}, which describes the behavior of the deformable mirror and its actuator influence function [TYS00]. Typical continuous faceplate DMs are well modeled by $\kappa_{DM} = 0.35$. The residual phase error σ is estimated for a certain actuator spacing r_c (in the entrance pupil of the telescope) and a worst case r_0 assuming a Kolmogorov spectrum by [HUD77]

$$\sigma^2 = \kappa_{DM} \cdot \left(\frac{r_c}{r_0}\right)^{5/3} \tag{4.27}$$

and the resulting Strehl ratio is estimated using approximation (4.17)

$$S = \exp\left(-\kappa_{DM}\left(\frac{r_c}{r_0}\right)^{5/3}\right). \tag{4.28}$$

In the opposite direction the actuator spacing can be derived from r_0 and a required S by

$$r_c = r_0 \left(\frac{\ln S}{-\kappa_{DM}}\right)^{3/5}. \tag{4.29}$$

The number of required actuators with spacing r_c over the full aperture of the telescope can be estimated by

$$N_a = \frac{\pi \cdot \left(\frac{D^2}{4}\right)}{r_c^2} = \frac{\pi}{4}\left(\frac{D}{r_c}\right)^2. \tag{4.30}$$

As a rule of thumb the actuator spacing can be assumed to be equal to the minimum r_0 to be corrected under the assumption of the weak fluctuation regime. This would result in a Strehl ratio of about S=0.7. For strong fluctuations with phase singularities, a higher actuator respectively sensor resolution is required (see Section 4.4.1.2).

4.2.3 Modal Analysis with Zernike Polynomials

The modal analysis shows the performance of an AO system for a partial correction with N Zernike modes. The higher the number of corrected modes, the lower the residual phase error and the better the Strehl ratio will be. Figure 4.7 shows the correction performance as a function of the ratio D/r_0. Five curves with different degree of correction (N = 1 no correction (piston is ignored), N = 3 tip/tilt correction, N = 8, N = 20, N=100) are shown. The graph is based on the equations in Table 4.1 and the approximate relation between residual error and Strehl ratio (4.17).

A simple tip-tilt correction (N = 3) suffices to achieve a Strehl ratio of 0.5 assuming a ratio D/r_0=2.5. For a ratio D/r_0 = 8 about N = 20 modes have to be corrected. In Chapter **3** typical values for the atmospheric coherence length r_0 are given. At 5 degrees elevation, r_0 values are as low as 2cm. Assuming telescopes diameters of D=10-40cm, it becomes obvious that wavefront errors pose a problem to achieve reasonable Strehl ratios respectively residual phase errors. Thus, phase distortions are a problem for fiber coupled or coherent communication system, as they rely on the quality of the received wavefront.

Apart from the phase distortions, scintillation on the signal become very strong at low elevation angles. The strength of the power scintillation at the level of a fiber-coupled receiver can be reduced by using larger telescope apertures taking advantage of the aperture-averaging effect; however, this of course directly increases the demands on the AO system in terms of required resolution (sensor and corrector) and the number of required Zernike modes.
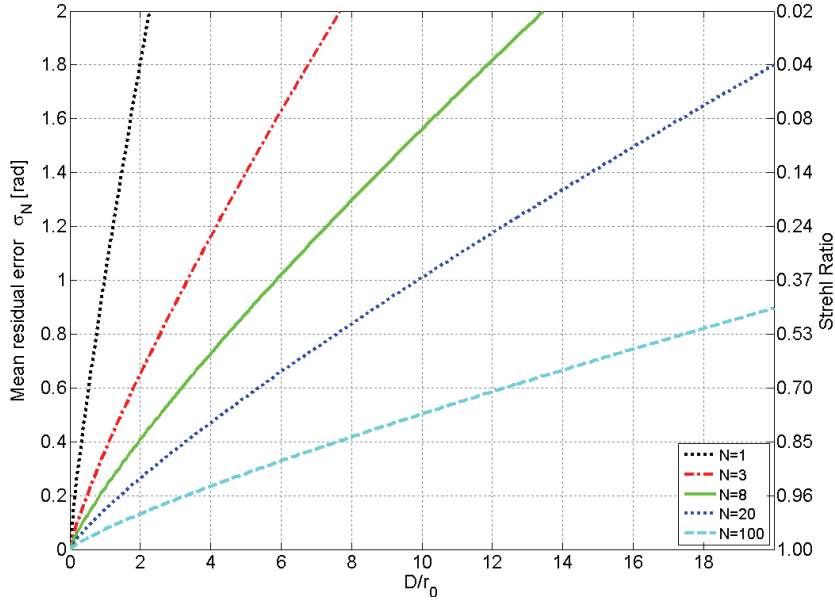
Figure 4.7: Mean residual phase error for selected orders of modal phase correction (N=1,3,8,20,100) as a function of D/r_0. The corresponding Strehl ratio calculated with approximation (4.17) can be seen on the right axis.

4.2.4 Temporal Analysis – Bandwidth Requirements

An important parameter of an AO system is the required bandwidth to achieve a desired correction performance. Greenwood [GRE77] developed a method, based on a joint work with Fried [GRE76], to estimate the bandwidth requirements of an AO system using the Taylor "frozen turbulence" hypothesis. He expressed the mean residual phase error of the corrected wavefront due to bandwidth limitations by

$$\sigma_G^2 = \int_0^\infty \left|1 - H\left(f, f_{3dB}\right)\right|^2 P(f)\, df \tag{4.31}$$

where $P(f)$ denotes the disturbance power spectrum over the frequency f. The performance of the AO system can be modeled in various ways. Greenwood used a sharp cut-off function and a simple first order (RC) filter. The RC filter with the 3dB cut-off frequency f_{3dB} is assumed for the following discussion and the closed-loop servo response is modeled by

$$H\left(f, f_{3dB}\right) = \left(1 + \frac{if}{f_{3dB}}\right)^{-1} \tag{4.32}$$

and consequently

$$\left|1 - H(f)\right|^2 = \frac{f^2}{f_{3dB}^2 + f^2}\ . \tag{4.33}$$

The residual phase error σ_G of the system can then be expressed in dependence of f_{3dB} and the Greenwood frequency f_G, which is characteristic for the atmospheric turbulence and wind conditions

$$\sigma_G^2 = \left(\frac{f_G}{f_{3dB}}\right)^{5/3} \quad \text{or} \quad f_{3dB} = \frac{f_G}{\sigma_G^{6/5}}\ . \tag{4.34}$$

The Greenwood frequency f_G is given by

$$f_G = 2.31 \cdot \lambda^{-6/5} \left[\int C_n^2(z) \cdot v_\perp^{5/3}(z) dz \right]^{\frac{3}{5}} . \tag{4.35}$$

It depends on the effective velocity $v_\perp$ of the inhomogeneous media, which moves transversal across the beam. It includes the wind velocity and the angular speed due to the satellite motion. Eq. (4.35) is given for the asymptotic limit of infinite aperture diameters.

Figure 4.8 shows the Greenwood frequency over the elevation angle for a static link, which includes only the wind speed (Bufton only), and a dynamic link to a LEO satellite, which includes the wind speed and the satellite motion (Sat. +Bufton). The simulations are based on the $HV_{5/7}$ turbulence and the Bufton wind model with the parameters specified in Chapter 3. At low elevation angles the bandwidth requirements for a satellite link significantly increase, as the beam travels a longer distance through the atmosphere and the transversal motion of the beam linearly increases with the distance to the ground station, i.e. angular slew rate times distance $\omega_s \cdot z$.

Figure 4.9 depicts the resulting Strehl ratio with an AO system as a function of the cut-off frequency f_{3dB} based on Eq. (4.34) and (4.17). Also this graph shows very high bandwidth requirements for low elevation angles.
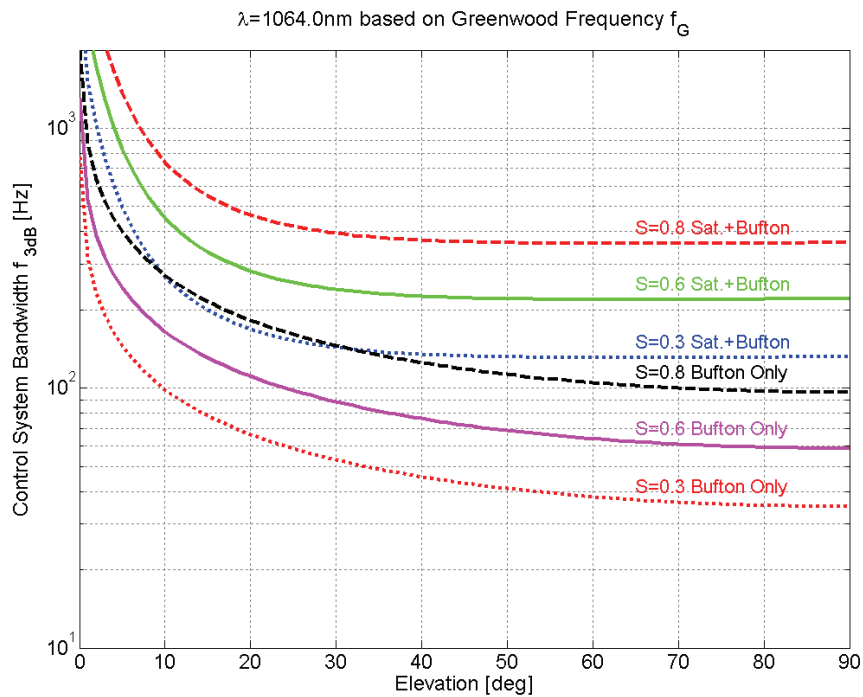
Figure 4.8: Control-system bandwidth f_{3dB} requirements at 1064nm over the elevation. The upper three curves give the bandwidth requirements for a LEO satellite SGL, taking the satellite motion and the Bufton wind model into consideration. The lower three curves represent a static link as in a GEO link considering only the atmospheric wind influence. Three different Strehl ratios (S=0.3, 0.6, 0.8) are plotted for each scenario.
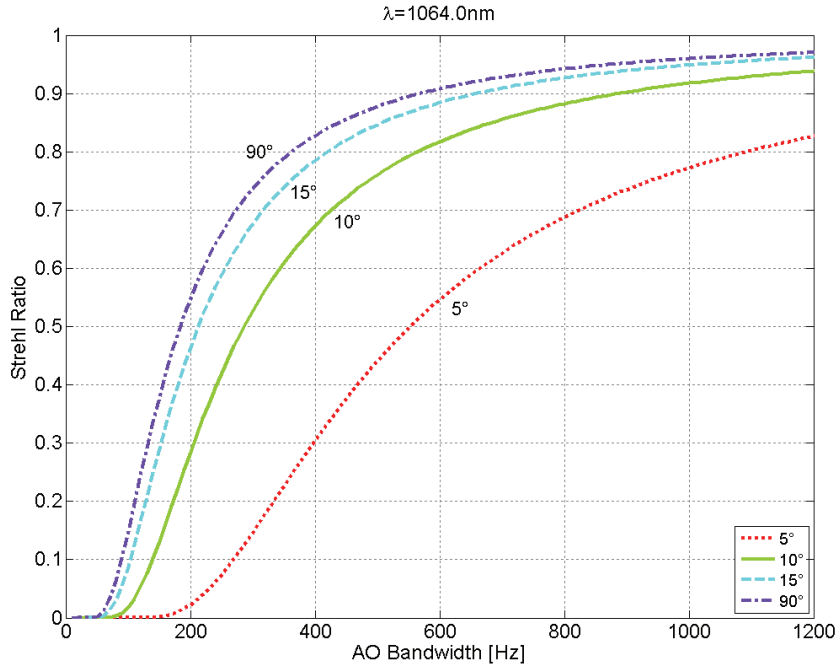
Figure 4.9: Resulting Strehl ratio at 1064nm over the 3dB cut-off frequency f_{3dB} of the AO system. Each curve represents a certain elevation angle. The graph is given for an SGL scenario from a LEO satellite.

Tyler [TYL94] developed an expression for the centre-of-gravity (G-tilt) power spectrum of an atmospheric link and deduced a characteristic frequency f_{T_G}, also called the tilt Greenwood frequency due to its similarity to the Greenwood frequency. It is given by

$$ f_{T_G} = 0.331 \frac{D^{-1/6}}{\lambda} \left[\int C_n^2(z) v_\perp^2(z) dz \right]^{1/2} . \tag{4.36} $$

The according residual one-axis tilt variance is estimated again in dependence of the 3dB cut-off frequency f_{3dB} of the AO system

$$ \sigma_\theta^2 = \left(\frac{f_G}{f_{3dB}} \right)^2 \left(\frac{\lambda}{D} \right)^2 . \tag{4.37} $$

Figure 4.10 shows the tilt Greenwood frequency for a 0.2m telescope over the elevation angle, which gives an estimate for the bandwidth requirements of a tip-tilt correction system. Again the bandwidth requirement shows an increase for low elevation angles. Figure 4.11 shows the residual tilt variance as a function of the control-loop bandwidth.
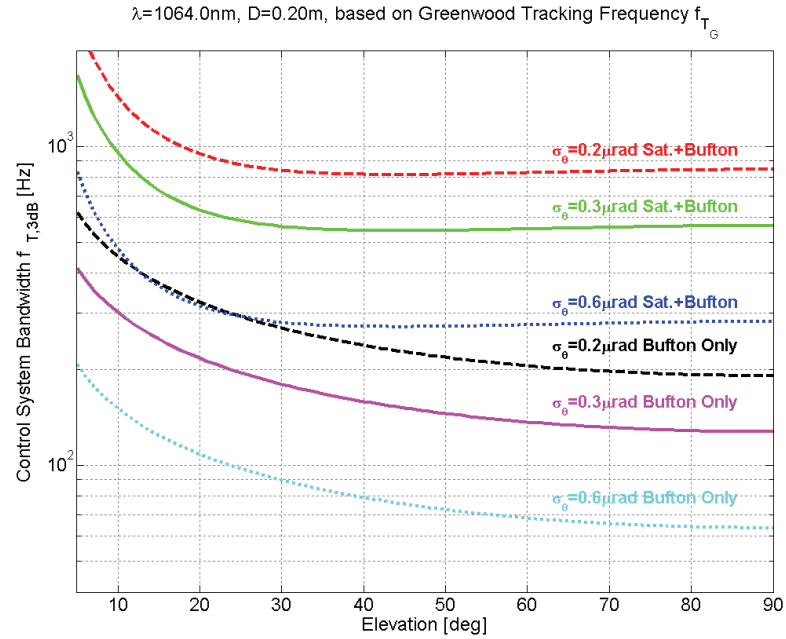
Figure 4.10: Control-system bandwidth f_{3dB} for a tip-tilt correction over the elevation angle for a static beam and a moving beam due to a LEO satellite motion. The static beam assumes a transversal wind velocity calculated from the Bufton model. The dynamic beam assumes the satellite motion together with the wind velocity. Simulation parameters are λ=1064nm, D=20cm.
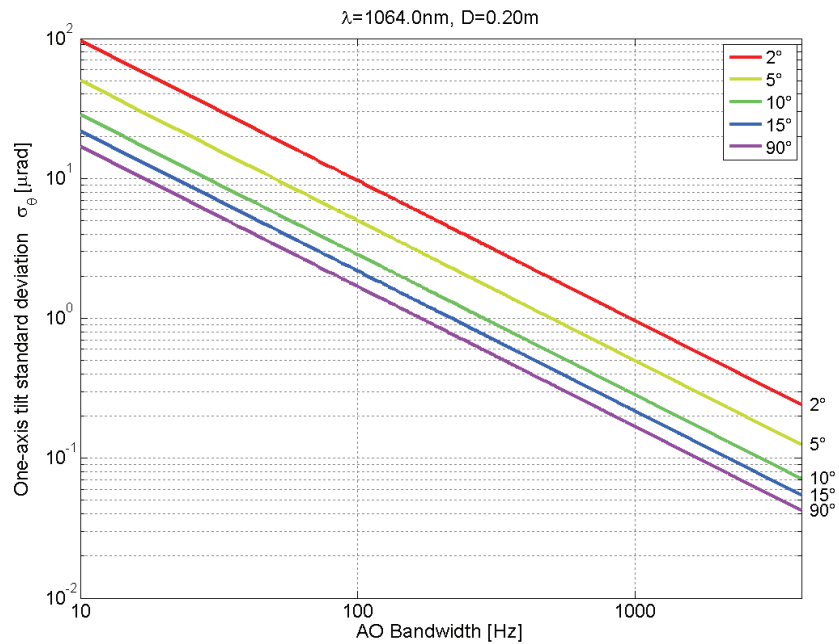
Figure 4.11: Residual tilt variance over the 3dB cut-off frequency f_{3dB} of the AO system as a function of the elevation angle. Simulation parameters are λ=1064nm, D=20cm in a SGL scenario from a LEO satellite.

75

4.3 Effects of Strong Scintillation and Phase Singularities

The strength of intensity scintillation is commonly classified from the weak (intensity) fluctuation regime over the moderate to strong fluctuation regime. Most of the calculations describing the effects of the atmosphere can only be applied for the weak fluctuation regime, as they are based on the Rytov theory which is only valid under weak fluctuations. A measure of the scintillation level on a path through the atmosphere is the Rytov index (variance) given for an SGL, i.e. transmitter in space and assuming a plane wave, by

$$\sigma_R^2 = 2.25k^{7/6} \int_0^L C_n^2(z) \cdot z^{5/6} dz , \qquad (4.38)$$

where z is the distance from the ground station, $C_n^2(z)$ the atmospheric-turbulence structure constant at the distance z, and L the distance to the satellite. Typically, values of $\sigma_R^2 < 0.3$ are assumed to be in the weak fluctuation regime. Higher values indicate moderate to strong fluctuations. The Rytov index corresponds to the normalized variance of the intensity for a plane wave under weak fluctuations and assuming a Kolmogorov turbulence spectrum. Figure 4.12 shows the Rytov index for an SGL over the elevation angle. The strong fluctuation regime approximately starts below an elevation angle of 30 degrees at $\sigma_R^2 > 0.3$.
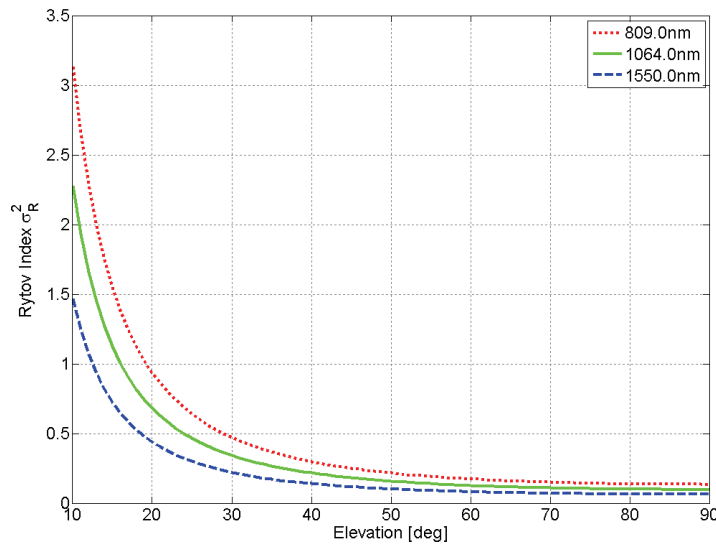
Figure 4.12: The Rytov index for a plane wave as a function of the elevation angle for three communication wavelengths. A HV$_{5/7}$ turbulence model was taken (Section 3.1.3.1).

Several authors have investigated the occurrence of phase singularities (also called branch points, phase dislocations) in atmospheric laser links [BAR83][FRI98]. Voitsekhovich et al. [VOI98] and Tyler [TYL00] gave expressions for the density of phase singularities. Tyler suggested that singularities appear at $\sigma_R^2 > 0.3$, which is confirmed by our own simulations with the phase screen approach. Fried [FRI98] and Tyler [TYL00] studied the influence of phase singularities on the least-square type phase reconstruction usually employed for standard Shack-Hartmann wavefront sensors, whose performance steeply deteriorates in the presence of singularities (see Section 4.4.1.1). Fried [FRI01], Barchers et al. [BAR02a], and Murphy et al. [MUR08] analyzed more advanced reconstruction methods, e.g. the complex exponential or the branch point potential method, to improve the performance in the strong fluctuation regime.

4.3.1 Branch Points in Laser Physics

For the understanding of phase dislocations it is instructive to study their appearance in laser physics. Vasnetsov [VAS99] and Soskin [SOS01] described in detail how to create phase dislocations with Gaussian, Laguerre-Gaussian, and Hermite-Gaussian beams. They distinguished between edge/circular dislocations and screw dislocations, which are described in the following sections.

4.3.1.1 Circular Edge Dislocation

Although in atmospheric laser communications only screw dislocations are observed, as a first example of an artificially created dislocation a circular dislocation is shown, as this type can be simply generated by the superposition of two Gaussian beams. A Gaussian beam travelling along the z-axis is described by

$$E(\rho,z) = |E_G| \frac{w_0}{w_G(z)} \exp\left(-\frac{\rho^2}{w_G^2(z)}\right) \exp\left(i\frac{k\rho^2}{2R(z)} - i\arctan\frac{z}{z_R} + ikz + i\phi_0\right), \quad (4.39)$$

where E_G gives the amplitude, w_0 the waist radius, $w_G(z)$ the beam radius (1/e for the amplitude and 1/e² for the intensity), $R(z)$ the radius of curvature, z_R the Rayleigh range, $k = \frac{2\pi}{\lambda}$ the wave-number and Φ_0 a constant phase offset. The beam radius is given by $w_G(z) = w_0\sqrt{1 + z^2/z_R^2}$, the beam radius of curvature by $R(z) = z\left(1 + z_R^2/z^2\right)$ and the Rayleigh range by $z_R = \frac{1}{2}kw_0^2$.

The superposition of two Gaussian beams E_1 and E_2 both with the waist at z=0 gives

$$E(\rho,z=0) = |E_1|\exp\left(-\frac{\rho^2}{w_{01}^2}\right)\exp(i\phi_{01}) + |E_2|\exp\left(-\frac{\rho^2}{w_{02}^2}\right)\exp(i\phi_{02}). \quad (4.40)$$

$|E_1|$, $|E_2|$ and w_{01}^2, w_{02}^2 denote the amplitudes and the waist radii of the first and second beam. If the phase of the beams is shifted by a value of π, i.e. $\phi_{02} - \phi_{01} = \pm\pi$, it is obvious that the amplitude of the combined beam drops to zero for

$$|E_1|\exp\left(-\frac{\rho^2}{w_{01}^2}\right) = |E_2|\exp\left(-\frac{\rho^2}{w_{02}^2}\right), \quad (4.41)$$

forming a zero-amplitude ring at the radius

$$\rho = \sqrt{\frac{w_{01}^2 w_{02}^2}{w_{02}^2 - w_{01}^2}\ln\left(\frac{|E_1|}{|E_2|}\right)}. \quad (4.42)$$

Figure 4.13 and Figure 4.14 show an example of two beams at z=0. The following parameters were assumed: $|E_1| = 1$, $|E_2| = 0.5$, w_{01}=10, w_{01}=100, and k=1. Taking Eq. (4.42) the zero-amplitude circle appears at ρ_0=8.36. Figure 4.13 depicts the two beam amplitudes (left). At the crossing point, i.e. equal amplitude, the zero-amplitude ring appears (right).
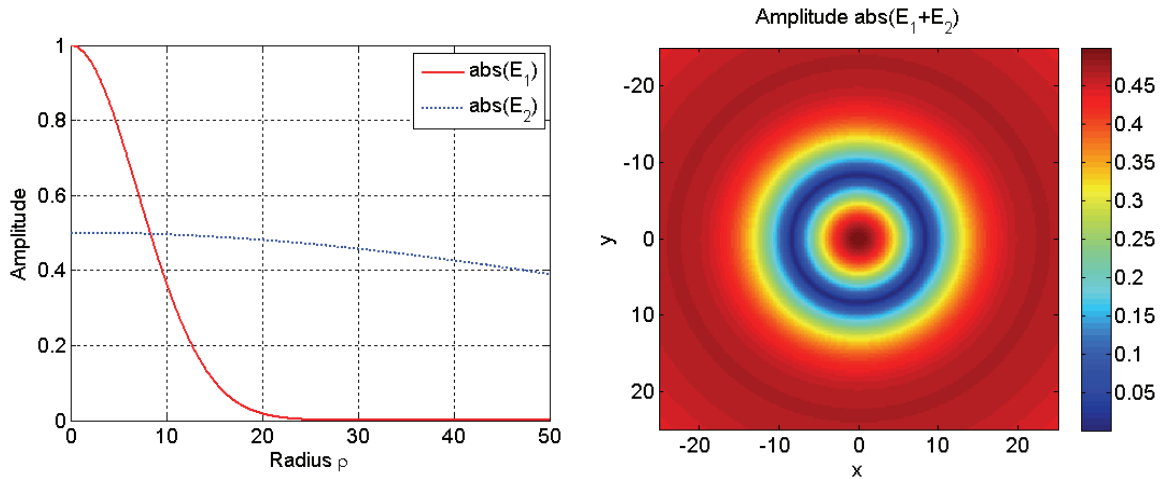
Figure 4.13: Appearance of a zero amplitude ring at locations, where the superposed beams have equal amplitude but opposite phase ($\phi_{02} - \phi_{01} = \pm\pi$). On the left the crossing point of the amplitudes is shown over the radius ρ. On the right side the resulting zero-amplitude ring can be observed.

Figure 4.14 shows the phase of the combined beams in a cut along the ρ-z plane. At the waist z=0 and ρ_0=8.36 the expected dislocation can be observed at the location of zero amplitude. From the dislocations the lines of equal phase radiate in a star-like fashion. An extra wavefront sheet is introduced to the right of the dislocation.
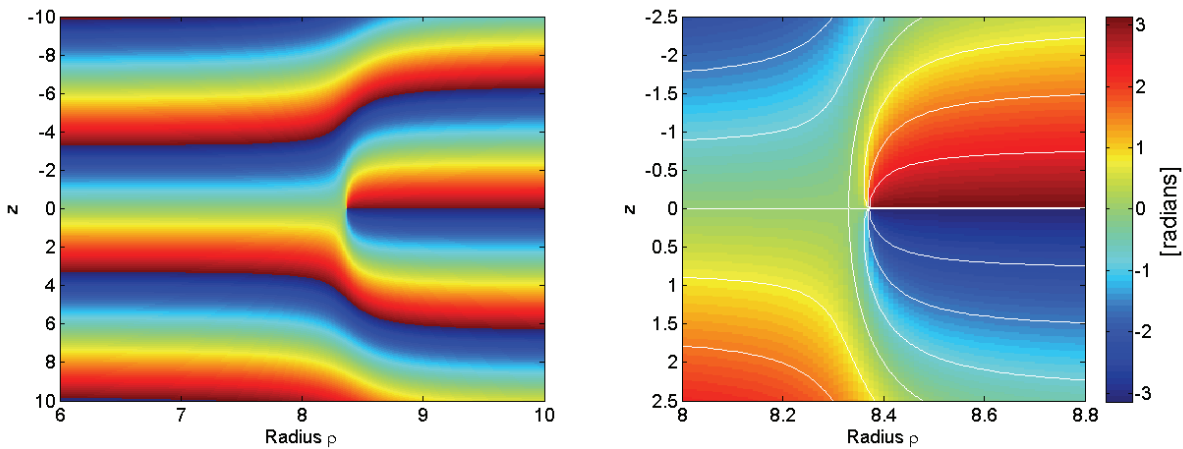
Figure 4.14: Phase shown in the ρ-z plane. In the center the circular dislocation can be seen, which extends into the viewing plane. A zoomed-in view is shown on the right, including lines of equal phase. To the right of the dislocation an extra wavefront sheet is introduced. To the left of the dislocation the typical saddle point is found.

4.3.1.2   Screw Dislocation

Soskin [SOS99] describes in his work the generation of screw dislocations using a superposition of a Laguerre-Gaussian (LG) and a Hermite-Gaussian (HG) beam, both propagating along the z-axis. Details on LG and HG beams can be found for example in Saleh and Teich [SAL91]. The more physical realization of laser beams to generate dislocations is studied in Smith et al. [SMI99]. The LG beam LG_1^0 is described by

$$E_{LG_1^0}\left(\rho,z\right)=E_{LG_1}\frac{w_0}{w(z)}\left(\frac{2\rho^2}{w(z)^2}-1\right)\exp\left(-\frac{\rho^2}{w(z)^2}\right)\exp\left(i\frac{k\rho^2}{2R(z)}+ikz-3i\Xi\right) \quad (4.43)$$

and the HG beam HG_{01} by

$$E_{HG_{01}}\left(\rho,\psi,z\right)=E_{HG}\frac{w_0\rho}{w(z)^2}\sin\psi\cdot\exp\left(-\frac{\rho^2}{w(z)^2}\right)\exp\left(i\frac{k\rho^2}{2R(z)}+ikz-2i\Xi\right), \quad (4.44)$$

where the Gouy phase is given by $\Xi(z)=\arctan\left(\frac{z}{z_R}\right)$. (ρ,ψ) are the polar coordinates in the transverse plane. The HG beam can be created by the combination of two LG beams $iE_{HG}=E_{LG_0^1+}-E_{LG_0^1-}$. The required LG beams $E_{LG_0^1\pm}$ are given by

$$E_{LG_0^1\pm}\left(\rho,\psi,z\right)=\tfrac{1}{2}\cdot E_{HG}\frac{w_0\rho}{w(z)^2}\exp\left(-\frac{\rho^2}{w(z)^2}\right)\exp\left(i\frac{k\rho^2}{2R(z)}+ikz\pm i\psi-2i\Xi\right). \quad (4.45)$$

The combination of the LG and HG beam $E_{LG_1^0}+iE_{HG_{01}}$ is illustrated in Figure 4.15 at $z=0$ (waist). The LG_1^0 beam has a zero-amplitude ring at radius $\rho=\frac{w_0}{\sqrt{2}}$, and the HG_{01} beam has a zero-amplitude line at $y=0$. In the combination two zero-amplitude locations appear at $\left(x=\pm\frac{w_0}{\sqrt{2}},y=0,z=0\right)$.
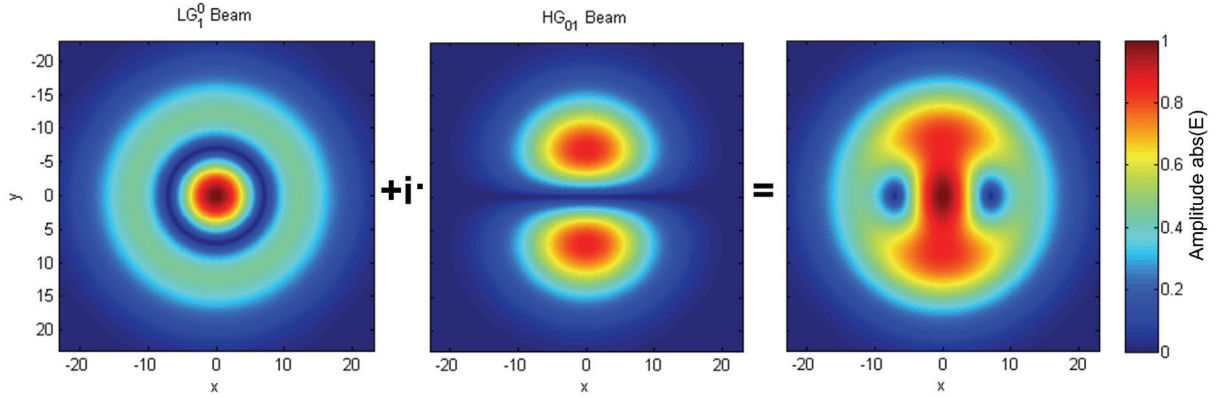
Figure 4.15: The combination of the Laguerre-Gaussian and Hermite-Gaussian beam $E_{LG_1^0}+iE_{HG_{01}}$ results in two locations with zero-amplitude and therefore two screw-dislocations with opposite charge.

Figure 4.16 shows the phase function in the waist plane with the two vortices (dipole) of the dislocations. The white lines denote equiphase lines with a spacing of $\lambda/30$, which terminate or originate at the dislocations. For a dipole dislocation the equiphase lines inter-connect the singularity points.
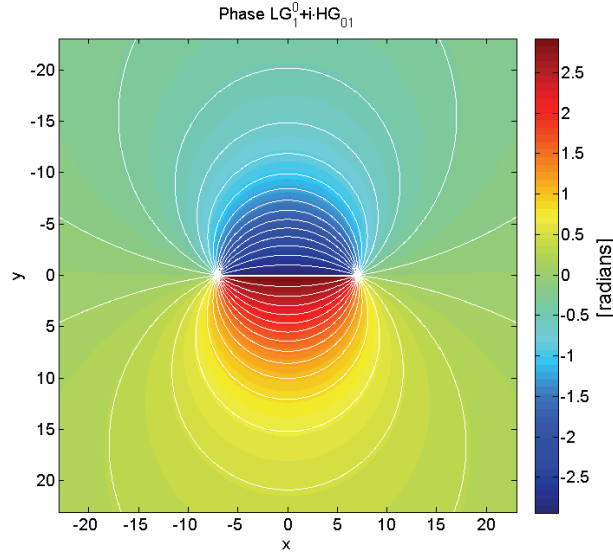
Figure 4.16: Phase image [radians] in the waist plane for the combined LG and HG beam. The two screw-dislocations with the typical screw like structure can be observed.

Taking Eq. (4.43) and (4.44), collecting all real factors in A, neglecting $i\dfrac{k\rho^2}{2R(z)}$ and the Gouy phase for small z, the combined beam close to the waist plane can be written as

$$E_{LG_1^0} + iE_{HG_{01}} = A \cdot \exp(ikz) \cdot \left[\left(\frac{2\rho^2}{w_0^2} - 1 \right) + i\frac{\rho}{w_0}\sin(\psi) \right]. \qquad (4.46)$$

The $\dfrac{\rho}{w_0}\sin(\psi)$ is a monotonically increasing function walking around the dislocations, i.e. forming the phase screw. The local (polar) coordinates (r,ϕ) and Cartesian coordinates (a,b) around the right dislocation expressed in polar coordinates (ρ,φ) of the origin are

$$a = r\cos\phi = \rho\cos\psi - \frac{w_0}{\sqrt{2}} \qquad (4.47)$$

$$b = r\sin\phi = \rho\sin\psi . \qquad (4.48)$$

Transforming (4.48) to

$$\rho = \frac{r\sin\phi}{\sin\psi} , \qquad (4.49)$$

inserting this into (4.47) and assuming that $\cos\psi \approx 1$ for $r \ll 1$ gives

$$\sin\phi = \frac{\sin\psi}{r}\left(r\cos\phi + \frac{w_0}{\sqrt{2}} \right). \qquad (4.50)$$

Taking the results from (4.49) and (4.50), the last term in (4.46) results to

$$\left[\left(\frac{2\rho^2}{w_0^2} - 1 \right) + i \frac{\rho}{w_0} \sin(\psi) \right] = \frac{4r}{\sqrt{2}w_0} \cos\phi + ir \sin\phi , \tag{4.51}$$

which describes an ellipse in the immediate vicinity of the dislocation and shows a monotonically increasing phase from $0 - 2\pi$ around the dislocation. The ellipse is very elongated along the *b*-axis for small *r*, and becomes more circular for increasing *r*. The phase component of (4.51) can be expressed by a function $\varphi(a,b,r)$. With this the surfaces of equal phase (wavefronts) are given by

$$\varphi(a,b,r) + kz = 2\pi n \quad (n = 0,1,2...)$$

which describes a helical shape of a screw dislocation similar to the one shown in Figure 4.17 for a circular shape of $\varphi(a,b,r)$. A similar derivation can be performed for the other dislocation.
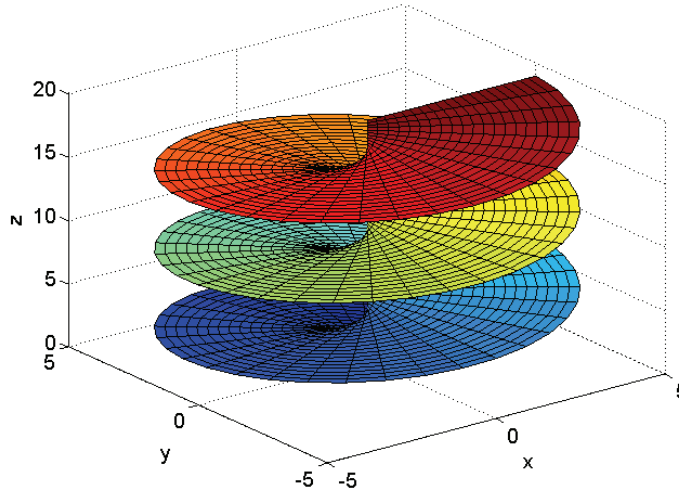
Figure 4.17: Helical shape of a screw dislocation.

4.3.1.3 Dislocations in a Convergent Beam

Circular/edge and screw dislocations also appear in a convergent beam after a focus lens. This is even the case, if the input beam before the lens does not contain any zero amplitude locations or phase dislocations.

Circular dislocations can be observed for an ideal focus spot with an Airy distribution. Around the zero amplitude rings in the focus a similar phase distribution as shown in Figure 4.14 appears. Figure 4.18 shows the phase and amplitude distribution of the Airy pattern in the vicinity of the focus in a *ρ-z* plane. The amplitude plot clearly shows the first two zero-amplitude rings on each side of the beam axis *ρ*=0. The dislocations are visible at the same locations in the phase plot, with alternating charge.
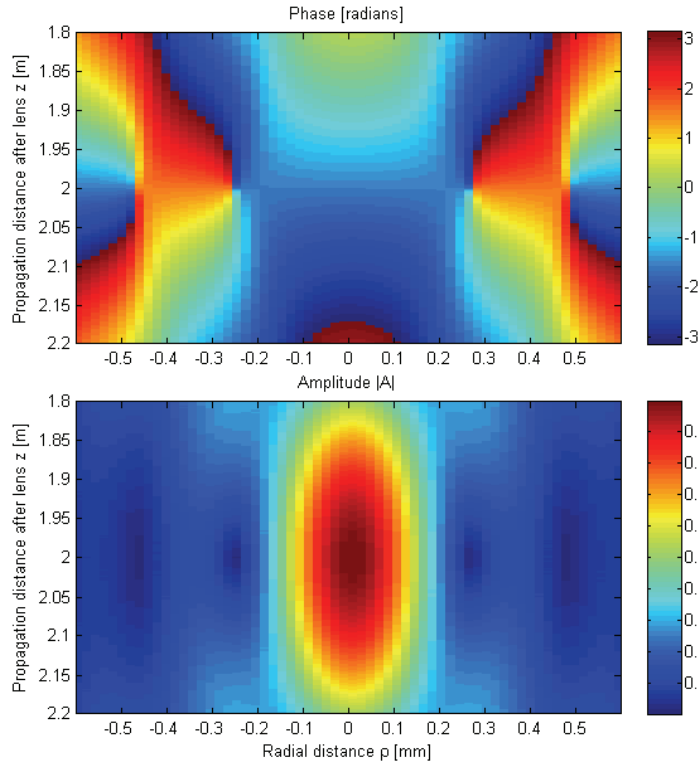
Figure 4.18: Sagittal plane cut for the phase and amplitude of the ideal Airy distribution around the focus.

As soon as there are slight wavefront distortions in the incoming beam, the circular dislocations disappear and screw dislocations appear. Towards the focus plane an increase of the number of dislocations can be observed. Figure 4.19 and Figure 4.20 show transversal cuts through the beam of an ideal plane wave and a distorted wave.
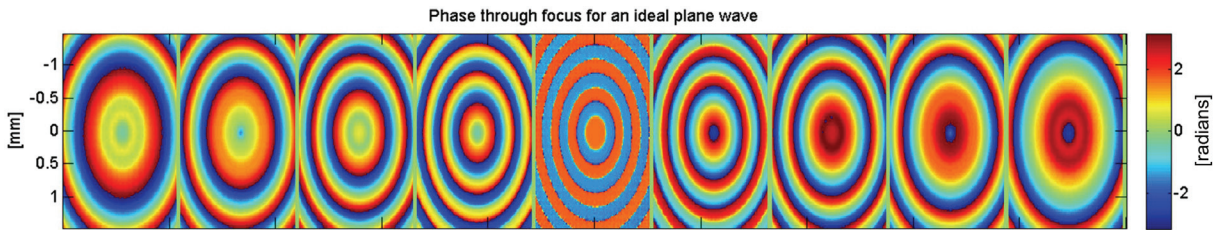
Figure 4.19: Phase distribution in the transverse plane with the central image in the focus plane. On the left planes before and on the right planes after the focus are shown. Circular dislocation can only be recognized in the focus plane at the edge of each band.
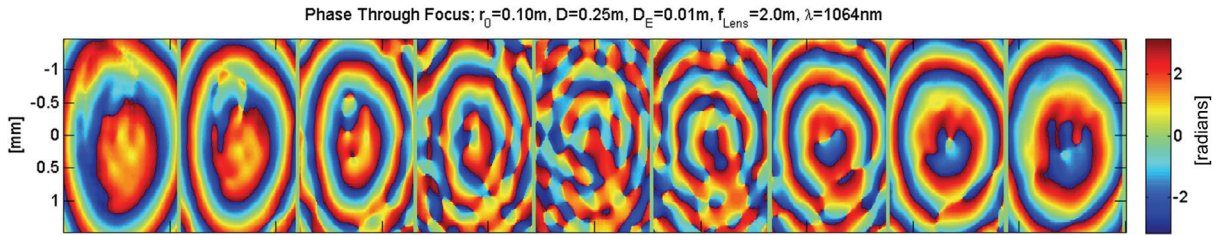
Figure 4.20: The same planes as in Figure 4.19 are shown, however the input wavefront is slightly distorted (r_0=0.1m). In the vicinity of the focus a large number of screw dislocations appear and the circular dislocations have disappeared.

4.3.2 Branch Points in Atmospheric Beam Propagation

Screw dislocations, or branch points as they are mostly called in the laser communication community, appear in the atmosphere in strong turbulence conditions with long paths through the atmosphere. Their appearance is caused by interference effects similar to the ones described in Section 4.3.1. They are called branch points due to the split up of one interference fringe into two. They appear at locations where the amplitude (intensity) drops to zero, i.e. a point where both the real and imaginary part of the complex field E become zero. In the consequence branch points are always located at the intersection of the lines real(E)=0 and imaginary(E)=0. The crossing divides the field around the branch point into the four quadrants of the 2π phase circle, already suggesting the phase screw.

Optical phase dislocations caused by atmospheric turbulence have been studied by several authors. Fried and Vaughn [FRI92] described the origin of branch points. Voitsekhovich [VOI98] studied the density of turbulence-induced phase dislocations. Wide attention to this topic was also given in the Soviet Union, e.g. the work of Baranova and Zeldovich can be mentioned [BAR81]. Several authors specifically worked on the impact of branch points to adaptive optics (AO) systems. Fried [FRI98] and Tyler [TYL00] analyzed the performance deterioration of AO system especially with phase reconstruction algorithms as used in Shack-Hartmann wavefront sensors. Details on this will be given in the analysis of Shack-Hartmann sensors in Chapter 4.4.1. Baranova et al. [BAR83] discussed restrictions of adaptive mirrors in the presence of branch points. Murphy et al. [MUR08] investigated the detection and correction of branch points using the branch point potential method introduced by [WIL99]. Fried [FRI01] discussed the complex exponential method to reconstruct a correct phase estimate with a Shack-Hartmann sensor in strong scintillation.

Simulations of the atmospheric turbulence with the DLR tool PILab [PER05], which is based on a phase-screen approach, confirmed the appearance of branch points below about 20 degrees elevation. Figure 4.21 shows a section of the amplitude and phase (wrapped phase $0\text{-}2\pi$) of a typical LEO satellite-to-ground link (SGL) at 10 degrees elevation. White lines indicate real(E)=0 and black lines imaginary(E)=0. At each crossing point a branch point is located. In the amplitude figure it can be seen that the branch points are always located in regions with relatively low amplitude.
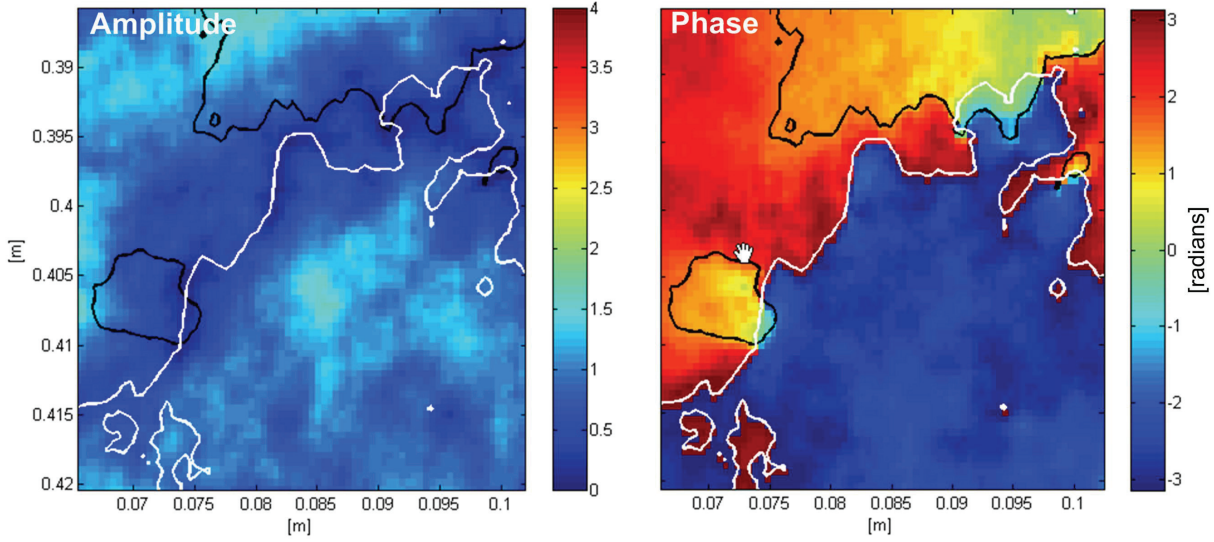
Figure 4.21: Simulated received field in a LEO SGL at 10 degrees elevation. On the left the amplitude of the field and on the right the phase. The black and white lines indicate lines of zeros of the real respectively imaginary part of the complex field E. At the crossings of a white and a black line screw dislocations can be observed in the phase image. At the same positions zero amplitude points are visible in the amplitude plot.

Branch points are always located at zero-amplitude points. Therefore a first approach to detect branch points would be to search for zero-amplitude points; however, in real sensor systems it is not possible to distinguish between zero amplitude and almost zero amplitude. This is due to sensor noise and also sensor resolution. Fried [FRI98] suggested a different approach by measuring the rotational component of the phase gradients, i.e. measuring the slope of the screw. For this Fried introduced the principal value gradient $\bar{g}^{pv}\left(x,y\right)=\begin{pmatrix} g_x^{pv}(x,y) \\ g_x^{pv}(x,y) \end{pmatrix}$.

The gradient in x-direction (and accordingly in y-direction) is given by

$$g_x^{pv}\left(x,y\right)=\lim_{\delta\to 0}\left[\frac{\mathrm{PV}\left\{\varphi\left(x+\delta,y\right)-\varphi\left(x,y\right)\right\}}{\delta}\right].\tag{4.52}$$

The principal value operator limits the gradient to the range $-\pi$ to $+\pi$ by adding or subtracting 2π. A branch point can now be detected with the closed-line integral

$$\oint_C \bar{t}\left(\xi\right)\cdot\bar{g}^{pv}\left(\bar{r}\left(\xi\right)\right)d\xi=\begin{cases} \pm 2\pi & \text{if a branch point is enclosed} \\ 0 & \text{if no branch point is enclosed} \end{cases},\tag{4.53}$$

where $\bar{t}\left(\xi\right)$ is the tangential vector to the closed shape. An equivalent formulation can be given for the discrete case. Figure 4.22 shows detected branch points in the simulated field already shown in Figure 4.21.
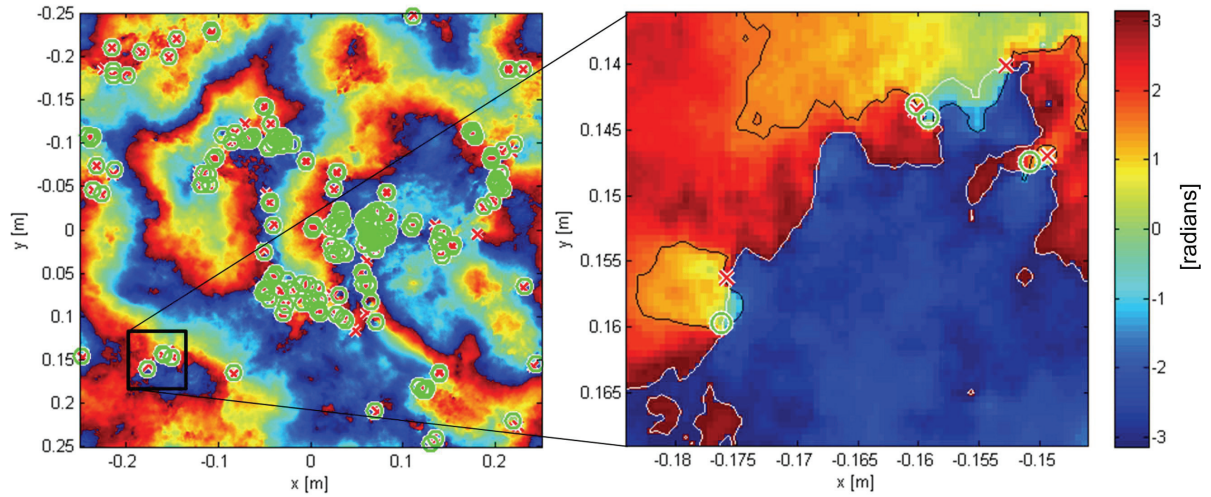
Figure 4.22: Detected branch points in SGL at 10 degrees elevation. Left: Full simulated field 50cm square with green rings and red crosses indicating opposite charge of the vortices. Right: Detailed view of the rectangular area with the same dimensions as in Figure 4.21.

The steep increase of the number of branch points in an SGL below an elevation angle of 30 degrees elevation could also be observed in the simulated fields as it is shown in Figure 4.23. The number of branch points was detected as a function of the elevation angle for the 50cm square field of the simulation with a resolution of 1024x1024 pixels at a wavelength of λ=1064nm.
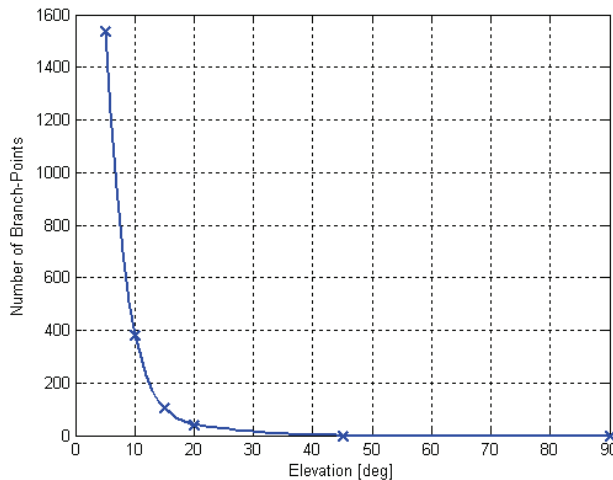
Figure 4.23: Number of phase singularities in the simulation for the satellite SGL. Simulation area 50x50cm, 1024x1024 pixels, λ=1064nm. Fields were simulated at 5, 10, 20, 45, and 90 degrees elevation.

As branch points always appear in regions of the incoming field with very little amplitude, they are difficult to measure with noise limited sensors. Figure 4.24 shows the intensity measurements with a Shack-Hartmann sensor setup for different elevation angles between 10 and 40 degrees elevation during the SGLs from OICETS. Larger regions of low intensity can be recognized at 10 and 20 degrees elevation. This makes it difficult to detect branch points for example by the measurement of the rotational component of the slopes as suggested in Eq. (4.53). Another difficult issue is the very large dynamics of the received intensity, i.e. the range between fades and surges, which can be observed at low elevation angles. At 40 degrees elevation less variation can be seen in the telescope pupil.
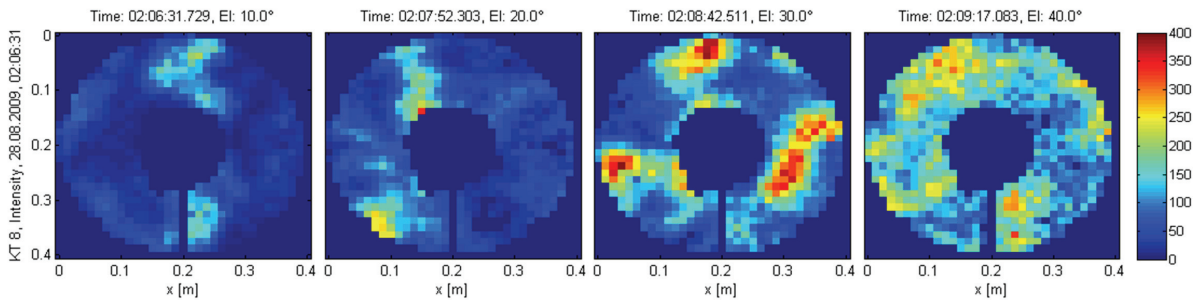
Figure 4.24: Typical intensity distribution (pixel values of the sensor) in the 40cm telescope aperture recorded with the Shack-Hartmann sensor during an SGL from OICETS at 10, 20, 30, and 40 degrees elevation. The slit at the bottom of the aperture is part of the telescope spider.

4.4 Wavefront Sensors

This section surveys the range of major wavefront sensors described in the literature and investigates their properties under the specific conditions of LEO satellite-to-ground links, which distinguish the use of the wavefront sensor from that in astronomical applications.

Atmospheric conditions are much more severe in SGL scenarios:

- Very strong phase distortions due to the long path through the atmosphere at low elevation angles.

- Very strong intensity fluctuations due to the long path through the atmosphere at low elevation angles.

- Phase singularities, which impair the performance of wavefront sensors and might prohibit the use of continuous deformable mirrors.

- Challenging temporal requirements due to the fast motion of the beam through the atmosphere.

- Preferably deployment of the ground stations at non-astronomical sites at low altitudes and therefore at worse atmospheric turbulence conditions.

In addition, the scenario exhibits some properties very specific to satellite-to-ground links:

- Comparatively high received power levels, as the communication system at several Gbps requires a sufficient link budget.

- The communication laser is always a point source.

- Usually the source will be highly monochromatic and coherent.

- Relatively small telescope apertures (<=1m) for near Earth scenarios will be used for communication, compared to several meters in Astronomy.

- The AO correction will be for a very small field-of-view, as a point source is observed. In the consequence no multi-conjugate system will be required even for strong turbulence.

Typical free-space optical (FSO) communication systems use various sensors for the pointing, acquisition, and tracking (PAT) systems for the link build-up and sustainment. Four-quadrant sensors have been widely used, but with the further development of standard CCD cameras also high-resolution imaging sensors have become available at low cost. Especially the latter might offer an interesting solution for a dual use sensor, providing data for the PAT system and at the same time for the reconstruction or at least partly reconstruction of the wavefront distortions.

FSO communication systems at least in the near Earth region, up to GEO satellites, work at high received power levels, as the communication system for high data-rates requires sufficient power levels for sufficient bit-error rates. As the distances are rather short, rather small telescope apertures (<1m) compared to astronomical systems are used. This simplifies the task of wavefront correction, however the scale sizes of phase distortions become rather small with Fried parameters r_0 on the order of a few centimeters. This has to be taken into consideration for the spatial resolution of the wavefront sensors as well as the correcting elements.

Table 4.2 shows a coarse classification of the wavefront sensor types. On a first level the techniques can be classified into iterative and deterministic techniques. Iterative techniques attempt in several steps to obtain an estimate of the wavefront distortions by minimizing a quality measure. Phase retrieval and phase diversity methods can be mentioned here, which are discussed in Section 4.4.4. Also wavefront "sensorless" systems belong to this category in a wider sense. They use a single measurement point, for example the power coupled into a fiber, to improve the correction of the wavefront in a gradient-optimization fashion. In this way they also gain an estimate of the wavefront distortions. As they measure the phase in a very indirect way, they are not discussed with the wavefront sensors, but in Section 4.5.

The deterministic techniques can be classified into geometric optics methods and interferometric methods. Classical wavefront sensors from astronomy like the Shack-Hartmann sensor (Section 4.4.1) and the curvature sensor (Section 4.4.2) belong to the group of geometric optics methods. Interferometric methods are better known from optical shop testing. Of the interferometric methods common-path interferometer, unequal path point-diffraction interferometer, and shearing interferometer are introduced in Section 4.4.3. A detailed discussion will be given in Chapter 5. Common-path and unequal-path interferometers are presented in a self-referencing design, i.e. the reference beam of the interferometer is generated from the received and distorted wave by a spatial filter in a Fourier plane, transmitting only the zero-order (spatial) spectral component of the beam.

Common-path and unequal path interferometer can be setup in a way that they directly measure the phase and no reconstruction of the wavefront is necessary from the sensor images, i.e. the phase is directly mapped to intensity on the sensor. Therefore they can be called direct wavefront sensors.

Table 4.2: Classification of wavefront sensor types

Iterative Techniques	Deterministic Techniques			
	Geometric Optics	Interferometric Methods		
		Shearing Interfero-meter	Common Path Interferometer	Unequal Path PDI Interferometer
Phase Retrieval Phase Diversity Wavefront Sensorless AO Systems	Shack-Hartmann Sensor Curvature Sensor Pyramid Sensor		Zernike Phase Contrast	Twyman-Green Mach-Zehnder

4.4.1 Shack-Hartmann Wavefront Sensor

One of the most common wavefront sensors in AO systems is the Shack-Hartmann wavefront sensor (SHS). This is due to the physical robustness of the sensor and its ease of implementation. The sensor consists of a lenslet array, placed in a plane conjugate to the telescope pupil, and a pixellated detector, placed in the back focal plane of the lenslet array.

Each lenslet of the array produces a focus spot on the detector (Figure 4.25). The displacement of each spot is proportional to the (averaged) gradient (tilt) of the wavefront across the lenslet. More details on the SHS can be found in many publications, e.g. [HAR98].
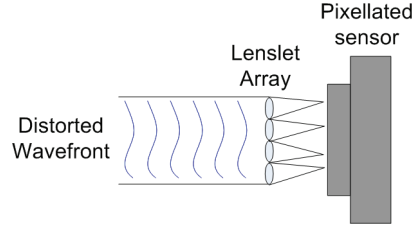
Figure 4.25: Principle of a SHS with a lenslet array and a pixellated sensor (camera).

The SHS is based on the simple principle that the difference between two neighboring phase points φ_1 and φ_2 is proportional to the gradient g between these points (e.g. two lenslets)

$$g_1 \propto \varphi_2 - \varphi_1 . \tag{4.54}$$

For the whole array of gradient measurements and corresponding wavefront phase points (both stacked in a vector) a relation can be established with the geometry matrix A_{geo} by

$$\vec{g}_i = A_{geo} \vec{\varphi}_i , \tag{4.55}$$

which can be inverted for example by a least-square method in order to obtain the phase from the Shack-Hartmann gradient measurements

$$\vec{\varphi}_i = \left(A_{geo}^T A_{geo} \right)^{-1} A_{geo}^T \vec{g}_i . \tag{4.56}$$

The subscript i with the phase points and gradients indicates a discrete formulation (sampled on a grid), in contrast to $\varphi(\bar{x})$ and $\vec{g}(\bar{x})$ in the continuous formulation of the next section. A direct inversion of A_{geo} is not possible, as A_{geo} is not a square matrix. Details on solving such systems of linear equations can be found e.g. in [PRE92]. Problems with so-called waffle modes (appearance of checker board patterns in the reconstruction), corresponding to singular mode spaces of the geometry matrix, are for example treated in [GAV03].

Eq. (4.56) holds in the weak fluctuation regime. In the next section the impact of strong fluctuations including phase singularities is further examined.

An example image recorded with a Shack-Hartmann sensor in a ground-ground scenario over about 500m can be seen in Figure 3.28 on the left. The displacements of the spots due to wavefront distortions are visible. Central obscuration and the telescope spider obstruct part of the incoming wave. On the right side the reconstructed wavefront is depicted.

4.4.1.1   Phase Singularities and the Shack-Hartmann Sensor

Tyler [TYL00] studied the effect of singularities on the phase reconstruction of a Shack-Hartmann sensor extending the work of Fried [FRI98] and others. He showed that any vector field $\vec{g}(\bar{x})$ can be expressed as the gradient of a scalar (potential) field $\varphi_{LS}(\bar{x})$ and the curl of a vector field $\vec{V}(\bar{x})$

$$\vec{g}(\bar{x}) = \nabla \varphi_{LS}(\bar{x}) + \nabla \times \vec{V}(\bar{x}) . \tag{4.57}$$

The Shack-Hartmann sensor measures the gradient $\vec{g}(\vec{x}) = \begin{pmatrix} g_x(\vec{x}) \\ g_y(\vec{x}) \end{pmatrix}$ and reconstructs the phase $\varphi(\vec{x})$ typically by a least-square reconstructor as in Eq. (4.56). A least-square reconstructor implicitly assumes that the gradient $\vec{g}(\vec{x})$ is derived only from the gradient $\nabla \varphi_{LS}(\vec{x})$ of the scalar potential, where LS denotes the least-square phase. This however neglects the second, curl component of the vector potential, which gives a contribution in the presence of phase singularities.

The benefit of Tyler's work is that he presented a closed form of the scalar potential and the vector field based on the gradients measured by the Shack-Hartmann sensor

$$\varphi_{LS}(\vec{x}) = \iint \frac{\kappa_x G_x(\vec{\kappa}) + \kappa_y G_y(\vec{\kappa})}{2\pi i |\vec{\kappa}|^2} \exp\left(2\pi i \vec{\kappa} \cdot \vec{x}\right) d\vec{\kappa} \qquad (4.58)$$

$$V(\vec{x}) = \iint \frac{\kappa_y G_x(\vec{\kappa}) - \kappa_x G_y(\vec{\kappa})}{2\pi i |\vec{\kappa}|^2} \exp\left(2\pi i \vec{\kappa} \cdot \vec{x}\right) d\vec{\kappa} \qquad (4.59)$$

$$\vec{V}(\vec{x}) = V_{Hz}(\vec{x}) \vec{e}_z \qquad (4.60)$$

G_x and G_y are the two-dimensional Fourier transforms of g_x and g_y. $\vec{e}_z$ denotes the unit vector along the z-axis, so that the vector field $\vec{V}(\vec{x})$ has only a z-component, which follows from the fact that $\vec{g}(\vec{x})$ has only non-zero components in x and y. The double integrals with $\exp\left(2\pi i \vec{\kappa} \cdot \vec{x}\right)$ denote a Fourier transform. Tyler confirmed the scalar potential as the result of the least-square reconstruction and V_{Hz} as the phase discrepancy component, which Fried called the hidden phase. V_{Hz} has only non-zero values, if singularities are present in the incoming field. It is the vector potential equal to the Hertz vector mentioned in [FRI98].

In this way the total gradient can be expressed as a sum of the least-square component g_{LS} and the slope discrepancy component g_{SD}, i.e.

$$g_{total}(\vec{x}) = g_{LS}(\vec{x}) + g_{SD}(\vec{x}). \qquad (4.61)$$

In a similar way the phase can be decomposed in a least-square and a slope-discrepancy component

$$\varphi_{total}(\vec{x}) = \varphi_{LS}(\vec{x}) + \varphi_{SD}(\vec{x}), \qquad (4.62)$$

where

$$\nabla_{\perp} \varphi_{SD}(\vec{x}) = \nabla \times \vec{V}(\vec{x}). \qquad (4.63)$$

Taking the above formulations it can be seen, why a standard least-square reconstructor is blind to phase singularities. In the discrete formulation of the conventional least-square reconstructor (4.56), the first operation is a multiplication with the transpose of the geometry matrix A^T. Transposing A it can be shown that the multiplication with A^T is equal to a discrete version of a divergence operator [TYL00, FRI98]. As the gradient g includes the curl of a vector field as shown in (4.57), and noting that the divergence of a curl operation is zero (Appendix A.5)

$$\nabla \cdot \left(\nabla \times \vec{g} \right) = 0, \tag{4.64}$$

it becomes clear that a least-square reconstructor inherently cannot not see the component of the slope-discrepancy phase, i.e. yielding wrong results in the presence of phase singularities.

Numerically simulated fields in an SGL scenario for 5 and 10 degrees elevation in Figure 4.26 and Figure 4.27 illustrate these findings. In a simulated field, where the incoming field is known, it is easy to calculate the slope discrepancy phase φ_{SD} from the difference of the original phase and the least-square phase φ_{LS} obtained from Eq. (4.58). Each figure gives from left to right the original phase, the least-square phase (LS-Phase) and the slope-discrepancy phase (SD-Phase). At 5 degrees, as expected, a strong SD phase component can be observed, and the LS phase, which a standard least-square reconstructor would yield, shows almost no resemblance to the original phase. At 10 degrees elevation already a strong resemblance of the LS phase to the original phase can be seen, although there is still a significant SD component. Phase singularities can be easily recognized in the SD phase images.

A detailed view of a slope discrepancy phase is shown in Figure 4.28. The black lines are lines of equal phase, which nicely show the interconnection between two branch points with opposite charge.

A Hertz potential $V_{Hz}\left(\bar{x} \right)$ for 10 degrees elevation calculated from Eq. (4.59) is shown in Figure 4.29. Extrema appear at the locations of the phase singularities. The charge can be seen in the sign of the potential.
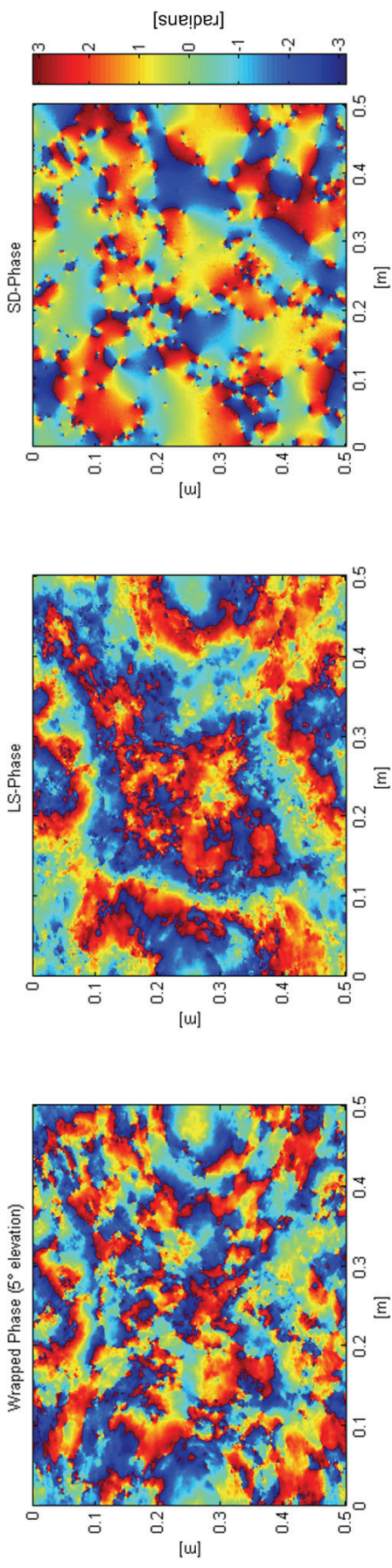
Figure 4.26: Simulated phase of an SGL at 5 degrees elevation (D=0.5m, λ=1064nm, 1024x1024 pixels).
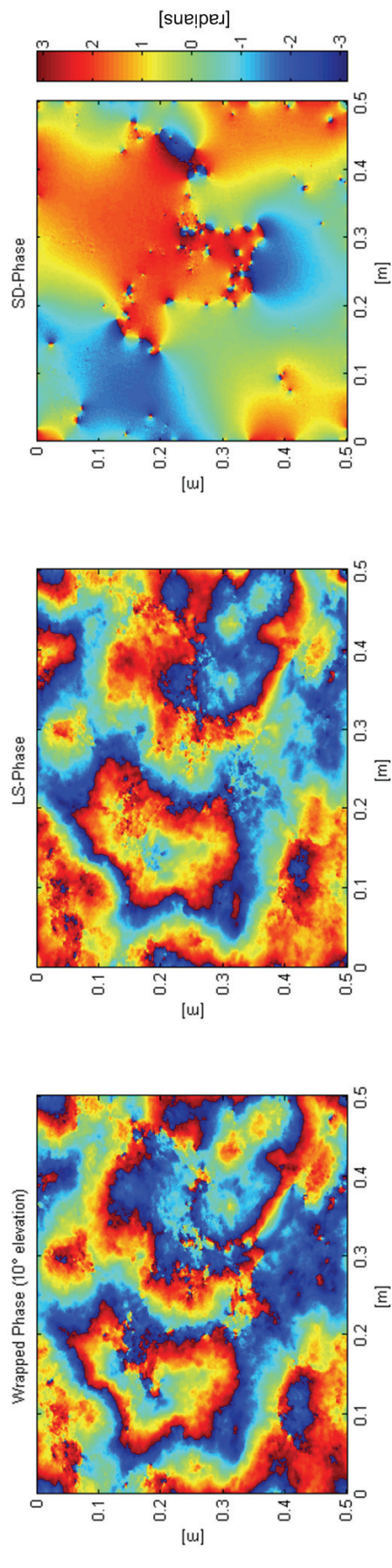
Figure 4.27: Simulated phase of an SGL at 10 degrees elevation (D=0.5m, λ=1064nm, 1024x1024 pixels).
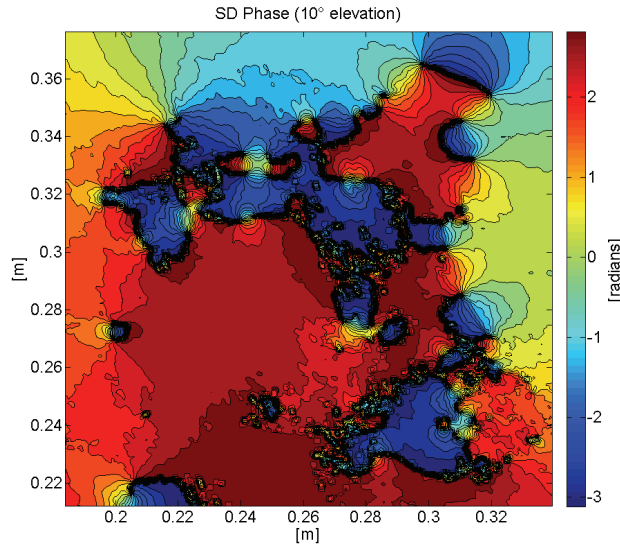
Figure 4.28: Slope discrepancy phase (wrapped) for an SGL at 10deg elevation.
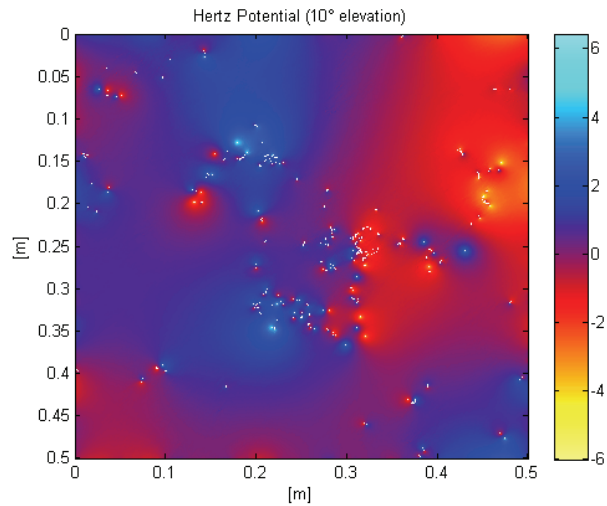
Figure 4.29: Hertz potential at 10deg elevation. Phase singularities are marked with a white spot. It can be seen that most singularities appear in pairs, which are close together.

4.4.1.2   Performance of the Shack-Hartmann

Barchers et al. [BAR02a] analyzed the performance of Shack-Hartmann sensors in strong turbulence conditions. As expected they observed a severe performance deterioration for a conventional least-square reconstructor for Rytov indices $\sigma_R^2 > 0.2$, which implies an increasing number of phase singularities. They also deployed a complex exponential reconstructor (CER) [FRI01], which showed a significant improvement also in the strong fluctuation regime, as the CER is able to detect the slope-discrepancy phase. The performance improvement however could only be achieved for a high-resolution sensor. The CER algorithm gave a performance improvement, if the ratio between the lenslet diameter d_L and the atmospheric coherence length r_0 was $d_L / r_0 < 1/4$.

This implies that the resolution requirement for the SHS becomes much stricter in the strong fluctuation regime compared to the standard rule of thumb introduced in Section 4.2.2, where a ratio of $d_L / r_0 \leq 1$ is suggested.

92

Especially with the above condition for the resolution under strong turbulence fluctuations and if each focus spot is resolved with several pixels, a SHS requires a large number of pixels. This limits the sampling rate of the SHS, as cameras are limited with the number of pixel samples they can send to the processing system. The closed-loop bandwidth of the full AO system becomes limited by the camera's frame rate and the speed of the processing algorithm. This poses a problem for the high bandwidth requirements in a LEO SGL scenario.

4.4.2 Curvature Sensor

4.4.2.1 Introduction

Curvature sensing as described by Roddier [ROD88] is based on the measurement of two intensity distributions in planes shortly before and after the geometric focus (focal length f) as shown in Figure 4.30 (Planes P_1 and P_2). The distance from the geometric focus to the two measurement planes is given by $\triangle z$.
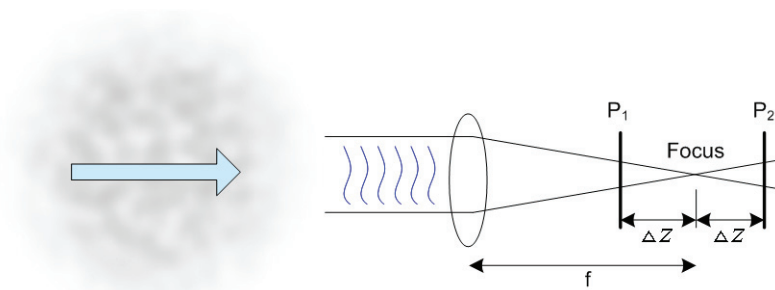
Figure 4.30: Principle of the curvature sensor.

The principle of the curvature sensor can be derived from the irradiance transport equation as it was shown by Roddier [ROD90]. Streibl [STR84], Teague [TEA83], and Ichikawa [ICH88] give more details on the irradiance transport equation. Van Dam and Lane [DAM02] investigated non-linear effects in curvature sensing, which had been neglected in previous works.

4.4.2.2 Derivation of the Irradiance Transport Equation

Based on the time-independent Helmholtz equation

$$\left(\nabla^2 + k^2\right)u(\bar{x}) = 0 ,$$

Teague [TEA83] derived a paraxial wave equation in a Fresnel approximation for a wave u_z travelling in z-direction

$$\left(\frac{\nabla_\perp^2}{2k} + i\frac{\partial}{\partial z} + k\right) \cdot u_z(\bar{r}) = 0 . \tag{4.65}$$

$\nabla_\perp$ denotes the Laplacian operator in transversal direction

$$\nabla_\perp = \begin{pmatrix} \partial/\partial x \\ \partial/\partial y \end{pmatrix} \text{ and } \nabla_\perp^2 = \frac{\partial^2}{\partial x^2} + \frac{\partial^2}{\partial y^2} \tag{4.66}$$

and k the wave number $k = 2\pi / \lambda$. Expressing the complex field u_z at the transversal coordinate $\vec{r}$ in terms of the intensity I and the phase φ [radians] gives

$$u_z(\vec{r}) = \left[I(\vec{r}) \right]^{1/2} \exp\left[i\varphi(\vec{r}) \right].$$
(4.67)

In order to understand the functionality of the curvature sensor, it is useful to bring Eq. (4.65) into a different form by writing

$$u_z^{\,*}(\vec{r}) \cdot \left(\frac{\nabla_\perp^2}{2k} + i\frac{\partial}{\partial z} + k \right) \cdot u_z(\vec{r}) = 0$$
(4.68)

$$u_z(\vec{r}) \cdot \left[\left(\frac{\nabla_\perp^2}{2k} + i\frac{\partial}{\partial z} + k \right) \cdot u_z(\vec{r}) \right]^* = 0$$
(4.69)

The star * denotes the complex conjugate. Eq. (4.67) is inserted in (4.68) and (4.69). The first term in the round brackets gives (omitting the dependence on $\vec{r}$)

$$\frac{1}{2k} \nabla_\perp^2 \left[I^{1/2} \exp\left(i\varphi \right) \right] =$$

$$= \frac{1}{2k} I^{1/2} \exp\left(i\varphi \right) \cdot \left[-\frac{1}{4} I^{-2} \left(\nabla_\perp I \right)^2 - \left(\nabla_\perp \varphi \right)^2 + iI^{-1} \nabla_\perp \varphi \cdot \nabla_\perp I + \frac{1}{2} I^{-1} \nabla_\perp^2 I + i\nabla_\perp^2 \varphi \right]$$

(4.70)

and the second term

$$i\frac{\partial}{\partial z} \left[I^{1/2} \exp\left(i\varphi \right) \right] = iI^{1/2} \exp\left(i\varphi \right) \left[\frac{1}{2} I^{-1} \frac{\partial}{\partial z} I + i\frac{\partial}{\partial z} \varphi \right]$$
(4.71)

Subtracting Eq. (4.69) from (4.68) results in a description of the intensity distribution along the z-axis (Irradiance Transport Equation ITE)

$$\boxed{k\frac{\partial}{\partial z} I = -I\nabla_\perp^2 \varphi - \nabla_\perp I \cdot \nabla_\perp \varphi}$$ (ITE).
(4.72)

This can be interpreted as the change of the intensity along the z-direction [ICH88]. The first term on the right side can be considered a lens term, describing the local convergence and divergence of the beam. The second term is a prism term, which describes the local redirection of the beam intensity according to the ray direction $\nabla_\perp \varphi$. Eq. (4.72) can be rewritten in a slightly different form, which can be considered to be a law of light energy conservation.

$$\boxed{k\frac{\partial}{\partial z} I = -\nabla_\perp \cdot \left(I\nabla_\perp \varphi \right)}.$$
(4.73)

The divergence of $I\nabla_\perp \varphi$, i.e. a flux through a plane transverse to the z-direction, equals the change of the intensity in the z-direction.

The addition of Eq. (4.68) and (4.69) shows the propagation effects on the wavefront phase (Wavefront Transport Equation WTE)

$$2kI^2 \frac{\partial}{\partial z}\varphi = \frac{1}{2}I\nabla_\perp^2 I - \frac{1}{4}\left(\nabla_\perp I\right)^2 - I^2\left(\nabla_\perp\varphi\right)^2 + 2k^2I^2 \quad \text{(WTE)}. \tag{4.74}$$

In the original derivation of the curvature sensor a uniform illumination I_{P0} in the pupil plane was assumed, i.e. I_{P0} within the aperture and zero outside. Hence $\nabla_\perp I$ becomes zero in the pupil area, except on the pupil rim

$$\nabla_\perp I = -I_{P0}\vec{n}\delta_c, \tag{4.75}$$

where δ_c is a linear Dirac distribution along the rim and $\vec{n}$ a unit vector perpendicular to the rim pointing outward. Consequently Eq. (4.72) becomes

$$k\frac{\partial}{\partial z}I = I_{P0}\frac{\partial}{\partial n}\varphi\cdot\delta_c - I_{P0}\nabla_\perp^2\varphi, \tag{4.76}$$

where $\frac{\partial}{\partial n}\varphi = \nabla\varphi\cdot\vec{n}$, i.e. the derivative of φ in a direction perpendicular to the aperture rim. Therefore the intensity distributions in the planes P_1 and P_2 can be written as

$$I_1 = I_{P0} + \frac{\partial}{\partial z}I\cdot{\scriptstyle\triangle} z \text{ and } I_2 = I_{P0} - \frac{\partial}{\partial z}I\cdot{\scriptstyle\triangle} z \tag{4.77}$$

and from this the sensor signal S is derived with the scaling factor c by

$$S = c\frac{I_1 - I_2}{I_1 + I_2} = c\frac{1}{I_{P0}}\frac{\partial}{\partial z}I\cdot{\scriptstyle\triangle} z = \frac{c}{k}\left(\frac{\partial}{\partial n}\varphi\delta_c - \nabla_\perp^2\varphi\right)\cdot{\scriptstyle\triangle} z. \tag{4.78}$$

For the optical setup the effective propagation distance $f\left(f - {\scriptstyle\triangle} z\right)/{\scriptstyle\triangle} z$ is composed of the distance to the first plane $\left(f - {\scriptstyle\triangle} z\right)$ and the scaling of the planes P_1 and P_2 by $f/{\scriptstyle\triangle} z$ compared to the telescope aperture. The larger the distance $\left(f - {\scriptstyle\triangle} z\right)$, the stronger the angles of the gradient operations influence the sensor signal. And the smaller the images in the planes P_1 and P_2 are, the stronger the signal will be.

$$S = \frac{I_2\left(-\bar{x}\right) - I_1\left(\bar{x}\right)}{I_2\left(-\bar{x}\right) + I_1\left(\bar{x}\right)} = \frac{f\left(f - {\scriptstyle\triangle} z\right)}{k\cdot{\scriptstyle\triangle} z}\left(\frac{\partial}{\partial n}\varphi\left(\tfrac{f}{{\scriptstyle\triangle} z}\bar{x}\right)\delta_c - \nabla_\perp^2\varphi\left(\tfrac{f}{{\scriptstyle\triangle} z}\bar{x}\right)\right). \tag{4.79}$$

A minus sign is introduced with the operand of I_2, as the image is flipped. With the wavefront a scaling factor $f/{\scriptstyle\triangle} z$ is added to account for the convergent beam. An additional lens is inserted at the focus with a focal length of $f/2$ to ensure that the two images are of the same scale.

4.4.2.3 Performance of the Curvature Sensor

The original derivation of the curvature sensor assumed a constant intensity in the telescope aperture and relatively weak phase distortions, so that the wavefront change in z-direction $\frac{\partial}{\partial z}\varphi$ described in Eq. (4.74) could be neglected and the formulas became easy to handle.

Taking intensity fluctuations over the aperture into account, the term $\nabla_\perp I \cdot \nabla_\perp \varphi$ in Eq. (4.72) cannot be neglected as in the original derivation. With this additional term the sensor output signal becomes

$$S = \frac{f(f-\triangle z)}{k \cdot \triangle z}\left(\frac{\partial}{\partial n}\varphi\left(\tfrac{f}{\triangle z}\vec{x}\right)\delta_c - \nabla_\perp^2\varphi\left(\tfrac{f}{\triangle z}\vec{x}\right) - \frac{\nabla I \cdot \nabla \varphi}{I} \right), \tag{4.80}$$

where the new term can be seen as an error signal influencing the curvature sensing. Voitsekhovich [VOI03] gave an expression for this error term by a ratio of the mixed phase/intensity term $\frac{1}{I}\nabla_\perp I \cdot \nabla_\perp \varphi$ and the curvature term $\nabla_\perp^2 \varphi$

$$\sigma_S^2 = \frac{\left\langle \left(\frac{1}{I}\nabla_\perp I \cdot \nabla_\perp \varphi\right)^2 \right\rangle}{\left\langle \left(\nabla_\perp^2 \varphi\right)^2 \right\rangle}. \tag{4.81}$$

From atmospheric theory in the weak fluctuations regime he calculated values for σ_S^2 based on C_n^2 profiles typically found in astronomical scenarios. For these scenarios he predicted scintillation errors up to 20%. For SGLs much stronger effects can be expected due to strong scintillation and phase distortions.

Van Dam [DAM02] analyzed the curvature sensor taking the wavefront transport equation into account, describing not only the intensity changes with the propagation of the beam, but also the wavefront changes itself. This leads to a nonlinear relation between the intensity measurement and the curvature estimate; in addition, phase distortions cause diffraction and thus blurring effects, which are not predicted by the geometric optics approach.

An interesting observation is based on the fact that the curvature is the divergence of the gradient. Following the observations of Section 4.4.1.1 that the gradient field is the sum of the least-square and the slope discrepancy component

$$\vec{g}(\vec{x}) = \nabla\varphi_{LS}(\vec{x}) + \nabla \times \vec{V}(\vec{x}) \tag{4.82}$$

and that curvature is the divergence of the gradient $d = \nabla \cdot \vec{g}$, it becomes clear, using the vector identity $\nabla \cdot (\nabla \times \vec{V}) = 0$, that

$$d = \nabla \cdot (\nabla\varphi_{LS} + \nabla \times \vec{V}) = \nabla \cdot (\nabla\varphi_{LS}). \tag{4.83}$$

This shows that the curvature sensor cannot detect the phase component caused by singularities, which results in a wrong phase estimation similar to what has been shown for the Shack-Hartmann sensor.

4.4.2.4 Simulation Results

The behavior of the curvature sensor is simulated to evaluate the sensor's performance. The simulation is based on the concepts introduced in Appendix A.2. The simulated propagation consists of three parts as shown in Figure 4.31:

- Free-space propagation from the pupil plane to the lens $L = f_{Lens}$;

- Multiplication with the lens phase factor $t(x, y) \approx h_0 \exp\left[ik_0 \dfrac{x^2 + y^2}{2f}\right]$;

- Free-space propagation from the lens to the image plane $L = f_{Lens} + \vartriangle z$.

f_{Lens} gives the focus length of the lens. The two free-space propagation sections are calculated in the Fourier domain, while the lens factor is multiplied in the spatial domain.
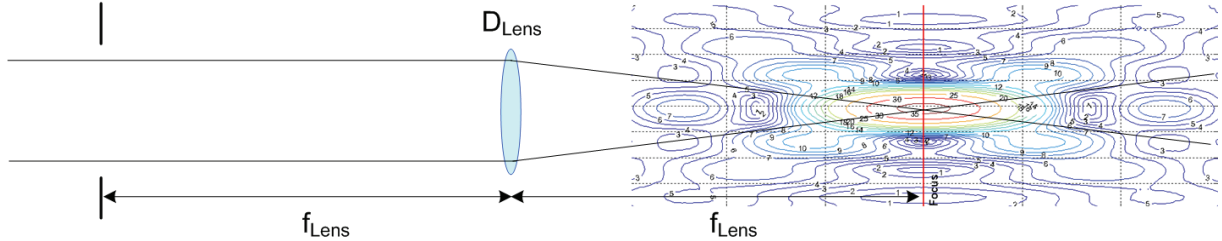
Figure 4.31: Simulation concept of the amplitude distributions near the focus.

Two examples of simulated propagations are shown in Figure 4.32 and Figure 4.33. Figure 4.32 shows the intensity distribution in a cut in the meridional plane in the vicinity of the focus for an unaberrated, plane wave. In the upper section example intensity distributions in transversal planes are shown. The focus diameter to the first zero-crossing is calculated from the pupil diameter D_{Lens}, the focal length f_{Lens}, and the wavelength λ

$$D_{Airy} = 2.44 \cdot \lambda \cdot \frac{f}{D_{Lens}} . \tag{4.84}$$

Figure 4.33 shows an example for an aberrated wave but with uniform amplitude. The input phase was generated by a phase simulation with $r_0 = 5cm$ and a lens diameter $D_{Lens} = 20cm$. In the top-right corner the phase distortions [in radians] in the pupil is depicted also showing the circular aperture. The principle of the curvature sensor can be intuitively understood observing that the local curvatures in areas with negative phase values (blue) (also rather having negative curvature) move intensity areas before the nominal focus plane, while areas with positive phase values (red) (rather having positive curvature) move intensity areas after the nominal focus plane. The structures can be recognized in the transversal image planes.

The graphs use normalized coordinates u and v as they are given by Born and Wolf [BOR99]

$$
\begin{aligned}
u &= \frac{2\pi}{\lambda}\left(\frac{D_{Lens}}{2f}\right)^2 z \\
v &= \frac{2\pi}{\lambda}\left(\frac{D_{Lens}}{2f}\right) r
\end{aligned}
, \tag{4.85}
$$

corresponding to the propagation axis z and the radial distance r. $u = 0$ shows the nominal focus plane.
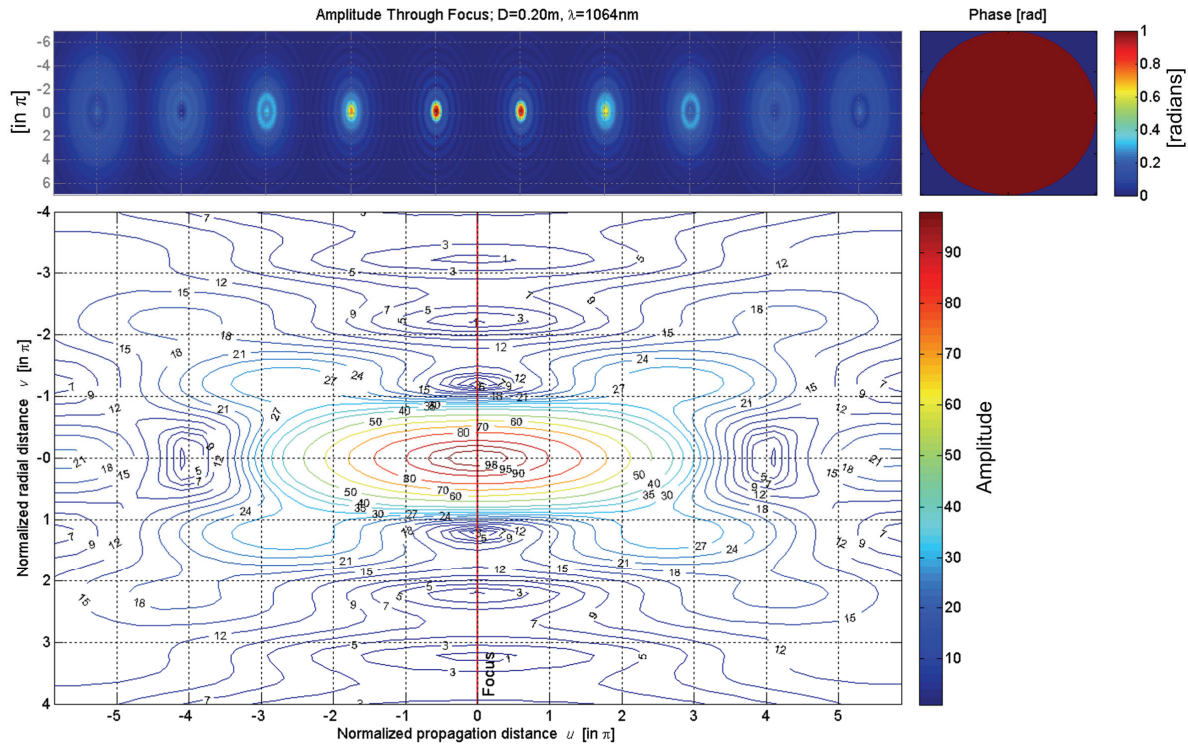
Figure 4.32: The contour plot shows the amplitude distribution in a meridional plane near the focus. This distribution is given for a plane wave and a circular aperture. The upper plot shows several intensity distributions in transversal planes through the focus. The distribution in the focus plane is shown in the center and the normalized coordinate u gives the distance to the focus plane (4.85).
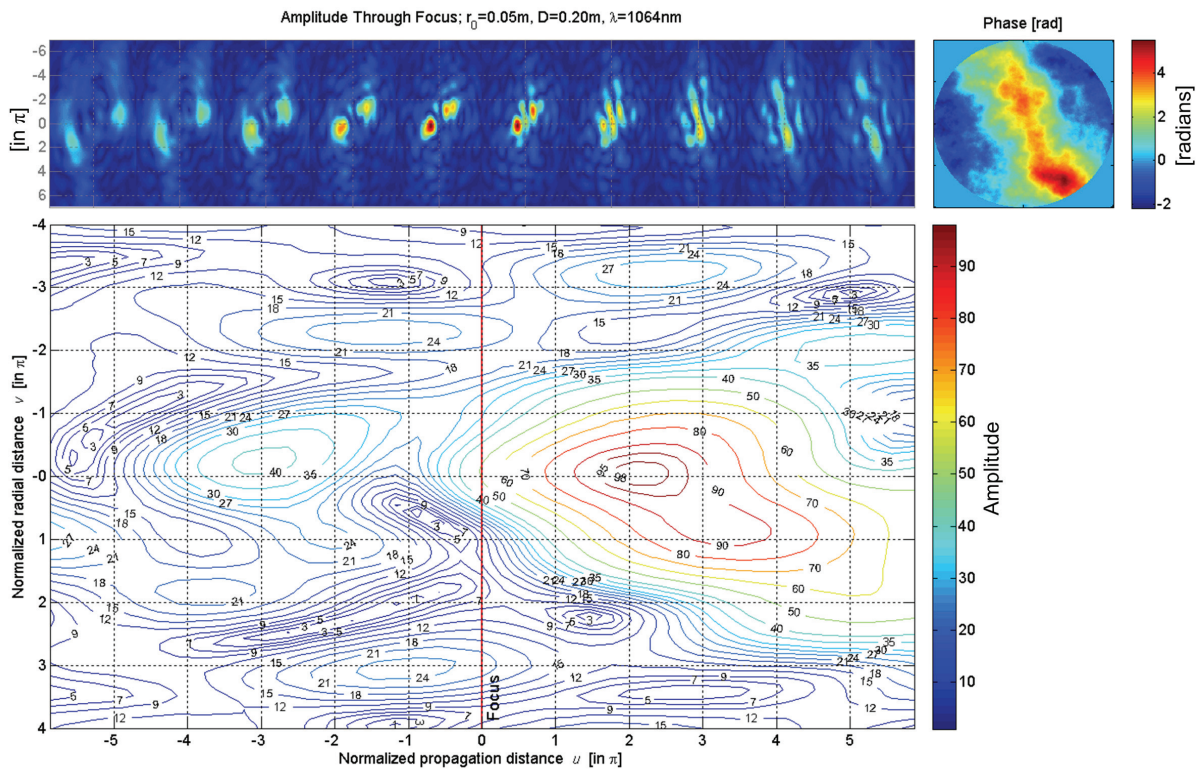
Figure 4.33: Similar graph as in Figure 4.32. This distribution is given for a distorted wavefront at the telescope pupil with a constant intensity distribution. An atmospheric coherence length of r_0=5cm was taken.

4.4.3 Interferometric Methods

Interferometric wavefront sensors are based on a very similar principle as coherent communication receivers. The received signal beam U_S, which is the object beam with a distorted wavefront in adaptive optics, is superposed with a local beam U_L, which can be approximated by a plane wave. The intensity of the superposed signal is then given by [RYU94]

$$
\begin{aligned}
I(x,y) &= |U_L + U_S|^2 \\
&= I_L + I_S(x,y) + 2\sqrt{I_L I_S(x,y)} \cos\left[(\omega_S - \omega_L)t + \varphi_S(x,y) + \varphi_L\right]
\end{aligned}
\tag{4.86}
$$

where the electric fields of the signal and local wave with the optical frequencies ω_S, ω_L and the phase shifts φ_S, φ_L are given by

$$
U_S(x,y) = |U_S(x,y)| \cdot e^{i\omega_S t + i\varphi_S(x,y)}
\tag{4.87}
$$

$$
U_L = |U_L| \cdot e^{i\omega_L t - i\varphi_L}
\tag{4.88}
$$

The term $(\omega_S - \omega_L)t$ is called the beat signal at an intermediate frequency of the signal and local oscillator wave. In homodyne communication systems the frequency of the local beam is matched to the signal frequency by a phase-locked loop. In the consequence the beat term becomes zero and the signal is not time-varying anymore. If ω_S and ω_L are not equal a heterodyne demodulation scheme has to be applied.

In a first approximation the local beam is constant in phase and amplitude over the receiver plane. The error in the phase-match between local and signal beam goes into the superposition efficiency and determines the sensitivity of the receiver. There are two principle ways to apply this superposition method to interferometric wavefront measurements:

The distorted wavefront is superposed with a local, undistorted beam. This would be the same method applied for coherent communication receivers. Advantage is a high sensitivity of the system, which would allow the operation at low received powers; however, the phase of the local laser would have to be phase-locked to the signal phase, which implicates a significant technical effort complicated by a varying signal phase and intensity over the aperture. Especially intensity scintillation caused by the atmosphere can also hinder the correct operation of the phase-locked loop, which has been an issue for coherent communication SGLs from TerraSAR-X.
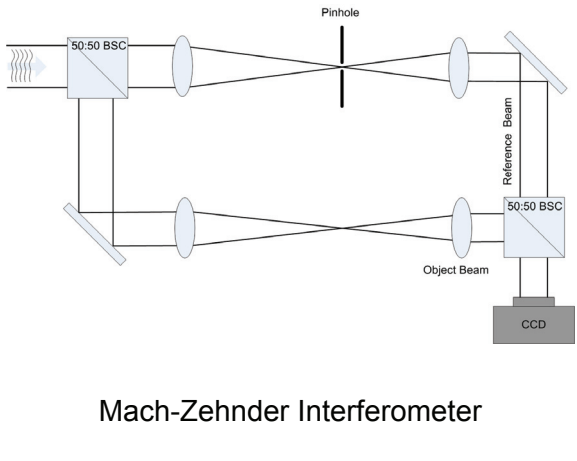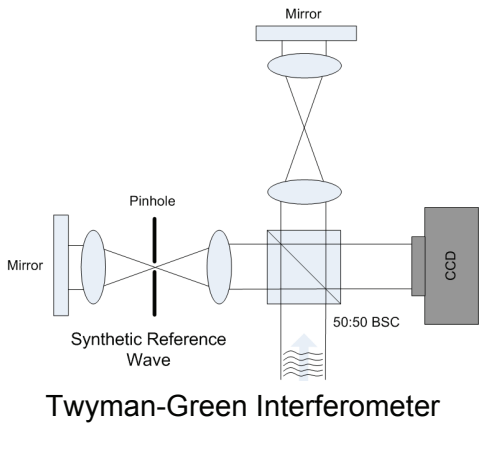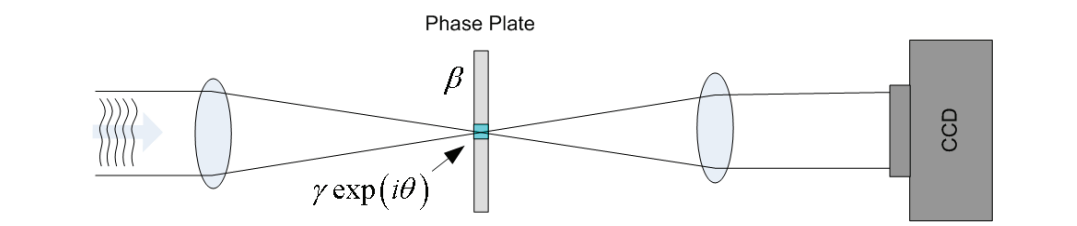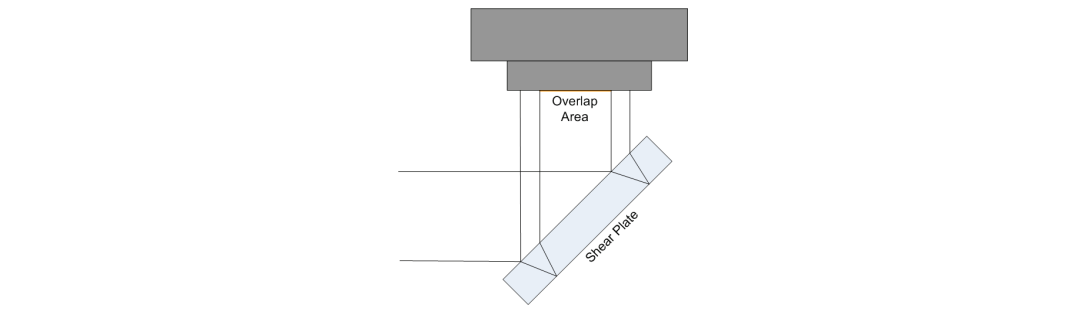
Self-referencing interferometers present the second approach for interferometric wavefront sensors. Here the beam for the superposition is taking from the received signal itself. In the consequence phase stabilization as phase-locked loops are not required. Table 4.3 shows several types of self-referencing interferometers. Point-diffraction interferometers split the beam into the object wave (the distorted wave) and the reference wave. In the reference arm a lens focuses the beam, and the still distorted wave is thus transformed into the Fourier (spatial frequency) domain. Here a spatial filter (e.g. a pin-hole) blocks higher-order frequencies of the signal and only allows the zero-order (low order) signal to pass. In this way an approximately plane wave reference beam is generated. An important question is how much light passes through the spatial filter, i.e. how strong is the reference wave. This has an impact on the visibility of the fringe pattern of the interferometer. At least a tip-tilt correction of the beam has to be applied to get enough signal strength of the reference beam. Typical setups of point diffraction interferometer are Mach-Zehnder or Twyman-Green interferometer.

Common-path interferometers have a similar principle, but combine the separate arms of e.g. a Mach-Zehnder interferometer in one common path. The spatial filter is replaced by a

more general phase plate. Both interferometer types can be described in a similar way and are therefore explained together in Section 4.4.3.1.

Shearing interferometer also use the signal beam to measure the wavefront, however they do not use a spatial filter to produce a plane reference wave. Their principle is based on laterally shifting one of the two beams by some distance and in this way generating the derivatives of the wavefront.

Table 4.3: Self-referencing interferometers.

| Point-Diffraction Interferometer | Mach-Zehnder Interferometer | Twyman-Green Interferometer |

| Common-Path Interferometer | |

| Shearing Interferometer | |

4.4.3.1 Common-Path and Point-Diffraction Interferometers

Common-path interferometers are based on Zernike's phase contrast method, for which he was awarded the Nobel Prize in 1953. The beauty of this method is that a phase disturbance is directly converted to an intensity modulation. Therefore the method can be called a direct wavefront sensor, as the information on the sensor chip does not have to be further processed to obtain a phase estimate. The principle of phase contrast has been described in many publications since then [GOO96, BOR99]. More detailed analyses were performed by Glückstad [GLU01] and Vorontsov [VOR01], which will be further discussed in Chapter 5.

The principle design of a wavefront sensor based on the phase contrast method is shown in Table 4.3. A phase plate is positioned in the lenses' common focus. The phase plate typically has a small circular area or dot in the center, which modifies the focused wave for low-order spatial frequencies, similar to the pin-hole in a point-diffraction interferometer. A general phase plate with a circular central area can be modeled by

$$
\begin{aligned}
T(\vec{q}) &= \gamma e^{i\theta} \quad && for \; |\vec{q}| < q_0 \\
T(\vec{q}) &= \beta \quad && otherwise
\end{aligned}
, \tag{4.89}
$$

where $\vec{q}$ gives the position in the focal plane, q_0 the size of the filter dot, $\gamma \leq 1$ is the value of absorption of the dot, and θ is the phase shift of the dot. Typically the dot size is on the order of the diffraction limited focal spot. The transmission outside the dot is β. The classical Zernike filter has $\gamma = \beta = 1$ and a phase shift of $\pi/2$. The Smartt point diffraction interferometer [SMA75] has an opaque dot, i.e. $\gamma = 0$ and $\beta = 1$.

The basic idea of this sensor can be expressed in the following way. The incoming field, assuming a weak phase distortion $\varphi(x, y)$ and a constant intensity over the aperture, is expressed (not showing the time dependence) by

$$
f(\vec{x}) = e^{i\varphi(\vec{x})} \approx 1 + i\varphi(\vec{x}), \tag{4.90}
$$

neglecting all higher terms of the Taylor expansion $e^x = 1 + x + \dfrac{x^2}{2} + \dots$. The transformation of Eq. (4.90) into the Fourier plane gives

$$
F(\vec{k}) \approx \delta(\vec{k}) + i\Phi(\vec{k}), \tag{4.91}
$$

where $\delta(\vec{k})$ denotes a Dirac impulse and thus approximating the Fourier transform of an undistorted, plane wave. Φ is the Fourier transform of φ. The phase plate with the phase dot acts on the Dirac impulse introducing a phase shift of a quarter wavelength or a factor $i = e^{i\pi/2}$. The field after the phase plate can then be expressed as

$$
E(\vec{k}) \approx i\delta(\vec{k}) + i\Phi(\vec{k}). \tag{4.92}
$$

Transforming this back by an inverse Fourier transform gives

$$
e(\vec{x}) = i(1 + \varphi(\vec{x})), \tag{4.93}
$$

and the intensity on the sensor

$$
I_e(\vec{x}) = |e(\vec{x})|^2 = \left[1 + \varphi(\vec{x})\right]^2 \approx 1 + 2\varphi(\vec{x}) + \dots. \tag{4.94}
$$

Assuming small wavefront distortions, this yields in a first approximation a linear relationship between the intensity and the phase, i.e. a direct wavefront sensor, which does not require any reconstruction to obtain the phase. This relationship is not valid anymore for larger wavefront distortions or amplitude fluctuations, which directly influence the result.

The huge advantage of a direct sensor is the fast processing speed. All processing is done optically and no digital reconstruction, which would introduce delays, is necessary; in addition, each sensor pixel will give one phase-point measurement. This allows very high

resolution without high speed. In Chapter 5 details will be given on how to extend the direct sensor capability to the full 2π phase circle even in strong intensity fluctuations using e.g. phase-shifting techniques.

4.4.3.2 Shearing Interferometer

In a lateral shearing interferometer two versions of the same wavefront with a lateral shift (shear) $\triangle x$ or $\triangle y$ in one direction are superposed. The two waves can be produced by a parallel-sided shear plate, where the incoming wave is reflected twice, once on the front and once on the back side (Table 4.3). The two reflections are laterally separated due to the finite thickness of the plate. Details on lateral shearing interferometers can be found for example in Malacara [MAL07].

The resulting wavefront difference between the two waves (here shifted in x-direction) is given by

$$\triangle\varphi\left(x,y\right)=\varphi(x-\frac{\triangle x}{2},y)-\varphi\left(x+\frac{\triangle x}{2},y\right). \tag{4.95}$$

Interference fringes appear at

$$\triangle\varphi\left(x,y\right)=n\lambda, \tag{4.96}$$

where the integer n is the order of the interference fringe and λ the wavelength. The fringes of a shearing interferometer are the loci of constant average wavefront slope over the shear distance. This is different from other types of interferometers like Twyman-Green, where the fringes are loci of constant wavefront phase. There is a resemblance between the Shack-Hartmann sensor and the shearing interferometer, which can be observed in Eq. (4.95) and (4.54). The wavefront difference $\triangle\varphi\left(x,y\right)$ is approximated for small lateral shifts by the partial derivate

$$\triangle\varphi\left(x,y\right)\approx\frac{\partial}{\partial x}\varphi\left(x,y\right)\cdot\triangle x \text{ or } \triangle\varphi\left(x,y\right)\approx\frac{\partial}{\partial y}\varphi\left(x,y\right)\cdot\triangle y. \tag{4.97}$$

The output of lateral shearing interferometers can be simply calculated with Eq. (4.97) and the power series expansion of primary aberration. For example spherical aberration is given by

$$\varphi\left(x,y\right)=k_{Defocus}\left(x^2+y^2\right), \tag{4.98}$$

and therefore the phase difference in a lateral shift in x becomes

$$\triangle\varphi\left(x,y\right)=k_{Defocus}\cdot2x\cdot\triangle x. \tag{4.99}$$

Similar function can be found for other primary aberrations. The main aberrations are summarized in Table 4.4. The constants k gives the strength of the specific aberration. The interferograms of these aberrations are shown in Figure 4.34 before, in, and after the focus, i.e. with an additional negative, zero, and positive defocus term. In the first line, showing only the defocus component, an additional tilt in y-direction between the two waves $\triangle\varphi\left(x,y\right)=k_{y-Tilt}\cdot y$ has been introduced, which results in the characteristic rotation of the fringes during the pass through the focus. This tilt is usually introduced with a slight angle

between the front and backside of the testing device, and enables preciser beam collimation as in a non-tilted setup.

Table 4.4: Main primary aberrations and their phase differences in a shearing interferometer.

Primary Aberration	Phase	Phase difference
Defocus	$\varphi(x,y) = k_{Defocus}\left(x^2 + y^2\right)$	$\triangle\varphi(x,y) = k_{Defocus} \cdot 2x \cdot \triangle x$
Spherical	$\varphi(x,y) = k_{Spherical}\left(x^2 + y^2\right)^2$	$\triangle\varphi(x,y) = k_{Spherical} \cdot 4\left(x^2 + y^2\right)x \cdot \triangle x$
Coma in y	$\varphi(x,y) = k_{Coma}\, y\left(x^2 + y^2\right)$	$\triangle\varphi(x,y) = k_{Coma} \cdot 2xy \cdot \triangle x$
Astigmatism	$\varphi(x,y) = k_{Astigmatism}\left(x^2 + y^2\right)$	$\triangle\varphi(x,y) = k_{Astigmatism} \cdot 2x \cdot \triangle x$
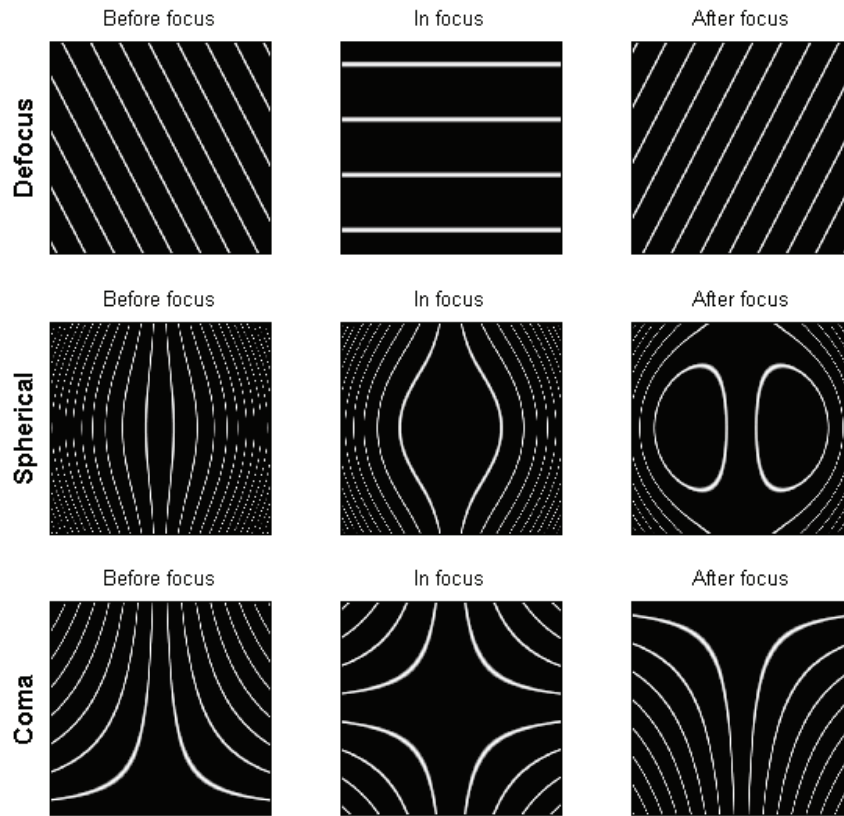
Figure 4.34: Interference fringes for three primary aberrations (Defocus, Spherical, Coma). In the first line, showing only the defocus component, an additional tilt in y-direction between the two waves $\triangle\varphi(x,y) = k_{y-Tilt} \cdot y$ **has been introduced, which results in the characteristic rotation of the fringes.**

The signal of the shearing interferometer is given by

$$I(x,y) = \left| U\left(x - \frac{\triangle x}{2}, y\right) + U\left(x + \frac{\triangle x}{2}, y\right) \right|^2$$

$$= \left| U\left(x - \frac{\triangle x}{2}, y\right) \right|^2 + \left| U\left(x + \frac{\triangle x}{2}, y\right) \right|^2 + 2\left| U\left(x + \frac{\triangle x}{2}, y\right) \right| \left| U\left(x - \frac{\triangle x}{2}, y\right) \right| \cos\left[\varphi\left(x - \frac{\triangle x}{2}, y\right) - \varphi\left(x + \frac{\triangle x}{2}, y\right) \right]$$

(4.100)

This can be simplified assuming an approximately equal field amplitude for $\pm \triangle x / 2$ by

$$I(x,y) = 2|U(x,y)|^2 \left[1 + \cos\left(\frac{\partial}{\partial x} \varphi(x,y) \cdot \triangle x \right) \right].$$

(4.101)

Stacking the phase values $\varphi(x,y)$ into vector $\bar{\varphi}$ and the phase differences $\triangle\varphi(x,y)$ into $\triangle\bar{\varphi}_x / \triangle\bar{\varphi}_y$ for lateral shear in x-/y-direction, the relation between the phase and phase differences can be written with the two geometry matrices A_x and A_y

$$\begin{aligned} \triangle\bar{\varphi}_x &= A_x \bar{\varphi} \\ \triangle\bar{\varphi}_y &= A_y \bar{\varphi} \end{aligned},$$

(4.102)

which can be also written similar to the technique for the Shack-Hartmann sensor in one system of linear equations

$$\begin{bmatrix} \triangle\bar{\varphi}_x \\ \triangle\bar{\varphi}_y \end{bmatrix} = \begin{bmatrix} A_x \\ A_y \end{bmatrix} \cdot \bar{\varphi} \text{ or } \triangle\bar{\varphi} = A \cdot \bar{\varphi}.$$

(4.103)

This can again be solved by a least-square solver in the fashion

$$\bar{\varphi} = \left(A^T A \right)^{-1} A^T \triangle\bar{\varphi}.$$

(4.104)

The phase differences or gradient $\triangle\bar{\varphi}$ can be expressed as the derivative of a scalar field and the curl of a vector field (see Eq. (4.57)) as discussed in Section 4.4.1.1 on phase singularities with the Shack-Hartmann sensor. Remembering that A^T is the matrix equivalent of a divergence operator, it becomes clear that the shearing interferometer suffers from the same limitations as the Shack-Hartmann sensor in the presence of phase singularities due to the fact that the divergence of a curl operation is zero.

Barchers et al. [BAR02b] studied the performance of shearing interferometer in the presence of phase singularities in strong scintillation. For the reconstruction step they compared the performances of a least-square reconstructor and a complex exponential reconstructor [FRI01]. The least-square reconstructor was not able to reconstruct the part of the phase associated with the curl of the vector potential. In the consequence a sharp drop of the performance occurred for Rytov variances $\sigma_R^2 > 0.2$, as already had been shown in previous studies for the Shack-Hartmann sensor [BAR02a, TYL00]. The complex exponential reconstructor correctly estimated the phase even in the presence of phase singularities, as long as the ratio of the lateral shear and the atmospheric coherence length $\triangle x / r_0$ was sufficiently small. The performance deterioration was especially pronounced for the least-square reconstructor, even for ratios $\triangle x / r_0 = 1/2$. This is caused by the fact, that shearing interferometers suffer from the fact, that phase differences outside the interval $[-\pi, \pi]$ are

not correctly measured and errors of $\pm 2\pi$ occur. This can be recognized from Eq. (4.101). Large phase differences occur when the atmospheric coherence length r_0 approaches the lateral shear $\triangle x$. The 2π measurement errors have a direct effect on the phase estimation of a least-square reconstructor. In contrast there is no effect of the 2π errors on the complex exponential reconstructor due to the operation of the complex exponential, as $\exp(i2\pi)=1$; however, for large ratios $\triangle x / r_0 \geq 1$ the performance of both reconstructors deteriorates due to measurement noise, i.e. the large variance of the signal over the shear distance.

4.4.4 Phase Retrieval Methods

Phase retrieval algorithms attempt to recover the field, i.e. intensity and phase, in the entrance pupil plane of the telescope by measuring one or more intensity distributions in different planes in the optical system. The original algorithm proposed by Gerchberg and Saxton [GER72] used two measurements of the intensity, in the telescope pupil plane $|u|=\sqrt{I_{pupil}}$ and the focus intensity $|U|=\sqrt{I_{focus}}$. The algorithms were further developed e.g. by Fienup [FIE82, FIE87], in order to reduce the number of iterations and also to investigate the possibility to retrieve the telescope-pupil field from one intensity measurement in the focus plane. For the latter one additional constraints, such as zero intensity outside the telescope aperture, were applied. The question of the uniqueness of the retrieved phase was discussed in several publications [MIA98][FOL81].

Phase retrieval algorithms are of interest for the application in communication systems, as typical optical communication receivers in mobile scenarios measure the intensity distribution in the focus to operate the tracking system to point the telescope to the counter terminal. In this sense it would be interesting to use the already available and anyway required information to also drive an AO system, maybe with a low-order modal correction, and taking the specific conditions of the scenarios into account.

However, the algorithms are computationally very demanding due to their iterative character and the large number of Fourier transforms required. One of the important requirements for AO systems in the SGL scenarios is high speed, which would not be achievable with phase retrieval algorithms. Nevertheless, a basic introduction is given to this method as it might be a good starting point for further investigations in this direction and in this way simplifying AO systems for communication scenarios.

4.4.4.1 Basic Phase Retrieval Algorithms

The first phase retrieval algorithm was proposed in [GER72][FIE82] with the error-reduction method. It was based on the measurement of the intensity in the telescope pupil plane and the focus plane. The electrical field in the focus plane U is related to the field in the telescope pupil plane u by a focus transformation, which can be mathematically expressed by a Fourier transform (Appendix A.2.3)

$$U(\vec{q}) = \frac{1}{\lambda f} FT\{u(\vec{x})\} = \frac{1}{\lambda f} \iint u(\vec{x})\exp(2\pi i \vec{q}\cdot\vec{x})d\vec{x} , \qquad (4.105)$$

where

$$u(\vec{x}) = |u(\vec{x})|\exp(i\varphi(\vec{x}))$$
$$U(\vec{q}) = |U(\vec{q})|\exp(i\phi(\vec{q})) \qquad (4.106)$$

The complex constants of the focus transformation are neglected, as they do not have an influence on the measured intensities in the focus/pupil plane and cancel out in the forward and back transformation.

105

In the following variables in the Fourier plane (Focus plane) are designated with capital letters, while variables in the telescope pupil plane are shown with lower-case letters.

The algorithm starts with an estimate of the field in the pupil plane. This could be just the aperture function (i.e. one inside, zero outside the aperture) of the telescope with diameter D. The following steps state the phase retrieval algorithm:

1. Fourier transform an estimate of the field in the pupil plane to get an estimate of the field in the focus plane.
2. Replace the modulus of the estimated field in the focus plane with the measured intensity $|M|$.
3. Transform the modified field of the focus plane back to the pupil plane by an inverse Fourier transform.
4. In the pupil plane apply additional constraints to estimate the field in the pupil plane. Constraints could be another intensity measurement or just again the assumption that the field outside the telescope aperture is zero.

The principle is summarized in Figure 4.35. The convergence of the process can be checked by the amount by which the constraints in the pupil and Fourier domain are violated. For the Fourier plane this gives an error for the jth iteration E_j

$$E_j = \frac{1}{A} \iint_A |U_j(\bar{q}) - U'_j(\bar{q})|^2 \, d\bar{q} = \frac{1}{A} \iint_A \left[|U(\bar{q})| - |M(\bar{q})|\right]^2 \, d\bar{q} \tag{4.107}$$

and for the pupil plane e_j

$$e_j = \frac{1}{A} \iint_A |u_{j+1}(\bar{x}) - u'_j(\bar{x})|^2 \, d\bar{x}. \tag{4.108}$$

The respective area of integration is denoted by A. For a two-intensity measurement problem with a measured intensity $|m|$ in the pupil plane, the error value in the focus transforms to

$$e_j = \frac{1}{A} \iint_A \left[|u'_j(\bar{x})| - |m(\bar{x})|\right]^2 \, d\bar{x}. \tag{4.109}$$

For a single intensity measurement in the focus plane and the additional pupil-plane constraint, that the intensity outside the telescope aperture is zero, the error value in the pupil plane becomes

$$e_j = \frac{1}{\bar{A}} \iint_{\bar{A}} \left[|u'_j(\bar{x})|\right]^2 \, d\bar{x}, \tag{4.110}$$

where $\bar{A}$ denotes the area outside the telescope aperture.

A numerical simulation of phase retrieval with two intensity measurements is shown in Figure 4.36. A phase and intensity distribution was generated with a ratio of aperture diameter and atmospheric coherence length of D/r_0=2. Statistical independence of phase and intensity was assumed. The upper row shows the original field (phase and amplitude) in the pupil and the focus amplitude. The middle row gives the retrieved field after 20 iterations. In the lower row the differences in the pupil phase are shown and the convergence of the algorithm with the squared error in the pupil (4.110) and in the focus plane (4.107). This shows a nice

convergence with two intensity measurements, however the convergence is not always guaranteed.

A related algorithm was suggest by Paxman and Fienup [PAX88], called Phase Diversity. This algorithm is based on two measurements of the intensity distribution, one in the focus plane and one in an intentionally defocused plane. Again a nonlinear, iterative optimization technique is used to find the phase distribution.

$$u = |u|\exp(i\varphi) \quad \xrightarrow{\quad FT \quad} \quad U = |U|\exp(i\phi)$$

Satisfy Pupil Constraints

Satisfy Fourier Constraints

$$u' = |u'|\exp(i\varphi') \quad \xleftarrow{\quad FT^{-1} \quad} \quad U' = |M|\exp(i\phi)$$
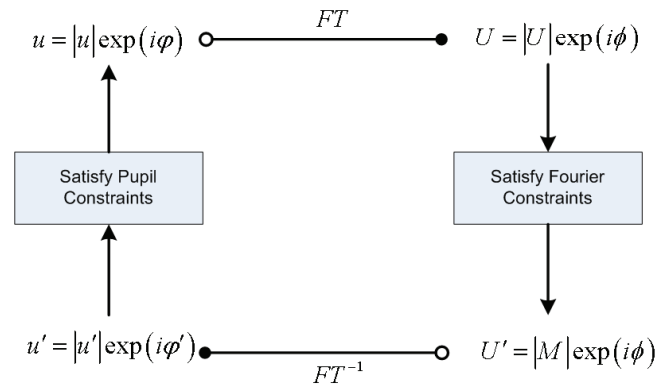
Figure 4.35: Principle of the phase retrieval algorithm based on an error-reduction method.

107
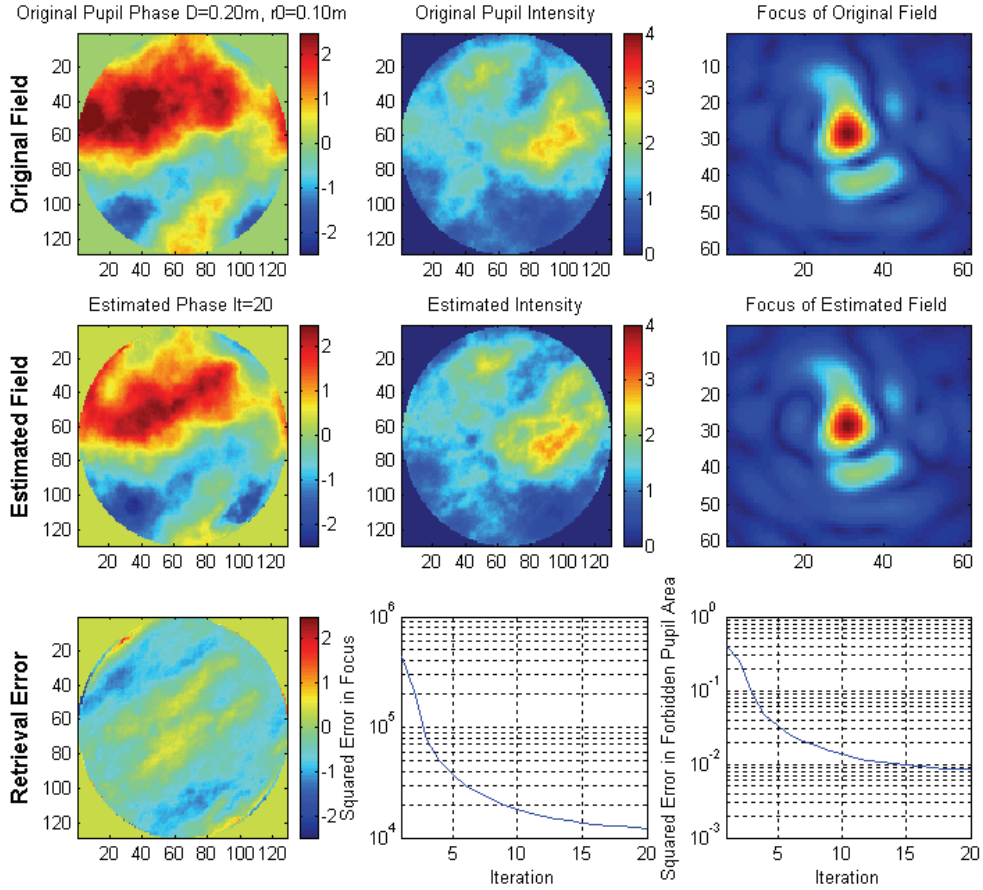
Figure 4.36: Retrieval of the phase distribution in the pupil plane from intensity measurements in the pupil and the focus plane. Original field created for an aperture *D*=0.2m and *r₀*=0.1m. Scintillation were added to the field. In the first row the original field with phase/amplitude in the pupil plane and the focus amplitude. In the second row the reconstructed field after 20 iterations. In the bottom row the phase error in the pupil plane and the development of the focus and pupil plane error values.

A slightly different approach was suggested by Southwell [SOU77]. He described the estimated phase by Zernike polynomials with the coefficients stacked in the vector $\vec{a}$. An estimate for the Zernike coefficients is obtained by minimizing the difference between the measured intensity distribution I_M and the intensity distribution I_a estimated from the Zernike coefficients. Both intensities are taken in the focus plane.

$$e = \sum_{x,y} \left[I_M(x,y) - I_a(x,y,\vec{a}) \right]^2 / \sigma(x,y)^2 \qquad (4.111)$$

Each pixel value (x,y) is scaled by its expected noise variance $\sigma(x,y)^2$ assuming a Gaussian distribution. I_a is calculated by the squared modulus of the Fourier transform of the estimated phase, assuming a constant intensity distribution I_0 in the telescope pupil plane. The minimization can be performed by any non-linear optimization algorithm. As the algorithms before, this method cannot solve the ambiguity issues described in the next section, and it is only applicable with the assumption of a constant intensity distribution in the pupil plane, which is not realistic for SGL scenarios.

4.4.4.2 Uniqueness

Considerations on the uniqueness of the phase retrieval problem can be found in [MIA98][BAT82]. Some problems of the uniqueness can be already analyzed in the properties of the Fourier transform. The discrete Fourier transformation, i.e. the relation between the complex field in the telescope pupil plane and the focus plane, is given by

$$G(\bar{k}) = \sum_{n_x,n_y=0}^{N-1} g(\bar{n}) \exp(2\pi i \bar{k} \cdot \bar{n} / N), \tag{4.112}$$

where $\bar{k} \cdot \bar{n} = k_x n_x + k_y n_y$ and k and n are integer numbers. Consequently the intensity in the Fourier plane is written by

$$\left| G(\bar{k}) \right|^2 = \left| \sum_{n_x,n_y=0}^{N-1} g(\bar{n}) \exp(2\pi i \bar{k} \cdot \bar{n} / N) \right|^2. \tag{4.113}$$

Eq. (4.113) can be seen as a set of non-linear equations. In the one-dimensional case, there are N equations, but $2N$ unknowns, namely the real and complex parts of $g(n)$. Equivalently there are $2N^2$ unknowns in the two-dimensional case. The reason for the under-determined system lies in the fact, that only the modulus of the field but not the phase can be measured in the focus.

Because of the loss of the phase in the focus field, there are some fundamental ambiguities in the retrieval process. Any of the following three quantities $g(x)$, $g(x+x_0)e^{i\theta_c}$, $g^*(-x+x_0)e^{i\theta_c}$, i.e. phase constant, translation, and conjugate image, are equal in the modulus of the Fourier transform. The corresponding Fourier properties are (see Appendix A.1.3)

Table 4.5: Fourier properties, which explain the ambiguities in the phase retrieval.

a)	$e^{i\theta_c} g(x) \rightarrow e^{i\theta_c} G(k)$	Multiplication with a complex constant
b)	$g(x-x_0) \rightarrow e^{-i2\pi x_0 k} G(k)$	Shift in the signal domain
c)	$g^*(-x) \rightarrow G^*(k)$	Complex conjugate and mirroring

Figure 4.37 shows an example for the reconstruction of a phase in the pupil plane using the intensities in the focus plane and the pupil plane. Clearly the ambiguity in the reconstruction can be seen. The estimated field is the complex conjugate of the original field mirrored at the image center. The ambiguity appears according to property c) in Table 4.5. Although the phase is not correctly estimated, the Fourier transform of the estimated field gives a very good estimate of the focus spot, and the error measures in the focus and the pupil plane nicely decrease; however, an AO system would not work in this case, as the phase estimate is wrong.
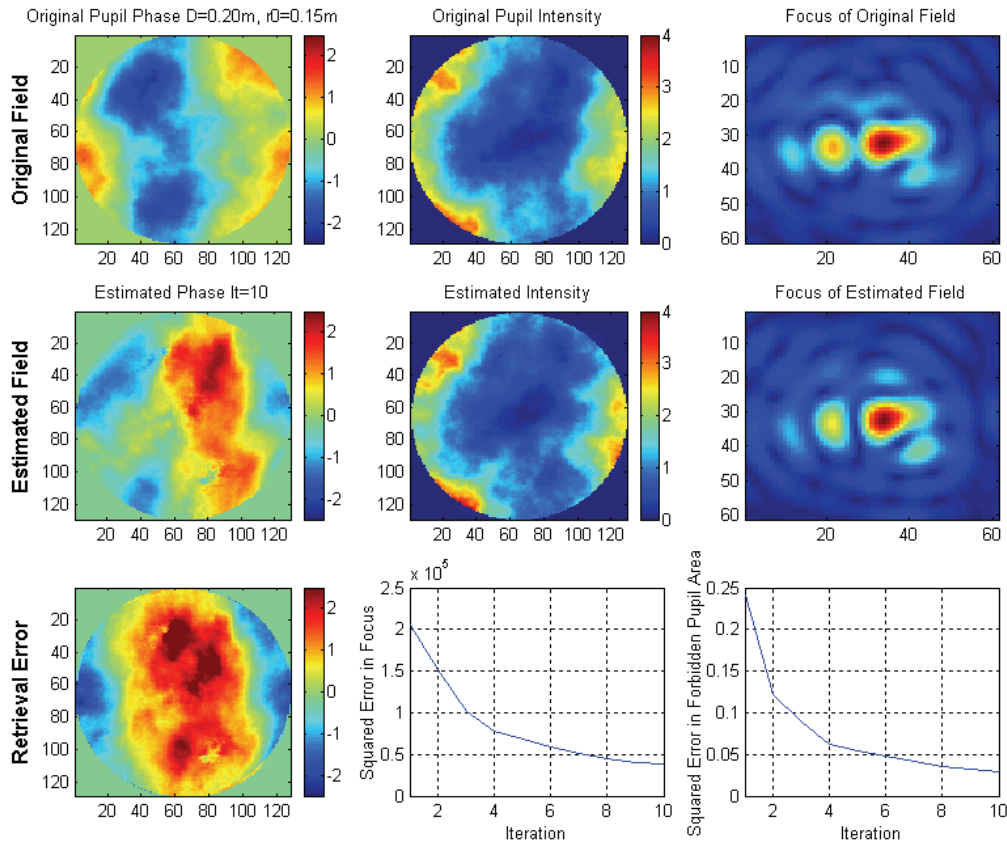
Figure 4.37: Retrieved phase by the error-reduction algorithm. The estimated field is the complex conjugate of the original field mirrored at the image center.

4.5 Other Adaptive Optics Concepts

4.5.1 Wavefront Sensorless Adaptive Optics Systems

Interesting for fiber-coupled communication receivers appear to be so called wavefront-sensorless AO systems, which use a performance metric, e.g. image sharpness or power coupled into a fiber, to correct phase distortions with an iterative method [VOR02]. The natural performance metric for a communication system would be the power coupled into the receiver fiber and thus the directly optimization of the communication SNR. The main challenge in this iterative approach is convergence speed, where the limiting component is not the sensor but the deformable mirror. Fast state-of-the-art mirrors have a bandwidth of a few kilohertz. This issue appears to be especially critical for the high-bandwidth requirements of links through the atmosphere, where only few hundred micro-seconds are available to find a good approximation of the wavefront.

Wavefront sensorless systems are based on an implicit phase reconstruction without the help of a wavefront sensor. The measured performance metric $J = J(\vec{u})$ is a function of the control parameters $\vec{u} = \{u_1, u_2, ..., u_N\}$, which are usually the control signals for the adaptive mirror. The performance metric is optimized by some type of gradient-descent optimization technique [PRE92]. Figure 4.38 shows the typical design of a wavefront-sensorless system. Vorontsov et al. have studied the performance of different optimization techniques [VOR98][VOR00][VOR02].
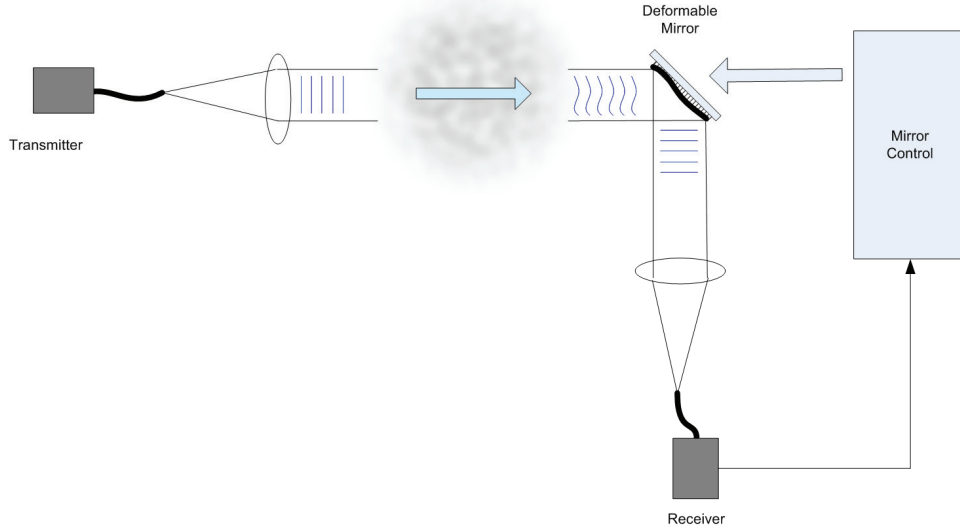
Figure 4.38: Principle concept of a wavefront sensorless AO system.

Sequential gradient-descent algorithms incrementally adjust the control parameters u to improve the value of the performance metric by means of a real-time estimation of the gradient

$$\bar{J}' = \nabla \bar{u} = \left\{ \frac{\partial}{\partial u_1} J, ..., \frac{\partial}{\partial u_N} J \right\}. \qquad (4.114)$$

J' can be estimated by applying small changes in the control parameters δu_j, where u_j indicates the jth control parameter. An estimate for gradient can then be given by $J'_j = \dfrac{\delta J}{\delta u_j}$ in place of the real, partial derivative gradient.

In the sequential gradient-descent method the control parameters are impinged one after the other with a small delta δu_j, and the approximation for each partial derivative is calculated. In this method the convergence time increases with the number N of control channels, at least on the order N^2 [VOR98].

The algorithm updates the control channels to maximize the performance metric J by

$$u_l^{(m+1)} = u_l^{(m)} + \mu \frac{\partial J^{(m)}}{\partial u_l}, \qquad (4.115)$$

where μ is a small constant controlling the speed of the control parameter update and m indicates the iteration number.

The convergence-time problem could potentially be reduced by a multidithering approach as described in [OME77]. Small harmonic signals with different dithering frequencies are applied to each control channel in parallel. Estimates of the gradients can then be obtained from synchronous, coherent signal detection in the performance metric. Difficulties arise from the large bandwidth requirements of the approach to achieve an adequate frequency spacing of the dithering excitations, and also the necessity of the frequencies to be above the frequency spectrum of the atmospheric disturbance.

An alternative approach is the Stochastic Parallel-Gradient-Descent Optimization Technique (SPGD) [VOR98]. In this method small stochastic (random) perturbations

$\delta u_j \quad j = 1..N$ are synchronously (in parallel) applied to all control channels. The change of the performance metric is then

$$\delta J = J(u_1 + \delta u_1, ..., u_N + \delta u_N) - J(u_1, ..., u_N) .\tag{4.116}$$

The channel update for the parallel gradient-descent method is then given similar to Eq. (4.115) but without the knowledge of the exact gradient of each channel

$$u_l^{(m+1)} = u_l^{(m)} + \mu \cdot \delta J^{(m)} \cdot \delta u_l^{(m)}, \quad l = 1, ..., N .\tag{4.117}$$

In contrast to the sequential method, it is not intuitive to expect a convergence of the algorithm for the parallel gradient-descent method, however Vorontsov could derive an expression proving the actual convergence of such an algorithm. Although the parallel approach provides an increase of the convergence speed, the technique is still significantly limited by the actuator speed and appears not be applicable to drive the AO system. Actuators with a bandwidth of several 100kHz would be required. With current technology this approach could be well suited to correct slow drifts of the whole optical system due to thermal effects or a change in the telescope orientation.

4.5.2 Phased-Array Concepts in Pupil and Focus Plane

Another promising technique for adaptive optics correction in free-space optical communication systems are phased fiber arrays. The idea is not a new one, in fact the very first AO systems were developed on the principle of coherent beam combining, using a 'glint reflection' from a target as a feedback for the phasing of beams [BRI74].

Over the last 15 years, adaptive phase-locked fiber arrays have been considered as a way to make scalable, light weight launch systems, capable of correcting higher-order phase-aberration errors as well as the traditional use for beam steering [KUD94]. Figure 4.39 shows the principle method of the phase-locked fiber arrays.
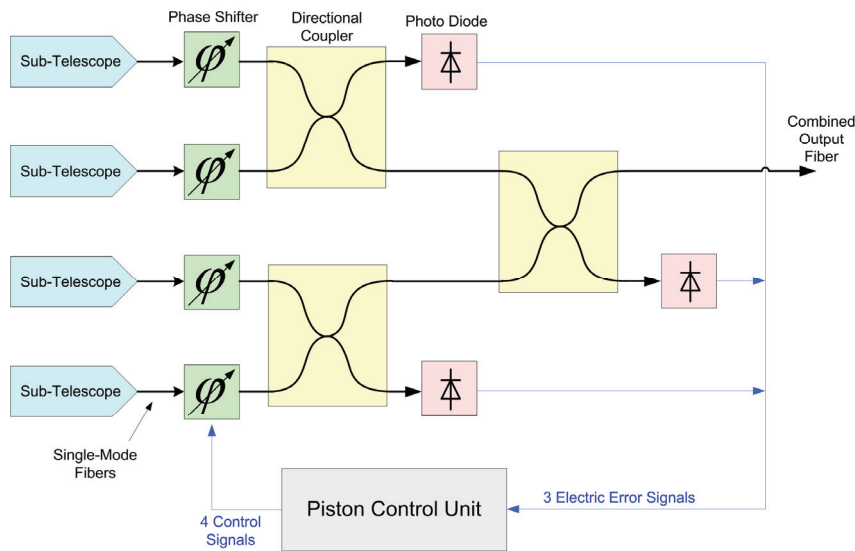
Figure 4.39: Example of a four-aperture receive-telescope array. The radiation from the sub-telescopes is combined via two stages of directional fiber couplers. The phase of each sub-arm is adapted by a phase shifter (piston actuator), so that the power values on the measurement photo diodes become minimal and at the same time the combined output is maximized [KUD94].

There are many advantages in using a fiber bundle transceiver, such as the ease of separation of transmit and receive wavelengths using wavelength division multiplex (WDM) techniques and the ability to use readily available fiber components and detectors, as well as the possibility of using fiber amplifiers [BRU05]. Very high correction rates are possible (100kHz) by using phase-shifting fibers. The feasibility of such a system has recently been demonstrated by [VOR09].

Focal array receivers (FAR) [GIG04] are a related technique. Several heterodyne receivers are implemented in the focal plane. Only one local oscillator (LO) is applied to all receiver elements, so that each receiver element requires individual electronics to produce the signal in the base band. The signal combination is achieved in the electric domain in contrast to fiber arrays, where the signal combination is performed in the optical domain.
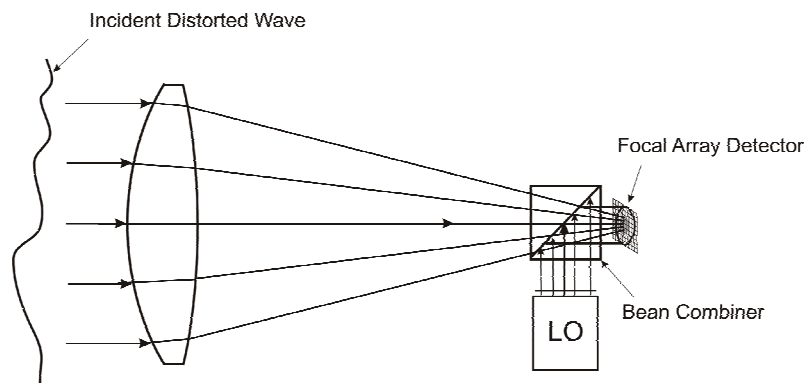
Figure 4.40: Principle design of a Focal Array Receiver [GIG04]. The incident wave is superposed with the local oscillator in the focal plane.

4.6 Discussion

Chapter 4 discussed the specific conditions on satellite-to-ground links and investigated the performance of several wavefront sensors and adaptive optics concepts under these conditions. Among the important questions for each wavefront sensor were the type of reconstruction, the robustness to strong phase distortions and intensity fluctuations, the robustness to phase singularities, the possible speed of the wavefront sensor taking the pixel to phase point measurement ratio into account, and the complexity of the setup.

Table 4.6 tries to summarize properties of the wavefront sensors under the discussed conditions of the scenario. A plus +, a minus – and an o indicate rather positive, negative and neutral characteristics of the specific sensor. It is clear that wavefront sensors are complex systems and difficult to characterize with a few parameters, but it was attempted to give a quick overview of the findings in this chapter and especially their usability in the SGL scenario at low elevation angles of the satellite.

- **Resolution:** This parameter characterizes the spatial resolution of a wavefront sensor. Interferometers score well here, as they have a favorable ratio between required sensor pixels and phase measurement points. This ensures high frame rates and high processing speed with low delays due to the camera frame transfer.

- **Complexity of reconstruction – speed:** The complexity of the reconstruction is an important factor for the speed or bandwidth of the AO system. Self-referencing common-path and unequal path interferometers (as described by Zernike) belong to the direct sensors, which do not require an explicit (numerical) reconstruction, and they have a favorable pixel/measurement point ratio. In the consequence they appear to be well suited for the application in

113

SGL scenarios. Shack-Hartmann, curvature, and shearing interferometer sensor require advanced reconstruction methods (e.g. a complex exponential reconstructor) to cope with phase singularities making them potentially slow. Phase retrieval and wavefront-sensorless systems are inherently slow due to their iterative character.

- **Robustness to singularities:** Self-referencing common-path and unequal path interferometers simply detect phase singularities without any complex reconstruction, while Shack-Hartmann, curvature, and shearing interferometer sensors require a complex reconstruction step with a high sensor resolution, if a correct reconstruction of the singularities is possible at all.

- **Sensitivity to scintillation:** Especially the iterative methods react sensitive to intensity scintillation, but also the curvature sensor relies on weak intensity fluctuations across the pupil.

- **Complexity of the optical setup:** Wavefront-sensorless systems have a clear advantage in terms of setup complexity; however, they do not show the potential for an overall fast AO performance.

Table 4.6: Overview of wavefront sensors and their characteristics.

Wavefront Sensor	Resolution	Complexity of Reconstruction – Speed	Robustness to Singularities	Sensitivity to Scintillation	Complexity of Setup (Optics)
Shack-Hartmann	-	o (Unwrapped phase)	-	+	+
Curvature Sensor	o	- (++ for a bimorph mirror)	-	-	o
Phase Retrieval from Focus Intensity	-	Slow and instable	-	-	+
Wavefront Sensorless	-	Slow but simple	+	o	++
Lateral Shearing Interferometer	+	-	o	+	o
Common-Path Interferometer	+	o (wrapped phase, iterative)	+	o	+
Phase-Shifting Interferometer	+	+ (wrapped phase)	+	+	-

This chapter has shown that interferometric wavefront sensors exhibit some favourable characteristics in strong-fluctuation scenarios, where the conventional sensors like Shack-Hartmann and curvature sensor appear to have weaknesses, which can be only compensated, if at all, with a high (and expensive) technical effort.

Interferometric sensors can provide very high resolution due to a favourable pixel to phase point ratio, and thus potentially can help to achieve a fast closed-loop bandwidth. Some of the interferometric techniques yield phase estimates almost without numerical processing (phase-shifting interferometer) and are at the same time highly robust to phase singularities and scintillation.

Interferometric wavefront sensors exist in a large variety. Several techniques and technical implementations will be further investigated in the following chapter, also illuminating the properties of the different techniques in respect to resolution, complexity and reconstruction speed, singularities, strong scintillation, and the complexity of the optical setup.

5   Interferometric Wavefront Sensors in Strong Turbulence

This section analyzes in detail interferometric wavefront sensors for the application in satellite-to-ground links (SGL). Special emphasis will be again given to the particular conditions found in these scenarios [KNA09]. Apart from the general atmospheric conditions already presented in Section 4.4, there are conditions specific to interferometers, which have to be taken into account for the development of suitable wavefront sensors and adaptive optics (AO) systems. The most important conditions are summarized in the following:

- A **self-referencing interferometer** type is required, generating the reference wave from the input wave by a spatial filter in the Fourier plane;

- **Strong phase distortions** over the entrance aperture and therefore large variations of the strength of the reference wave (at least in the initial phase of the wavefront correction);

- **Strong intensity fluctuations** over the entrance aperture;

- **Full 2π phase circle** measurements are required and ambiguities have to be resolved;

- **Difficult environmental conditions** for the operation of the AO system with some amount of vibration (e.g. mount motion) and temperature variations (e.g. solar radiation);

- **Highly monochromatic and polarized laser source** in space with a long coherence length;

- The **integration of the interferometric sensor into an AO system** makes certain iterative techniques possible;

Self-referencing interferometers appear to be especially interesting for the application in SGL scenarios. The term self-referencing implies that the reference wave is obtained from the incoming wave itself by applying a spatial filter in a Fourier plane. A separate reference beam is not used, which would require a local, phase-locked laser as in coherent communication receivers. A detailed analysis of the properties of self-referencing interferometers can be found in the literature on common-path interferometers (CPI) [GLU01, AND95], which is presented in Section 5.1.1 with a focus on the creation of the synthetic reference wave. Some considerations are also given to non-common path point-diffraction interferometers (PDI) in Section 5.1.2.

A single CPI (as described by Zernike) does not resolve the phase ambiguities of the cosine term in the interferometer Eq. (4.86) and also does not take into account effects from varying intensity distributions in the object wave and the reference wave. These issues are approached in the Section 5.2 with phase-shifting interferometers (PSI), which use several interferograms (at least three) to recover the unique phase even in the presence of intensity fluctuations [CRE88, MAL07]. Sections 5.2.2 and 5.2.3 contain an overview of PSI evaluation techniques and relevant error sources, where especially phase-shifter errors, nonlinearities, detector noise, and vibrations appear significant for the satellite communication scenarios. Section 5.3 treats design issues of self-referencing interferometers for the deployment in an optical ground station for satellite-to-ground communications. Here Fourier fringe analysis (FFA) techniques as discussed by Takeda [TAK82], instantaneous PSIs [SIV03, DUN03, NOT07, MIL05], and also iterative CPI methods [VOR01] are presented. First, encouraging experimental results from laboratory setups are shown in Chapter 6.

5.1 Self-Referencing Interferometer

5.1.1 Common-Path Interferometer

The original description of the common-path interferometer (CPI), as it was invented by Zernike, gave the simplified equation $I_e(\bar{x}) \approx 1 + 2\varphi$ for the relation between phase and intensity (see Section 4.4.3.1, Eq. (4.90)). This result is only valid for weak phase fluctuations and assumes a constant intensity distribution over the aperture. Also fluctuations of the synthetic reference wave are not taken into account. Section 5.1.1.1 presents a more detailed derivation of the equations of the CPI including intensity fluctuations, wavefront distortions over the complete 2π phase circle, and generalized filter parameters. Section 5.1.1.2 is devoted to the analysis of the synthetic reference wave (SRW). Both sections can be applied not only to CPIs, but also help for the understanding of non-common path point-diffraction interferometers (PDI) (Section 5.1.2).

5.1.1.1 Detailed Derivation of Common-Path Interferometers and their Variations

The derivation of the CPI shown here is based on the work of Glückstad [GLU01] and Vorontsov [VOR01], however with some modifications to accommodate the specific requirements of the scenario. In particular a non-uniform intensity distribution in the input plane was assumed.
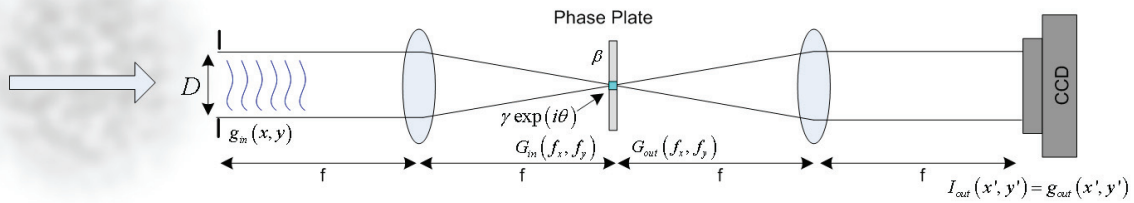
Figure 5.1: Principle setup of a common-path interferometer.

Figure 5.1 shows the detailed design of a CPI in a 4-f configuration. The incoming wave with the electric field $g_{in}(x,y) = |g_{in}(x,y)| e^{i\varphi(x,y)}$ is distorted by the atmospheric turbulence. The filter plate is located in the focus plane of the first lens, where the field is proportional to the Fourier transform so that $G_{in}(\bar{f}) = h_l \cdot FT\{g_{in}(\bar{r})\}$. $FT\{\}$ denotes the Fourier transformation. h_l is a complex scaling factor (see Appendix A.2.3 Optical Fourier Transform), which however can be neglected, as it cancels out during the inverse Fourier transformation of the second lens. The vector $\bar{r} = (x,y)$ gives the transversal coordinates in the spatial domain, while $\bar{f} = (f_x, f_y)$ gives the frequencies in the Fourier domain. The scaling of the frequencies to the spatial coordinates is given by $(f_x, f_y) = \left(\dfrac{q_x}{\lambda f}, \dfrac{q_y}{\lambda f}\right)$, where $\bar{q} = (q_x, q_y)$ denotes the spatial coordinates in the Fourier plane, f the focal length of the lenses and λ the wavelength.

A general phase plate with a circular central area (filter dot) is given by the transfer function

$$
\begin{aligned}
H_{dot}(\bar{q}) &= \gamma e^{i\theta} \quad for \; |\bar{q}| < q_0 \\
H_{dot}(\bar{q}) &= \beta \quad\quad otherwise
\end{aligned}
, \tag{5.1}
$$

where γ denotes the transmission (attenuation) and θ the phase shift of the filter dot. The transmission (attenuation) of the area around the filter dot is denoted by β. In the following the filter dot is assumed to have infinitely small dimensions ($q_0 \rightarrow 0$) in order to simplify the formulas and to make the characteristics of the CPI easier to understand. Thus, the filter dot is modelled by a Dirac impulse $\delta(\vec{f})$. The transfer function of the filter plate can now be written by

$$H_{dot}(\vec{f}) = \beta\left[1 - \delta(\vec{f})\right] + \gamma e^{i\theta}\delta(\vec{f}) = \beta + \delta(\vec{f})\left(\gamma\, e^{i\theta} - \beta\right). \tag{5.2}$$

The field directly before the filter $G_{in}(\vec{f})$ is multiplied with the filter function $H_{dot}(\vec{f})$, which yields the output field $G_{out}(\vec{f})$

$$G_{out}(\vec{f}) = \beta G_{in}(\vec{f}) + \left(\gamma e^{i\theta} - \beta\right)G_{in}(\vec{f})\delta(\vec{f}). \tag{5.3}$$

Here the second term $\left(\gamma e^{i\theta} - \beta\right)G_{in}(\vec{f})\delta(\vec{f})$ can be interpreted as a synthetic reference wave similar to the synthetic reference wave generated in a non-common path PDI (Section 5.1.2). Performing the inverse Fourier transform gives the field at the image sensor

$$g_{out}(\vec{r}) = \frac{1}{h_l}FT^{-1}\left\{G_{out}(\vec{f})\right\} = \beta g_{in}(\vec{r}) + \left[\gamma e^{i\theta} - \beta\right]\cdot g_0, \tag{5.4}$$

where the complex constant (spatially constant but not temporally) g_0 is the averaged complex field over the aperture area A in the entrance pupil and therefore the field at the filter dot at $\vec{f} = (0,0)$. The Fourier transformation of the input field $g_{in}(\vec{r})$ into the focus plane is given by

$$G_{in}(\vec{f}) = h_l \cdot \iint\limits_A \left|g_{in}(\vec{r})\right| e^{i\varphi(\vec{r})} e^{i2\pi\vec{r}\cdot\vec{f}}d^2\vec{r} \tag{5.5}$$

with $\vec{r}\cdot\vec{f} = x\cdot f_x + y\cdot f_y$. A denotes the area of the input pupil with diameter D. Consequently, the field at the filter dot is

$$G_{in}(0,0) = h_l \cdot \iint\limits_A \left|g_{in}(\vec{r})\right| e^{i\varphi(\vec{r})}d^2\vec{r} = g_0. \tag{5.6}$$

The intensity distribution on the camera chip is calculated by

$$I(\vec{r}) = \left|g_{out}(\vec{r})\right|^2 = g_{out}(\vec{r})\cdot g_{out}^{*}(\vec{r}). \tag{5.7}$$

The star * denotes the complex conjugate. Putting Eq. (5.4) into (5.7) results in

$$I(\vec{r}) = g_{out}(\vec{r})\cdot g_{out}^{*}(\vec{r}) = \left|\beta\left|g_{in}(\vec{r})\right| e^{i(\bar{\varphi} + \tilde{\varphi}(\vec{r}))} + \left(\gamma e^{i\theta} - \beta\right)\left|g_0\right| e^{i\bar{\varphi}}\right|^2, \tag{5.8}$$

117

where $g_0 = |g_0| e^{i\overline{\varphi}}$ as shown in Eq. (5.6). $\overline{\varphi}$ and $\tilde{\varphi}$ are the average and variable parts of the input phase, so that $\varphi(\overline{r}) = \overline{\varphi} + \tilde{\varphi}(\overline{r})$. The constant factor $e^{i\overline{\varphi}}$ drops out due to the absolute value, so that the CPI equation becomes

$$I(\overline{r}) = \left| \beta |g_{in}(\overline{r})| e^{i\tilde{\varphi}(\overline{r})} + (\gamma e^{i\theta} - \beta)|g_0| \right|^2. \tag{5.9}$$

Expanding this yields

$$I(\overline{r}) = \beta^2 |g_{in}(\overline{r})|^2 + |g_0|^2 (\beta^2 + \gamma^2 - 2\beta\gamma \cos\theta) + 2\beta |g_{in}(\overline{r})||g_0| \left[\gamma \cos(\tilde{\varphi}(\overline{r}) - \theta) - \beta \cos\tilde{\varphi}(\overline{r}) \right],$$

from which the equations of some of the known CPIs can be derived with the according filter parameters θ, β, γ.

Positive Zernike phase contrast filter

The classical Zernike phase contrast filter is given by the filter parameters $\theta = \pi/2, \beta = 1, \gamma = 1$. Thus,

$$I_{zer}^{(+)}(\overline{r}) = |g_{in}(\overline{r})|^2 + 2|g_0|^2 + 2|g_{in}(\overline{r})||g_0| \left[\sin\tilde{\varphi}(\overline{r}) - \cos\tilde{\varphi}(\overline{r}) \right]. \tag{5.10}$$

Assuming $|g_{in}(\overline{r})|^2 = |g_0|^2 = 1$, using the Taylor expansions of $\sin\varphi = \varphi - \dfrac{\varphi^3}{6} + ...$ and $\cos\varphi = 1 - \dfrac{\varphi^2}{2} + ...$ and neglecting higher order terms for small φ, this equation can be simplified to

$$I_{zer}^{(+)}(\overline{r}) = 3 + 2\left[\sin\tilde{\varphi}(\overline{r}) - \cos\tilde{\varphi}(\overline{r}) \right] \approx 1 + 2\tilde{\varphi}(\overline{r}) + \tilde{\varphi}^2(\overline{r})... \tag{5.11}$$

showing the expected linear relationship between phase and intensity already given in Section 4.4.3.1.

Negative Zernike phase contrast filter

Similar results are obtained with the negative Zernike phase contrast filter: $\theta = -\pi/2, \beta = 1, \gamma = 1$

$$I_{zer}^{(-)}(\overline{r}) = |g_{in}(\overline{r})|^2 + 2|g_0|^2 + 2|g_{in}(\overline{r})||g_0| \left[-\sin\tilde{\varphi}(\overline{r}) - \cos\tilde{\varphi}(\overline{r}) \right]. \tag{5.12}$$

Differential Zernike filter [VOR01]
Subtracting Eq. (5.12) from (5.10) gives

$$I_{dif}(\overline{r}) = I_{zer}^{(+)}(\overline{r}) - I_{zer}^{(-)}(\overline{r}) = 4|g_{in}(\overline{r})||g_0| \sin\tilde{\varphi}(\overline{r}). \tag{5.13}$$

Simplifying with $|g_{in}(\overline{r})|^2 = |g_0|^2 = 1$, the differential filter becomes

$$I_{dif}\left(\vec{r}\right) = I_{zer}^{(+)}\left(\vec{r}\right) - I_{zer}^{(-)}\left(\vec{r}\right) = 4\sin\tilde{\varphi}\left(\vec{r}\right) = 4\left(\tilde{\varphi}\left(\vec{r}\right) - \frac{\tilde{\varphi}^3\left(\vec{r}\right)}{6} + ...\right). \tag{5.14}$$

Thus, the output of the differential Zernike filter is, in a first approximation, directly proportional to the phase. The non-linear terms start with $\tilde{\varphi}^3$ in contrast to the simple Zernike filters, e.g. (5.11), and therefore the linear range of the phase-intensity mapping is extended.

Henning filter

Henning filter [HEN74]: $\theta = \pi/4, \beta = 1/\sqrt{2}, \gamma = 1$

$$I\left(\vec{r}\right) = \frac{1}{2}\left|g_{in}\left(\vec{r}\right)\right|^2 + \frac{1}{2}\left|g_0\right|^2 + \left|g_{in}\left(\vec{r}\right)\right|\left|g_0\right|\sin\tilde{\varphi}\left(\vec{r}\right). \tag{5.15}$$

Simplifying with $\left|g_{in}\left(\vec{r}\right)\right|^2 = \left|g_0\right|^2 = 1$, the Henning filter becomes

$$I\left(\vec{r}\right) = 1 + \sin\tilde{\varphi}\left(\vec{r}\right) \approx 1 + \tilde{\varphi}\left(\vec{r}\right) - ... \tag{5.16}$$

Figure 5.2 compares the three shown Zernike configurations, the positive Zernike filter, the differential Zernike filter, and the Henning filter. It can be seen, that the positive (classical) Zernike filter has only a very small range of linear phase-intensity mapping. Significant improvement is achieved with the differential and the Henning filter configurations, where the assumption of linearity is valid for $\left|\tilde{\varphi}\right| < \pi/3$. The curves are shown for the simplification $\left|g_{in}\left(\vec{r}\right)\right|^2 = \left|g_0\right|^2 = 1$, i.e. intensity fluctuations and a varying synthetic reference wave are not considered.
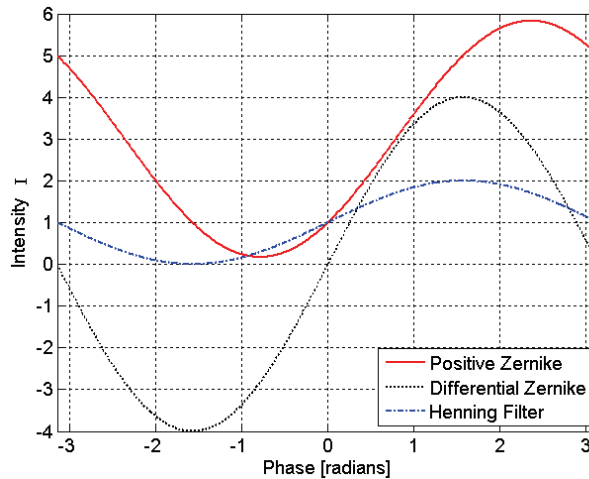
Figure 5.2: Comparison of the linear range of three Zernike filter configurations (Positive Zernike, Differential Zernike, Henning Filter).

5.1.1.2 Generation of the Synthetic Reference Wave

A detailed analysis of the generation of the synthetic reference wave (SRW) was given by Glückstad and Mogensen [GLU01] partly based on the work of Anderson [AND95]. They describe the effect of a finite filter-dot diameter on the quality of the SRW and thus the

accuracy of the phase estimation. This detailed analysis of the SRW is important especially due to the strong phase and amplitude fluctuations of the incoming wave for the considered scenarios. Two approximations of the SRW are compared here, an own one and the one of Glückstad.

The field distribution in the focus (filter-dot) plane is given by Eq. (5.5) and (5.6). In the first approximation a constant field $\left|G_{in}(0,0)\right|e^{i\overline{\varphi}}$ is assumed over the circular filter dot (neglecting any variations), now with finite radius q_0. The resulting intensity distribution in the sensor plane $I_{SRW}(\rho')$ results to an Airy distribution [SAL91]

$$I_{SRW}(\rho') = I_{SRW}(0,0)\left(\frac{2J_1(2\pi q_0\rho'/\lambda f)}{2\pi q_0\rho'/\lambda f}\right)^2.$$
(5.17)

The power over the full Airy pattern P_0 equals the power over the filter dot due to conservation of energy, which can be used to determine the value for the center intensity $I_{SRW}(0,0)$. Integrating Eq. (5.17) in polar coordinates over an infinite plane gives the entire power P_0

$$P_0 = I_{SRW}(0,0)\int_{\rho'=0}^{\infty}\int_{\varphi=0}^{2\pi}\frac{4J_1^2(2\pi q_0\rho'/\lambda f)}{(2\pi q_0\rho'/\lambda f)^2}\rho'd\varphi\,d\rho',$$
(5.18)

which can be integrated with [GRA81, eq. 6.574]

$$\int_{x=0}^{\infty}\frac{J_1^2(\alpha x)}{x}dx = \frac{1}{2}.$$
(5.19)

The center intensity of the Airy distribution becomes with the area A_d of the filter dot

$$I_{SRW}(0,0) = \frac{P_0A_d}{\lambda^2 f^2} = \frac{I_0A_d^2}{\lambda^2 f^2},$$
(5.20)

where $I_0 = \left|G_{in}(0,0)\right|^2$ denotes the (constant) intensity across the filter-dot aperture. This also shows, as expected, that the smaller the filter dot, the lower is the central intensity of the Airy distribution and thus the visibility of the fringe pattern is decreased (See Section 5.1.1.3).

The radius of the Airy distribution to the first intensity zero in the focus plane in dependence of the telescope aperture diameter D is

$$r_{Airy} = 1.22\frac{f\cdot\lambda}{D},$$
(5.21)

and the ratio η of the filter-dot radius q_0 and the radius of the Airy in the focus plane r_{Airy} is given by

$$\eta = \frac{q_0}{r_{Airy}} = \frac{q_0 D}{1.22 f\lambda}.$$
(5.22)

Therefore the intensity distribution in the sensor plane combining Eq. (5.18), (5.20) and (5.22) becomes

$$I_{SRW}(\rho') = \frac{I_0 A_d^2}{\lambda^2 f^2} \left(\frac{2J_1(2.44\pi\eta\rho'/D)}{2.44\pi\eta\rho'/D} \right)^2. \tag{5.23}$$

From this approximation of the intensity distribution of the SRW in the sensor plane, it is easy to understand that a small filter dot generates a broader SRW, where the intensity is relatively constant over the aperture diameter. This is important, as a drop in the intensity to the edge of the aperture directly influences the quality of the phase estimation. A similar situation is given for the phase of the Airy distribution, which can be seen in Figure 4.18 and Figure 4.19.

Glückstad [GLU01] gave a different approximation of the SRW. He assumed an ideal Airy intensity distribution in the filter plane created by the telescope entrance aperture. He then weighted this distribution with the aperture function of the filter dot with radius q_0 and Fourier transformed the result to the sensor plane, so that

$$g_{SRW}(r,\phi) = |g_0| \int\limits_{q'=0}^{q_0} \int\limits_{\varphi=0}^{2\pi} \frac{2J_1(\pi Dq'/\lambda f)}{\pi Dq'/\lambda f} e^{2\pi i \vec{r}'\cdot\vec{q}} q'\, d\varphi \cdot dq'. \tag{5.24}$$

Consequently, the distribution in the focus (filter-dot) plane is not constant anymore. Glückstad simplified the integral (5.24) with a zero-order Hankel transformation [GOO96] and solved the remaining one-dimensional integral with a Bessel power series expansion. Figure 5.3 compares the approximation of the constant amplitude over the filter dot (Eq. (5.23), left) and Glückstad's approximation (right). Both approximations show a similar decrease of the amplitude to the edge of the aperture. The first approximation (5.23) slightly underestimates the amplitude.
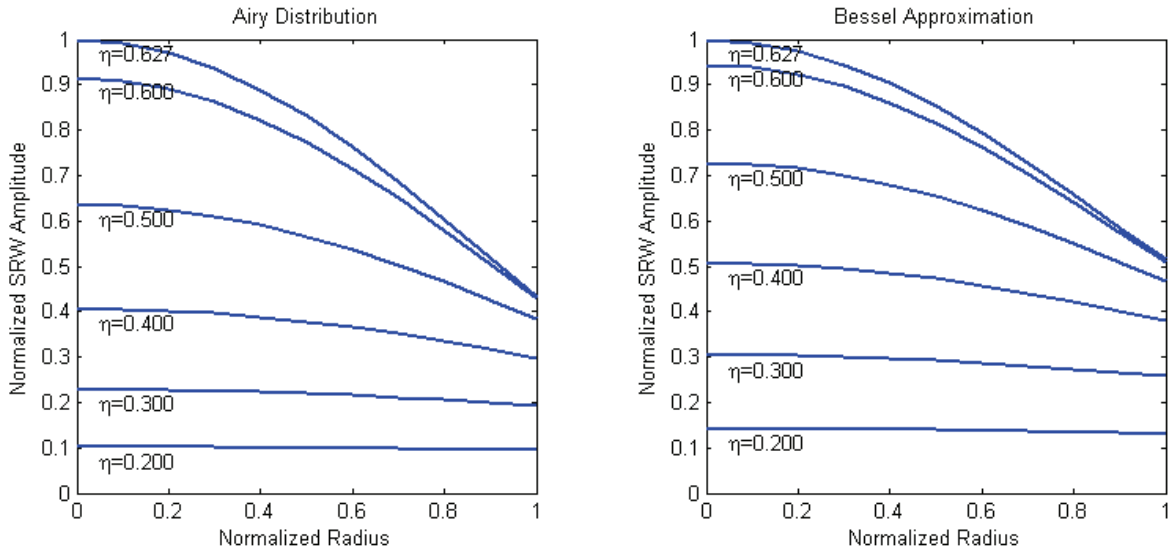
Figure 5.3: Normalized SRW amplitude over the radius in the sensor plane for different ratios η of the Airy diameter in the focus plane and the filter dot diameter. Left: Approximation with an Airy distribution in the sensor plane. Right: Approximation with Bessel functions [GLU01].

Both Glückstad [GLU01] and Anderson [AND95] suggested a filter dot size of $\eta = 0.4$ as a good compromise between a sufficiently constant SRW over the aperture and sufficient power of the SRW.

5.1.1.3   Visibility of the Interference Fringes

An important issue for the performance of interferometers in atmospheric applications is the visibility of the interference fringes, i.e. the contrast of the fringes. The visibility was studied by Anderson [AND95] in the context of CPIs. The basic formula for the visibility is

$$V = \frac{I_{max} - I_{min}}{I_{max} + I_{min}}, \tag{5.25}$$

where I_{max} and I_{min} give the maximum and minimum of the interferometer intensity as a function of the phase φ. Taking the output of a Henning CPI from Eq. (5.15), the visibility calculates to

$$V = \frac{2\left|g_{in}\left(\vec{r}\right)\right|\left|g_0\right|}{\left|g_{in}\left(\vec{r}\right)\right|^2 + \left|g_0\right|^2}. \tag{5.26}$$

The maximum intensity of the interference term is

$$I_{max} = \left|g_{in}\left(\vec{r}\right)\right|\left|g_0\right|. \tag{5.27}$$

Two effects influence the visibility and the maximum intensity: The intensity $\left|g_{in}\left(\vec{r}\right)\right|$ at a certain position, which is a consequence of scintillation on the atmospheric path, and the intensity $\left|g_0\right|$ at the filter dot, which is mainly influenced by phase distortions and determines the strength of the SRW. The tip-tilt error of the incident phase has an especially strong impact on the filter dot intensity, as it moves the focus spot off the filter dot or pin hole in a PDI.

In both cases, if the received intensity at a certain position or the filter-dot intensity tend towards zero, the visibility and the maximum intensity I_{max} also decrease towards zero. Low visibility or low maximum intensity implicate that the quantization noise of the sensors increases, as fewer bits of the sensor's dynamic range are used for the analogue to digital conversion, and the effect of sensor noise increases.

Another factor influencing the fringe visibility is the transmit laser's degree of coherence and the optical path difference of the interferometer arms. Extending the basic self-referencing interferometer Eq. (5.36) with the degree of coherence [BOR99, p.564] gives

$$I\left(x, y\right) = I_R + I_0\left(x, y\right) + 2\sqrt{I_R I_0\left(x, y\right)} \cdot \left|\gamma_{12}\right| \cos\left(\varphi\left(x, y\right) + \theta\right), \tag{5.28}$$

where $\left|\gamma_{12}\right|$ is the modulus of the complex degree of coherence, which includes in the interferometer setup the optical path difference, i.e. $\left|\gamma_{12}\left(s_2 - s_1\right)\right|$ with the optical path lengths s_2, s_1 of the interferometer arms. Since $\left|\gamma_{12}\right| \leq 1$, it can be seen that a reduced coherence decreases the fringe visibility and thus affects the quality of the reconstructed phase.

Also the degree of polarization of the incoming wave could be an issue for the phase reconstruction, however to a negligible degree for self-referencing interferometers, which will have the same polarization for the object and the reference wave independent of the incoming wave; in addition, Toyoshima et al. [TOY09] could show in experiments with OICETS, that the effect of depolarization in SGL scenarios due to the atmosphere is rather week guaranteeing a degree of polarization of around 99% even for low elevation angles.

5.1.1.4 Graphical Method for the Evaluation of CPIs

Glückstad [GLU98] developed a graphical method to evaluate the properties of different CPI setups. Slightly modifying Eq. (5.9) gives

$$I(\vec{r}) = \beta^2 \left\| g_{in}(\vec{r}) \left| e^{i\tilde{\varphi}(\vec{r})} - \left| g_0 \right| \left(1 - \gamma\beta^{-1}e^{i\theta}\right) \right\|^2, \tag{5.29}$$

forming the basis for the graphical method.

Figure 5.4 shows the positive Zernike phase contrast method (see Section 5.1.1.1) in the graphical representation. The filter-dot parameters are $\theta = \pi/2, \beta = 1, \gamma = 1$, and Eq. (5.29) reduces to

$$I(\vec{r}) = \left| e^{i\tilde{\varphi}(\vec{r})} - \left| g_0 \right| \left(1 - e^{i\theta}\right) \right|^2, \tag{5.30}$$

assuming a constant input amplitude $\left| g_{in}(\vec{r}) \right| = 1$. Both terms in the difference of Eq. (5.30), $e^{i\tilde{\varphi}(\vec{r})}$ and $\left| g_0 \right| \left(1 - \gamma\beta^{-1}e^{i\theta}\right)$ are shown in the graph of the complex plane. The real part is applied on the horizontal and the imaginary part on the vertical axis. The left circle around the origin shows $e^{i\tilde{\varphi}}$, i.e. is dependent on the sought phase, and the circles on the right show $\left| g_0 \right| \left(1 - e^{i\theta}\right)$, i.e. circles around $\left| g_0 \right|$, which is the amplitude at the filter dot. Originating now at $\left| g_0 \right| \left(1 - e^{i\theta}\right)$ the difference between the two terms is indicated by an intensity axis (red arrow), which crosses the left circle at $e^{i\tilde{\varphi}}$. The square relationship of the distance and the intensity is indicated with the axis below the graph. This illustrates nicely the relation between the phase and the intensity, and the linear regions can be estimated. An unique relation can be achieved for $-\frac{1}{4}\pi < \varphi < \frac{3}{4}\pi$, which matches with Figure 5.2.
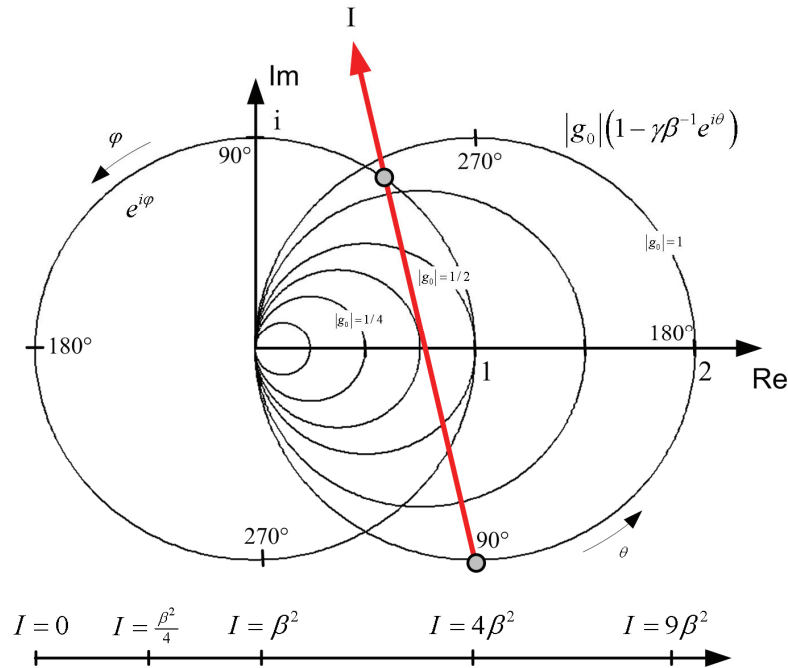
Figure 5.4: Graphical representation of the positive Zernike phase contrast ($\theta = \pi/2, \beta = 1, \gamma = 1$).

Figure 5.5 shows the graph for the Henning phase contrast method ($\theta = \pi/4, \beta = 1/\sqrt{2}, \gamma = 1$), assuming $\left|g_{in}(\vec{r})\right| = \left|g_0\right| = 1$. Under these conditions there is an unique mapping between phase φ and intensity for $-\frac{1}{2}\pi < \varphi < \frac{1}{2}\pi$, which is confirmed by Figure 5.2; however, for an optimum operation this scheme would require the amplitudes $\left|g_{in}(\vec{r})\right|$ and $\left|g_0\right|$ to be controlled.

More examples for the graphical evaluation method of CPI variations can be found in [GLU98] and [GLU01].
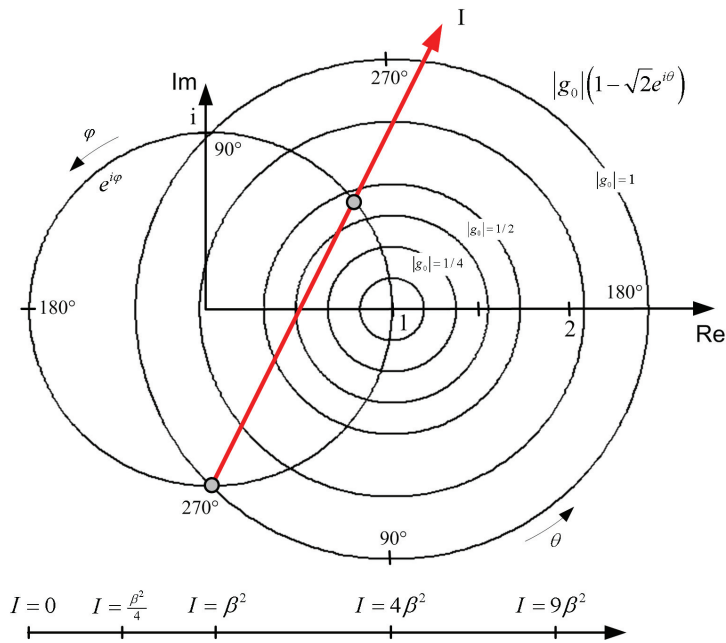
Figure 5.5: Graphical representation of the Henning phase contrast method ($\theta = \pi/4, \beta = 1/\sqrt{2}, \gamma = 1$).

5.1.2 Point Diffraction Interferometer (Non-Common Path)

Common-path interferometer (CPI) and point diffraction interferometer (PDI) have very similar properties and can be described with the same methodologies. In particular the description of the synthetic reference wave (SRW) as shown in Section 5.1.1.2 is equal for CPIs and PDIs. The principle setup of a PDI is shown in Figure 5.6.
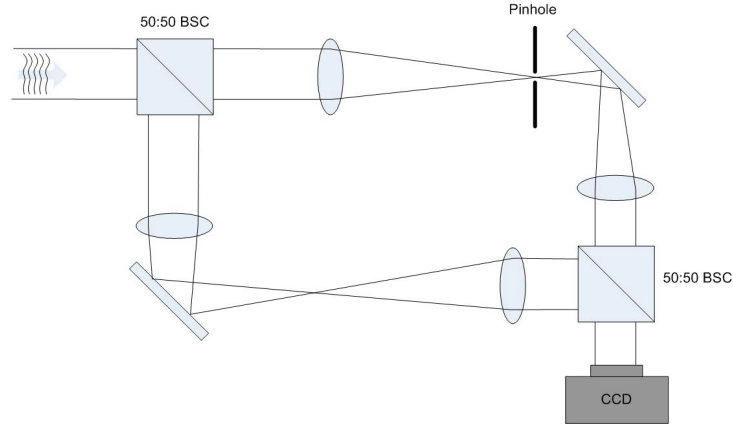
Figure 5.6: Point-diffraction interferometer in a Mach-Zehnder configuration. The SRW is generated by a pin hole in a Fourier plane.

The incoming field distribution at the entrance pupil is given by

$$U_0(x,y) = |U_0(x,y)| \cdot e^{i\varphi(x,y)}, \tag{5.31}$$

and the reference wave is described for simplicity as a plane wave, which is shifted by a phase value of θ

$$U_R = |U_R| \cdot e^{-i\theta} \tag{5.32}$$

The intensity in the camera plane is then given by

$$\begin{aligned}
I(x,y) &= |U_R + U_0(x,y)|^2 \\
&= I_R + I_0(x,y) + 2\sqrt{I_R I_0(x,y)} \cos(\varphi(x,y)+\theta)
\end{aligned}, \tag{5.33}$$

where $I_R = U_R \cdot U_R^* = |U_R|^2$ and $I_0 = U_0 \cdot U_0^* = |U_0|^2$. The phase shift θ in a PDI configuration is unknown, as it is determined by the path length of the two interferometer arms. In a CPI this path difference is known, as it is determined by the filter-dot phase shift. Apart from the filter dot, both waves otherwise have the same path in a CPI.

   If the first beam splitter in the PDI is substituted by a polarizing beam-splitter, reference wave and object wave attain perpendicular polarizations. This is an interesting feature for the instantaneous phase-shifting interferometers, as they are discussed in Section 5.3.2. Both the designs by Sivakumar (Section 5.3.2.1) and Notaras (Section 5.3.2.2) require perpendicularly polarized reference and object waves.

5.2 Phase-Shifting Interferometry

Common-path and point-diffraction interferometers in a Zernike phase contrast configuration are direct wavefront sensors requiring no phase reconstruction step, and they have a very favorable ratio between measurement and phase points. In this sense they are of interest for the application in SGL scenarios, where high speed is required; however, their results are only valid for very small phase distortions. Apart from the ambiguous relationship between the phase and the intensity for larger phase distortions, the amplitude distribution of the incoming wave and the strength of the SRW are unknown and change the results.

Phase-shifting interferometers (PSI) offer a solution to overcome these limitations, measuring the interference fringes for different phase shifts θ_j of the reference wave against the object wave. These methods are usually classified by the number of phase shifts they use to calculate the phase. Phase shifts can be generated in a sequential fashion for example by a moving mirror, which is commonly known by the term temporal phase shifting. A piezo-electric actuator might drive the mirror. Or phase shifts are created by optical elements in different optical arms, which is often called geometrical or spatial phase shifting. An overview of spatial and temporal phase-shifting methods is given for example in [MAL07].

If the created interferograms with different phase shifts are recorded synchronously, this is referred to by the term instantaneous phase-shifting interferometry, as in one instant a sufficient number of interferograms, each with a certain phase shift θ_j, is detected on the (synchronized) sensor chips (or only one sensor chip) to unambiguously calculate the incoming phase. Instantaneous PSI methods are usually less sensitive to vibrations and are faster, as they require only one sampling period instead of several as for the sequential methods. Optical designs of instantaneous PSI methods are presented in Section 5.3.2.

Section 5.2.1 introduces the basic principles of PSIs and presents some of the common algorithms. Section 5.2.2 discusses evaluation methods to optimize PSI algorithms for the application scenario. Section 5.2.3 analyzes error sources in PSIs and their effects on different algorithms. Special attention will be given to vibration and noise effects. The systems are intended to work under difficult environmental conditions and possibly with vibrations from a telescope mount. Noise effects are important, as low-light levels are expected to occur due to atmospheric scintillation. The used cameras for the infrared (InGaAs) have very poor performance in terms of detector noise, but they have a good sensitivity in the required wavelength range.

5.2.1 Algorithms of Phase-Shifting Interferometry

Introductions to PSI can be found for example in [MAL07], which also gives an extensive listing of different PSI algorithms. An earlier overview was given by Creath [CRE88].

The incoming field distribution at the entrance pupil is given by

$$U_0(x,y) = |U_0(x,y)| \cdot e^{i\varphi(x,y)}, \tag{5.34}$$

and the reference wave, possibly generated with the methods introduced in Section 5.1.1.2, is described for simplicity as a plane wave, which is delayed by a phase value of θ_j

$$U_R = |U_R| \cdot e^{-i\theta_j}. \tag{5.35}$$

$|U_0|$ and $|U_R|$ denote the amplitudes of the object and reference wave. The intensity in the camera plane is then given by

$$\begin{aligned} I(x,y) &= |U_R + U_0(x,y)|^2 \\ &= I_R + I_0(x,y) + 2\sqrt{I_R I_0(x,y)} \cos\left(\varphi(x,y) + \theta_j\right) \end{aligned}, \tag{5.36}$$

where $I_R = U_R \cdot U_R^* = |U_R|^2$ and $I_0 = U_0 \cdot U_0^* = |U_0|^2$. Distributions over the telescope aperture are indicated with the coordinate dependence (x,y), in contrast to the (spatially) constant reference wave. Eq. (5.36) shows, that there are basically three unknowns, an offset component $I_R + I_0(x,y)$, a fringe modulation component (or contrast) $2\sqrt{I_R I_0(x,y)}$, and of course the sought phase $\varphi(x,y)$. This assumes that the phase shifts θ_j are well known.

Deviations from the nominal phase shifts introduce so-called phase-shift errors. This is discussed in more detail in Section 5.2.3.1.

As there are three unknowns, at least three phase steps are required to obtain the sought wavefront phase. An example for a three-step PSI algorithm is given by Wyant et al. [WYA84] with the steps $\theta_j = \frac{1}{4}\pi, \frac{3}{4}\pi, \frac{5}{4}\pi$. For the given phase steps the three interferometer equations based on (5.36) are

$$
\begin{aligned}
I_1 &= I_R + I_0 + 2\sqrt{I_R I_0} \, \cos\left(\varphi + \tfrac{1}{4}\pi\right) \\
I_2 &= I_R + I_0 + 2\sqrt{I_R I_0} \, \cos\left(\varphi + \tfrac{3}{4}\pi\right) \\
I_3 &= I_R + I_0 + 2\sqrt{I_R I_0} \, \cos\left(\varphi + \tfrac{5}{4}\pi\right)
\end{aligned}
\tag{5.37}
$$

The coordinates (x,y) with the object-wave intensity and the phase were omitted for clarity. The phase can then be calculated by

$$
\varphi = \arctan_2\left(I_3 - I_2, I_1 - I_2\right),
\tag{5.38}
$$

where $\arctan_2$ is the two-variable version of the arctangent to get the phase over the full 2π circle. Eq. (5.38) is derived by using the trigonometric relation $\cos(\alpha \pm \beta) = \cos\alpha \cos\beta \mp \sin\alpha \sin\beta$:

$$
\frac{I_3 - I_2}{I_1 - I_2} = \frac{\cos\left(\varphi + \tfrac{5}{4}\pi\right) - \cos\left(\varphi + \tfrac{3}{4}\pi\right)}{\cos\left(\varphi + \tfrac{1}{4}\pi\right) - \cos\left(\varphi + \tfrac{3}{4}\pi\right)} = \frac{\sin\varphi}{\cos\varphi},
\tag{5.39}
$$

A generalized symmetric three-step method was suggested by Creath [CRE88][MAL07] with the phase steps $\theta_j = -\triangle, 0, +\triangle$.

$$
\begin{aligned}
I_1 &= I_R + I_0 + 2\sqrt{I_R I_0} \, \cos\left(\varphi - \triangle\right) \\
I_2 &= I_R + I_0 + 2\sqrt{I_R I_0} \, \cos\left(\varphi\right) \\
I_3 &= I_R + I_0 + 2\sqrt{I_R I_0} \, \cos\left(\varphi + \triangle\right)
\end{aligned}
\tag{5.40}
$$

The phase is then calculated by

$$
\varphi(x, y) = \arctan\left(\frac{1 - \cos\triangle}{\sin\triangle} \cdot \frac{I_1 - I_3}{2I_2 - I_1 - I_3}\right).
\tag{5.41}
$$

The interferograms modulation $2\sqrt{I_R I_0}$ is given by

$$
2\sqrt{I_R I_0} = \frac{\sqrt{\left[\left(I_1 - I_3\right)\left(1 - \cos\triangle\right)\right]^2 + \left[\left(2I_2 - I_1 - I_3\right)\sin\triangle\right]^2}}{2\left(1 - \cos\triangle\right)\sin\triangle}
\tag{5.42}
$$

and the offset term by

$$
I_R + I_0 = \frac{I_1 + I_3 - 2I_2 \cos\triangle}{2\left(1 - \cos\triangle\right)}.
\tag{5.43}
$$

The ratio $\dfrac{2\sqrt{I_R I_0}}{I_R + I_0}$ represents a convenient value to assess the modulation depth and thus to identify data points with insufficient modulation, which appear in areas with low object-beam intensities due to atmospheric scintillation or during a drop of the SRW strength.

This method can be nicely applied to the instantaneous PSI methods discussed in Section 5.3.2, where the phase shift is $\vartriangle = \pi / 2$. With this Eq. (5.40) and (5.41) simplify to

$$I_1 = I_R + I_0 + 2\sqrt{I_R I_0}\,\sin\varphi$$
$$I_2 = I_R + I_0 + 2\sqrt{I_R I_0}\,\cos\varphi \tag{5.44}$$
$$I_3 = I_R + I_0 - 2\sqrt{I_R I_0}\,\sin\varphi$$

and

$$\varphi(x,y) = \arctan\left(\frac{I_1 - I_3}{2I_2 - I_1 - I_3}\right). \tag{5.45}$$

Eq. (5.42) and (5.43) simplify to

$$2\sqrt{I_R I_0} = \tfrac{1}{2}\sqrt{\left(I_1 - I_3\right)^2 + \left(2I_2 - I_1 - I_3\right)^2} \tag{5.46}$$

and

$$I_R + I_0 = \frac{I_1 + I_3}{2}. \tag{5.47}$$

The ratio $\dfrac{2\sqrt{I_R I_0}}{I_R + I_0}$ then becomes

$$\frac{2\sqrt{I_R I_0}}{I_R + I_0} = \frac{\sqrt{\left(I_1 - I_3\right)^2 + \left(2I_2 - I_1 - I_3\right)^2}}{I_1 + I_3}. \tag{5.48}$$

Similar equations can be produced for four-step algorithms with the phase shifts $\theta_j = 0, \tfrac{1}{2}\pi, \pi, \tfrac{3}{2}\pi$. The intensities of the four interferometers are

$$I_1 = I_R + I_0 + 2\sqrt{I_R I_0}\,\cos\left(\varphi\right)$$
$$I_2 = I_R + I_0 + 2\sqrt{I_R I_0}\,\cos\left(\varphi + \tfrac{1}{2}\pi\right) = I_R + I_0 - 2\sqrt{I_R I_0}\,\sin\left(\varphi\right)$$
$$I_3 = I_R + I_0 + 2\sqrt{I_R I_0}\,\cos\left(\varphi + \pi\right) = I_R + I_0 - 2\sqrt{I_R I_0}\,\cos\left(\varphi\right) \tag{5.49}$$
$$I_4 = I_R + I_0 + 2\sqrt{I_R I_0}\,\cos\left(\varphi + \tfrac{3}{2}\pi\right) = I_R + I_0 + 2\sqrt{I_R I_0}\,\sin\left(\varphi\right)$$

and the phase is calculated by

$$\varphi = \arctan_2\left(I_2 - I_4, I_3 - I_1\right). \tag{5.50}$$

The presented methods measure the interferograms at discrete phase steps. This can be slightly modified to an integrating-bucket technique [e.g. CRE88]. Here the relative phase between the reference and object beam is varied at a constant rate rather than in discrete steps. This has advantages especially for the mechanical adjustment of the relative phase and can increase the measurement speed for temporal PSI methods. Main focus of this thesis however will be on geometrical and especially instantaneous PSI algorithms.

Figure 5.7 shows the simulation of a three-step interferometer on an input field of an SGL scenario at 10 degrees elevation. Phase singularities in the field are correctly displayed by the phase reconstruction based on Eq. (5.38). For this example the input amplitude was set to a constant value, which allows seeing the phase structures in the individual interferograms. Figure 5.8 shows the interferograms for the same scenario but with scintillation in the input amplitude. The separate interferograms mainly show the amplitude distribution of the input field, and the required dynamic range for the interferograms is significantly increased. This has to be taken into account for the specification of the camera sensors.
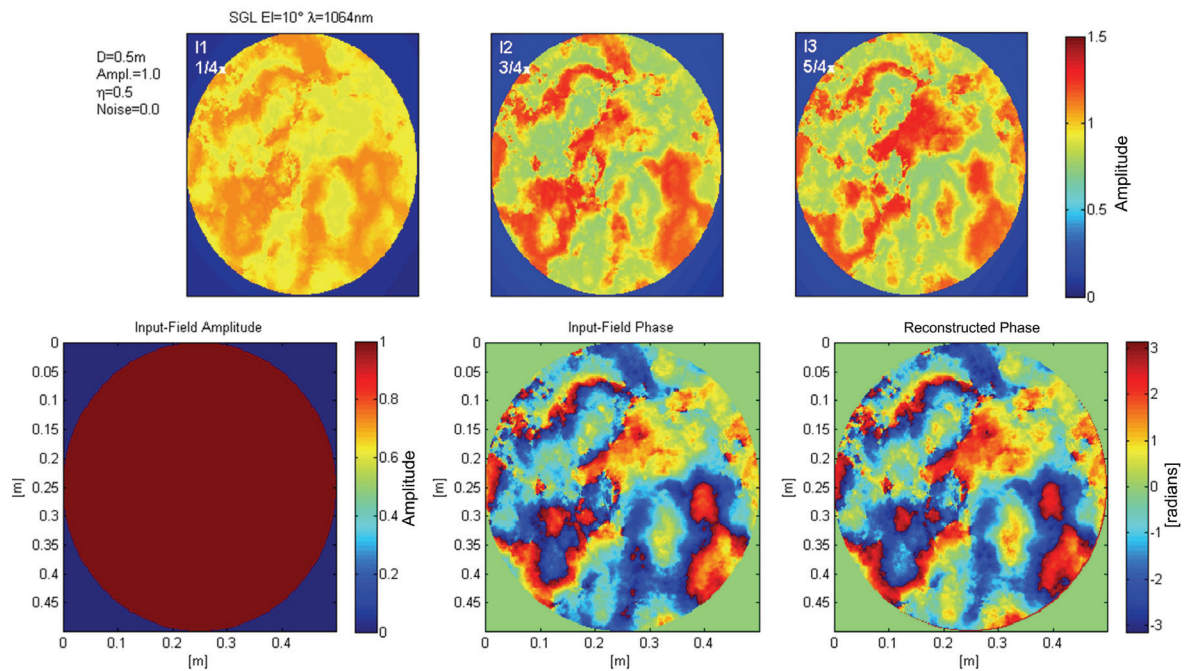
Figure 5.7: Simulation of a three-step interferometer: The upper row shows the three interferograms *I1-I3* taken for the phase steps $\theta_j = \frac{1}{4}\pi, \frac{3}{4}\pi, \frac{5}{4}\pi$ **; The lower row shows the input-field amplitude/phase and the estimated phase calculated from the images *I1-I3* by Eq. (5.38). The input field is a simulated phase distribution for an SGL scenario at 10 degrees elevation. The input phase distribution contains a large number of singularities, which are correctly reproduced from the PSI. The input amplitude is set to a constant value to make the phase structures in the separate interferograms visible.**
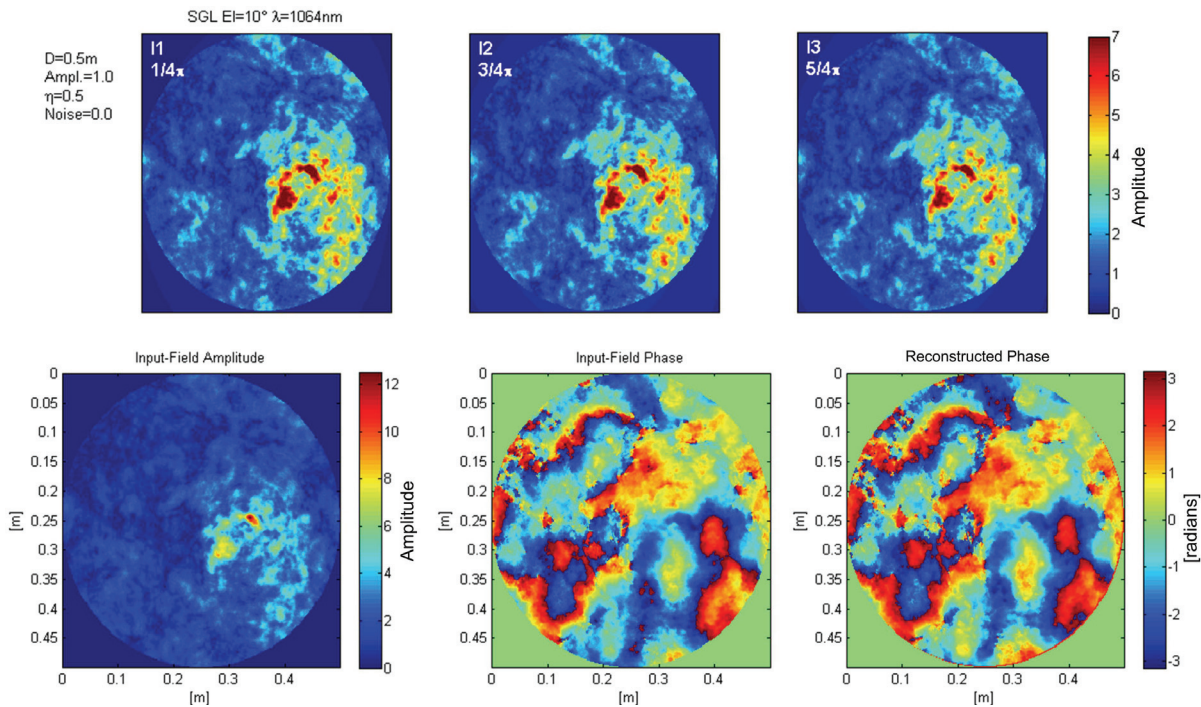
Figure 5.8: Same plot as Figure 5.7, only now with a varying input-amplitude distribution. The separate interferograms now show mainly the amplitude distribution of the input field. The reconstruction result is the same, however, the required sensor dynamics is significantly increased.

Table 5.1 summarizes common 3, 4, and 5 step phase-shifting algorithms discussed in the literature. The behavior of these algorithms to various error sources will be discussed in Section 5.2.2 and 5.2.3. The table was limited to up to 5 steps, as one of the main requirements of the discussed scenario is the speed increase and the complexity reduction of the AO system. A larger number of phase measurements comes with more complex algorithms, a higher number of sensor pixels, and therefore with a lower overall speed.

Chapter 5: Interferometric Wavefront Sensors in Strong Turbulence

Table 5.1: Overview of 3-5 step algorithms [MAL07]. The filter functions F_1, F_2 and the characteristic polynomials $P(x)$ are explained in Section 5.2.2.

#	N	$\tan\varphi =$	Phase Steps	Filter Functions F_1, F_2 and Characteristic Polynomial $P(x)$	Reference
1.	3	$\dfrac{I_1 - 2I_2 + I_3}{I_1 - I_3}$	$\theta_j = (j-1)\dfrac{\pi}{2}$	$F_1(\nu) = -4\sin^2\left(\dfrac{\pi}{4}\dfrac{\nu}{\nu_f}\right)\exp\left(-i\dfrac{\pi}{2}\dfrac{\nu}{\nu_f}\right)$ $F_2(\nu) = 4i\sin\left(\dfrac{\pi}{4}\dfrac{\nu}{\nu_f}\right)\cos\left(\dfrac{\pi}{4}\dfrac{\nu}{\nu_f}\right)\exp\left(-i\dfrac{\pi}{2}\dfrac{\nu}{\nu_f}\right)$ $P(z) = (-1+i)z^2 - 2iz + (1+i) = (-1+i)(z-1)(z+i)$	Wyant [WYA84]
2.	3	$\dfrac{\sqrt{3}(I_2 - I_3)}{-2I_1 + I_2 + I_3}$	$\theta_j = (j-1)\dfrac{2\pi}{3}$	$F_1(\nu) = 2i\sqrt{3}\sin\left(\dfrac{\pi}{3}\dfrac{\nu}{\nu_f}\right)\exp\left(-i\pi\dfrac{\nu}{\nu_f}\right)$ $F_2(\nu) = -2 + 2\cos\left(\dfrac{\pi}{3}\dfrac{\nu}{\nu_f}\right)\exp\left(-i\pi\dfrac{\nu}{\nu_f}\right)$ $P(z) = (1-\sqrt{3}i)z^2 + (1+\sqrt{3}i)z - 2 = (1-\sqrt{3}i)(z-1)\left[z+\left(0.5+\tfrac{\sqrt{3}}{2}i\right)\right]$	Bruning [BRU74]
3.	4	$\dfrac{I_2 - I_4}{I_3 - I_1}$	$\theta_j = (j-1)\dfrac{\pi}{2}$	$F_1(\nu) = -2i\sin\left(\dfrac{\pi}{2}\dfrac{\nu}{\nu_f}\right)\exp\left(-i\pi\dfrac{\nu}{\nu_f}\right)$ $F_2(\nu) = 2i\sin\left(\dfrac{\pi}{2}\dfrac{\nu}{\nu_f}\right)\exp\left(-i\dfrac{\pi}{2}\dfrac{\nu}{\nu_f}\right)$ $P(z) = -iz^3 + z^2 + iz - 1 = -i(z-1)(z+1)(z+i)$	Bruning [BRU74]
4.	4	$\dfrac{\sqrt{3}(I_2 - I_3)}{-I_1 + I_2 + I_3 - I_4}$	$\theta_j = (j-1)\dfrac{2\pi}{3}$	$F_1(\nu) = 2i\sqrt{3}\sin\left(\dfrac{2\pi}{3}\dfrac{\nu}{\nu_f}\right)\exp\left(-i2\pi\dfrac{\nu}{\nu_f}\right)$	Larkin and Oreb [LAR92]

#	Reference	Equations	θ_j	N	$\tan\varphi$
		$F_2(\nu)=-4\sin\left(\dfrac{2\pi}{3}\dfrac{\nu}{\nu_f}\right)\sin\left(\dfrac{4\pi}{3}\dfrac{\nu}{\nu_f}\right)\exp\left(-i2\pi\dfrac{\nu}{\nu_f}\right)$ $P(z)=-z^3+(1-\sqrt{3}i)z^2+(1+\sqrt{3}i)z-1$ $=-(z-1)\left[z-\left(0.5-\tfrac{\sqrt{3}}{2}i\right)\right]\left[z-\left(-0.5-\tfrac{\sqrt{3}}{2}i\right)\right]$			
5.	Surrel [SUR93]	$F_1(\nu)=2i\left[\sin\left(2\pi\dfrac{\nu}{\nu_f}\right)-3\sin\left(\dfrac{2\pi}{3}\dfrac{\nu}{\nu_f}\right)\right]\exp\left(-i2\pi\dfrac{\nu}{\nu_f}\right)$ $F_2(\nu)=-4\sqrt{3}\sin\left(\dfrac{2\pi}{3}\dfrac{\nu}{\nu_f}\right)\sin\left(\dfrac{4\pi}{3}\dfrac{\nu}{\nu_f}\right)\exp\left(-i2\pi\dfrac{\nu}{\nu_f}\right)$ $P(z)=(\sqrt{3}-i)z^3+(-\sqrt{3}+3i)z^2+(-\sqrt{3}-3i)z+(\sqrt{3}+i)$ $=(\sqrt{3}-i)(z-1)^2\left[z-\left(-0.5-\tfrac{\sqrt{3}}{2}i\right)\right]$	$\theta_j=(j-1)\dfrac{2\pi}{3}$	4	$\dfrac{I_1-3I_2+3I_3-I_4}{\sqrt{3}\left(I_1-I_2-I_3+I_4\right)}$
6.	Schwider [SCH93]	$F_1(\nu)=1-3e^{-i\frac{\pi\,\nu}{2\nu_f}}+2e^{-i\frac{5\pi\,\nu}{4\nu_f}}\cos\left(\dfrac{\pi}{4}\dfrac{\nu}{\nu_f}\right)$ $F_2(\nu)=1+e^{-i\frac{\pi\,\nu}{2\nu_f}}-3e^{-i\pi\frac{\nu}{\nu_f}}+e^{-i\frac{3\pi\,\nu}{2\nu_f}}$ $P(z)=(1+i)z^3+(-3+i)z^2+(1-3i)z+(1+i)=(1+i)(z-1)(z+i)^2$	$\theta_j=(j-1)\dfrac{\pi}{2}$	4	$\dfrac{I_1-3I_2+I_3+I_4}{I_1+I_2-3I_3+I_4}$
7.	Schmit, Creath [SCH95]	$F_1(\nu)=2i\left[\sin\left(\pi\dfrac{\nu}{\nu_f}\right)-4\sin\left(\dfrac{\pi}{2}\dfrac{\nu}{\nu_f}\right)\right]e^{-i\pi\frac{\nu}{\nu_f}}$ $F_2(\nu)=2\left[2\cos\left(\pi\dfrac{\nu}{\nu_f}\right)+2\cos\left(\dfrac{\pi}{2}\dfrac{\nu}{\nu_f}\right)-3\right]e^{-i\pi\frac{\nu}{\nu_f}}$	$\theta_j=(j-1)\dfrac{\pi}{2}$	5	$\dfrac{I_1-4I_2+4I_4-I_5}{I_1+2I_2-6I_3+2I_4+I_5}$

		$P(z) = (1-i)z^4 + (2+4i)z^3 - 6z^2 + (2-4i)z + (1+i)$ $= (1-i)(z-1)(z+i)^3$	
8.	5	$\dfrac{-2I_2 + 2I_4}{I_1 - 2I_3 + I_5}$	$\theta_j = (j-1)\dfrac{\pi}{2}$	$F_1(\nu) = -4i\sin\left(\dfrac{\pi}{2}\dfrac{\nu}{v_f}\right)e^{-i\pi\frac{\nu}{v_f}}$ $F_2(\nu) = 2\left[\cos\left(\pi\dfrac{\nu}{v_f}\right)-1\right]e^{-i\pi\frac{\nu}{v_f}}$ $P(z) = z^4 + 2iz^3 - 2z^2 - 2iz + 1 = (z-1)(z+1)(z+i)^2$	Schwider [SCH83]

5.2.2 Evaluation of PSI Algorithms

Two powerful analytical techniques are introduced in this section to evaluate the performance of different PSI algorithms. Freischlad and Koliopoulos [FRE90] used a Fourier method, which describes the phase retrieval step as a filtering process in the frequency domain. The second technique presented here is the evaluation of the PSI methods based on the characteristic polynomial as suggested by Surrel [SUR96].

5.2.2.1 Fourier Method

Freischlad assumed for the Fourier method that the introduced phase shift linearly increases with time, i.e. a phase shift of $\theta = 2\pi v_s t$. With this the measured intensity on a (linear) sensor is modulated in a sinusoidal fashion and is given by

$$I(t) = I_R + I_0 + 2\sqrt{I_R I_0}\,\cos\left(\varphi + 2\pi v_s t\right). \tag{5.51}$$

φ denotes the sought phase. The dependence of the spatial coordinates is omitted in this section. Taking for example the PSI algorithm of Brunning [BRU74] (Algorithm #3 in Table 5.1), the phase φ is obtained by

$$\varphi = \arctan_2\left(\frac{I_2 - I_4}{I_3 - I_1}\right) = \arctan_2\left(\frac{I\left(\frac{T_s}{4}\right) - I\left(\frac{3T_s}{4}\right)}{I(0) - I\left(\frac{T_s}{2}\right)}\right). \tag{5.52}$$

The period T_s is given by $T_s = \dfrac{1}{v_s}$, where v_s is the modulation frequency of the phase shift. In general the phase reconstruction can be described by a correlation of the modulated intensity with two filter functions f_i so that

$$c_i = \int_{-\infty}^{\infty} I(\tau) f_i(\tau)\,d\tau, \qquad i = 1, 2 \tag{5.53}$$

which is the correlation at $t = 0$. This is equivalent to a heterodyne phase measurement, where the signal is mixed with two sinusoidal signals 90 degrees out of phase. Using Parseval's theorem

$$\int_{-\infty}^{\infty} f(x) g^*(x)\,dx = \int_{-\infty}^{\infty} F(v) G^*(v)\,dv, \tag{5.54}$$

noting that the intensity and the filter functions are real functions, and taking the symmetry properties of real functions in the Fourier domain (see Appendix A.1.3) into account, the correlation can be written in the Fourier domain by

$$c_i = 2\,\mathrm{Re}\left\{\int_0^{\infty} I_F(v) F_i^*(v)\,dv\right\}. \qquad i = 1, 2 \tag{5.55}$$

Here $I_F(v)$ denotes the Fourier transform of $I(t)$ and v the frequency. From this it can be seen that the functions F_i filter or transmit certain frequencies.

So far only purely sinusoidal signals as in Eq. (5.51) have been considered. To consider higher harmonics of the signal, i.e. disturbances, the signal can be expanded in a discrete Fourier transform assuming a periodic signal

$$I(t) = \sum_{m=0}^{\infty} s_m \cos\left(2\pi m \nu_s t\right),$$ (5.56)

where s_m are the complex coefficients of the decomposition. The Fourier transform of $\cos\left(2\pi m \nu_s t + \varphi_m\right)$ is given by

$$\cos\left(2\pi m \nu_s t + \varphi_m\right) \rightarrow \frac{1}{2}\left[\delta\left(\nu + m\nu_s\right) + \delta\left(\nu - m\nu_s\right)\right]e^{i\varphi_m}.$$ (5.57)

As the signal is periodic, formed of cosine functions based on the frequency ν_s, the Fourier transform becomes a series of Dirac impulses

$$I_F(\nu) = 2\sum_{n=-\infty}^{\infty} s_n \delta\left(\nu - n\nu_s\right).$$ (5.58)

The phase values φ_m of each harmonic are now contained in the coefficients s_n. The sought phase is contained in s_1. To determine the phase of the input signal the ratio of the two correlations in Eq. (5.55) is formed

$$r = \frac{c_1}{c_2} = \frac{s_0 F_1(0) + 2\,\mathrm{Re}\left\{\sum_{m=1}^{\infty} s_m F_1^*\left(m\nu_s\right)\right\}}{s_0 F_2(0) + 2\,\mathrm{Re}\left\{\sum_{m=1}^{\infty} s_m F_2^*\left(m\nu_s\right)\right\}}.$$ (5.59)

If the two Fourier filters are 90 degrees out of phase for the sought (signal) frequency (m=1), i.e.

$$F_1(\nu_s) = iF_2(\nu_s),$$ (5.60)

then the phase can be obtained by the arc tangent of the ratio r

$$\varphi_m = \arctan(r) + const.$$ (5.61)

The modified arctan (arctan$_2$) should be used to obtain the full 2π circle.

As an example Schwider's algorithm with N=4 (Table 5.1, #6) is evaluated in more detail. The algorithm is given by

$$\varphi = \arctan\left(\frac{I_1 - 3I_2 + I_3 + I_4}{I_1 + I_2 - 3I_3 + I_4}\right) = \arctan\left(\frac{I(0) - 3I\left(\frac{T_s}{4}\right) + I\left(\frac{2T_s}{4}\right) + I\left(\frac{3T_s}{4}\right)}{I(0) + I\left(\frac{T_s}{4}\right) - 3I\left(\frac{2T_s}{4}\right) + I\left(\frac{3T_s}{4}\right)}\right).$$ (5.62)

The according filter functions in the spatial domain are

$$f_1(t) = \delta(t) - 3\delta\left(t - \tfrac{T_f}{4}\right) + \delta\left(t - \tfrac{2T_f}{4}\right) + \delta\left(t - \tfrac{3T_f}{4}\right)$$

$$f_2(t) = \delta(t) + \delta\left(t - \tfrac{T_f}{4}\right) - 3\delta\left(t - \tfrac{2T_f}{4}\right) + \delta\left(t - \tfrac{3T_f}{4}\right)$$

(5.63)

The filter functions are based on the period $T_f = \dfrac{1}{v_f}$, indicating the possible discrepancy between the signal period T_s and the filter period T_f. The Fourier transforms of the Eq. (5.63) are given by

$$F_1(v) = 1 - 3e^{-i\frac{\pi\, v}{2\, v_f}} + 2e^{-i\frac{5\pi\, v}{4\, v_f}} \cos\left(\frac{\pi\, v}{4\, v_f}\right).$$

$$F_2(v) = 1 + e^{-i\frac{\pi\, v}{2\, v_f}} - 3e^{-i\pi\frac{v}{v_f}} + e^{-i\frac{3\pi\, v}{2\, v_f}}$$

(5.64)

Putting Equations (5.64) into (5.59) for $v = v_s = v_f$ with a purely sinusoidal signal (5.51), it is easy to verify Eq. (5.60) and to derive the expected result

$$r = \frac{\sin\varphi}{\cos\varphi}.$$

(5.65)

Figure 5.9 and Figure 5.10 show the filter functions in the Fourier domain for the PSI algorithms presented in Table 5.1. Two interesting properties of the algorithms can be evaluated from the graphs, robustness to signal harmonics ($m>1$) and to phase-shifting errors $(v_s \neq v_f)$.

An algorithm is insensitive to a harmonic component of the signal ($m>1$), if both F_1 and F_2 are zero at the frequency mv_s with $m = 2, 3, 4 \ldots$. Harmonics in the signal appear for example due to a nonlinear behaviour of the detector. Among the shown algorithms such zeros can only be observed for the algorithms #3 (Bruning 1974, $N=4$) and #8 (Schwider 1983, $N=5$), both for the second harmonics ($m=2$). Algorithms with more samples can suppress a number of harmonics; however, in the context of the SGL scenarios and their bandwidth requirements, it does not seem reasonable to use more than 5 samples. In particular for the instantaneous PSI methods, as they are discussed in Section 5.3.2., only algorithms using samples distributed over less than 2π are suitable. These are algorithms with $N \leq 4$.

Phase-shifting errors can be modelled by a difference in the signal frequency v_s and the filter sampling frequency v_f. Robustness to phase-shifting errors is given, if the amplitude gradient of the two filter functions in the Fourier domain are equal at $m=1$. This is true for algorithms #3, #6, #7, and #8.
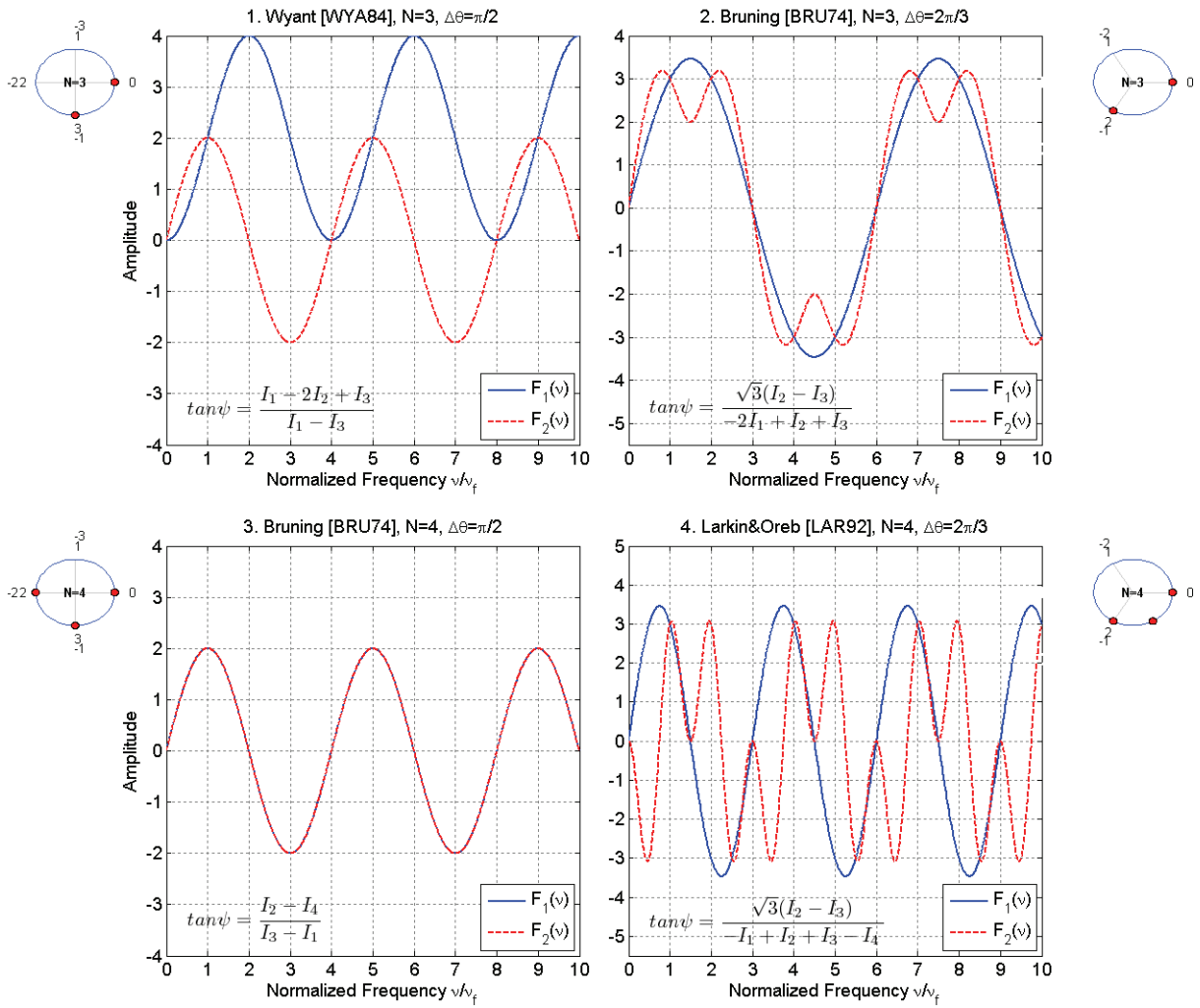
Figure 5.9: Filter functions amplitudes F_1, F_2 and the graphical representation of the characteristic polynomials for the PSI methods #1-#4 of Table 5.1. N denotes the number of phase steps and $\triangle\theta$ the phase step size. The third method (Brunning) with N=4 suppresses second harmonics, and therefore shows some robustness against detector non-linearity.
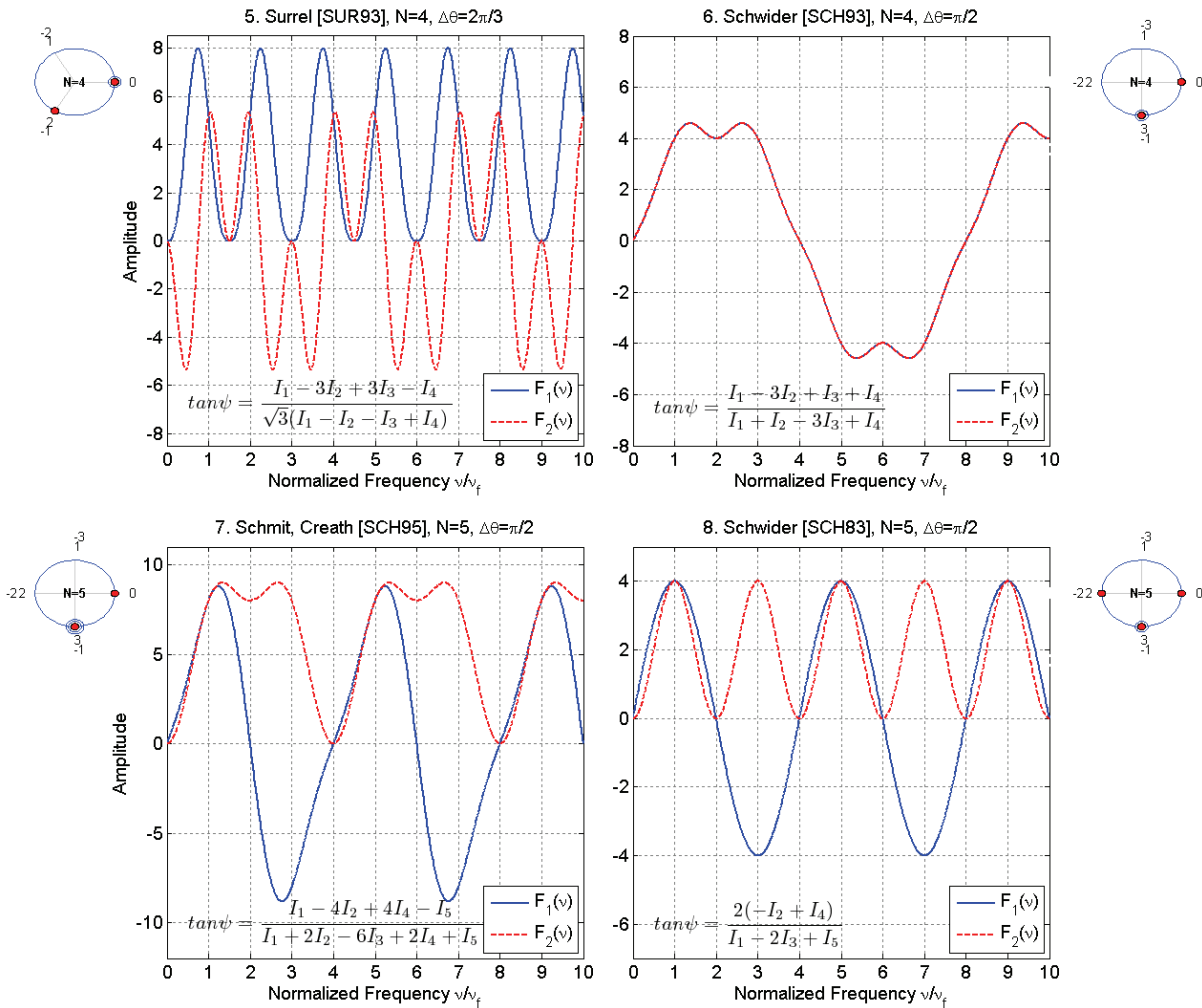
Figure 5.10: Filter functions amplitudes F_1, F_2 and the graphical representation of the characteristic polynomials for the PSI methods #5-#8 of Table 5.1. N denotes the number of phase steps and $\triangle\theta$ the phase step size. Method #6 (Schwider 1993, N=4) and method #7 (Schmit/Creath 1995 N=5) have an equal gradient of the filter functions at the normalized frequency one and therefore are robust against linear phase-shifting errors. Method #8 (Schwider 1983, N=5) also shows this behavior plus zeros at the second harmonics. This algorithm however requires five phase steps, which is not realizable with instantaneous PSI methods.

5.2.2.2 Characteristic Polynomial

Surrel [SUR96] developed an evaluation method based on the fact that every PSI algorithm can be described by a characteristic polynomial $P(z)$, which shows the performance of the algorithm in respect to signal harmonics and linear phase-shifter errors. The method is related to Freischlad's Fourier technique described in the previous section.

Starting from Eq. (5.51) the intensity signal is developed in a discrete Fourier series to account for non-sinusoidal waveforms

$$I(\varphi+\theta)=\sum_{n=-\infty}^{\infty}s_n e^{in(\varphi+\theta)}\,,\qquad(5.66)$$

where the output intensity is given for a PSI phase shift θ. The sought phase φ is in this PSI technique not estimated via the arctangent function, but the argument of a complex linear combination

$$\varphi = \arg\left\{ \sum_{k=0}^{N-1} \overbrace{\left(a_k + ib_k\right)}^{c_k} I\left(\varphi + k\theta\right) \right\},$$ (5.67)

where the coefficients a_k and b_k are taken from the equations of the PSI algorithms as in Table 5.1, and $c_k = a_k + ib_k$. The coefficients of the nominator are taken for b_k and of the denominator for a_k. Setting the results from Eq. (5.66) into (5.67) yields

$$\varphi = \arg\left\{ \sum_{n=-\infty}^{\infty} s_n e^{in\varphi} \underbrace{\sum_{k=0}^{N-1} c_k \underbrace{\left[e^{in\theta} \right]}_{z}^{k}}_{P(z)} \right\},$$ (5.68)

where the characteristic polynomial $P(z)$ is now given by

$$P(z) = \sum_{k=0}^{N-1} c_k \underbrace{\left[e^{in\theta} \right]}_{z}^{k} = \sum_{k=0}^{N-1} c_k z^k.$$ (5.69)

It can be now seen, that if the phase φ is supposed to be independent of certain harmonics of the signal for $n \neq 1$, that the characteristic polynomial $P\left(e^{in\theta}\right)$ has to be zero at the positions $e^{in\theta}$. In other words $e^{in\theta}$ is a root of the characteristic polynomial $P(z)$. Of course the exponential $e^{i\theta}$, i.e. $n = 1$, should not be a root of $P(z)$, as this is the term to obtain the sought phase.

Taking Schwider's PSI algorithm (Table 5.1, #8)

$$\varphi = \arctan\left(\frac{-2I_2 + 2I_4}{I_1 - 2I_3 + I_5} \right)$$ (5.70)

as an example, the characteristic polynomial is calculated to

$$P(z) = z^4 + 2iz^3 - 2z^2 - 2iz + 1.$$ (5.71)

The coefficients in Eq. (5.70) of the denominator become the real parts and the nominator the imaginary parts in $P(z)$. The factorization of Eq. (5.71) shows the roots $z = \{-1, 1, -i\}$ of the polynomial

$$P(z) = (z-1)(z+1)(z+i)^2.$$ (5.72)

Remembering that $z = e^{in\theta}$ it is clear that the roots have to be located on the unit circle in the complex plane and that the roots have to be of the form $e^{in\theta}$. Figure 5.11 shows a graphical representation of the characteristic polynomial. It can be seen that there are roots at $n = 0, -1, -2, 2, 3$ (not showing higher orders). This shows that the algorithm is insensitive to second order harmonics, as the polynomial contains the roots for $n = -2$ and $n = 2$. The roots for $n = 0$ and $n = -1$ have to be included for all PSI algorithms. And as expected $n = 1$ is not a root of the polynomial being required for the measurement of the phase φ.
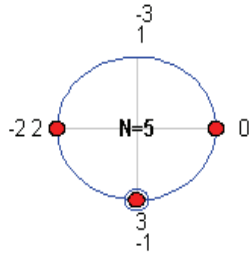
Figure 5.11: Graphical representation of the characteristic polynomials here for Schwider's PSI algorithm [SCH83], (Table 5.1, #8), with *N*=5 signal samples. The gray lines in the central area indicate the phase steps (here $\theta = n\pi/2$). The red dots denote single roots of $P(z)$, a circle around the dot indicates a double root. The numbers around the unit circle show the degree *n*.

An important issue of PSI algorithms, apart from the sensitivity to signal harmonics, is the sensitivity to phase-shifter errors, which can be also estimated from the characteristic polynomial. The real phase shift is given by

$$\theta' = (1+\varepsilon)\theta \tag{5.73}$$

with the nominal phase shift θ and the shifting error ε. Thus, the first order Taylor expansion of $P(z)$ in θ' becomes

$$
\begin{aligned}
P\left(e^{in\theta'}\right) \quad &= P\left(e^{in\theta}\right)+\left(\theta'-\theta\right)P'\left(e^{in\theta}\right)\cdot ine^{in\theta}+\ldots \\
&= P\left(e^{in\theta}\right)+in\varepsilon\theta\cdot e^{in\theta}P'\left(e^{in\theta}\right)+\ldots
\end{aligned}
\tag{5.74}
$$

with

$$P'(z) = \frac{\partial}{\partial z}P(z). \tag{5.75}$$

Consequently, to ensure that $P(z)$ is zero for a certain harmonic *n* even in the presence of a phase-shifter error, also the first derivative of $P(z)$ has to be zero. This implies that $e^{\pm in\theta}$ has to be a double root of the characteristic polynomial. For *n*=0 a simple root is sufficient, and for *n*=-1 only $e^{-i\theta}$ has to be a double root.
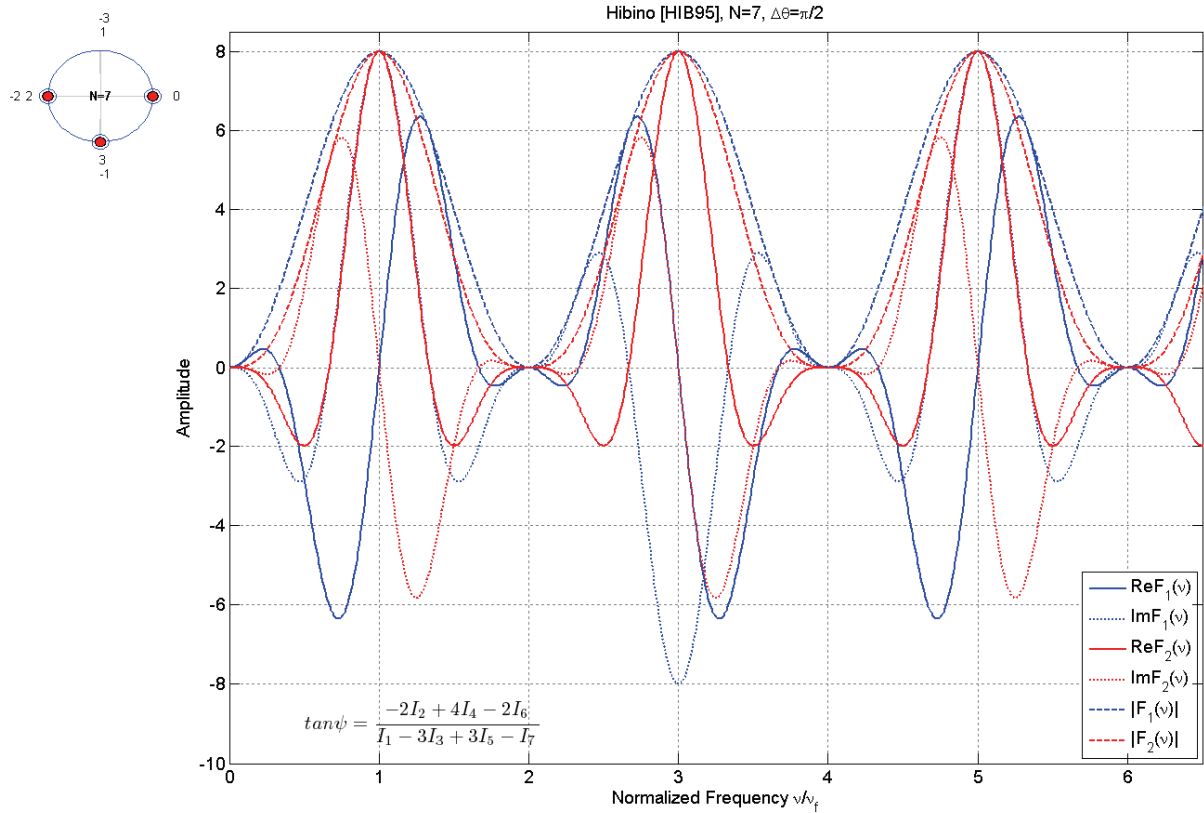
Figure 5.12: Fourier evaluation of an N**=7 PSI algorithm by Hibino [HIB95]. Second order harmonics** $n = 2$ **are suppressed with a double root, also reducing the influence of phase-shifter errors.**

To illustrate the consequences of the characteristic polynomial, two PSI algorithms by Hibino et al. [HIB95] with a larger number of intensity sample points are presented with their Fourier filter functions and the graphical representation of the characteristic polynomial. Figure 5.12 shows a N=7 algorithm, for which $P(z)$ and $P'(z)$ are zero for $e^{\pm i2\theta}$, i.e. $e^{\pm i2\theta}$ are each double roots of the characteristic polynomial. This can be seen from the filter functions, which are here plotted with the real, imaginary parts, and the amplitude of the functions. The filter functions have a zero at the normalized frequency $v/v_f = 2$. Therefore this algorithm is insensitive to the second signal harmonics including phase-shifting errors. The same conclusions can be drawn from the graphical representation of the characteristic polynomial. In addition, the gradient of the amplitudes at $v/v_f = 1$ is equal for both functions; therefore, also the detection term is insensitive to phase-shifting errors.

Suppression of higher order harmonics can be achieved with the N=10 algorithm by Hibino [HIB95], which is given in [MAL07]. Figure 5.13 shows the filter functions and the graphical representation of the characteristic polynomial. Here the harmonics $n = 2, 3, 4$ are suppressed with a double root.
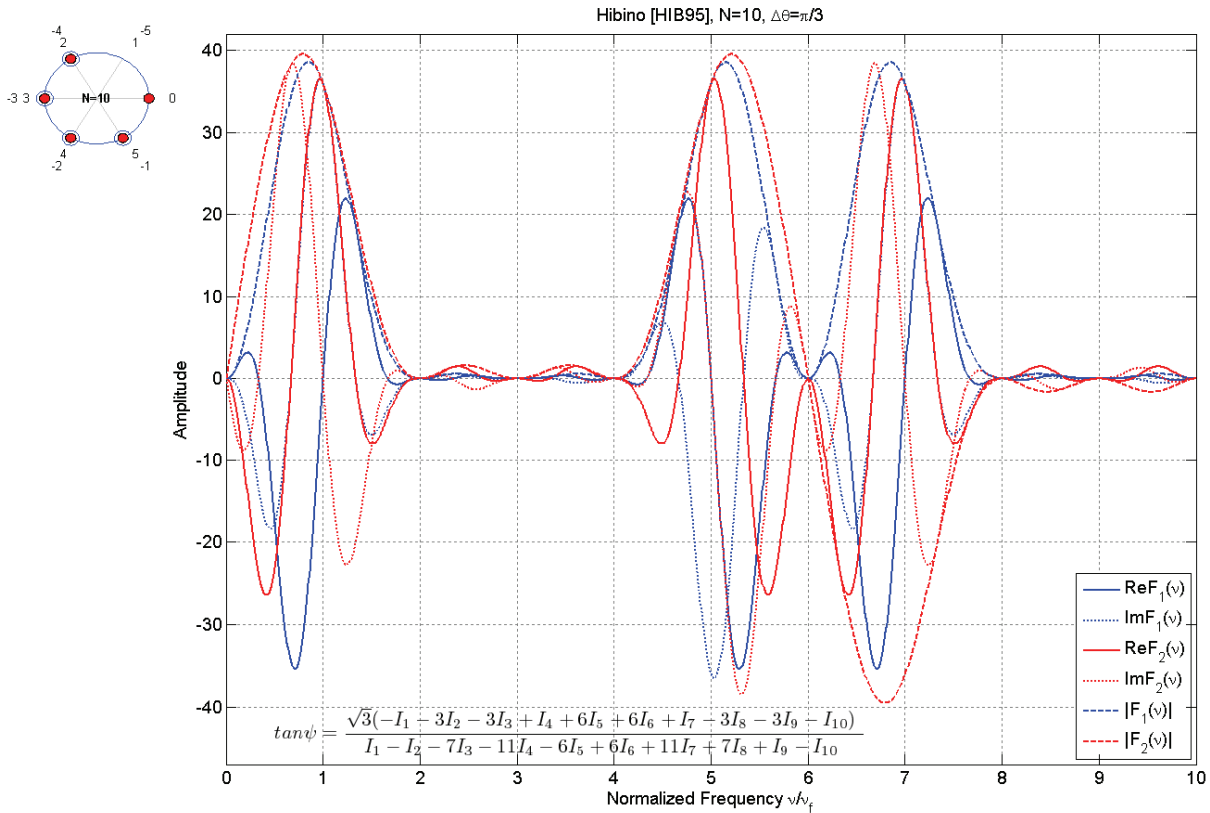
Figure 5.13: Fourier evaluation of an N=10 PSI algorithm by Hibino [HIB95]. Harmonics $n = 2, 3, 4$ are suppressed with a double root, also reducing the influence of phase-shifter errors.

5.2.3 Error Sources

There are a number of error sources, which affect the accuracy of phase measurements performed by the various PSI algorithms. Some of the PSI algorithms are less sensitive to particular error sources than others, which already has been discussed in the previous section. Typical error sources for phase-shifting interferometers are

- Phase-shifting errors
- Detector nonlinearities
- Detector noise and vibration errors
- Thermal effects
- Interferometer optical errors
- Quantization errors

Error contributions specific to each algorithm have been tabulated in various publications [WIN91, MAL07]. The algorithms list in Table 5.1 with N=3 to 5 phase steps are treated in this section in more details, as they provide promising solutions for the use with instantaneous PSI methods presented later in Section 5.3.2. Special emphasis will be given to systematic errors as phase-shifting errors and the detector nonlinearity, and the random errors as detector noise, vibration errors and thermal effects. Optical and quantization errors are not treated in this context.

5.2.3.1 Phase-Shifting Errors

Phase-shifting interferometers rely on the accuracy of the introduced phase shifts. A relative phase-shifting error ε directly influences the measurement results at the phase steps. The intensity for an interferometer with phase step $\theta_{j,\varepsilon}$ is given by

$$I(x,y) = I_R + I_0(x,y) + 2\sqrt{I_R I_0(x,y)} \cos\left(\varphi(x,y) + \theta_{j,\varepsilon}\right), \tag{5.76}$$

where $\theta_{j,\varepsilon}$ indicates the phase step impinged with the relative phase-shifting error ε, so that $\theta_{j,\varepsilon} = \theta_j(1+\varepsilon)$. Using Eq. (5.76) with the PSI algorithms presented in Table 5.1 allows the evaluation of the robustness of the PSI algorithms in respect to the phase-shifting error. The results are summarized in Figure 5.14.

An interesting algorithm appears to be the method by Schwider (Table 5.1, #6). It exhibits with only 4 steps a good robustness to linear phase-shifting errors compared to other 3 and 4 step methods. This was predicted by the evaluation methods presented in Section 5.2.2 and can be confirmed from Figure 5.10, as F_1 and F_2 have the same gradients at the detection frequency $v/v_s = 1$ and the algorithm shows a double root at n=-1.

An even better performance has the 5-step algorithm by Schmit and Creath (Table 5.1, #7) with a triple root at $n = -1$, but without the insensitivity to second harmonic disturbances. Algorithms #7 and #8 requires 5 steps over more than one period and cannot be implemented with instantaneous PSI algorithms as discussed in Section 5.3.2.
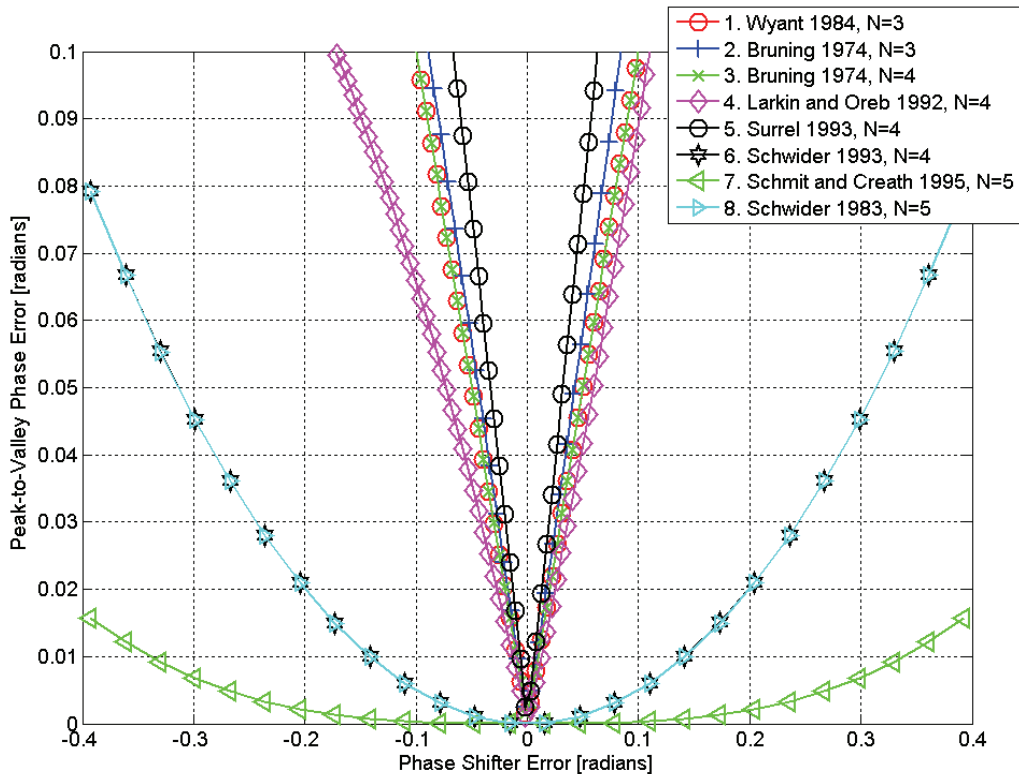

Figure 5.14: Sensitivity to phase-shifter errors of the PSI algorithms of Table 5.1.

5.2.3.2 Detector Nonlinearity

Detector nonlinearity produces significant errors in the phase reconstruction if the interferometer fringes have a large dynamic range. The performance of the discussed PSI algorithms can be inferred from the Fourier and characteristic polynomial methods in Section

5.2.2. Figure 5.9 and Figure 5.10 show the characteristic graphs for the 3 to 5 step methods. None of the investigated 3 step algorithms (Table 5.1, #1 and #2) is insensitive to second-order harmonics of the signal caused by detector nonlinearity. Among the 4- and 5-step algorithms only the method of Bruning (Table 5.1, #3, $N=4$) and Schwider (Table 5.1, #8, $N=5$) are insensitive to second-order harmonics of the signal, but higher order harmonics are also not suppressed by these algorithms, which would require a larger number of phase steps over more than one signal period. Also it has to be mentioned that no algorithm in Table 5.1 is insensitive to nonlinearity errors in the presence of phase-shifting errors, which would require a double root for the according harmonic order. Examples for such algorithms being insensitive to more than one harmonic order and phase-shifting errors are presented in Figure 5.12 ($N=7$) and Figure 5.13 ($N=10$).

5.2.3.3 Detector Noise

Detector noise is an important issue in the discussed scenarios as the received intensity exhibits strong signal fluctuations with deep fades. The fades can reach down to zero amplitude for phase singularities. In regions on the sensor with an intensity fade the noise of the sensor itself becomes significant for the performance of the wavefront reconstruction.

The following analysis of the detector noise is based on the derivation of Freischlad and Koliopoulos [FRE90]. Similar results were obtained with the characteristic polynomial method of Surrel [SUR97]. Assuming a linear combination y of M statistically independent variables x_j

$$y = \sum_{j=1}^{M} a_j x_j \,, \tag{5.77}$$

the combined noise variance is given by

$$\sigma_y^2 = \sum_{j=1}^{M} a_j^2 \sigma_j^2 \,. \tag{5.78}$$

σ_j^2 denotes the noise variance of the jth variable x_j. For any (nonlinear) function

$$y = f\left(x_1, \ldots, x_M\right). \tag{5.79}$$

the variance of y can be approximated by a first order linearization, using the first order of a Taylor expansion

$$\sigma_y^2 \cong \sum_{j=1}^{N} \left[\frac{\partial f\left(\langle x_1 \rangle, \ldots, \langle x_N \rangle\right)}{\partial x_j} \right]^2 \sigma_j^2 \,. \tag{5.80}$$

As an example Eq. (5.80) is applied to Wyant's three-step algorithm (Table 5.1, #1, $N=3$)

$$\varphi = \arctan\left(\frac{I_1 - 2I_2 + I_3}{I_1 - I_3} \right). \tag{5.81}$$

In a first step the partial derivatives are determined. The derivate $\dfrac{\partial \varphi}{\partial I_1}$ is given by

$$\frac{\partial \varphi}{\partial I_1} = \frac{2I_2}{\left(I_1 - I_3\right)^2 + \left(I_1 - 2I_2 + I_3\right)^2} \ . \tag{5.82}$$

Similar equations are found for the partial derivatives $\dfrac{\partial \varphi}{\partial I_2}$ and $\dfrac{\partial \varphi}{\partial I_3}$. Summing the squared

results with Eq. (5.80) and simplifying the notation with $I_c = I_0 + I_R$ and $V = \dfrac{2\sqrt{I_0 I_R}}{I_0 + I_R}$, the

results for the variance of the phase error σ_φ^2 in dependence of the detector noise σ_n^2 (equal

for I_1 to I_3) for the PSI algorithms in Table 5.1 are presented in Table 5.2.

The sensitivity to Gaussian noise is summarized in Figure 5.15. It can be seen that the algorithms, which are partly insensitive to higher order harmonics, also exhibit improved noise-rejection capabilities. Within the three-step algorithms, Bruning's algorithm #2 performs over 30% better than #1. Within the four-step algorithms, Bruning's algorithm #3 with an insensitivity to second-order harmonics performs approximately 35% better than the worst candidate. The best overall performance shows Schwider's algorithm #8. Naturally algorithms with a larger number of samples perform better, as they have more capabilities to average the results.

Table 5.2: Variance of the phase error σ_φ^2 in dependence of the detector noise σ_n^2.

| #	N	$\tan \varphi =$	Step Size	Additive Gaussian Noise	Reference
1.	3	$\dfrac{I_1 - 2I_2 + I_3}{I_1 - I_3}$	$\dfrac{\pi}{2}$	$\dfrac{\sigma_n^2}{\left(VI_c\right)^2}\left(1 + \tfrac{1}{2}\cos\left(2\varphi\right)\right)$	Wyant [WYA84]
2.	3	$\dfrac{\sqrt{3}\left(I_2 - I_3\right)}{-2I_1 + I_2 + I_3}$	$\dfrac{2\pi}{3}$	$\dfrac{2}{3}\dfrac{\sigma_n^2}{\left(VI_c\right)^2}$	Bruning [BRU74]
3.	4	$\dfrac{I_2 - I_4}{I_3 - I_1}$	$\dfrac{\pi}{2}$	$\dfrac{1}{2}\dfrac{\sigma_n^2}{\left(VI_c\right)^2}$	Bruning [BRU74]
4.	4	$\dfrac{\sqrt{3}\left(I_2 - I_3\right)}{-I_1 + I_2 + I_3 - I_4}$	$\dfrac{2\pi}{3}$	$\dfrac{1}{9}\dfrac{\sigma_n^2}{\left(VI_c\right)^2}\left(5 + \cos\left(2\varphi\right)\right)$	Larkin and Oreb [LAR92]
5.	4	$\dfrac{I_1 - 3I_2 + 3I_3 - I_4}{\sqrt{3}\left(I_1 - I_2 - I_3 + I_4\right)}$	$\dfrac{2\pi}{3}$	$\dfrac{1}{27}\dfrac{\sigma_n^2}{\left(VI_c\right)^2}\left(16 + 4\cos\left(2\varphi\right)\right)$	Surrel [SUR93]
6.	4	$\dfrac{I_1 - 3I_2 + I_3 + I_4}{I_1 + I_2 - 3I_3 + I_4}$	$\dfrac{\pi}{2}$	$\dfrac{1}{4}\dfrac{\sigma_n^2}{\left(VI_c\right)^2}\left(3 - \sin\left(2\varphi\right)\right)$	Schwider [SCH93]
7.	5	$\dfrac{I_1 - 4I_2 + 4I_4 - I_5}{I_1 + 2I_2 - 6I_3 + 2I_4 + I_5}$	$\dfrac{\pi}{2}$	$\dfrac{1}{32}\dfrac{\sigma_n^2}{\left(VI_c\right)^2}\left(21 - 3\cos\left(2\varphi\right)\right)$	Schmit, Creath [SCH95]
8.	5	$\dfrac{-2I_2 + 2I_4}{I_1 - 2I_3 + I_5}$	$\dfrac{\pi}{2}$	$\dfrac{1}{16}\dfrac{\sigma_n^2}{\left(VI_c\right)^2}\left(7 + \cos\left(2\varphi\right)\right)$	Schwider [SCH83]
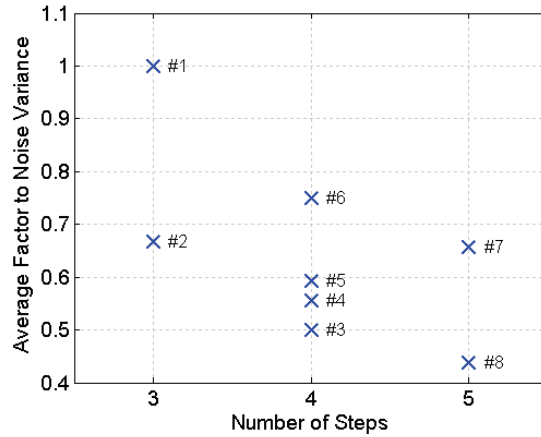
Figure 5.15: Average noise scaling factor (additive Gaussian noise) taken from Table 5.2. The averaging was performed over all phase values φ.

Figure 5.16 and Figure 5.17 show the simulated results of a three-step interferometer (Bruning 1974, #2, N=3). The simulated input field was generated for an SGL at 10° elevation and for a telescope diameter of D=0.5m with a $HV_{5/7}$ C_n^2 profile (Section 3.1.3.1) at $\lambda = 1064nm$. The diameter of the filter-dot was chosen to be 50% of the Airy diameter ($\eta = 0.5$) to produce the synthetic reference wave. Figure 5.16 shows the simulation for a signal strength of 1 (arbitrary normalization). The noise level was set to 0.1. The upper row shows the three interferograms containing a significant noise level. The second row shows the original phase and the reconstructed phase, which is disturbed by noise. Figure 5.17 shows the same interferograms, but with a four times larger signal strength. The signal-to-noise ratio is significantly improved.
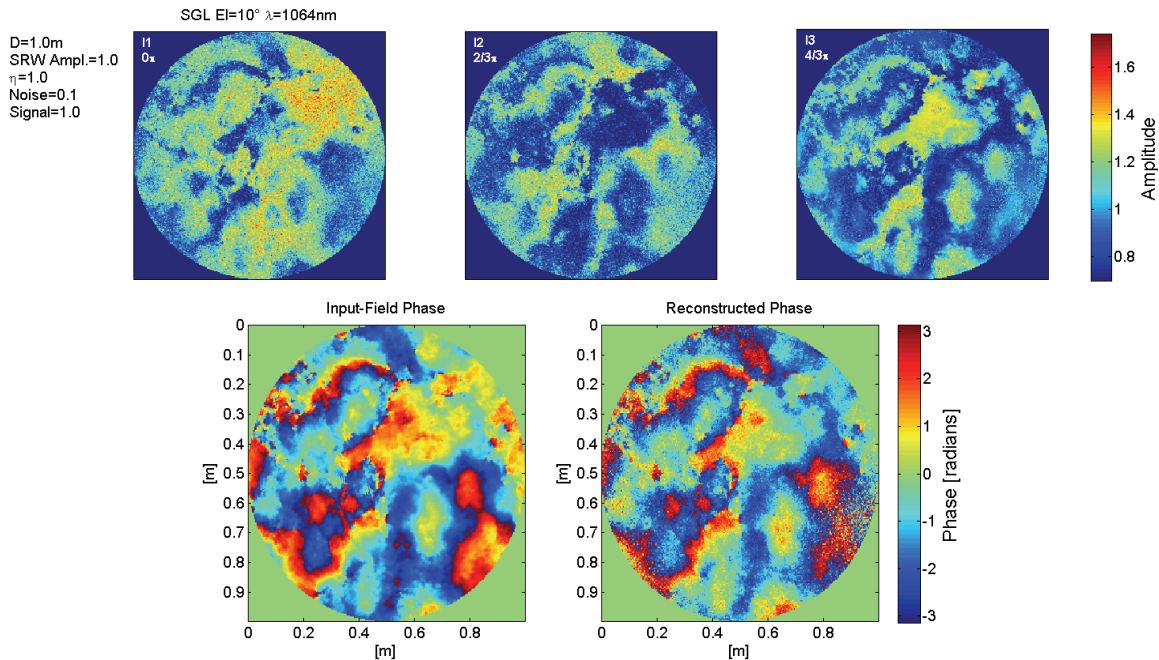

Figure 5.16: Simulation of a three-step interferometer (Bruning 1974, #2, N=3): The upper row shows the three interferograms I1-I3 for the phase-steps $\delta = 0, \frac{2}{3}\pi, \frac{4}{3}\pi$; The lower row shows the input, original phase and the reconstructed phase calculated from the images I1 to I3. Images I1 to I3 were disturbed by a normal distributed noise with σ_n=0.1. Signal strength was 1 (arbitrary normalization).
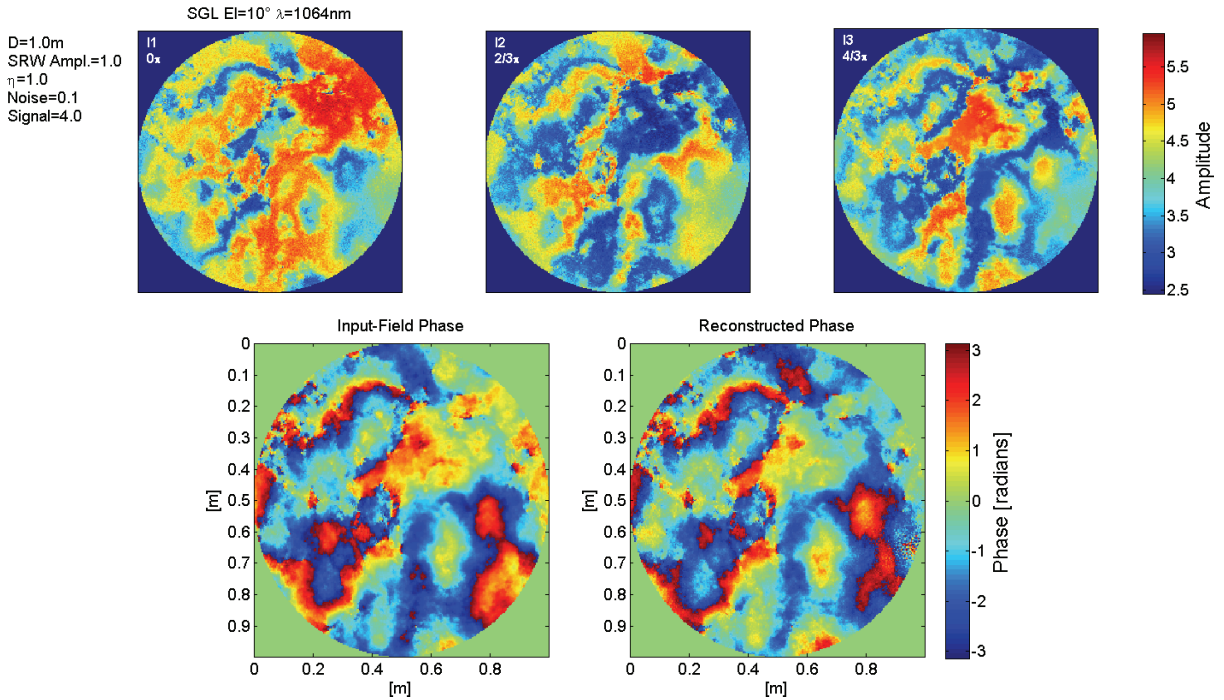
Figure 5.17: Same as Figure 5.16, but with a 4 times larger signal strength. It can be seen that the signal-to-noise ratio in the output is significantly improved.

5.2.3.4 Vibration Errors

Mechanical vibrations are a difficult issue for interferometric measurements [MAL07]. Their presence can be detrimental to the point of completely obliterating interference fringes; however, vibrations cannot be avoided in all cases. In the discussed scenario the AO system with the interferometric sensor may have to be mounted on a telescope mount, which will have some amount of vibrations. Therefore, it is important to optimize the interferometric sensors to be as far as possible insensitive to these disturbances.

Small-scale vibrations manifest itself in a similar way as the phase-shifting errors discussed in Section 5.2.3.1. PSI implementations, which are insensitive to phase-shifting errors, also tend to be insensitive to mechanical vibrations. Common-path interferometers in general are more robust, as the vibrations affect both the reference and the object beam. The PSI setups discussed in Section 5.3.2 use common paths for the object and reference waves over large sections, and should therefore be more robust to vibrations. Non-common path in these setups is the generation of the reference wave.

De Groot and Deck discussed numerical simulations of vibration effects in PSI configurations [GRO96][MAL07]. The idea is to numerically determine the root-mean square (RMS) value of the phase measurement error. The signal of the interferometer with vibration disturbance is given for the sought (real) phase φ by

$$I(t) = I_R + I_0 + 2\sqrt{I_R I_0} \cos\left(2\pi\nu_s t + \varphi + A_v \cos\left[2\pi\nu_v t + \alpha_v\right]\right), \qquad (5.83)$$

where A_v denotes the amplitude of the vibrations, ν_v the frequency of the vibration, and α_v the phase shift of the vibration. The RMS value for the frequency ν_v is calculated with the error term $\triangle\varphi = \varphi(\varphi, \alpha_v, \nu_v) - \varphi$ by

$$RMS(\nu_v) = \sqrt{\int_0^{2\pi}\int_0^{2\pi}\left(\triangle\varphi(\varphi,\alpha_v,\nu_v) - \langle\triangle\varphi(\alpha_v)\rangle\right)^2 d\varphi d\alpha_v}, \qquad (5.84)$$

147

integrating over all combinations of the phase φ and the vibration phase shift α_v. $\varphi(\varphi, \alpha_v, v_v)$ denotes the measured phase, disturbed by a vibration with the parameters (A_v, α_v, v_v). The averaged phase in the integral is given by

$$\langle \triangle \varphi(\alpha_v) \rangle = \frac{1}{2\pi} \int_{-\pi}^{\pi} \triangle \varphi(\varphi, \alpha_v) d\varphi .$$
(5.85)

Figure 5.18 and Figure 5.19 show the RMS course over the vibration frequency v_v for the algorithms given in Table 5.1 and the 10-point algorithm by Hibino [HIB95] (Figure 5.13). The graphs show a strong variation in sensitivity as a function of vibration frequency.

De Groot assumed an integrating bucket scheme, where the intensity of the interferometer is not only measured at an instant of time, but integrated over the sampling period τ. Thus, the measured intensity of the jth sample can be written with the averaging integral

$$\bar{I}_j = \frac{1}{\tau} \int_{-\tau/2}^{\tau/2} I(\varphi, t_j + t) dt .$$
(5.86)

The integration causes the decrease of the RMS error to higher vibration frequencies, as they are simply averaged out for vibration frequencies greater than the sampling frequency. This can be seen from Eq. (5.83).
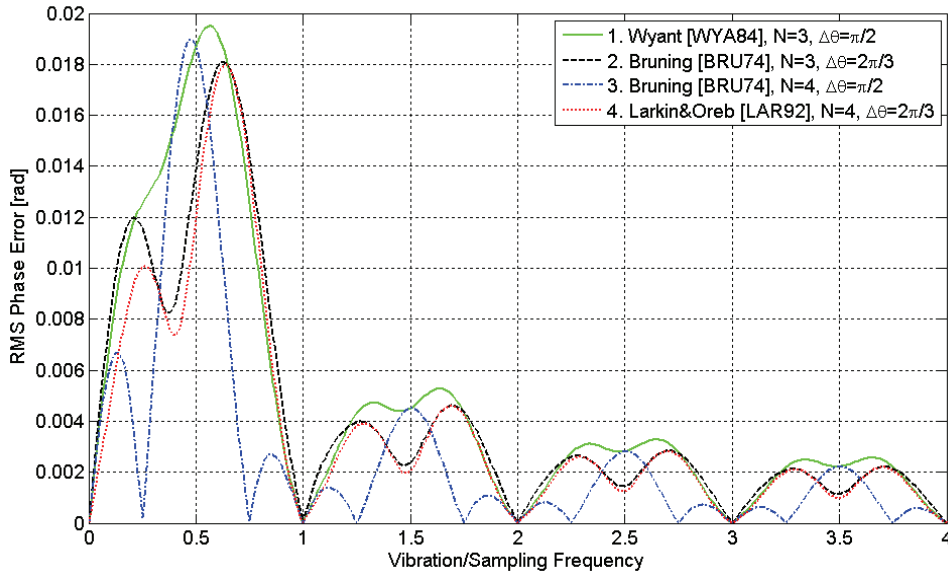

Figure 5.18: Sensitivity of the PSI algorithms presented in Table 5.1 (Algorithms #1-#4) to vibrations expressed as the RMS phase error.
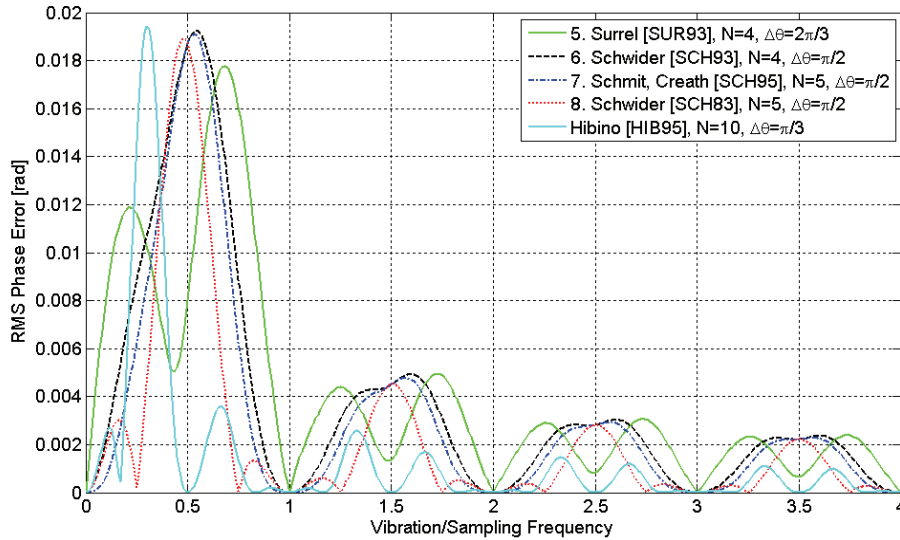
Figure 5.19: Sensitivity of the PSI algorithms presented in Table 5.1 (Algorithms #5-#8) to vibrations expressed as the RMS phase error. Additionally, the algorithm by Hibino [HIB95] introduced in Section 5.2.2.2 is shown to illustrate the robustness of this algorithm.

Integrating the RMS values over all vibration frequencies gives an overall sensitivity value s_v for each presented algorithm

$$s_v = \int_0^\infty RMS(v_v)dv_v \,. \tag{5.87}$$

Figure 5.20 shows the relative sensitivity values normalized to the s_v value of the PSI algorithm #1. Among the three- and four-step algorithms the methods of Bruning [BRU74], among the five-step algorithms Schwider's method [SCH83] perform best. This is an expected result from the algorithm evaluation in Section 5.2.2, Figure 5.9 and Figure 5.10, as these two algorithms also suppress second-order signal harmonics. The algorithm of Hibino [HIB95] is overall a strong method with the best performance in vibration suppression, however requiring 10 sample points.
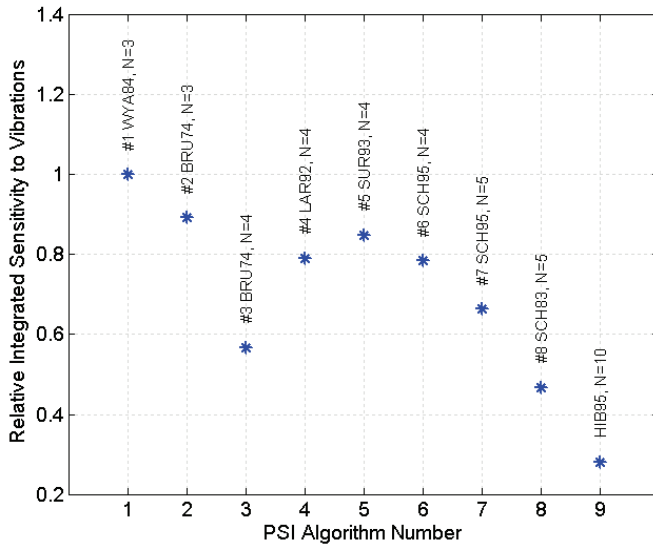

Figure 5.20: Comparison of vibration sensitivity values s_v of the presented PSI algorithms.

5.2.4 Phase Singularities and Phase-Shifting Interferometer

The behavior of PSI techniques in the presence of phase singularities as described in Section 4.3 was tested with a numerically simulated field. The parameters of the simulation were adapted for an SGL at 10 degrees elevation and for a telescope diameter of D=0.5m with a HV$_{5/7}$ C_n^2 profile (Section 3.1.3.1) at $\lambda = 1064nm$.

The simulated field, which has been already shown in Figure 5.16 and Figure 5.17, contains a larger number of phase singularities due to the low elevation angle. The Rytov variance is $\sigma_R^2 \approx 1$. Figure 5.21 shows an enlarged area of the input wave with several singularities recognizable from the typical phase screw. The singularities are, as expected, accurately reconstructed by the deployed three-step PSI.

Another interesting aspect of PSIs is that all phase measurements are related to the reference wave. Therefore local minima of the received intensity can influence the quality of the reconstructed phase only locally, but all other regions produce a valid phase, even if some areas in the aperture are encircled by an almost-zero intensity barrier. This kind of behavior is not guaranteed for wavefront sensors as the Shack-Hartmann, which performs a global reconstruction of the phase taking all focus spots into account. Separated regions do not have a common reference, as only derivatives of the wavefront are known from the sensor. As a consequence piston phase shifts between the separated regions might appear, depending on the used algorithms.
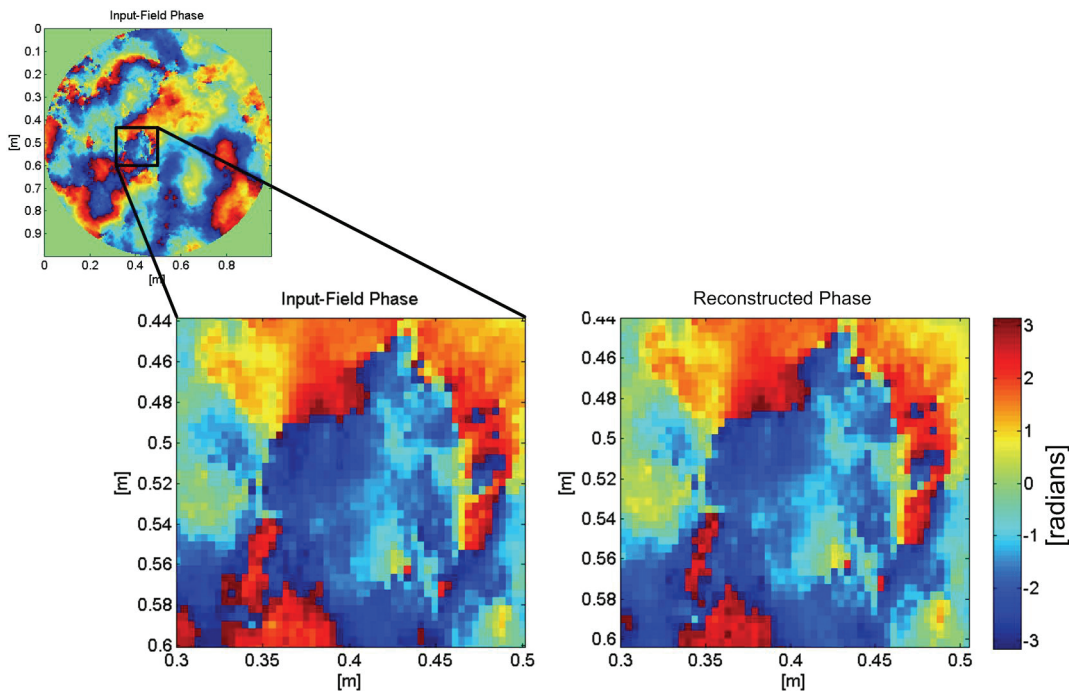

Figure 5.21: Enlarged area of the input and reconstructed phase distributions as in Figure 5.16 and Figure 5.17. The singularities are clearly reconstructed by the three-step PSI (Table 5.1, #2, N=3).

5.3 Interferometer Designs for the SGL Scenario

This section presents several possible interferometer designs, which appear to be especially suitable for the deployment in the SGL scenarios. Sections 5.3.1 and 5.3.3 introduce concepts, which use only one interferometer, while Section 5.3.2 shows the use of synchronous or instantaneous phase-shifting interferometers.

5.3.1 Single Mach-Zehnder Interferometer with a Fourier Fringe Analysis

Takeda [TAK82] described a method to retrieve the phase of the input field with a single interferometer, calling it a Fourier fringe analysis (FFA) technique. Certain aspects of Takeda's approach were also discussed by Roddier and Roddier [ROD87], including the boundary problem of the telescope aperture. This method was applied by Notaras and Paterson [NOT08] in an adaptive optics system in strong scintillation.

Taking Eq. (5.33) describing the point-diffraction interferometer, and tilting one of the arms of the interferometer by a small angle, a regular interference pattern appears with the input intensity and phase structure superposed

$$I_1(x,y) = I_R + I_0(x,y) + 2\sqrt{I_R I_0(x,y)} \cos\left(\varphi(x,y) + 2\pi f_0 x\right). \tag{5.88}$$
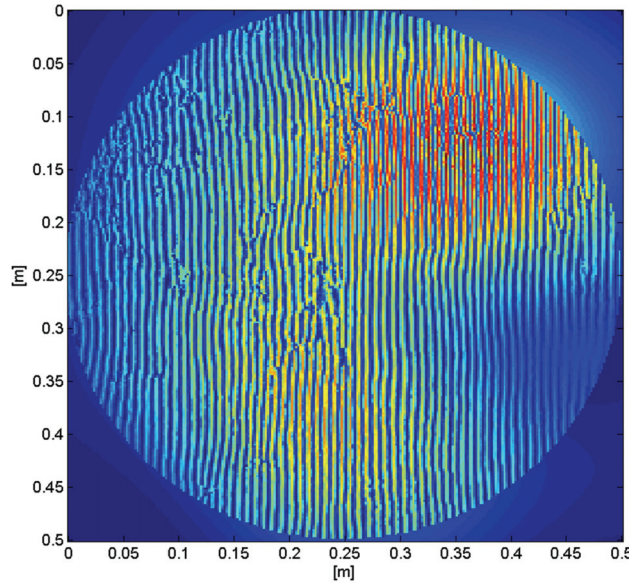
Figure 5.22: Interference fringes due to the tilted wavefront of one interferometer arm. The phase distribution of the incoming wave distorts the ripple pattern. The intensity distribution is superposed to the fringe pattern and also changes the fringe modulation depth.

The interference pattern due to the tilted interferometer arm can be seen in the vertical line pattern of Figure 5.22. The intensity modulation frequency f_0 increases with the tilt angle between reference and object wave. Expressing the cosine function in (5.88) with exponential functions yields

$$
\begin{aligned}
I_1(x,y) &= I_R + I_0(x,y) + \sqrt{I_R I_0(x,y)} \left[e^{i\varphi(x,y)+2\pi i f_0 x} + e^{-i\varphi(x,y)-2\pi i f_0 x} \right], \\
&= a(x,y) + b(x,y) e^{2\pi i f_0 x} + b^*(x,y) e^{-2\pi i f_0 x}
\end{aligned}
\tag{5.89}
$$

where $b(x,y) = \sqrt{I_R I_0(x,y)} e^{i\varphi(x,y)}$ and the star denotes the complex conjugate. Fourier transforming Eq. (5.89) results to

$$I_F(f_x, f_y) = A(f_x, f_y) + B(f_x - f_0, f_y) + B^*(f_x + f_0, f_y). \tag{5.90}$$

I_F, A, and B denote the Fourier transforms of the corresponding values I_1, a, and b in the spatial domain. The exponential functions of the modulation frequency f_0 cause a translation of B in the Fourier domain. If the spatial variations of a, b and φ are slow in comparison with

the spatial frequency f_0, the three components A, B, and B^* are separated as shown in Figure 5.23. Taking the peak B in the Fourier domain, moving it to the center, and taking the inverse Fourier transform, the component $b(x,y)$ can be retrieved. From this the phase $\varphi(x,y)$ can be simply calculated either by the *angle* function or the *log* function

$$\log\big(b(x,y)\big) = \log\sqrt{I_R I_0(x,y)} + i\varphi(x,y). \tag{5.91}$$

Also the amplitude distribution of the input wave can be determined by taking the absolute value of b, if the distribution of the reference wave is known.
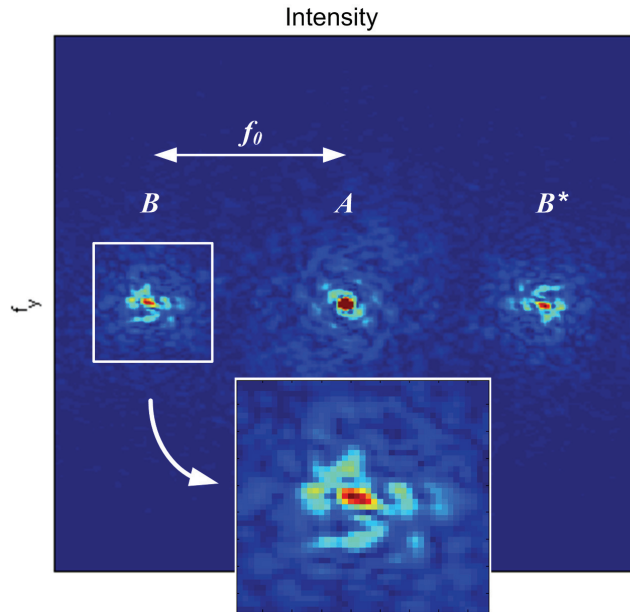
Figure 5.23: Separation of the components A, B, and B^* by a modulation with frequency f_0. To retrieve the phase $\varphi(x,y)$, B is taken and moved to the center.

Figure 5.24 demonstrates the phase reconstruction for a simulated field of a 10 degree elevation SGL. A resolution of 512x512 pixels was used. Although the input field contains a larger number of phase singularities and strong scintillation, the phase reconstruction provides a quite accurate phase estimate with a Strehl ratio of S=0.92 for the corrected field.
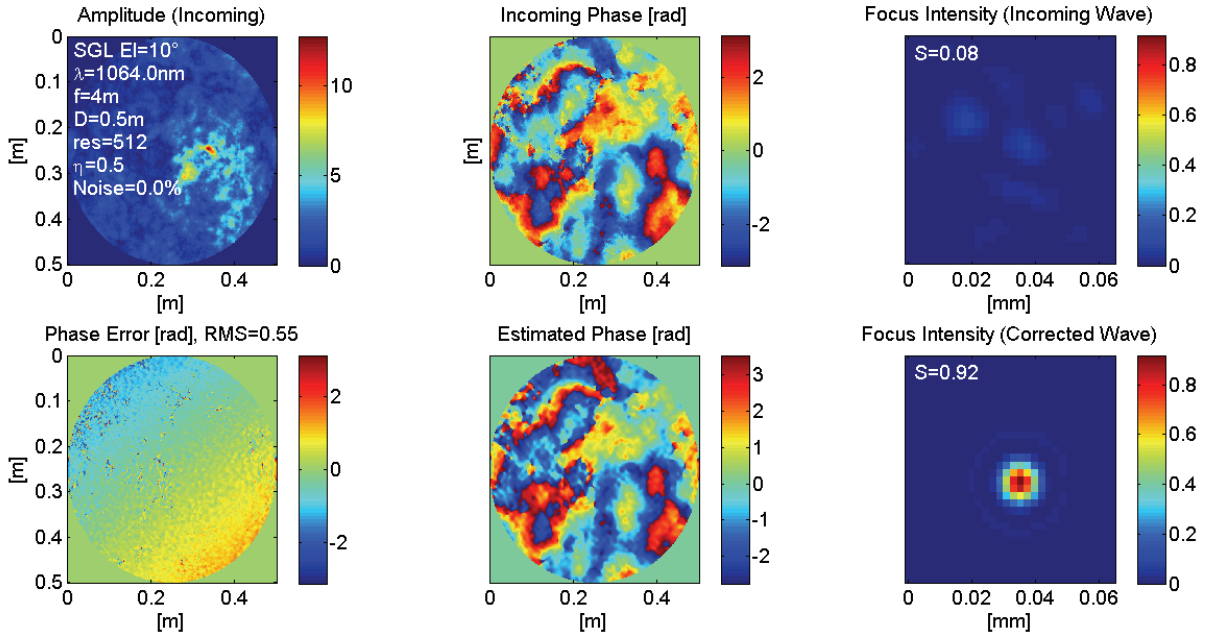
Figure 5.24: Simulation of a phase reconstruction with a single interferometer based on the FFA method. First row: Incoming amplitude, phase, and focus spot intensity. Second row: Phase error of the reconstruction, estimated phase, and resulting focus spot intensity with the corrected phase. Simulation parameters: $\eta = 0.5$ (pin-hole diameter), resolution: 512x512 pixels.

For lower resolutions the three peaks in Figure 5.23 move closer together, which can lead to aliasing effects, i.e. parts of the central peak spill into the side peaks. This effect can be reduced by also using the second, destructive-interference arm of the combining beam splitter [VAN03]. The interferogram of the destructive-interference arm is given by

$$I_2(x,y) = I_R + I_0(x,y) - \sqrt{I_R I_0(x,y)} \left[e^{i\varphi(x,y)+2\pi i f_0 x} + e^{-i\varphi(x,y)-2\pi i f_0 x} \right]$$
$$= a(x,y) - b(x,y) e^{+2\pi i f_0 x} - b^*(x,y) e^{-2\pi i f_0 x}$$
(5.92)

Now Fourier transforming I_1 (5.89), I_2 and subtracting the results yields

$$I_{F,1-2}(f_x, f_y) = 2B(f_x - f_0, f_y) + 2B^*(f_x + f_0, f_y).$$
(5.93)

This has eliminated the central peak and, in addition, doubled the amplitudes of the side-peaks increasing the SNR. Without the central peak the windowing function to extract the required side-peak can be chose to be larger, which increases the resolution of the technique. Considerations about the resolution can be found in [KOS93] for the single-interferogram technique and in [VAN03] for the differential technique. Figure 5.25 shows the effects of both techniques. The upper graph gives the three peaks of a single interferogram. In the middle the two peaks of the differential technique are shown. In the lower row cuts through the interferograms along the dash-dotted green lines are depicted. The doubling of the amplitude and the disappearance of the central peak can be nicely seen for the differential method.
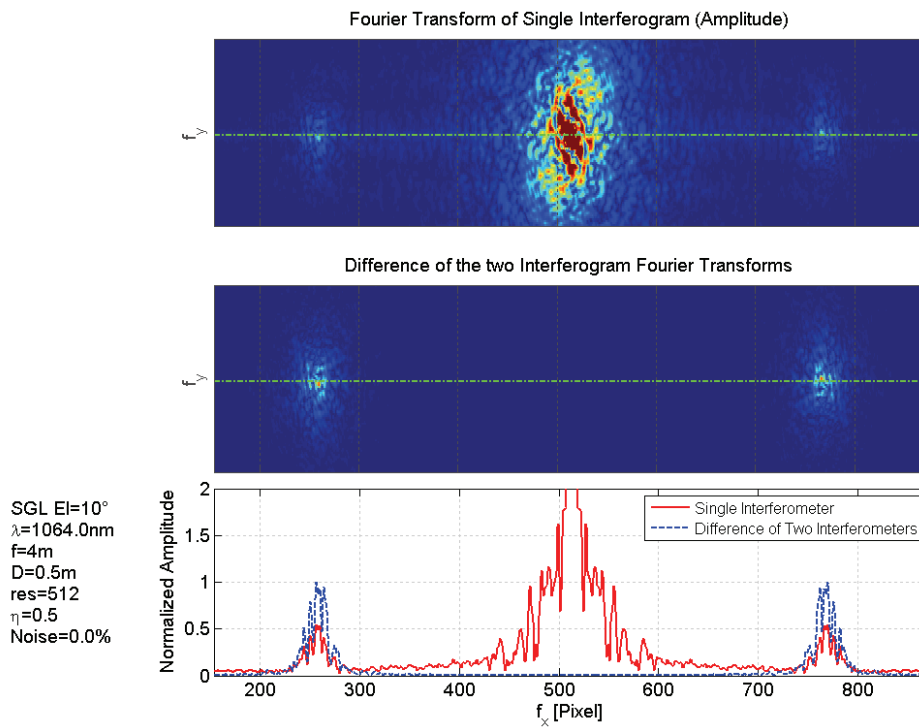
Figure 5.25: The upper graph gives the three peaks of a single interferogram. In the middle the two peaks of the differential technique are shown. In the lower row cuts through the interferograms along the dash-dotted green lines are depicted.

Figure 5.26 shows several variations of the FFA technique. Images B and C compare reconstruction quality of a single interferogram with the differential interferogram technique of Eq. (5.93). Both interferograms were taken at a relatively low resolution of 128x128 pixels. The Strehl ratio of the differential interferogram technique significantly improves (0.74 against 0.46). The advantage of a lower resolution is that the camera can run with a higher frame rate due to a smaller region-of-interest, and that the required time for the two Fourier transforms is shortened. Lower resolution, however, also implies that higher frequencies are cut off in the reconstruction and the resolution is decreased.

Image D demonstrates the effect of noise. The noise is given as a percentage of the maximum amplitude of the interferogram, i.e. the frame taken from the camera chip, which then simulates camera noise. The reconstructed phase with a resolution of 512x512 pixels is quite good with a Strehl ratio of 0.62 despite the high noise level of 20%.
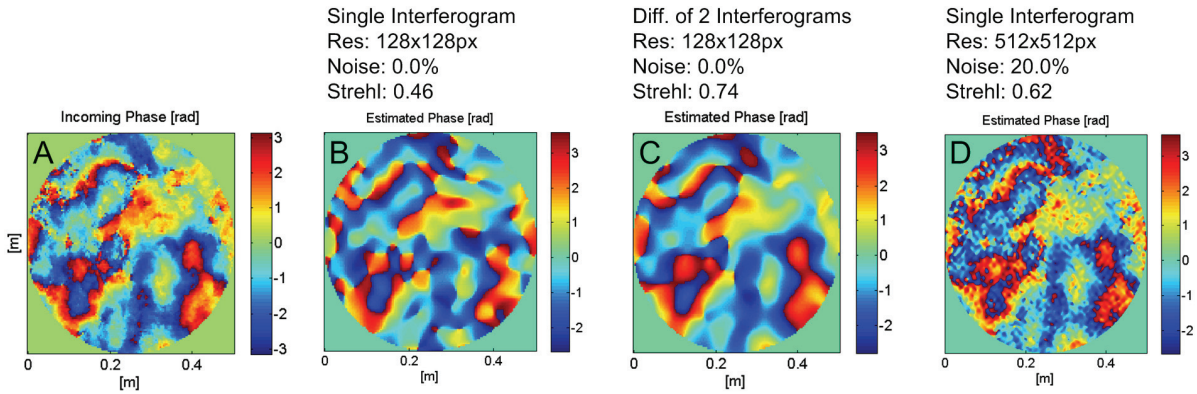
Figure 5.26: Effects of different variations of the FFA technique. A. Simulated input phase for a 10 degree elevation SGL; B. Reconstructed phase from a single interferogram with 128x128 pixels resolution resulting in a Strehl ratio of 0.46; C. Reconstructed phase from the differential techniques with 128x128 pixels resolution resulting in a Strehl ratio of 0.74; D. Reconstructed phase from a single interferogram with 512x512 pixels resolution and 20% noise on the interferogram resulting in a Strehl ratio of 0.62.

Figure 5.27 shows the effect of an additional obscuration under the influence of noise. Comparing images A with obscuration and B without obscuration, it can be seen that the effect of obscuration is localized to the area of the obscuration, where of course no valid phase estimate can be retrieved. The effect of the obscuration on the Strehl ratio is rather low, which shows in the resulting focus spots. The input phase was the same as in Figure 5.26-A. The obscured area can be detected from the absolute value of the output shown in Figure 5.28. This can be also used to detect regions with low illumination levels to assess the reliability of the phase reconstruction.
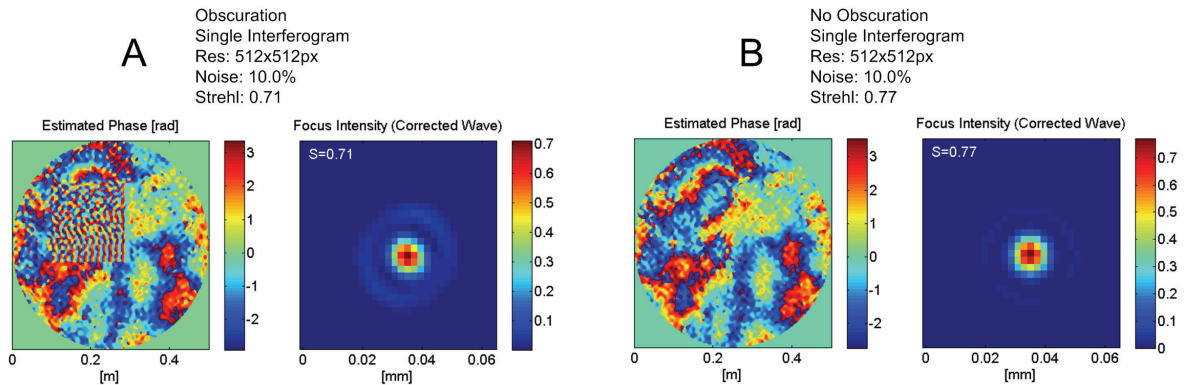
Figure 5.27: Effects of an obscuration; Reconstructed phase from a single interferogram with 512x512 pixels resolution and 10% noise on the interferogram: A. With a rectangular obscuration yielding a Strehl ratio of 0.71; B. Without the obscuration, yielding a Strehl ratio of 0.77.
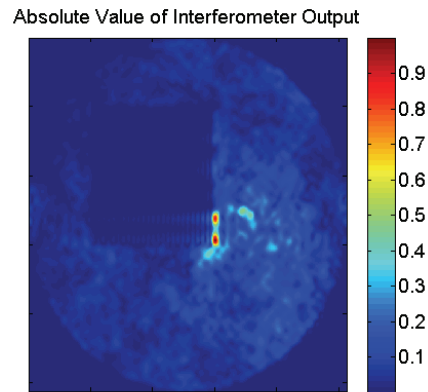
Figure 5.28: The obscuration, but also areas with low illumination, can be detected from the absolute value of the interferogram.

5.3.2 Instantaneous Phase-Shifting Interferometers

This section presents possible designs for instantaneous phase-shifting interferometers (PSI). Instantaneous means, that several interferograms are recorded at the same instant of time. Phase-shifting is for example achieved by a combination of quarter-wave plates and polarizers (or polarizing beam splitters). This approach is called geometric PSI in contrast to temporal PSI. Instantaneous PSIs have important advantages over sequential, temporal PSIs. They take several, usually three or four, interferograms at the same time. There are no moving mechanical parts involved and usually interfering beams take the same path through the interferometer. In the consequence this PSI type is robust to vibrations and other environmental effects, and the rate of the phase reconstruction is increased in comparison to temporal PSIs. These factors are important in the discussed application scenarios.

5.3.2.1 Four-Camera IPSI

Sivakumar et al. [SIV03] suggested an instantaneous PSI with four synchronized CCD cameras. The working principle is shown in Figure 5.29. The reference beam (horizontal-linear polarization) and the object beam (vertical-linear polarization) are split by three non-polarizing beam splitters (NPBS) into four interferometer arms. Each arm contains a combination of a polarizer and a quarter-wave plate to obtain the required phase shifts of 0°, 90°, 180°, and 270° between the reference and the object beam. With these four interferograms the phase of the incoming object wave can be estimated according to the methods presented in Section 5.2. The phase shifts can be calculated using Jones vectors and matrices, which describe the polarization state of a wave and the effects of polarization devices on the wave. Details are given in the Section A.6 Polarization and Jones Matrix.
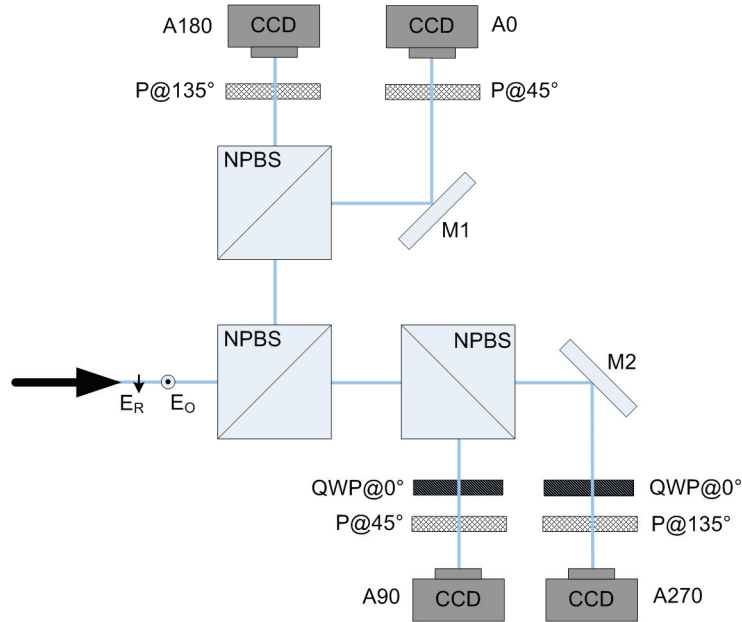
Figure 5.29: Design of an instantaneous PSI as suggested by Sivakumar et al. [SIV03]. Non-polarizing beam-splitters (NPBS) generate four interferometer arms (A0/90/180/270). Each arm contains a combination of a quarter-wave plate (QWP) and a polarizer (P). The degree value indicates the rotation of the device against the x-axis. The interference patterns are recorded by synchronized CCD cameras.

The polarization properties of each arm are listed in Table 5.3. Arms A0° and A180° contain a polarizer rotated by 45 degrees (P@45°) respectively 135 degrees (P@135°) against the x-axis. This allows the perpendicular input reference and object beam to interfere and produces relative phase shifts of 0 and 180 degrees. The according Jones matrices are

given by $J_{P@45°} = \dfrac{1}{2}\begin{bmatrix} 1 & 1 \\ 1 & 1 \end{bmatrix}$ and $J_{P@135°} = \dfrac{1}{2}\begin{bmatrix} 1 & -1 \\ -1 & 1 \end{bmatrix}$.

Arm A90° and A270° contain an additional quarter-wave plate (QWP@0°), which is oriented so that the fast axis is aligned with the horizontal x-axis. This introduces a phase shift of 90 degrees between the reference and the object beam. The Jones matrix of the

QWP is given by $J_{QWP@0°} = \begin{bmatrix} 1 & 0 \\ 0 & -i \end{bmatrix}$.

The additional mirrors (M1, M2) in arms A0° and A270° are essential to obtain images with the right orientation.

Reference and object beam are separated by a point-diffraction interferometer setup as described in Section 5.1.2. A polarizing beam splitter is used to obtain perpendicularly polarized reference and object beams.

Table 5.3: Summary of the polarization states and the phase-shifting properties of the interferometer arms. The reference wave E_R is horizontally and the input object wave E_O vertically polarized.

$J_R = \begin{pmatrix} 1 \\ 0 \end{pmatrix}$ $J_O = \begin{pmatrix} 0 \\ 1 \end{pmatrix}$	Jones Matrices	Output Polarization Reference, Object Wave	Polarization Devices
A0°	$\begin{bmatrix} 1 & 1 \\ 1 & 1 \end{bmatrix}$	$\begin{pmatrix} 1 \\ 1 \end{pmatrix}, \begin{pmatrix} 1 \\ 1 \end{pmatrix}$	P@45°
A90°	$\begin{bmatrix} 1 & -1 \\ -1 & 1 \end{bmatrix}\begin{bmatrix} 1 & 0 \\ 0 & -i \end{bmatrix}$	$\begin{pmatrix} 1 \\ -1 \end{pmatrix}, \begin{pmatrix} i \\ -i \end{pmatrix} = e^{i\pi/2}\begin{pmatrix} 1 \\ -1 \end{pmatrix}$	QWP@0° P@135°
A180°	$\begin{bmatrix} 1 & -1 \\ -1 & 1 \end{bmatrix}$	$\begin{pmatrix} 1 \\ -1 \end{pmatrix}, \begin{pmatrix} -1 \\ 1 \end{pmatrix} = e^{i\pi}\begin{pmatrix} 1 \\ -1 \end{pmatrix}$	P@135°
A270°	$\begin{bmatrix} 1 & 1 \\ 1 & 1 \end{bmatrix}\begin{bmatrix} 1 & 0 \\ 0 & -i \end{bmatrix}$	$\begin{pmatrix} 1 \\ 1 \end{pmatrix}, \begin{pmatrix} -i \\ -i \end{pmatrix} = e^{-i\pi/2}\begin{pmatrix} 1 \\ 1 \end{pmatrix}$	QWP@0° P@45°

Sivakumar's design still has the disadvantage that four separate cameras are required to record the four interferograms. The cameras have to be synchronized and the solution becomes costly especially for expensive (fast) InGaAs cameras, which have to be used at wavelengths in the infrared, e.g. for the widely used communication wavelength 1550nm.

5.3.2.2 One-Cameras IPSI

Notaras and Paterson [NOT07] gave a solution for an instantaneous PSI without the requirement of separate cameras. Their solution is based on the work of Dunsby et al. [DUN03]. All four interferograms are imaged on one camera chip next to each other. The interferometer principle is shown in Figure 5.30, and its properties are summarized in Table 5.4. In this design the input object and reference beam can be inserted either on two sides of the PSI non-polarizing beam splitter (NPBS) (as in Figure 5.30) or on only one side. The insertion from two sides gives the advantage, that the NPBS of the PSI can be part of the system generating the synthetic reference wave. In Figure 5.30 the incoming beam is split up with a polarizing beam splitter (PBS). The incoming beam has to be circularly polarized or linearly polarized with an angle of 45 degrees.
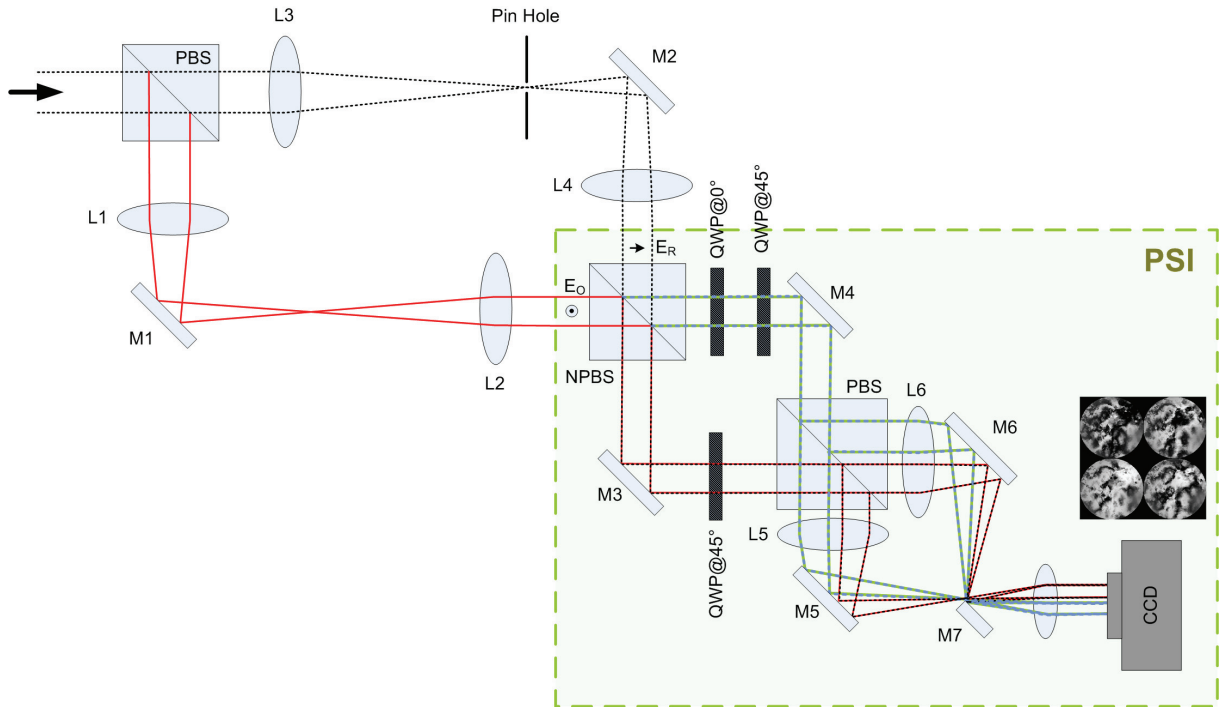
Figure 5.30: Design of an instantaneous PSI as suggested by Notaras and Paterson [NOT07] with the generation of a perpendicularly polarized reference wave. The four resulting interferograms of the PSI are imaged on one camera chip next to each other as shown in the inley. Key: Non-polarizing beam-splitter (NPBS), polarizing beam splitter (PBS), Quarter wave-plate with fast axis at 0 and 45 degrees to the x-axis (QWP@0°, QWP@45°), mirrors M1-7, lenses L1-6.

Table 5.4: Summary of the polarization states and the phase-shifting properties of the interferometer arms. The interferometer object wave E_O is vertically and the reference wave E_R horizontally polarized.

$J_R = \begin{pmatrix} 1 \\ 0 \end{pmatrix}$ $J_O = \begin{pmatrix} 0 \\ 1 \end{pmatrix}$	Jones Matrices	Output Polarization Object, Reference Wave	Polarization Devices
A0°	$\begin{bmatrix} 1 & 0 \\ 0 & 0 \end{bmatrix}\begin{bmatrix} 1 & i \\ i & 1 \end{bmatrix}\begin{bmatrix} 1 & 0 \\ 0 & -i \end{bmatrix}$	$\begin{pmatrix} 1 \\ 0 \end{pmatrix}, \begin{pmatrix} 1 \\ 0 \end{pmatrix}$	QWP@0° QWP@45° P@0°
A90°	$\begin{bmatrix} 1 & 0 \\ 0 & 0 \end{bmatrix}\begin{bmatrix} 1 & i \\ i & 1 \end{bmatrix}$	$\begin{pmatrix} 1 \\ 0 \end{pmatrix}, \begin{pmatrix} i \\ 0 \end{pmatrix} = e^{i\pi/2}\begin{pmatrix} 1 \\ 0 \end{pmatrix}$	QWP@45° P@0°
A180°	$\begin{bmatrix} 0 & 0 \\ 0 & 1 \end{bmatrix}\begin{bmatrix} 1 & i \\ i & 1 \end{bmatrix}\begin{bmatrix} 1 & 0 \\ 0 & -i \end{bmatrix}$	$\begin{pmatrix} 0 \\ i \end{pmatrix}, \begin{pmatrix} 0 \\ -i \end{pmatrix} = e^{i\pi}\begin{pmatrix} 0 \\ i \end{pmatrix}$	QWP@0° QWP@45° P@90°
A270°	$\begin{bmatrix} 0 & 0 \\ 0 & 1 \end{bmatrix}\begin{bmatrix} 1 & i \\ i & 1 \end{bmatrix}$	$\begin{pmatrix} 0 \\ i \end{pmatrix}, \begin{pmatrix} 0 \\ 1 \end{pmatrix} = e^{-i\pi/2}\begin{pmatrix} 0 \\ i \end{pmatrix}$	QWP@45° P@90°

Another design suitable as an instantaneous PSI was suggest by Kwon [KWO87], using a grating in a focus plane to split the object beam into three replicas. If the grating is laterally shifted by a quarter of the grating period, the three replicas obtain different phase shifts separated by $\pi/2$, which can then be used with a three-step algorithm. The principle design is shown in Figure 5.31. Another grating design was suggested by Hettwer et al. [HET00],

but here the grating was only used to split up the beam into three arms. The phase shifts were introduced by separate wave plates and polarizers.
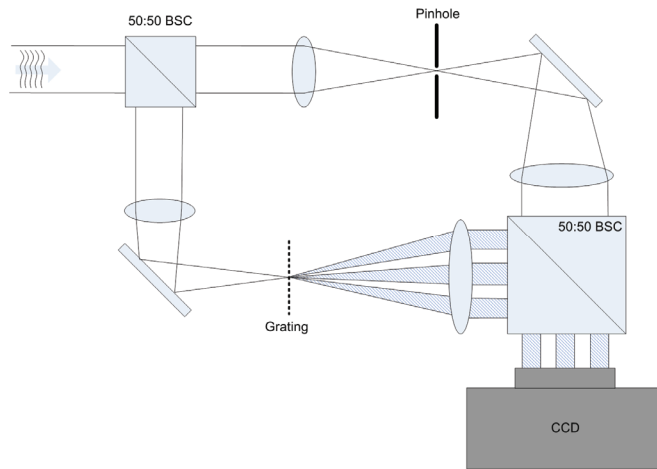

Figure 5.31: Instantaneous PSI using a laterally shifted grating [KWO87].

5.3.2.3 IPSI with a Pixelated Polarization Mask

Millerd et al. [MIL05] proposed an instantaneous PSI design with a polarizer mask as shown in Figure 5.32. The vertically polarized object beam and the horizontally polarized reference beam pass a quarter-wave plate rotated by 45 degrees to generate left and right circularly polarized beams (which are shifted by $\pi/2$). In front of the image sensor a polarizer mask is inserted with four different orientations of the polarization. Each pixel gets one of the four polarization orientations, and four pixels form a super-pixel, for which the input phase can be calculated over the 2π phase circle. According to the polarization orientations of 0, 45, 90 and 135 degrees, the phase shifts 0, 90, 180, and 270 degrees are generated within one super-pixel. Table 5.5 summarizes the resulting phase shifts of the four mask cells.
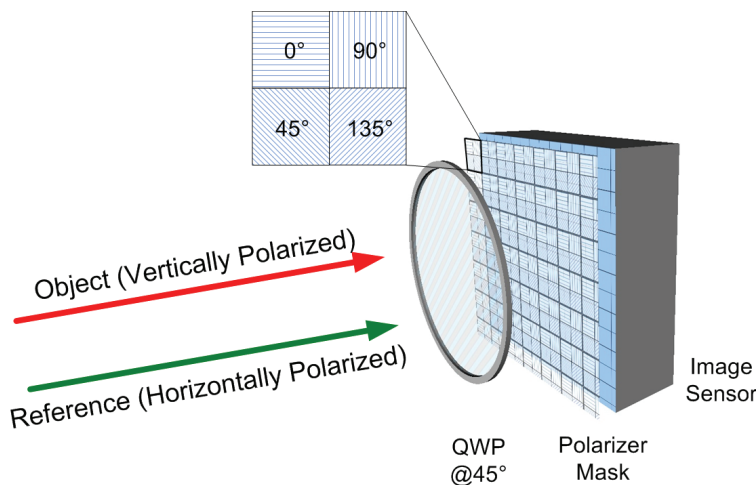

Figure 5.32: Design of an instantaneous PSI as suggested by Millerd [MIL05]. The linearly polarized object and reference beams are converted to circularly polarized beams with opposite sign. In front of the image sensor a polarizer mask is inserted with four different polarization states (0, 45, 90, 135 degrees). Always four pixels are joined to one super-pixel, which allows the phase reconstruction.

Table 5.5: Summary of the polarization states and the phase-shifting properties of the interferometer sections. The input object wave E$_O$ is vertically and the reference wave E$_R$ horizontally polarized.

$J_R = \begin{pmatrix} 1 \\ 0 \end{pmatrix}$ $J_O = \begin{pmatrix} 0 \\ 1 \end{pmatrix}$	Jones Matrices	Output Polarization Object, Reference Wave	Polarization Devices
A0°	$\begin{bmatrix} 1 & 1 \\ 1 & 1 \end{bmatrix}\begin{bmatrix} 1 & i \\ i & 1 \end{bmatrix}$	$\begin{pmatrix} 1+i \\ 1+i \end{pmatrix}, \begin{pmatrix} 1+i \\ 1+i \end{pmatrix}$	QWP@45° P@45°
A90°	$\begin{bmatrix} 1 & 0 \\ 0 & 0 \end{bmatrix}\begin{bmatrix} 1 & i \\ i & 1 \end{bmatrix}$	$\begin{pmatrix} 1 \\ 0 \end{pmatrix}, \begin{pmatrix} i \\ 0 \end{pmatrix} = e^{i\pi/2}\begin{pmatrix} 1 \\ 0 \end{pmatrix}$	QWP@45° P@0°
A180°	$\begin{bmatrix} 1 & -1 \\ -1 & 1 \end{bmatrix}\begin{bmatrix} 1 & i \\ i & 1 \end{bmatrix}$	$\begin{pmatrix} 1-i \\ -1+i \end{pmatrix}, \begin{pmatrix} -1+i \\ 1-i \end{pmatrix} = e^{i\pi}\begin{pmatrix} 1-i \\ -1+i \end{pmatrix}$	QWP@45° P@135°
A270°	$\begin{bmatrix} 0 & 0 \\ 0 & 1 \end{bmatrix}\begin{bmatrix} 1 & i \\ i & 1 \end{bmatrix}$	$\begin{pmatrix} 0 \\ i \end{pmatrix}, \begin{pmatrix} 0 \\ 1 \end{pmatrix} = e^{-i\pi/2}\begin{pmatrix} 0 \\ i \end{pmatrix}$	QWP@45° P@90°

5.3.3 Common-Path Interferometer with a Gradient Optimization Scheme

Vorontsov et al. [VOR01] and Justh et al. [JUS01] investigated the use of various phase contrast techniques, as they are discussed in Section 5.1.1.1, for high-resolution adaptive optics in combination with iterative methods. In iterative techniques usually some performance metric J has to be optimized. This could be for example

$$J(u) = S(\varphi, u) - \alpha_1 (\bar{u} - u_0)^2 - \alpha_2 \iint_A |\nabla u(\bar{r})|^2 d^2 r, \qquad (5.94)$$

where S denotes the Strehl ratio, u the actuator positions of the AO system, $\bar{u}$ the average of all actuator positions, u_0 the actuator target position. To avoid a phase drift of all actuators the penalty term $\alpha_1 (\bar{u} - u_0)^2$ is introduced. The third term penalizes large inter-actuator steps in order to keep the corrector phase smooth enough. α_1 and α_2 are appropriate scaling factors to fix the penalty term contribution. The Strehl ratio S can be substituted by a term integrating the input field over the aperture

$$J(u(\bar{r})) = \left| \iint_A |g_{in}(\bar{r})| e^{i[\varphi(\bar{r}) + u(\bar{r})]} d^2 r \right|^2 - \alpha_1 (\bar{u} - u_0)^2 - \alpha_2 \iint_A |\nabla u(\bar{r})|^2 d^2 r. \qquad (5.95)$$

The gradient of the performance metric

$$J'(\bar{r}) = \frac{\partial J(u(\bar{r}))}{\partial u(\bar{r})} \qquad (5.96)$$

is required to close the loop of an AO system with a gradient-optimization technique. Justh et al. could show that the gradient of the performance metric $J'(\bar{r})$ can be expressed taking the result of the differential Zernike filter (5.13)

$$I_{dif}(\bar{r}) = \frac{1}{2}\{I_{zer}^{(+)}(\bar{r}) - I_{zer}^{(-)}(\bar{r})\} = 2|g_{in}(\bar{r})||g_0|\sin(\tilde{\varphi}(\bar{r}) + u(\bar{r})), \qquad (5.97)$$

161

which now includes the actuator positions $u(r)$. $J'(\vec{r})$ can then be derived from (5.95) with (5.97)

$$J'(\vec{r}) = -I_{dif}(\vec{r}) - 2\alpha_1(\bar{u} - u_0) + 2\alpha_2 \nabla^2 u(\vec{r}). \tag{5.98}$$

This can be used to close the loop of the AO system to drive the corrector actuators (now showing the time dependences)

$$\frac{\partial u(\vec{r},t)}{\partial t} = -\kappa_0 I_{dif}(\vec{r},t) - \kappa_1(\bar{u}(t) - u_0) + \kappa_2 \nabla^2 u(\vec{r},t), \tag{5.99}$$

where $\kappa_0, \kappa_1, \kappa_2$ depend on the parameters α_1, α_2 and govern the closed-loop behavior. The correct effect of $I_{dif}(\vec{r})$ is relatively intuitive for small phase distortions where (5.97) can be substituted by the linear equation $2|g_{in}(\vec{r})||g_0|\sin\tilde{\varphi}(\vec{r}) \approx 2|g_{in}(\vec{r})||g_0|\tilde{\varphi}(\vec{r})$, however Justh's and own simulations showed that (5.99) even provides good correction results for phase distortions larger 2π. And even positive results were achieved with strong intensity fluctuations (not a constant amplitude over the aperture) of the input signal $|g_{in}(\vec{r})|^2$, as the sum-term $|g_{in}(\vec{r})|^2$ in (5.100) cancels out during the subtraction of the two interferometer images. Nevertheless an intensity dependent factor $|g_{in}(\vec{r})|$ remains in (5.97), which slightly decreases the performance of the closed-loop system.

Eq. (5.99) can also be built up with a single Zernike phase contrast interferometer as in (5.10) assuming a constant illumination over the telescope aperture

$$I_{zer}^{(+)}(\vec{r}) = |g_{in}(\vec{r})|^2 + 2|g_0|^2 + 2|g_{in}(\vec{r})||g_0|\{\sin[\tilde{\varphi}(\vec{r}) + u(\vec{r})] - \cos[\tilde{\varphi}(\vec{r}) + u(\vec{r})]\}. \tag{5.100}$$

Here the first two constant terms and of course the cosine term potentially destroy the closed-loop operation. But as long as the input amplitude is approximately constant, (5.100) in (5.99) provides good results. For a varying amplitude, $|g_{in}(\vec{r})|^2$ becomes a dominating term in (5.100), and the closed-loop operation fails. A solution for this is to separately measure the intensity distribution $|g_{in}(\vec{r})|^2$ in the aperture and to subtract it in (5.100). Thus, modifying (5.99) yields

$$\frac{\partial u(r,t)}{\partial t} = -\kappa_0'\left[I_{zer}^{(+)}(\vec{r},t) - |g_{in}(\vec{r})|^2\right] - \kappa_1(\bar{u}(t) - u_0) + \kappa_2 \nabla^2 u(r,t), \tag{5.101}$$

which allows an iterative closed-loop operation with only two measurements in the aperture, one interferometer and one amplitude distribution.

Figure 5.33 illustrates a simulated closed-loop operation with a constant amplitude distribution based on a differential Zernike interferometer approach (5.99). The Strehl ratio increases within 7 iterations form 0.06 to 0.84. In the images of the corrected phase (wrapped and unwrapped), phase walls can be spotted, which separate regions with 2π difference. These regions do not deteriorate the Strehl ratio, however, pose a problem for continuous membrane mirrors. This problem might be solved with optimized parameters of the second and third term in Eq. (5.99).
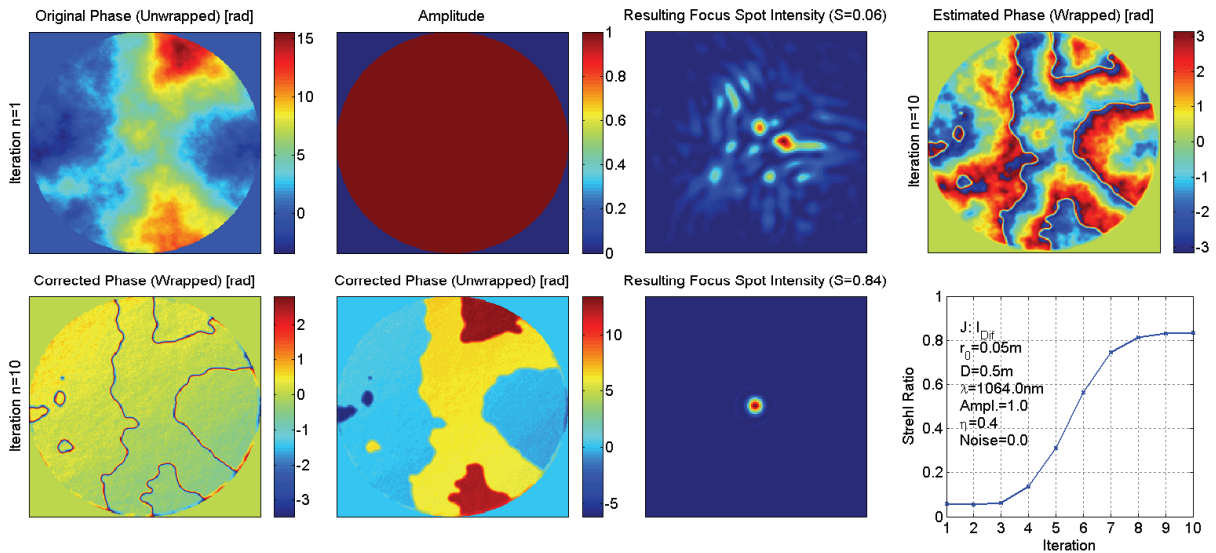
Figure 5.33: Iterative correction of a phase distortion with uniform amplitude distribution (A=1) and r_0=5cm on a 50cm telescope aperture. The AO system is based on (5.99). Top row: Uncorrected field (unwrapped phase/amplitude) with focus spot (iteration n=1), estimated phase after 10 iterations; Bottom row: Corrected phase (wrapped and unwrapped), focus spot after 10 iterations, and Strehl ratio.

Figure 5.34 illustrates a simulated closed-loop operation including amplitude variations based on a positive Zernike interferometer and an additional measurement of the intensity distribution in the aperture using Eq. (5.101). The Strehl ratio increases within 10 iterations form 0.05 to 0.63. The input field generated in a PILab simulation for a 10° elevation SGL scenario contains a number of phase singularities. The attempt to unwrap the corrected phase with a standard unwrapping algorithm fails due to phase singularities, causing vertical stripes.
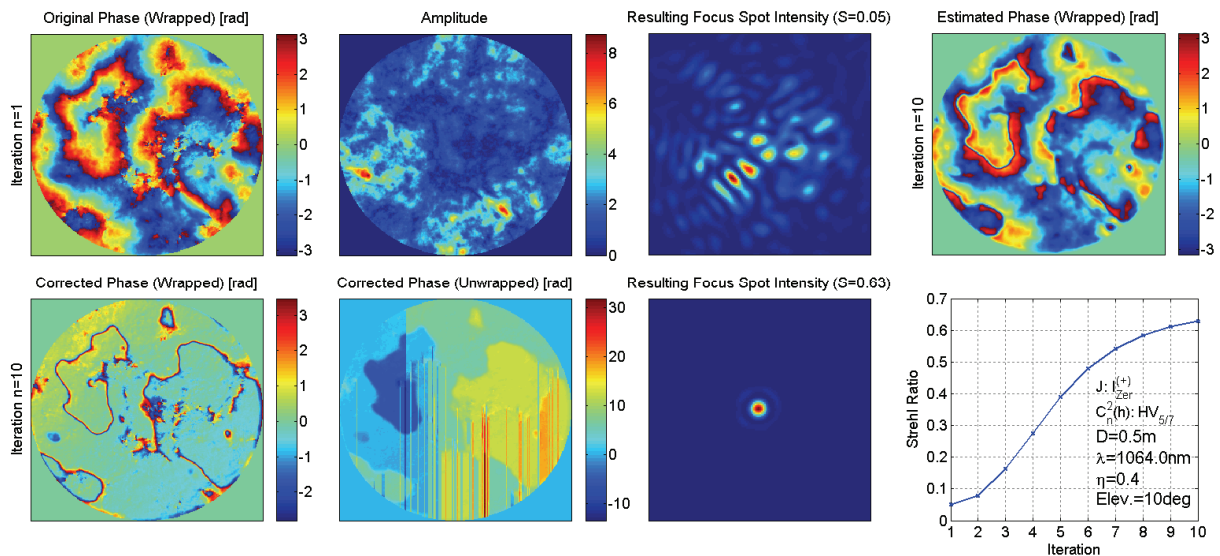

Figure 5.34: Iterative correction of a phase distortion including amplitude fluctuations. The input field simulates an SGL scenario at 10° elevation with a HV$_{5/7}$ C_n^2 profile at $\lambda = 1064 nm$. Aperture diameter is 50cm. The AO system is based on (5.101) using a single interferometer and an additional measurement of the intensity distribution in the aperture. Top row: Uncorrected field (wrapped phase/amplitude) with focus spot (iteration n=1), estimated phase after 10 iterations; Bottom row: Corrected phase (wrapped and unwrapped), focus spot after 10 iterations, Strehl ratio.

5.4 Control of the Corrector with a Wrapped Phase

Interferometric wavefront sensors return the measured phase wrapped in the interval $[-\pi, +\pi]$. It is intuitive to understand how to drive a segmented mirror with such a wrapped phase, but this becomes less obvious for a continuous mirror, which is not able to accurately reproduce the wrapped phase of the wavefront sensor. Principally there are two approaches to drive continuous mirrors with a wrapped phase:

- Control the mirror within the interval $[-\pi, +\pi]$: Simply control the mirror with the wrapped signal of the interferometric wavefront sensor. This limits the stroke of the mirror to a range of 2π. The 2π phase steps can be replicated by the continuous mirror only with limited accuracy.

- Unwrapping the phase by some method as described by Ghiglia and Pritt [GHI98]. The phase would be only wrapped, when it leaves the stroke of the mirror or when a continuous unwrapping is not possible due to branch points; however, unwrapping algorithms require processing power, especially the more complex techniques yielding good results also in the presence of branch points.

Notaras and Paterson [NOT07] presented an AO system with an instantaneous PSI sensor and evaluated the performance of the system. Their experiments confirmed that an AO system, which drives the continuous mirror with an unwrapped phase, performed better than simply driving the mirror with the wrapped phase.

The continuous mirror shows the largest fitting errors, if the driving phase has $2\pi m \; (m = \ldots -1, 0, 1, \ldots)$ steps. Therefore phase steps between neighboring actuators should be avoided, which is expressed in minimizing the following sum

$$\sum_{k=1}^{K-1}\sum_{l=1}^{L-1}\left\{\phi(k+1,l)-\phi(k,l)\right\}^2 + \left\{\phi(k,l+1)-\phi(k,l)\right\}^2 , \qquad (5.102)$$

where $\phi(k,l)$ is the phase $\varphi(k,l)$ corrected by $2\pi m(k,l)$ so that

$$\phi(k,l) = \varphi(k,l) + 2\pi m(k,l). \qquad (5.103)$$

(k,l) denote the discrete coordinates of the phase measurement points in the aperture, and $m(k,l)$ are integer values to get an optimum correction of the phase distortions with the continuous mirror.
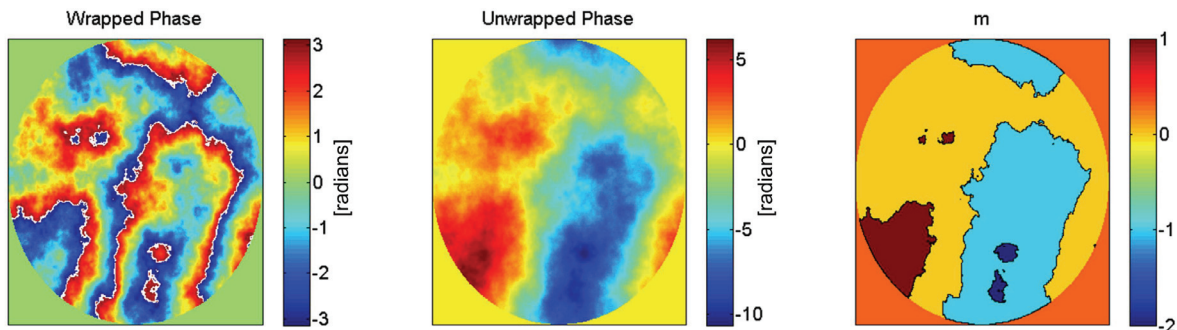
Figure 5.35: Comparison of a wrapped (simulated) phase in the interval $[-\pi, +\pi]$ (left) and an unwrapped phase (center). The 2π phase steps in the wrapped phase are marked with white lines. The right graph shows the integer values m to get an unwrapped phase.

An advantage of interferometric sensors is that they reconstruct the phase locally, not taking neighboring regions into account. Therefore in strong scintillation, where some parts of the

telescope aperture might not be illuminated, the mirror can still be driven in the areas, which have enough light. In the case of gradient sensors, like Shack-Hartmann or curvature sensor, the reconstruction of the phase is based on the slopes of the full aperture. As a consequence the reconstruction might give a wrong phase distribution over the aperture, if some of the slopes are not illuminated. The errors would not be confined to the dark regions but would affect the whole reconstructed phase

5.5 Discussion

Chapter 5 discussed various aspects of interferometric wavefront sensors. Section 5.1 introduced the fundamental concepts of common-path and point-diffraction interferometers. A critical issue in the discussed scenarios is the generation of the SRW, which itself is influenced by the atmospheric phase distortions. This is especially an issue to start-off the AO system. When the AO system is in operation, the remaining phase errors should be small enough to guarantee a stable SRW.

Section 5.2 presented in depth PSI algorithms and evaluated their robustness to error influences such as phase-shifting errors, nonlinearities, noise, and vibration errors. Among the 4-step PSIs only Bruning's algorithm (Table 5.1, #3, $N=4$) showed an increased robustness to nonlinearities and vibration errors. Schwider's algorithm (Table 5.1, #6, $N=4$) showed an improvement under phase-shifter errors.

Section 5.3 presented several interferometer designs. IPSI techniques should have the best performance in terms of speed, as they do not require complex calculations; however, the effort for the optical system is higher. Single interferometer techniques like the FFA method have a simple design, but require two Fourier transforms for the phase reconstruction. The iterative technique of Vorontsov requires one interferometer and one intensity measurement, but a good phase reconstruction is only achieved after several iterations, which slows the performance of the closed-loop AO system.

6 Experimental Verification of Interferometric Wavefront Sensors

6.1 Adaptive Optics Test Environment

Since 2008 a test environment for laser communications through the atmosphere and the correction of phase distortions by adaptive optics (AO) has been built up in a laboratory environment [MOL09]. This testbed is intended to optimize AO methods, test different wavefront sensors, and optimize fiber-coupling in connection with a phase correction.

The experiments presented here are not intended to show a finished AO system, but they demonstrate the basic principles of the interferometric wavefront sensors. Further developments are still required to achieve a fast enough processing and grabbing of the camera images to correct the phase distortions of the atmospheric turbulence generator or of an atmospheric field test-range.

Figure 6.1 shows the AO and fiber-coupling testbed. It contains a tip-tilt mirror, a deformable mirror, and as wavefront sensors a conventional Shack-Hartmann sensor and the test interferometer. The interferometer is designed in a Mach-Zehnder type configuration as in Figure 5.6. The used camera from Xenics (Cheetah CL640) has an InGaAs sensor chip. This reduces the quality of the obtained images, as InGaAs exhibits higher noise levels and larger variations in the pixel amplification factors, but it enables the use of the widespread communication wavelength of 1550nm. Some details on the components are summarized in Table 6.1.

The Shack-Hartmann sensor and the points-spread function camera are intended for a future comparison with the interferometric wavefront sensor. In this way the performance of the wavefront sensors can be directly evaluated without the need of a closed-loop AO system and the comparison with the Strehl ratio of the corrected phase.

Two laser sources with different quality at 1550nm are available to perform experiments with different coherence length. The setup of the interferometer has slightly different path lengths of the optical arms, since no measures were taken to make them equal except for a visual inspection. This causes a deterioration of the interferometer fringe visibility, if the path length difference reaches the order of the laser coherence length. The high-quality laser from TeraXion has a linewidth of $\triangle v_{FWHM} \approx 2.5 \text{kHz}$ and a very long coherence length. Fringe visibility is almost ideal. The IPG Photonics has a linewidth of $\triangle v_{FWHM} \approx 80 \text{GHz}$, which causes a slight deterioration of the fringe quality.

The deformable mirror is a continuous Boston Micromachines Multi-DM140 with 140 actuators and a fast response time with frequencies of up to 2-4kHz, which is required for the atmospheric conditions met in an SGL scenario with bandwidth demands of several 100Hz as shown in Section 4.2.4.
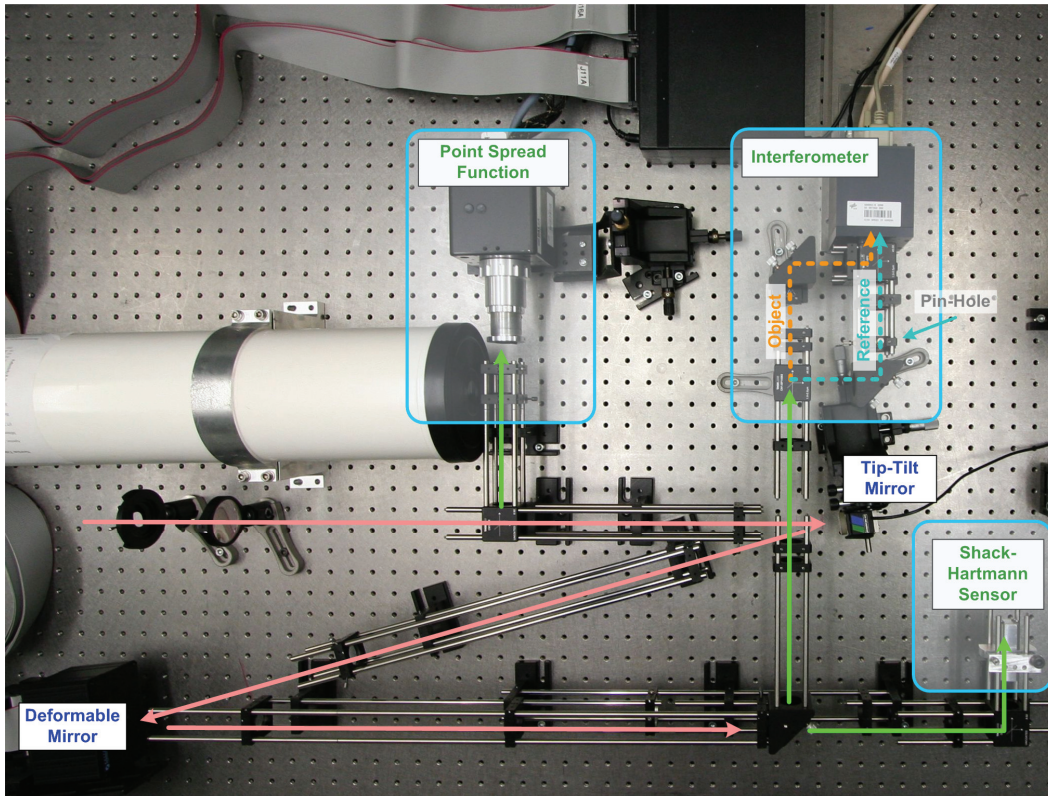
Figure 6.1: Setup of the AO system on the optical table. The incoming beam (red) with the distorted wavefront is reflected by a tip-tilt mirror and a deformable mirror. After the correcting elements the beam is directed to a Shack-Hartmann sensor and an interferometer experiment setup. The interferometer setup is implemented in a Mach-Zehnder configuration with the pin-hole in the reference arm.

Table 6.1: Components of the laboratory testbed.

System	Manufacturer Instrument Type	Specification
Camera SHS & Interferometer	Xenics Cheetah-640CL	InGaAs detector, λ=0.9-1.7µm, 640x512 pixels, pixel size 20x20µm, 400fps, CameraLink interface
Camera Point Spread Function	Dalsa CA-D1	Si detector, λ=0.4-1.0µm, 128x128 pixels, pixel size 16µm, 720fps
Deformable Mirror	Boston Micromachines Multi-DM140	12x12 actuators, 3.5µm stroke, pitch 400µm, 2-4kHz, protective-window coating for 635nm, 1064nm, 1550nm.
SHS Lenslet Array	aµs APO-Q-P150-R4.5	Square, pitch 150µm, curvature radius R=4.5mm, f=9.7mm, fused silica, plano-convex
Laser 1550nm High quality	TeraXion Pure Pure Spectrum PS-NLL-1550	Linewidth ~2.5kHz, 13mW transmit power
Laser 1550nm	IPG Photonics IPG-ELD-1-1550	Erbium fiber laser, linewidth ~80GHz or 0.6nm, 10mW-1W transmit power

The principle lab setup can be seen in Figure 6.2. The communication laser beam passes an optical turbulence generator (OTG) twice and reaches the test setup of the AO and fiber-coupled communication system.
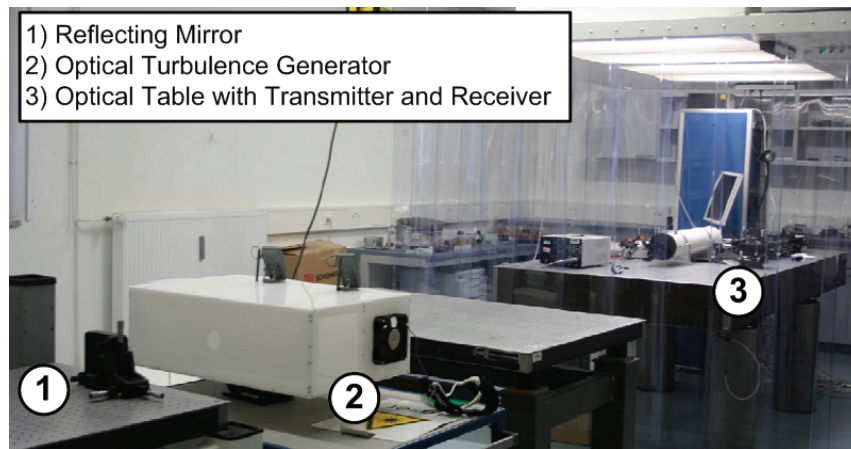

Figure 6.2: Adaptive optics testbed. The transmitter on the optical table under the clean room unit (3) sends the laser beam through the optical turbulence generator (OTG) (2). The beam is reflected with a flat mirror (1), propagates through the OTG a second time and reaches the receiver on the optical table (3).
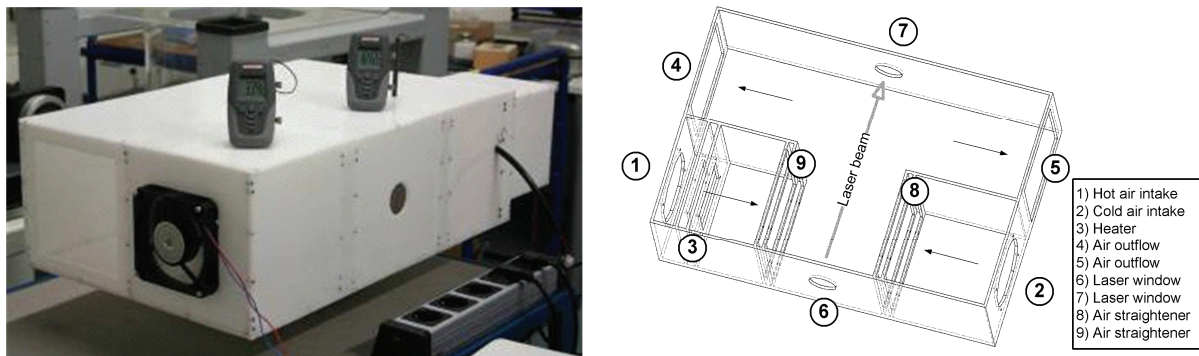

Figure 6.3: Concept of hot-air turbulence generator. The air is forced into the mixing chamber through inputs 1 and 2. A heating element warms up one of the flows and air straigtheners produce two laminar flows that collide in the mixing chamber. The mixed air leaves the box at the two outflows. The laser beam passes the turbulence through the holes at 6 and 7.

The atmospheric turbulence in the testbed is generated by an OTG (Figure 6.3), which is based on the mixing of two air flows, one heated and one at ambient temperature. Jolissaint [JOL06] gave a review on different methods to simulate atmospheric turbulence in lab setups. The specific setup in the DLR AO testbed was implemented by Florian Moll [MOL09] taking the specific environmental conditions of long atmospheric transmission paths into consideration. Moll also performed the characterization of the OTG to establish the relation between target atmospheric turbulence parameters, e.g. the atmospheric coherence length r_0, and the settings of the OTG, which are the speed and the temperature difference of the two air flows. This relation is plotted for several wavelengths in Figure 6.4, assuming a standard speed of the air flows (10V at the fans). The actual measurement was performed at 1064nm. Characteristic functions for other wavelengths λ' can be calculated with the scaling law

$$\frac{r_0'}{r_0} = \left(\frac{\lambda'}{\lambda} \right)^{6/5} ,$$

(6.1)

derived from turbulence theory as in Eq. (3.30). r_0 down to about 2mm can be achieved for a maximum temperature difference of 135K. The entrance aperture of the test setup on the optical table has a diameter of 15mm, therefore maximum ratios D/r_0 of about 7 can be reached taking the values of Figure 6.4.
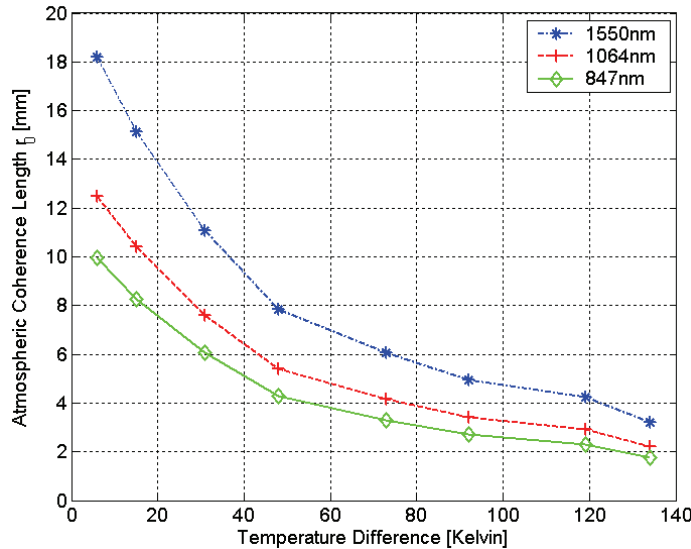

Figure 6.4: Measurement of r_0 over the temperature difference of the two air flows. The air-flow speed was set to a fixed value by the fan voltage (V_{fan} = 10V). The curves at 1550nm and 847nm were calculated with Eq. (6.1).

6.2 Interferometer Image Processing System

A first closed-loop AO system was setup with the interferometer shown in Figure 6.1. The interferometer processing is based on the FFA algorithm, implemented in a real-time AO system developed over the last years. The image processing is performed on a Matrox Odyssey Xpro+ PCI-X card with a Freescale G4 PowerPC. The functionality of the card is accessed with the Matrox Imaging Library (MIL). The software package itself is written in C++. A basic diagram of the Matrox Odyssey is shown in Figure 6.5. The card contains apart from the PowerPC an FPGA Altera Stratix II core, which is intended for a future extension of the wavefront-sensor image processing. The FPGA processing might prove especially interesting for phase-shifting techniques, which obviously can be parallelized and contain relatively simple numerical operations. More details on the processing system were described by Ramon Mata Calvo [MAT08], who also was responsible for the software development of the real-time system.

Figure 6.6 shows the graphical user interface of the AO real-time system. Basic functions as the camera control and area-of-interest adjustment are provided, but also functions to obtain the influence function between the wavefront sensor and the deformable mirror. In the left-lower corner the fringe pattern of the FFA algorithm is shown.
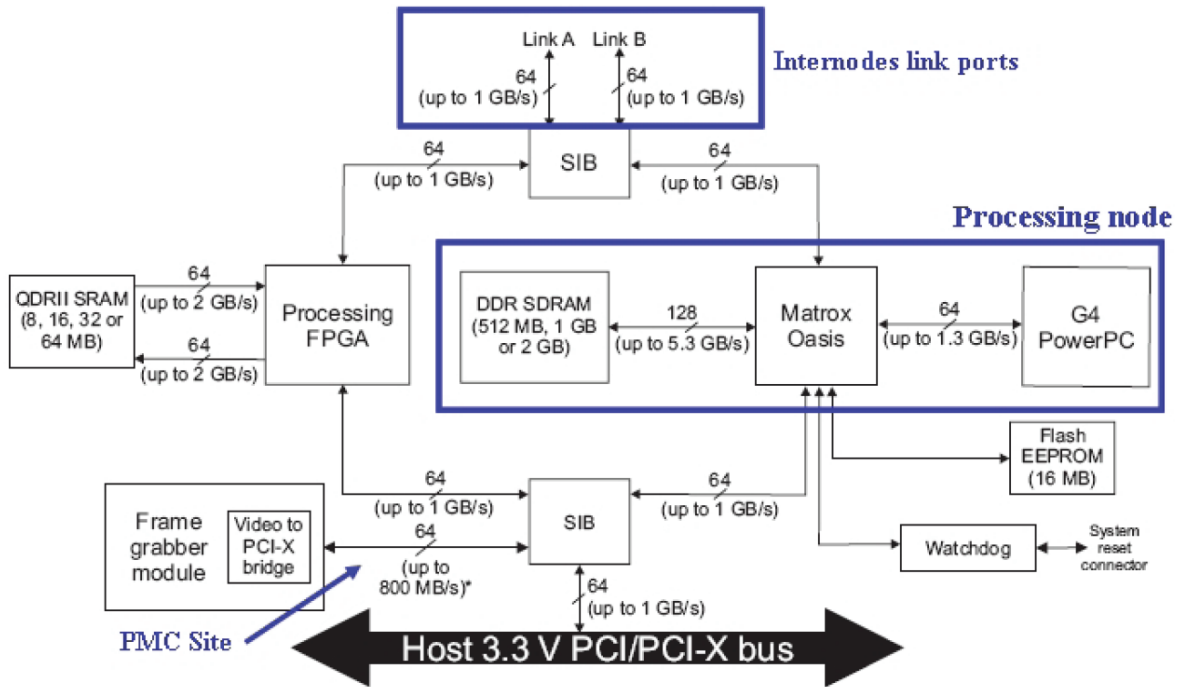
Figure 6.5: Scheme of the Matrox Odyssey XPro+ image-processing board with a frame grabber module (CameraLink), a G4 PowerPC, and an Altera Stratix II FPGA core.
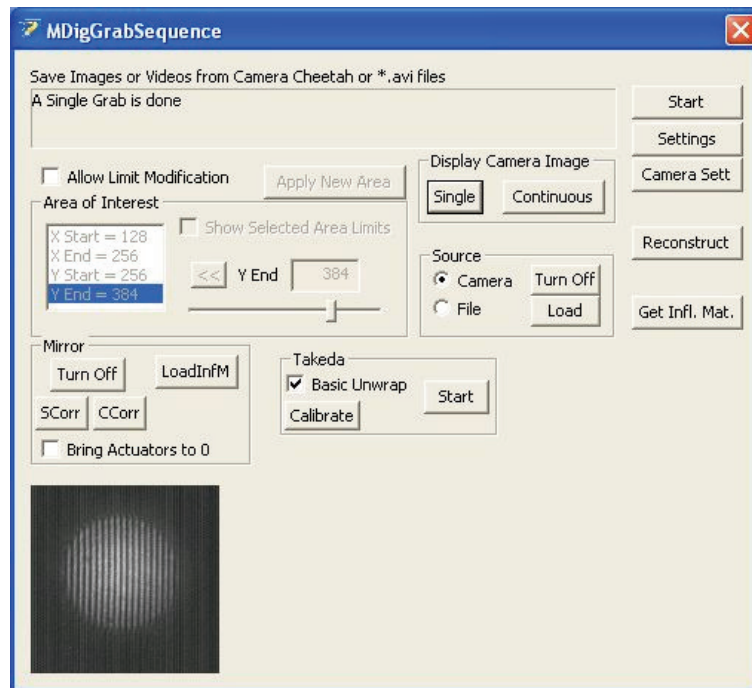

Figure 6.6: Graphical user interface to control the AO system.

Figure 6.7 shows the amplitude of the Fourier transform of the fringe pattern (compare Eq. (5.90)) for an undisturbed phase. The two side peaks and the central peak of the FFA technique can be seen. Due to the scaling the noise pattern around the three peaks becomes visible. The inlays show the fringe pattern and a cut through one of the side peaks.
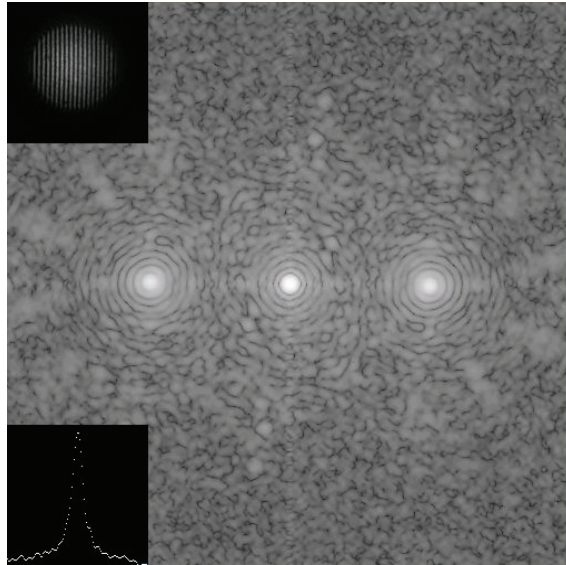
171

Figure 6.7: Amplitude of the Fourier transform of the FFA fringe pattern with the central peak and the two side peaks containing the phase information. Upper inlay: Fringe pattern from the camera. Lower inlay: Cut through the right side-peak.

6.3 Self-Referencing Interferometer in a Mach-Zehnder Configuration

A first test of the interferometer setup of Figure 6.1 and shown in more detail in Figure 6.8 is intended to illustrate the usability of a self-referencing interferometer under the atmospheric turbulence conditions generated by the OTG. The interferometer setup is based on the PDI description provided in Section 5.1.2.
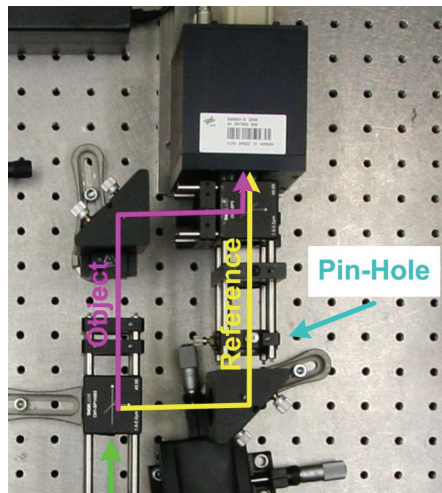

Figure 6.8: Self-referencing interferometer setup in a Mach-Zehnder configuration. The reference wave is created by a 75µm pin-hole $(\eta = 0.64)$**.**

Figure 6.9 shows the measured object wave intensity, reference wave intensity, and the resulting interferogram intensity distribution. The image of the object wave shows the intensity distribution in the entrance pupil of the system. A variable iris formed the entrance pupil. For the measurements the aperture had an open diameter of around 1cm and was imaged to a 1.6mm beam on the camera chip. Thus, with this optical system 80 pixels in diameter were illuminated on the camera. The area of interest of the camera chip was kept

small (128x128 pixels) to allow a higher frame rate. The image of the reference wave shows a Gaussian or Airy like distribution of the intensity.
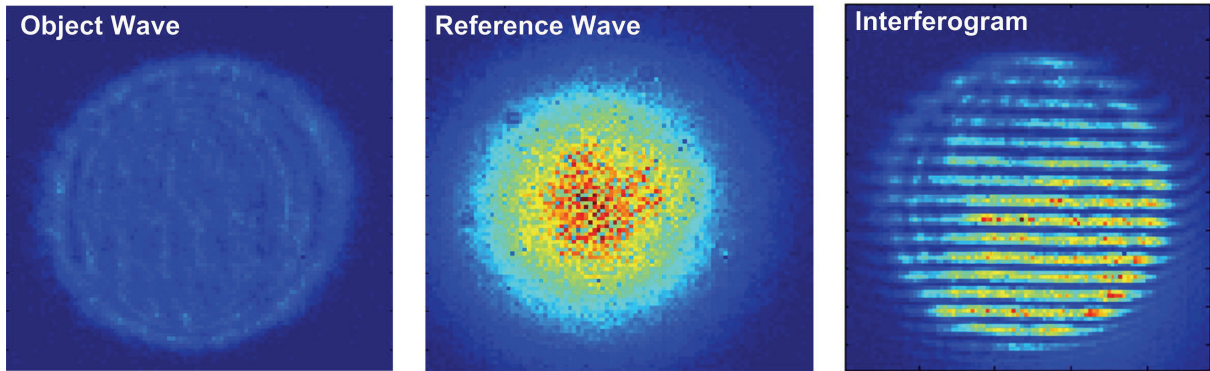

Figure 6.9: Object wave, synthetic reference wave, and the resulting interferogram from the self-referencing Mach-Zehnder interferometer. A slight tilt of the reference wave against the object wave was introduced for the Fourier reconstruction technique described in Section 5.3.1.

6.3.1 Characterization of the Reference Wave

Figure 6.10 shows in detail the shape of the reference wave on the camera chip. Assuming a 6.4mm beam diameter at the entrance lens of the interferometer, the diameter to the first zero of the Airy pattern at the pin-hole is given by Eq. (5.21)

$$D_{Airy} = 2.44 \frac{f \cdot \lambda}{D} \approx 118 \mu m \tag{6.2}$$

with the parameters $f = 200mm, \lambda = 1.55\mu m, D = 6.4mm$. A pin-hole with 75μm diameter was used to remove higher modes from the incoming beam, and thus the ratio of the Airy pattern and pin-hole diameter was $\eta \approx 0.64$. With this the intensity distribution in the aperture can be estimated from Figure 5.3, yielding a drop of the intensity at the rim of the aperture to about half of the maximum value. The cut through the amplitude distribution in the experiment (Figure 6.10) shows that the amplitude drops to about 40%, which is in good agreement with the theoretic predictions.
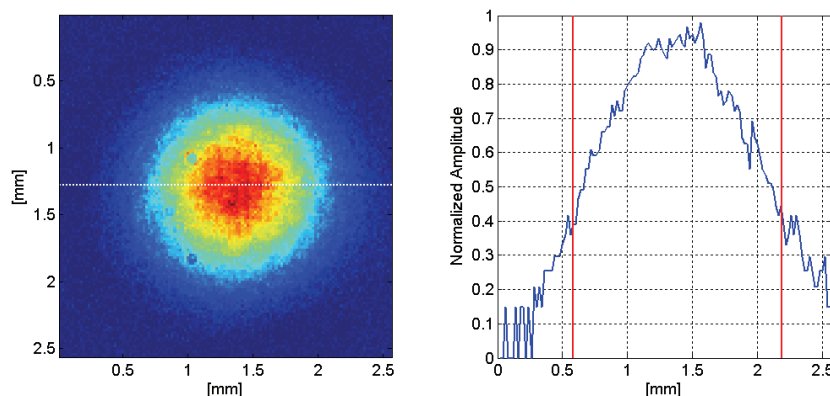

Figure 6.10: Example reference wave. Left: Amplitude distribution; Right: Cut through the distribution along the white line. The size of the pupil is indicated by vertical (red) lines showing that the amplitude drops to about 40% at the pupil rim. This is in good agreement with the values shown in Figure 5.3 for a pin-hole size of $\eta = 64\%$.

173

During the experiments it was observed that the Airy intensity distribution of the reference wave slightly moves with the tip-tilt error of the incoming wave (the extra tip-tilt correction was not active), while the pupil image produced by the object wave is fixed being an image of the entrance pupil. This has an effect on the visibility of the interferogram fringes, which varies over the aperture and over time. This problem can be improved, if the incoming wave is tip-tilt corrected by an independent system, which is anyway required to stabilize the strength of the reference wave (to hit the pin hole) before the initial start of the AO system.

Figure 6.11 illustrates the movement of the reference wave and the variations of its strength. Ten example images of the reference-wave intensity are shown in the top row, which were recorded during 1 second. Below the variance of the power fluctuations is shown, indicating power drops of 10dB due to the atmospheric disturbances of the OTG.
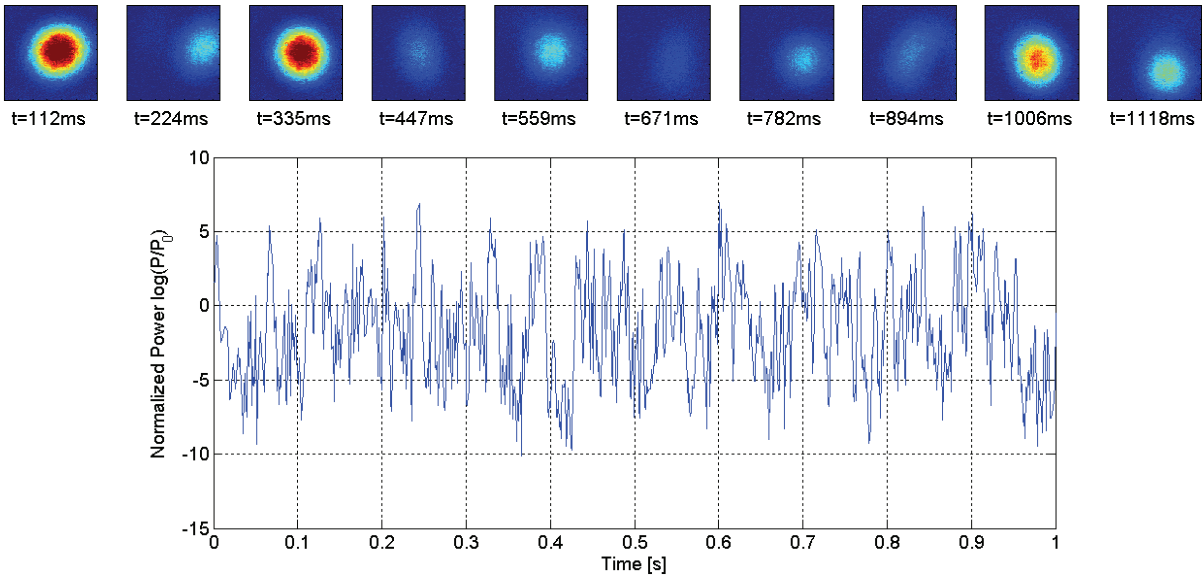
Figure 6.11: Behavior of the reference wave for a turbulence of $\triangle T \approx 80\text{K}$ **(Heating 70%,** $r_0 \approx 4\text{mm}$ **,** $D/r_0 \approx 2.5$ **). The graph shows the power values during 1s (~850 frames) normalized to the mean power. The power was taken over the area of the camera frame. Power fades of up to 10dB can be observed. In the upper line example images of the reference wave can be seen, illustrating the wander and the varying strength of the reference wave.**

6.3.2 Laser Linewidth and Fringe Visibility

The quality of the deployed lasers described by the laser linewidth $\triangle \nu_{FWHM}$ has a significant influence on the performance of the phase reconstruction, as the fringe visibility defined in Eq. (5.25) decreases with an increasing linewidth owing to the reduction of coherence between the waves in the two interferometer arms. The decrease of the fringe visibility depends on the coherence length of the used laser in relation to the optical path difference of the interferometer arms. The coherence length l_c of a laser is given by [SAL91, pp.346]

$$l_c = c \cdot \tau_c = \frac{c}{\triangle \nu_{FWHM}},$$

(6.3)

where c is the speed of light and $\tau_c = \dfrac{1}{\triangle \nu_{FWHM}}$ the coherence time. The degree of coherence is then given assuming a Gaussian distribution of the laser spectrum by

$$|\gamma_{12}| = \exp\left(-\frac{\pi \triangle \tau^2}{2\tau_c^2}\right) = \exp\left(-\frac{\pi \left(s_2 - s_1\right)^2}{2c^2 \tau_c^2}\right). \tag{6.4}$$

Here the optical path difference of the two arms is given by $s_2 - s_1$, resulting in a time difference of $\triangle \tau = \frac{s_2 - s_1}{c}$. The visibility of the fringes is also reduced by the factor $|\gamma_{12}|$ as shown in Eq. (5.28).

An experimental evaluation of the fringe visibility using the TeraXion $\left(\triangle \nu_{FWHM} = 2.5\text{kHz}\right)$ and the IPG Photonics $\left(\triangle \nu_{FWHM} = 80\text{GHz}\right)$ laser is depicted in Figure 6.12. The fringe visibility of the IPG Photonics laser was reduced by a factor 0.79, indicating a degree of coherence of $|\gamma_{12}| = 0.79$ assuming a perfect coherence for the TeraXion laser. The IPG Photonics laser has a coherence time $\tau_c = 12.5\text{ps}$ and therefore a coherence length $l_c = 3.8\text{mm}$. Using Eq. (6.4) this reduction could be explained by a (very plausible) path difference in the interferometer arms of about 1.4mm.

The reduced quality of the reconstruction can be also read from the ratio $\frac{I_{0,\max}}{I_{1,\max}}$ of the maximum intensities of the central peak $I_{0,\max}$ and the side peaks $I_{1,\max}$ in the Fourier transform. In the example the ratio increased from 3.1 to 7.5, i.e. the side peaks containing the phase information became weaker.
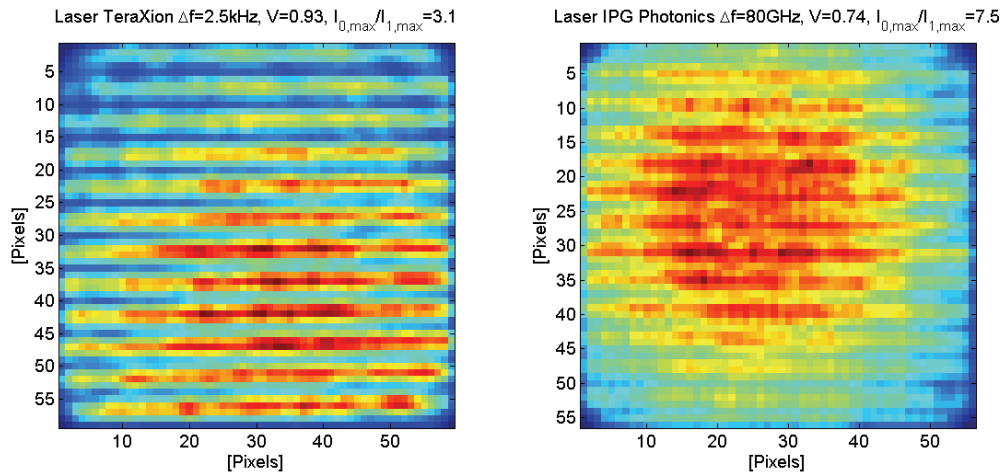
Figure 6.12: Deterioration of the fringe visibility due to the laser linewidth. Two 1550nm lasers with different quality were used yielding different fringe visibilities V**. Left: TeraXion** $\triangle \nu_{FWHM} = 2.5\text{kHz}$**,** V**=0.94; Right: IPG Photonics** $\triangle \nu_{FWHM} = 80\text{GHz}$**,** V**=0.75.**

6.3.3 Halo around the Interferogram

The halo around the interferogram stems from the intensity distribution of the reference wave (See Section 5.1.1.2) outside the pupil, where no interference occurs. Thus, the strength of the reference wave can be estimated by averaging the intensity distribution around the interferogram itself and knowing the shape of the intensity distribution in dependence of the pin-hole size as e.g. given in Eq. (5.23). A typical image of the halo, with the central interferogram region blinded out, is given in Figure 6.13. Slight errors probably due to a non-optimal imaging of the entrance pupil can be seen in the frayed rim, but the halo is well visible.
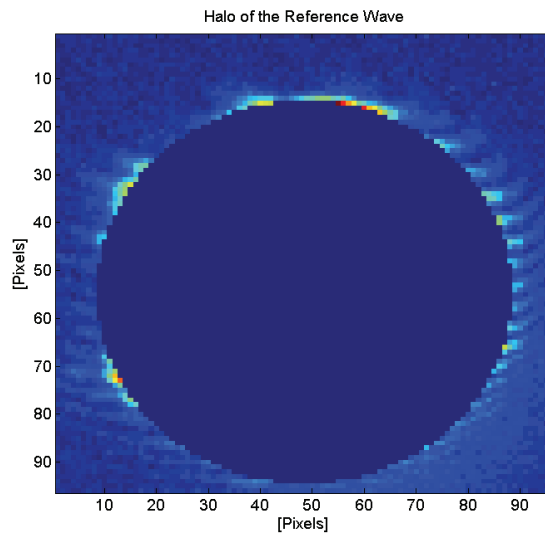
Figure 6.13: Halo around the interferogram caused by the reference wave outside the pupil. Some slight interference fringes remain and can be also seen around the central part of the interferogram, probably due to a non-optimal imaging of the entrance pupil.

6.3.4 Effects of Intensity Fades and Obscurations

In Section 5.3.1, Figure 5.27, it could be demonstrated in simulation that an obscuration of the interferogram affects only the corresponding area of the phase reconstruction, giving correct phase values for the unobstructed area. This could be also confirmed in the experiment. Figure 6.14 shows an obstructed fringe pattern (left) and the reconstructed phase (right) taken from the real-time software. The obscuration only influences the corresponding part, but allows correct phase values for the unobstructed side. This also confirms that scintillation fades cause wrong phase values only in the affected areas. The dark areas can be detected using the absolute value of the inverse Fourier transform as shown in Figure 5.28, and the unreliable phase values can be discarded.

Interesting to note is that the reference wave becomes visible in the obstructed area. This could be used to estimate the reference-wave strength in a telescope system with central obscuration, where the central part of the reference wave would be nicely observable.
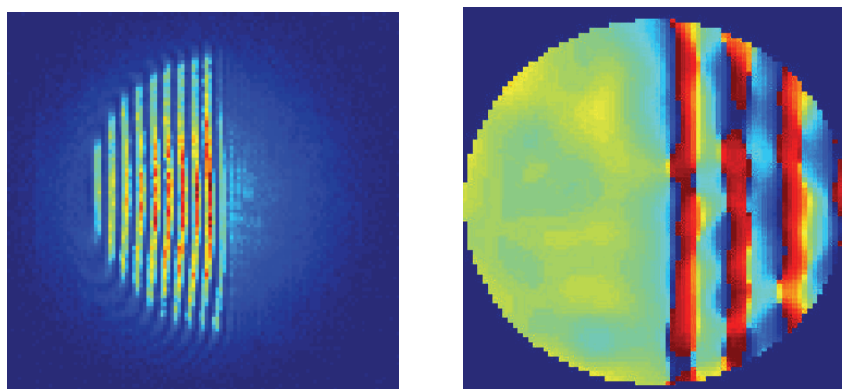

Figure 6.14: Test of masking a part of the interferometer image in the experiment. Left: The fringe pattern with the obscuration. Right: Result of the real-time phase reconstruction.

6.4 Fourier Fringe Analysis Technique for the Phase Reconstruction

Based on the Fourier Fringe Analysis (FFA) technique (Section 5.3.1) an analysis of a single interferometer was performed, and the phase was reconstructed. The density of the fringe pattern could be adjusted by tilting mirrors in the interferometer setup using micrometer

screws. The density was set to about 4 pixels per fringe. Figure 6.15 and Figure 6.16 show two examples. The interferogram of Figure 6.15 was recorded for a OTG temperature difference of the two air flows of about 20K with $r_0 \approx 9\text{mm}$ and $D/r_0 \approx 1$.
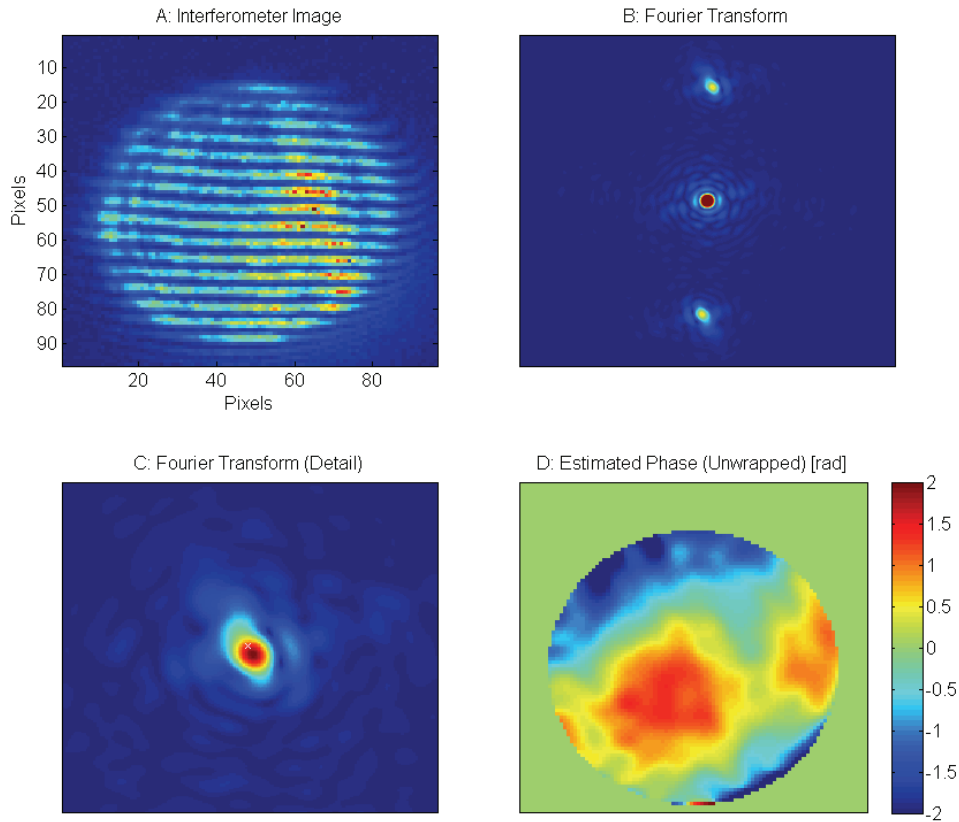
Figure 6.15: Fourier reconstruction algorithm for turbulence with $\triangle T \approx 20\text{K}$ (Heating 40%), $r_0 \approx 9\text{mm}$, $D/r_0 \approx 1$ at $\lambda = 1550\text{nm}$. A: Recorded fringe pattern; B: Fourier transform of the fringe pattern; C: Detailed view of the upper side peak in the Fourier transform; D: Reconstructed, unwrapped phase.

Figure 6.16 shows the interferogram pattern for a stronger turbulence scenario with $\triangle T \approx 80\text{K}$, $r_0 \approx 4\text{mm}$, $D/r_0 \approx 2.5$. Here phase singularities could be found in the reconstructed phase, which probably appear in the Fourier transforms due to noise. The intensity fades in this scenario are not strong enough to allow singularities due to atmospheric turbulence. The quality guided unwrapping technique presented in Ghiglia and Pritt [GHI98] was used for the phase unwrapping. In the fringe pattern stronger variations of the intensity and the visibility can be observed.
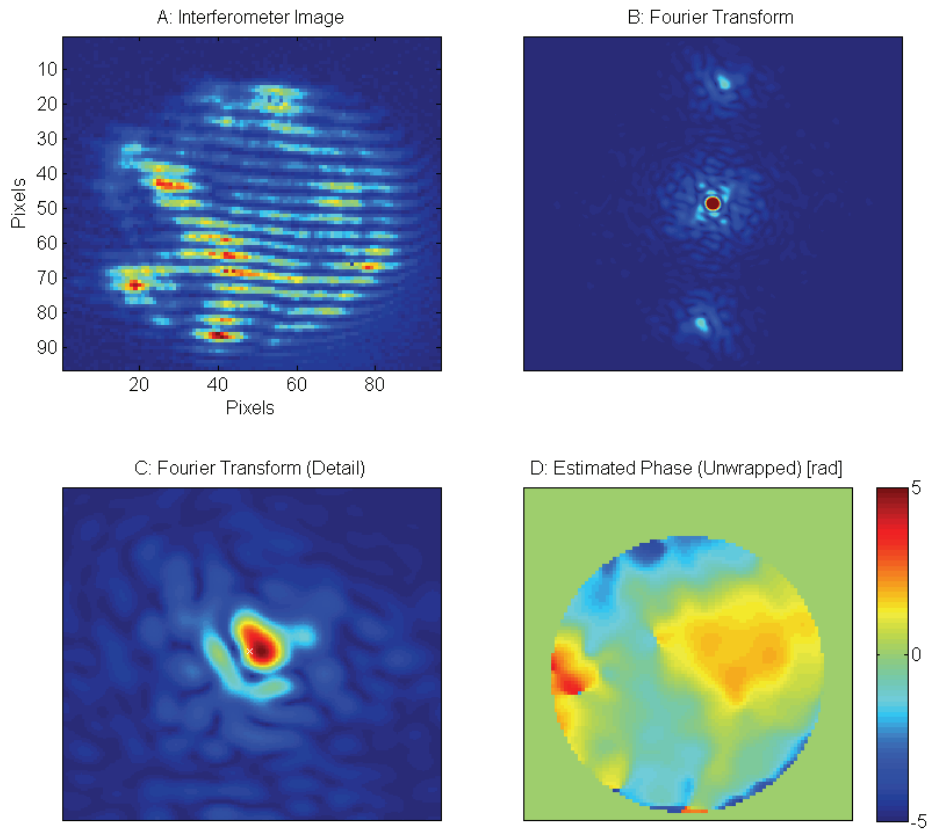
Figure 6.16: Fourier reconstruction algorithm for turbulence with $\triangle T \approx 80\mathrm{K}$ (Heating 70%), $r_0 \approx 4\mathrm{mm}$, $D/r_0 \approx 2.5$ at $\lambda = 1550\mathrm{nm}$. A: Recorded fringe pattern; B: Fourier transform of the fringe pattern; C: Detailed view of the upper side peak in the Fourier transform; D: Reconstructed, unwrapped phase.

6.5 Results of a First Closed-Loop System

Figure 6.17 shows the closed-loop performance of the AO system based on the FFA technique for a static phase disturbance, a transparent plastic plate. In the uncorrected case the focus spot is broken up in several speckles, while with the AO correction the focus is well corrected (almost diffraction limited) showing the first ring of the Airy distribution.

Currently, the real-time processing system is not optimized to achieve high frame rates and to correct the effects of the OTG. It was intended for a first demonstration of the phase reconstruction with an interferometer using the FFA technique. In a next step it is planned to increase the speed of the processing system to reach frame rates above 1kHz.
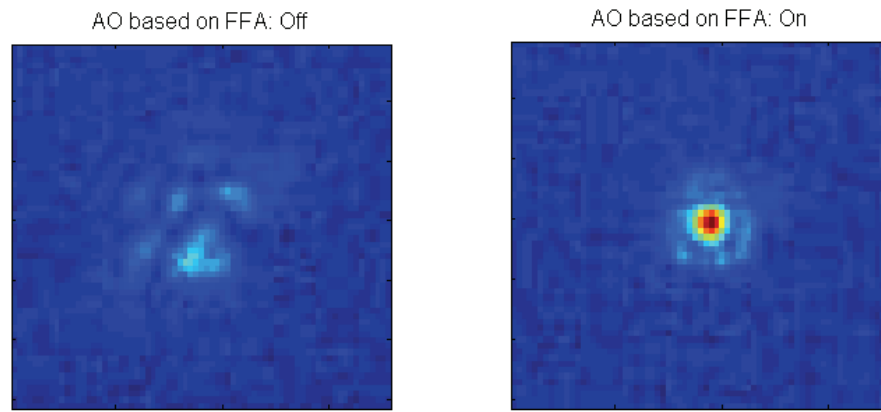
Figure 6.17: Performance of the closed-loop AO system with an FFA reconstruction. The phase disturbance was produced by a (low-quality) transparent plastic plate. Left: Focus spot of the uncorrected phase. Right: Focus spot with correction.

7 Conclusion and Future Work

7.1 Summary and Conclusions

This work has illustrated various aspects of adaptive optics (AO) systems, with an emphasis on wavefront sensors, for the deployment in LEO satellite-to-ground links (SGL). To my knowledge the applicability of AO systems in these scenarios has to date not been studied in this detail. For the understanding of the atmospheric conditions on the SGLs unique atmospheric measurements were performed with two satellites, OICETS and TerraSAR-X. The evaluation in this work, based on the measurement results and atmospheric theory, showed that typical wavefront sensors from astronomical applications are not very suitable for SGL scenarios. Severe phase distortions, intensity scintillations, and high bandwidth requirements on the AO system strongly impact on sensors such as the Shack-Hartmann. As an alternative, interferometric sensors provide a promising solution based on the analysis in Chapter 4 and 5. Interferometric wavefront sensors are widely used for surface testing, but they proved to have very favorable properties for the use in SGLs.

The content of this work is:

- General aspects of laser SGLs, current system designs of flight terminals, and ground stations.

- Overview on atmospheric conditions of SGLs based on theory, numerical simulations, and measurements in SGLs taking into account the effects on the communication beam. Description of the optical ground station and the measurement instruments.

- Derivation of AO requirements based on the presented atmospheric conditions.

- Performance analysis of various wavefront sensors under the presented atmospheric conditions.

- Selection of interferometric wavefront sensors as a promising approach and detailed analysis of interferometric techniques for the use in SGL scenarios.

- Experimental demonstration of an interferometric Fourier Fringe Analysis (FFA) technique with a single interferometer in the DLR atmospheric testbed.

- First closed-loop demonstration with the FFA technique.

The thesis structure is summarized in Figure 1.9 with the four main chapters: Atmospheric conditions, selection of a suitable wavefront-sensor concept for the atmospheric conditions in SGLs, analysis of interferometric sensors, and the experimental verification of an interferometric sensor in the atmospheric turbulence testbed.

LEO Satellite-To-Ground Links (Chapter 2)

LEO satellites are mostly seen under very low elevation angles, e.g. 90% of the link time below 30deg elevation at mid-range geographic latitude. Therefore, in order to achieve highest possible link durations, both the communication system and a possible AO system have to be able to cope with the difficult atmospheric turbulence conditions in these scenarios caused by the long path through dense regions of the atmosphere. Such scenarios are typically not found in astronomy, which operates at high elevation angles and at sites with extremely favorable seeing conditions.

Atmospheric Conditions (Chapter 3)

Strong power scintillation with fades down to zero are very disturbing for communication systems. These fades can be reduced with telescope apertures significantly larger than the intensity speckles of the received field (aperture averaging, e.g. D>20cm); however, this implies that phase distortions over the aperture become significant (the aperture becomes larger than the scales sizes of the phase distortions) and reveal their deteriorating impact on

coherent or fiber-coupled communication systems. As a consequence phase correction has to be implemented for reliable communication.

Several atmospheric measurement campaigns (at wavelengths $\lambda = 847\text{nm}$ and $\lambda = 1064\text{nm}$) have been performed with the DLR ground station between 2006 and 2009. The main results of these campaigns are presented here, with an emphasis on parameters significant to AO systems and communication links. SGLs are characterized by very strong scintillation ($\sigma_I^2 > 2$) and phase distortions (r_0 down to 1cm) at low elevation angles. Due to the motion of the beam through the atmosphere, the bandwidth requirements for an AO system are significantly increased ($f_G > 1\text{kHz}$) compared to astronomical applications; in addition, phase singularities appear below 30 degrees elevation, which potentially destroy the performance of some of the widely-used (mainly in astronomy) wavefront sensors.

Conventional Wavefront Sensors (Chapter 4)

The performance of several wavefront sensors has been studied under the described atmospheric turbulence conditions. Two widespread sensors, the Shack-Hartmann and the curvature sensor, show quickly deteriorating quality of the reconstructed phase in the strong fluctuation regime. Specialized reconstruction algorithms have been developed for the Shack-Hartmann sensor to cope with this situation, which, however, are more complex, numerically more demanding, and require a higher resolution of the sensor. High resolution implies that the frame rate of currently available cameras becomes too low in view of the severe bandwidth requirements in the SGL scenarios.

Shearing interferometers have a behavior similar to the Shack-Hartmann sensor, as they also reconstruct the phase from phase derivatives. Consequently, they suffer from similar problems as the Shack-Hartmann sensor.

Phase retrieval methods have the advantage that they allow a phase reconstruction from the intensity of a focus spot distribution. The focus spot anyway has to be measured for the tracking system and/or the communication system in typical ground stations; however, these algorithms show, apart from ambiguities in the reconstruction, a weak performance for larger D/r_0 ratios and under strong intensity scintillation; in addition, they require quite a large number of numerically demanding iterations (Fourier transforms) to reconstruct an acceptable phase estimate.

Self-Referencing Interferometers (Chapter 5)

Self-referencing interferometers based on common-path or point-diffraction setups provide a promising solution for SGL scenarios. These techniques are mainly applied for optical component testing, but they are here studied and demonstrated for the use in AO and communication systems. Main aspects for the evaluation of their performance are speed, robustness to phase/intensity fluctuations, phase singularities, and environmental influences. Three main types of interferometer designs were discussed:

- Instantaneous phase-shifting interferometers (IPSI) take three or four interferograms synchronously, each with a different phase shift. The calculations for the phase reconstruction are very simple, so that the sensor comes very close to a direct wavefront sensor. The ratio pixel over phase-point count is very favorable (3-4), phase singularities do not disturb the results, and telescope areas with low intensity levels can be easily detected. Taking into account the bandwidth requirements, the strong phase distortions, and intensity scintillation, this sensor type seems to be a good solution under the stated conditions, however, with an increased effort of several interferometer arms. Some optical setups of an almost common-path style are presented (Section 5.3.2), which should be robust to environmental disturbances like vibrations or temperature fluctuations (solar radiation). Several techniques to evaluate the performance in the presence of

> phase-shifting errors, detector nonlinearity/noise, and vibration errors are discussed (Section 5.2.2 and 5.2.3).

- The Fourier Fringe Analysis (FFA) technique (Section 5.3.1) recovers the phase from one or two interferograms. This technique is numerically more demanding (two Fourier transforms) but can be implemented with a good ratio pixel over phase-point count (1-2) making camera sensors very fast. The resolution of the phase reconstruction is slightly reduced due to the sampling requirements of the fringes. Phase reconstruction quality is disturbed only locally by low intensity levels, still allowing a good overall performance.

- The iterative technique of Vorontsov (Section 5.3.3) uses one interferometer and an additional measurement of the intensity distribution in order to estimate the phase in a closed-loop AO system. This technique is numerically very simple, has a good ratio pixel over phase-point count (1-2), but of course requires a few iterations ($n<10$) to obtain an adequate phase estimate.

IPSI techniques provide the most accurate phase estimates of the interferometers with a good bandwidth performance, however, with an additional effort for the optical system. If processing power is not the limiting factor and an optically simple solution is required, the FFA technique offers a promising solution. The iterative technique has the lowest processing requirements; however, the speed demands on the camera and the wavefront corrector are the highest to achieve high bandwidth despite the iterative character.

An issue of self-referencing interferometers is the strength and stability of the reference wave, which also depends on the impinging wavefront. This, however, should be only a problem to start off the AO system until the phase reconstruction and correction catches on. During operation the phase should be sufficiently corrected to ensure a relatively stable reference wave.

Experimental Demonstration (Chapter 6)

As a conclusion of this work a testbed for interferometric sensors and closed-loop AO systems has been setup in a lab environment in order to characterize the performance with an optical turbulence generator. First experiments have been performed for a point-diffraction interferometer setup with an FFA reconstruction. The results are promising and a first closed-loop AO system with such a sensor has been demonstrated.

7.2 Future Work

This thesis provided an investigation of wavefront sensing under extreme atmospheric conditions to develop AO systems for SGL scenarios. The next steps will be to study in detail the performance of several of the suggested interferometric wavefront sensors in laboratory experiments and compare their performance with the Shack-Hartmann sensor.

From the lab environment the system has to be taken to experiments on an outdoor test-range with a sufficiently long propagation distance (1-2km) providing severe atmospheric conditions close to the ground. In contrast to the actual satellite downlinks there is ample time on the test-range to optimize all parameters of the AO systems. In SGL scenarios link durations are only 8-12 minutes every couple of days. Therefore, the AO and communication systems have to be perfected first in ground tests to guarantee an optimal performance during the short measurement intervals of an SGL campaign.

A   Appendix

A.1   Fourier Transformation

A.1.1   Continuous Fourier Transformation

The Fourier transform $G(f)$ of a function $g(x)$ is defined by

$$G(f) = \int\limits_{-\infty}^{\infty} g(x)e^{-2\pi i f x}dx \tag{A.1}$$

$$g(x) = \int\limits_{-\infty}^{\infty} G(f)e^{2\pi i f x}df \ . \tag{A.2}$$

Fourier transform in two dimensions:

$$G(\bar{f}) = \iint g(\bar{x})e^{-2\pi i \bar{f}\cdot\bar{x}}d\bar{x} \tag{A.3}$$

$$g(\bar{x}) = \iint G(\bar{f})e^{2\pi i \bar{f}\cdot\bar{x}}d\bar{f} \ , \tag{A.4}$$

where $\bar{f} = (f_x, f_y)$, $\bar{x} = (x, y)$, and $\bar{f}\cdot\bar{x} = f_x\cdot x + f_y\cdot y$. In general Fourier transforms of functions in the spatial/time domain are indicated by the corresponding capital letter, e.g. $g(x) \rightarrow G(f)$.

A.1.2   Discrete Fourier Transformation

In the following a time or spatial function is sampled in the interval X_0. N sampling points are taken in intervals $\triangle x_a$, so that $X_0 = N\cdot\triangle x_a$. The sampled function might be padded with zeros to increase the resolution in the Fourier domain. The Fourier integral (A.1) can then be written as sum over N terms

$$\int\limits_{x=0}^{X_0=N\cdot\triangle x_a} g(x)e^{-2\pi i f x}dx \Rightarrow \triangle x_a\cdot\sum_{n=0}^{N-1}g(n\cdot\triangle x_a)e^{-2\pi i f_k n\cdot\triangle x_a} \ . \tag{A.5}$$

With the sampling frequencies $f_k = \dfrac{k}{N\cdot\triangle x_a}$, the discrete Fourier transformation becomes

$$G_d(k) = \sum_{n=0}^{N-1}g(n\cdot\triangle x_a)e^{-2\pi i k n / N} \tag{A.6}$$

$$g_d(n) = \frac{1}{N}\sum_{k=0}^{N-1}G(k\cdot\triangle f)e^{2\pi i k n / N} \ . \tag{A.7}$$

The spacing of the samples in the frequency domain is given by

$$\triangle f = \frac{1}{N \cdot \triangle x_a} = \frac{1}{X_0} . \tag{A.8}$$

Important to note is the absence of the factor $\triangle x_a$ in the definition of the discrete Fourier transform [SCH92], which has to be included to get the equivalent of the continuous Fourier transform and to achieve a correct scaling in the sense of energy conservation for example in the formulas of the optical Fourier transform (see section A.2.4). For this the discrete Fourier transformation has to be multiplied by the factor $\triangle x_a$ to get the equivalent of the Fourier transform in value and unit

$$G(f_k) = \triangle x_a \cdot G_d(f_k) . \tag{A.9}$$

The two-dimensional discrete Fourier transformation for the 2D spatial signal (matrix) $x(n_x, n_y)$ is then given by

$$G_d(k_x, k_y) = \sum_{n_x=0}^{N-1} \sum_{n_y=0}^{N-1} g(n_x, n_y) e^{-\frac{2\pi i(k_x n_x + k_y n_y)}{N}} \tag{A.10}$$

$$g(n_x, n_y) = \frac{1}{N^2} \sum_{n_x=0}^{N-1} \sum_{n_y=0}^{N-1} G_d(k_x, k_y) e^{\frac{2\pi i(k_x n_x + k_y n_y)}{N}} \quad , \tag{A.11}$$

which is sampled at the normalized frequencies $f_k = k / X_0$ in both dimensions. The size of the signal matrix in both dimensions is again given by $X_0 = N \cdot \triangle x_a$. Note that the discrete Fourier transformation has to be multiplied with the factor $\triangle x_a^2$ to approximate the result of the continuous Fourier transform. Consequently an energy conserving form of the discrete Fourier transform can be written as

$$G(k_x, k_y) = \triangle x_a^2 \sum_{n_x=0}^{N-1} \sum_{n_y=0}^{N-1} g(n_x, n_y) e^{-i\frac{2\pi(k_x n_x + k_y n_y)}{N}} = \triangle x_a^2 \cdot FT_d\left(g(n_x, n_y)\right) \tag{A.12}$$

$$g(n_x, n_y) = \frac{1}{N^2 \cdot \triangle x_a^2} \sum_{n_x=0}^{N-1} \sum_{n_y=0}^{N-1} G_d(k_x, k_y) e^{i\frac{2\pi(k_x n_x + k_y n_y)}{N}} = \frac{1}{\triangle x_a^2} FT_d^{-1}\left(G_d(k_x, k_y)\right), \tag{A.13}$$

where FT_d denotes the discrete Fourier transformation as given in (A.10).

A.1.3 Properties of the Fourier Transform

Table 2: Selected Fourier transform pairs based on Eq. (A.1) and (A.2).

	Time/Space Domain	Fourier Domain
1.	1	$\delta(f)$
2.	$\delta(x)$	1
3.	$\delta(x - x_0)$	$e^{-2\pi i x_0 f}$
4.	e^{iax}	$\delta\left(f - \dfrac{a}{2\pi}\right)$
5.	$\cos(ax)$	$\dfrac{1}{2}\left[\delta\left(f + \dfrac{a}{2\pi}\right) + \delta\left(f - \dfrac{a}{2\pi}\right)\right]$
6.	$\sin(ax)$	$\dfrac{i}{2}\left[\delta\left(f + \dfrac{a}{2\pi}\right) - \delta\left(f - \dfrac{a}{2\pi}\right)\right]$
7.	$\displaystyle\sum_{n=-\infty}^{\infty}\delta(x - nT)$	$\dfrac{1}{T}\displaystyle\sum_{k=-\infty}^{\infty}\delta\left(f - \dfrac{k}{T}\right)$

Table 3: Some selected properties of the Fourier transform.

	Time/Space Domain	Fourier Domain
Linearity	$h(x) = af(x) + bg(x)$	$H(f) = aF(f) + bG(f)$
Translation	$h(x) = g(x - x_0)$	$H(f) = \exp(-2\pi i x_0 f)G(f)$
Modulation	$h(x) = \exp(2\pi i x f_0)g(x)$	$H(f) = G(f - f_0)$
Scaling	$h(x) = g(ax)$	$H(f) = \dfrac{1}{|a|}G\left(\dfrac{f}{a}\right)$
Time-Reversal	$h(x) = g(-x)$	$H(f) = G(-f)$
Conjugation	$h(x) = g^*(x)$	$H(f) = G^*(-f)$
Convolution	$h(x) = f(x) * g(x)$	$H(f) = F(f) \cdot G(f)$

Symmetries:

$$u(x) = u_{R,even} \quad + u_{R,odd} \quad + iu_{I,even} \quad + iu_{I,odd}$$

$$U(f) = U_{R,even} \quad + U_{R,odd} \quad + iU_{I,even} \quad + iU_{I,odd}$$

where the indices R and I denote the real/imaginary parts, and even/odd the corresponding even/odd parts of the function.

Parseval's theorem: For two square-integrable functions $f(x)$ and $g(x)$ with their respective Fourier transformations $F(f)$ and $G(f)$ the Parseval's theorem is given by

$$\int_{-\infty}^{\infty} f(x) g^*(x) dx = \int_{-\infty}^{\infty} F(f) G^*(f) df, \tag{A.14}$$

where the star denotes the complex conjugate. Using only one function $g(x)$ this theorem is also called the Plancherel theorem. It is given for the continuous case by

$$\int_{-\infty}^{\infty} |g(x)|^2 dx = \int_{-\infty}^{\infty} |G(f)|^2 df \tag{A.15}$$

and in the discrete case by

$$\sum_{n=0}^{N-1} |g(n)|^2 = \frac{1}{N} \sum_{k=0}^{N-1} |G(k)|^2 \tag{A.16}$$

A.2 Simulation of Beam Propagation

The simulation of beam propagation is based on [SAL91] and [GOO96].

A.2.1 Free-Space Transmission

Given a complex electric field distribution $f(x,y)$ in the input plane, the field distribution $g(x,y)$ after a free-space transmission of distance d can be calculated in the Fourier or in the spatial domain. $F(\upsilon_x, \upsilon_y)$ and $G(\upsilon_x, \upsilon_y)$ are the corresponding Fourier transforms of $f(x,y)$ and $g(x,y)$. The free-space transmission in the Fourier domain is given by

$$G(\upsilon_x, \upsilon_y) = H(\upsilon_x, \upsilon_y) \cdot F(\upsilon_x, \upsilon_y) \tag{A.17}$$

with the **transfer function** of the free-space transmission in the Fresnel approximation

$$H(\upsilon_x, \upsilon_y) \approx H_0 \exp\left[i\pi\lambda d \cdot \left(\upsilon_x^2 + \upsilon_y^2 \right) \right] \tag{A.18}$$

with $H_0 = \exp(ikd)$. (υ_x, υ_y) give the spatial frequencies in the Fourier domain in the directions (x,y). The wavelength of the propagated wave is λ. In the discrete case (υ_x, υ_y) are given by

$$(\upsilon_x, \upsilon_y) = \left(\frac{k_x}{N \cdot \Delta x_a}, \frac{k_y}{N \cdot \Delta x_a} \right), \tag{A.19}$$

where Δx_a is the spacing in the spatial domain and (k_x, k_y) are the sampling values in the Fourier domain. In the spatial domain the free-space transmission is calculated by the convolution

$$g(x,y) = h(x,y) * f(x,y) = \int_{-\infty}^{\infty} \int_{-\infty}^{\infty} f(x',y') \cdot h(x-x', y-y') dx' dy' \, , \quad \text{(A.20)}$$

where the **impulse-response function** is given by

$$h(x,y) \approx h_0 \cdot \exp\left[-ik \frac{x^2 + y^2}{2d} \right] \quad \text{(A.21)}$$

with

$$h_0 = \left(\frac{i}{\lambda d} \right) \cdot \exp\left(-ikd \right). \quad \text{(A.22)}$$

Both transfer function and impulse-response function are given in the simplification of the Fresnel approximation, which assumes that the distances x and y are small compared to the distances f and d.

A.2.2 Thin Lens

The effect of a thin lens is given by

$$g(x,y) = t(x,y) \cdot f(x,y) \quad \text{(A.23)}$$

with the lens transmittance

$$t(x,y) \approx h_0 \exp\left[ik_0 \frac{x^2 + y^2}{2f} \right], \quad \text{(A.24)}$$

where $h_0 = \exp(-ink_0 d_0)$ with the index-of-refraction n of the lens material and d_0 the thickness of the lens. A plane wave is transformed into a paraboloidal wave. For a discrete simulation of a lens transmittance, it has to be considered that the term within the brackets $ik_0 \dfrac{x^2 + y^2}{2f}$ becomes rather large for usual lens configurations with an F-number of about 1-10, which causes the exponential function to quickly oscillate. This easily brings numerical simulations to the limit of spatial resolution. This can be solved with long focal lengths or alternatively small aperture sizes.

A.2.3 Optical Fourier Transform

The Fourier transform of an input wave can be "calculated optically" by a focus transformation of a lens. The modulus of the Fourier transformation can then be estimated by measuring the focus spot intensity with a camera.

Given a complex electric field distribution $f(x,y)$ in the input plane, the focal-plane field distribution $g(x,y)$ gives the Fourier transformation of $f(x,y)$ and is obtained as shown in Figure A.1 by a

- Free-space transmission with the distance d
- Transmission through a lens with focus length f
- Free-space transmission with the distance f
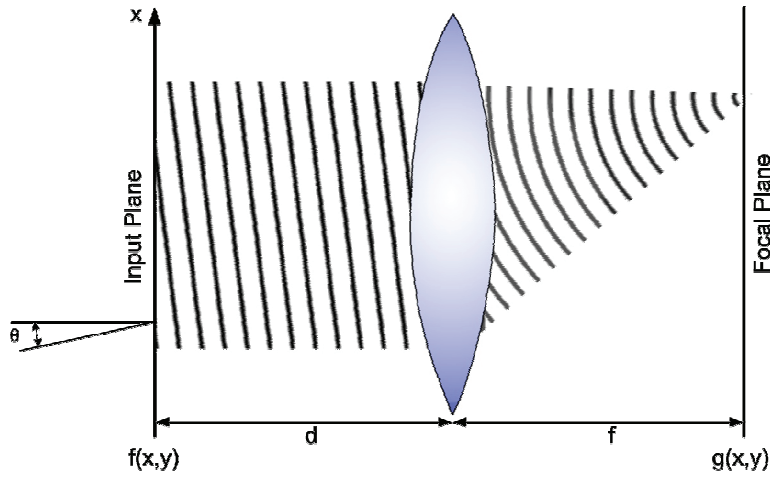
Figure A.1: The input field can be described as a superposition of plane waves. Each plane wave with a tilt angle of $\theta_{x,y}$ in the input plane produces the frequency component $\left(\upsilon_x,\upsilon_y\right)$ due to the tilt as it crosses the input plane. Each tilted wave is then mapped to a certain location in the focal plane, which yields the Fourier transform of the input field.

(x,y) are the spatial coordinates in the transversal plane. The according frequencies with unit [1/m] are given by $\left(f_x,f_y\right)=\left(\dfrac{x}{\lambda f},\dfrac{y}{\lambda f}\right)$.

Using the Fresnel approximation to calculate the propagation of light in free-space, the transformation of the field from the pupil plane to the focus plane can be written by the Fourier transform

$$g\left(x,y\right)=h_l\exp\left[i\pi\frac{\left(x^2+y^2\right)\left(d-f\right)}{\lambda f^2}\right]FT\left(\frac{x}{\lambda f},\frac{y}{\lambda f}\right),\tag{A.25}$$

where $h_l=\left(\dfrac{i}{\lambda f}\right)\exp\left[-ik(d+f)\right]$ and $k=\dfrac{2\pi}{\lambda}$. The intensity is proportional to the squared absolute value of the Fourier transform of $f(x,y)$

$$I(x,y)=\frac{1}{\left(\lambda f\right)^2}\left|FT\left(\frac{x}{\lambda f},\frac{y}{\lambda f}\right)\right|^2.\tag{A.26}$$

Observing the intensity in the focus plane ($d=f$) removes the exponential term in (A.25), so that

$$g(x,y)=h_lFT\left(\frac{x}{\lambda f},\frac{y}{\lambda f}\right),\tag{A.27}$$

where $h_l=\left(\dfrac{i}{\lambda f}\right)\exp\left[-i2kf\right]$. In the discrete case Eq. (A.27) changes to

$$g\left(n_x \cdot \frac{\lambda f}{\triangle x_a N}, n_y \cdot \frac{\lambda f}{\triangle x_a N} \right) = \frac{\triangle x_a^2}{\lambda \cdot f} \cdot \frac{1}{N} \cdot h_l FT\left(n_x, n_y \right),$$ (A.28)

where $\left(n_x, n_y \right)$ denote the sample points (n_x, n_y=-N/2…N/2) of the Fourier transform. The sampling points in the focus plane have the frequency values $\left(n_x \cdot \frac{\lambda f}{\triangle x_a N}, n_y \cdot \frac{\lambda f}{\triangle x_a N} \right)$.

A.2.4   Discrete Optical Fourier Transform

A two-dimensional Discrete Fourier Transform (DFT) is used for the numerical simulation of the optical Fourier transform. The input electrical field $f(m,n)$ and the field in the focus plane $g(m,n)$ are stored in complex matrices. An efficient implementation of the DFT is the Fast Fourier Transform (FFT), which reduces the computational complexity from $O\left(N^2 \right)$ of the DFT to $O\left(N \cdot \log(N) \right)$, where N denotes the matrix dimension of the sampled fields.

For a typical numerical implementation of the FFT, such as in Matlab, the relation of the input plane and the focal plane, assuming $d=f$ (see A.2.3), with the correct scaling is given by

$$F\left(k_x, k_y \right) = FFT\left(f(n_x, n_y) \right) \cdot \frac{\triangle x_a^2}{\lambda \cdot f}.$$ (A.29)

$\triangle x_f$ denotes the frequency spacing in the focal plane, and N gives the size of the field matrices $f(m,n)$ and $g(m,n)$, including possible zero padding, i.e. the field might be sampled with 256x256 values and is padded with zeros to a matrix size of 1024x1024 (N=1024). The relation between $\triangle x_a$ and $\triangle x_f$ is given for the focal length f by

$$\triangle x_f = \frac{\lambda \cdot f}{\triangle x_a \cdot N}.$$ (A.30)

Eq. (A.29) can be rewritten with (A.30) to give

$$F_d\left(k_x, k_y \right) = FFT\left(f(n_x, n_y) \right) \cdot \frac{\triangle x_a}{\triangle x_f} \cdot \frac{1}{N}.$$ (A.31)

Usually the frequency axis is inversed for two-dimensional FFTs, so that the lowest frequencies are mapped to the corners of the output matrix. Software packages like Matlab provide functions to rearrange the frequencies, e.g. FFTSHIFT in Matlab. The forward Fourier transform is given in Matlab by

```
Focus=FFTSHIFT(FFT2(FFTSHIFT(aperture)))*dxa^2/(lambda*focus)
```

A.3 Relations of Trigonometric Functions

Selected relations of trigonometric functions, e.g. [BRO93]:

1. $\quad \sin(\alpha \pm \beta) = \sin\alpha\cos\beta \pm \cos\alpha\sin\beta$

2. $\quad \cos(\alpha \pm \beta) = \cos\alpha\cos\beta \mp \sin\alpha\sin\beta$

3. $\quad \sin 2\alpha = 2\sin\alpha\cos\alpha$

4. $\quad \cos 2\alpha = \cos^2\alpha - \sin^2\alpha$

5. $\quad \sin\alpha + \sin\beta = 2\sin\dfrac{\alpha+\beta}{2}\cos\dfrac{\alpha-\beta}{2}$

6. $\quad \sin\alpha - \sin\beta = 2\cos\dfrac{\alpha+\beta}{2}\sin\dfrac{\alpha-\beta}{2}$

7. $\quad \cos\alpha + \cos\beta = 2\cos\dfrac{\alpha+\beta}{2}\cos\dfrac{\alpha-\beta}{2}$

8. $\quad \cos\alpha - \cos\beta = -2\sin\dfrac{\alpha+\beta}{2}\sin\dfrac{\alpha-\beta}{2}$

9. $\quad \sin\alpha\sin\beta = \dfrac{1}{2}\left[\cos(\alpha-\beta) - \cos(\alpha+\beta)\right]$

10. $\quad \cos\alpha\cos\beta = \dfrac{1}{2}\left[\cos(\alpha-\beta) + \cos(\alpha+\beta)\right]$

11. $\quad \sin\alpha\cos\beta = \dfrac{1}{2}\left[\sin(\alpha-\beta) + \sin(\alpha+\beta)\right]$

12. $\quad \sin^2\alpha = \dfrac{1}{2}(1 - \cos 2\alpha)$

13. $\quad \cos^2\alpha = \dfrac{1}{2}(1 + \cos 2\alpha)$

14. $\quad \cos\alpha = \dfrac{1}{2}\left(e^{i\alpha} + e^{-i\alpha}\right)$ $\qquad$ (Euler's formula)

15. $\quad \sin\alpha = \dfrac{1}{2i}\left(e^{i\alpha} - e^{-i\alpha}\right)$ $\qquad$ (Euler's formula)

A.4 Properties of Complex Conjugate

1. $(z + w)^* = z^* + w^*$

2. $(z - w)^* = z^* - w^*$

3. $(zw)^* = z^* w^*$

4. $\left(\dfrac{z}{w}\right)^* = \dfrac{z^*}{w^*},$ $\qquad$ if w is non-zero

5. $\left|z\right|^2 = z \cdot z^* = z^* \cdot z$

6. $\mathrm{Re}\{z\} = \dfrac{1}{2}\left(z + z^*\right)$

7. $\mathrm{Im}\{z\} = \dfrac{1}{2i}\left(z - z^*\right)$

A.5   Properties of Vector Operators (Gradient, Divergence, Curl)

The properties of vector operators can be found for example in [AND03, p.178] or [BRO93]. The nabla operator is given by

$$\nabla = \begin{pmatrix} \frac{\partial}{\partial x} \\ \frac{\partial}{\partial y} \\ \frac{\partial}{\partial z} \end{pmatrix}.$$

Scalar fields are denoted by lower letters and vector fields by capital letters with an arrow.

$$\nabla\left(fg\right) = g\nabla f + f\nabla g$$

$$\nabla \cdot \left(f\vec{G}\right) = f\left(\nabla \cdot \vec{G}\right) + \nabla f \cdot \vec{G}$$

$$\nabla \times \left(f\vec{G}\right) = f\left(\nabla \times \vec{G}\right) + \nabla f \times \vec{G}$$

$$\nabla \times \nabla f = 0 \qquad\qquad\qquad \text{Curl of a gradient is zero}$$

$$\nabla \cdot \nabla \times \vec{F} = \vec{0} \qquad\qquad\qquad \text{Divergence of a curl is zero}$$

$$\nabla \cdot \left(\vec{F} \times \vec{G}\right) = \vec{G} \cdot \left(\nabla \times \vec{F}\right) - \vec{F} \cdot \left(\nabla \times \vec{G}\right)$$

$$\nabla \times \left(\nabla \times \vec{F}\right) = \nabla\left(\nabla \cdot \vec{F}\right) - \nabla^2 \vec{F}$$

$$\nabla f\left(u\right) = \frac{df}{du}\nabla u \qquad\qquad\qquad \text{Chain rule}$$

$$\frac{\partial f\left(u,v\right)}{\partial x} = \frac{\partial f\left(u,v\right)}{\partial u}\frac{\partial u}{\partial x} + \frac{\partial f\left(u,v\right)}{\partial v}\frac{\partial v}{\partial x} \qquad \text{Chain rule}$$

A.6   Polarization and Jones Matrix

The explanation of polarization and the Jones vector/matrix is based on the presentation in [SAL91]. The electric field E can be expressed in the field components in x and y direction

$$E\left(z,t\right) = E_x \vec{e}_x + E_y \vec{e}_y, \qquad\qquad\qquad\qquad (A.32)$$

193

where

$$E_x = a_x \cos\left[2\pi f\left(t - \frac{z}{c}\right) + \varphi_x\right] = A_x \cos\left[2\pi f\left(t - \frac{z}{c}\right)\right]$$

$$E_y = a_y \cos\left[2\pi f\left(t - \frac{z}{c}\right) + \varphi_y\right] = A_y \cos\left[2\pi f\left(t - \frac{z}{c}\right)\right]$$

(A.33)

A_x and A_y are the complex envelope of the electric field and determine the polarization of the wave. The polarization state of a wave can be characterized by the Jones matrix $J = \begin{bmatrix} A_x \\ A_y \end{bmatrix}$.

Some examples for J are given in Table 4.

Table 4: Jones vector $J = \begin{bmatrix} A_x \\ A_y \end{bmatrix}$ **for some specific polarization states.**

Linear polarization in x- and y-direction	$\begin{bmatrix} 1 \\ 0 \end{bmatrix}, \begin{bmatrix} 0 \\ 1 \end{bmatrix}$
Linear polarization with an angle θ with the x-axis	$\begin{bmatrix} \cos\theta \\ \sin\theta \end{bmatrix}$
Right circular polarized	$\frac{1}{\sqrt{2}}\begin{bmatrix} 1 \\ i \end{bmatrix}$
Left circular polarized	$\frac{1}{\sqrt{2}}\begin{bmatrix} 1 \\ -i \end{bmatrix}$

The properties of polarization devices are modeled by the Jones matrix T, which is multiplied to the Jones vector J_1 by a matrix multiplication

$$J_2 = TJ_1.$$

Table 5: Jones matrices for some specific polarization devices.

Linear polarizer in *x*-/*y*-direction	$\begin{bmatrix} 1 & 0 \\ 0 & 0 \end{bmatrix}, \begin{bmatrix} 0 & 0 \\ 0 & 1 \end{bmatrix}$
Linear polarizer rotated by 45/135 degrees (or -135/-45 degrees)	$\frac{1}{2}\begin{bmatrix} 1 & 1 \\ 1 & 1 \end{bmatrix}, \frac{1}{2}\begin{bmatrix} 1 & -1 \\ -1 & 1 \end{bmatrix}$
Wave retarder (here the fast axis is along the x-direction)	$\begin{bmatrix} 1 & 0 \\ 0 & \exp(-i\triangle\varphi) \end{bmatrix}$
Quarter-wave plate at 45 degrees rotation	$\frac{1}{\sqrt{2}}e^{-i\pi/4}\begin{bmatrix} 1 & i \\ i & 1 \end{bmatrix}$
Polarization rotator; rotates the plane of polarization by the angle θ	$\begin{bmatrix} \cos\theta & -\sin\theta \\ \sin\theta & \cos\theta \end{bmatrix}$

A wave retarder with $\triangle\varphi = \pi/2$ is called a quarter-wave retarder/plate. It converts linear polarized light $\begin{bmatrix} 1 \\ 1 \end{bmatrix}$ into left circular polarized light $\begin{bmatrix} 1 \\ -i \end{bmatrix}$, and converts right polarized light $\begin{bmatrix} 1 \\ i \end{bmatrix}$ into linear polarized light $\begin{bmatrix} 1 \\ 1 \end{bmatrix}$.

Change of Coordinate System

The change of the coordinate system of a Jones vector and matrix is realized with the rotation matrix

$$R(\theta) = \begin{bmatrix} \cos\theta & \sin\theta \\ -\sin\theta & \cos\theta \end{bmatrix}, \tag{A.34}$$

where θ denotes the rotation angle to obtain the rotated coordinate axes *x'* and *y'*. A Jones vector in the rotated coordinate system is given by

$$J' = R(\theta)J \tag{A.35}$$

and a Jones matrix, i.e. equaling a rotated polarization device by the angle $-\theta$, in the new coordinate system is

$$T' = R(\theta) \cdot T \cdot R(-\theta). \tag{A.36}$$

B   Abbreviations

AO	Adaptive optics
ARTEMIS	ESA telecommunications satellite with optical communications terminal
ATM	Atmospheric Transmission Monitor
BER	Bit-Error Ratio
BPSK	Binary Phase-Shift Keying
CCD	Charge-Coupled Device
CDF	Cumulative Distribution Function
CMOS	Complementary Metal Oxide Semiconductor
CPI	Common-Path Interferometer
CTFA	Coherent Transmission Feasibility Analysis
DARA	Deutsch Agentur für Raumfahrtangelegenheiten, today part of the German Space Agency
DFT	Discrete Fourier Transform
DIMM	Differential Image Motion Monitor
DLR	Deutsches Zentrum für Luft- und Raumfahrt e.V., German Aerospace Center
DM	Deformable Mirror
ESA	European Space Agency
ESTEC	European Space Research and Technology Center
FAR	Focal Array Receiver
FFA	Fourier Fringe Analysis
FOV	Field of View
fps	Frames per Second
FSO	Free-Space Optical (Communication Systems)
Gbps	Giga-bits per second
GEO	Geo-Stationary Satellite
HAP	High-Altitude Platform
HG	Hermite-Gaussian (Beam)
HV	Hufnagel-Valley Model
HV$_{5/7}$	Hufnagel-Valley C_n^2 profile with standard parametrization (r_0=5cm and isoplanatic angle of 7µrad for λ=0.5µm)
IM/DD	Intensity Modulation/ Direct Detection
IPSI	Instantaneous Phase-Shifting Interferometer
ISL	Inter-Satellite Link
ITE	Irradiance Transport Equation
JAXA	Japanese Aerospace Exploration Agency, Tokyo
LCT	Laser Communications Terminal
LEO	Low Earth Orbit
LG	Laguerre-Gaussian (Beam)
LO	Local Oscillator
LOLA	Liaison Optique Laser Aéroportée

Abbreviations

Mbps	Mega-bits per second
NA	Numerical Aperture
NFOV	Narrow Field-of-View (Camera)
NICT	National Institute of Information and Communications Technology, Tokyo
NPBS	Non-Polarizing Beam Splitter
OCG	Optical Communication Group
OCT	Optical Communication Terminal
OGS	Optical Ground Station
OICETS	Optical Inter-Orbit Communications Engineering Test Satellite
OPALE	Optical Payload for Inter-Satellite Link Experiment (on SPOT-4)
OTG	Optical Turbulence Generator
PASTEL	Passager Telecom (on ARTEMIS)
PAT	Pointing, Acquisition, and Tracking
PBS	Polarizing Beam Splitter
PDF	Probability Density Function
PDI	Point-Diffraction Interferometer
Ph/b	Photons per bit
PILab	Propagation and Imaging Lab, DLR proprietary tool for simulation of atmospheric propagation
PSF	Point Spread Function
PSI	Phase-Shifting Interferometer (Interferometry)
PSK	Phase-Shift Keying
px	Camera pixels
QWP	Quarter-Wave Plate
RMS	Root Mean Square
RX	Receive
SCIDAR	Scintillation Detection and Ranging
SGL	Satellite-To-Ground Link
SHS	Shack-Hartmann Wavefront Sensor
SILEX	Semiconductor laser Inter-satellite Link Experiment (ARTEMIS-SPOT4)
SM	Single-Mode (Fiber)
SNR	Signal-to-Noise Ratio
SOLACOS	Solid State Laser Communications in Space
SPGD	Stochastic Parallel Gradient Descent Optimization Technique
SROIL	Short-Range Optical Inter-Satellite Link
SRW	Synthetic Reference Wave
Tbps	Tera-bits per second.
TX	Transmit
WDM	Wavelength Division Multiplex
WFOV	Wide Field-of-View Camera
WTE	Wavefront Transport Equation

C   Symbols and Notations

Symbol	Description	Unit
$\triangle$	Phase step	*rad*
α_g	Elevation angle	*rad*
α_θ	Tilt angle	*rad*
α_{ext}	Extinction coefficient	km^{-1}
α_v	Phase shift of the vibration disturbance in a phase-shifting interferometer	*rad*
β_g	Azimuth angle	*rad*
β	Transmission of the common path interferometer phase plate outside the central phase dot	
γ	Transmission of the common path interferometer phase plate inside the central phase dot	
γ_{12}	Complex degree of coherence	
$\Gamma(x)$	Gamma function	
$\delta(x)$	Dirac impulse	
δ_{ij}	Kronecker delta	
ε	Relative phase-shifter error in phase-shifting interferometers	
ε_a	Size of the annulus in percent of the aperture	
η	Ration of the Airy pattern diameter (first zero) and the pin-hole diameter in a point-diffraction interferometer	
η_{het}	Heterodyne efficiency	
θ	Phase shift of the common-path interferometer phase plate inside the central phase dot	*rad*
θ_j	Phase steps in the phase-shifting interferometry	*rad*
κ	Spatial/temporal frequency in the Fourier transformation	*1/m, 1/s*
κ_{DM}	Constant of the actuator influence function	
κ_X, κ_Y	Large- and small-scale spatial cutoff frequencies	*1/m*
λ	Wavelength	*m*
ν	Frequency in the spectral PSI analysis technique	*Hz*
$\triangle\nu_{FWHM}$	Spectral width or linewidth of a laser	*Hz*
ν_v	Frequency of the vibration disturbance in a phase-shifting interferometer	*Hz*
ρ	Normalized radius (polar coordinates)	
ρ_0	Spatial coherence radius	*m*

(ρ, ψ)	Polar coordinates with radius and azimuth angle	*m, rad*
σ	Standard deviation (σ^2 variance)	
σ_θ	Standard deviation of the tilt/angle-of-arrival	*rad*
σ_φ	Phase standard deviation	
σ_d^2	Variance of the spot position in the DIMM	*m²*
σ_G^2	Residual phase error limited due to AO bandwidth (Greenwood frequency)	*rad²*
σ_I^2	Intensity scintillation index	
$\sigma_{\ln x}^2, \sigma_{\ln y}^2$	Large/small scale log-irradiance scintillation index	
σ_n^2	Detector noise	
σ_N^2	Residual phase variance after correction with N Zernike modes	
σ_P^2	Power scintillation index	
σ_R^2	Rytov variance	
σ_S^2	Scintillation error of the curvature sensor	
$\Delta\tau$	Difference in run-time of the two interferometer arms $$\Delta\tau = \frac{S_2 - S_1}{c}$$	*s*
τ_c	Coherence time	*s*
φ	Wavefront phase	*rad*
φ_c	Wavefront shape of the corrector	*rad*
φ_L	Phase shift of the local oscillator	*rad*
φ_{LS}	Reconstructed phase in the least-square sense	*rad*
φ_S	Phase shift of the received signal	*rad*
φ_{SD}	Slope-discrepancy phase	*rad*
(r, ϕ)	Polar coordinates with radius and azimuth angle.	*m, rad*
Φ	Fourier transform of the phase φ	*rad⁻¹*
$\Phi_n(\kappa)$	Power spectrum model for refractive-index fluctuations	*m³*
(ρ, ψ)	Polar coordinates with radius and azimuth angle.	*m,rad*
ω_L	Optical frequency of the local oscillator	*Hz*
ω_S	Optical frequency of the received signal beam	*Hz*
ω_{sat}	Satellite slew rate	*rad/s*
$\nabla_\perp$	Transversal Laplacian operator	

(a,b)	Local Cartesian coordinates	m
a_j	Zernike coefficient of order j	
A	Area	m^2
$A\left(f_x,f_y\right)$	Central peak in the Fourier domain of the FFA technique	Ws/m^2
A_d	Area of the CPI filter dot	m^2
A_{geo}	Geometry matrix describing the relation between slopes and wavefront points in a Shack-Hartmann sensor	
a_k	Coefficients of the denominator in a PSI algorithm	
$B(\rho)$	Spatial covariance function	
$B\left(f_x,f_y\right)$	Side peak in the Fourier domain of the FFA technique	Ws/m^2
$b_I(\rho)$	Normalized spatial covariance function of the intensity	
$B_I(\rho)$	Spatial covariance function of the intensity	
b_k	Coefficients of the nominator in a PSI algorithm	
C	Speed of light $c = 3\cdot10^8\,\frac{m}{s}$	m/s
$C_n^2(h)$	Refractive-index structure function	$m^{-2/3}$
d	Aperture separation distance in the DIMM	m
d_L	Aperture diameter of a lenslet in a Shack-Hartmann sensor	m
D	Aperture diameter	m
$D_n(\rho)$	Index-of-refraction structure function	
D_{Sub}	Sub-aperture diameter	m
E	Electric field	V/m
f	Focal length	m
$\bar{f}=\left(f_x,f_y\right)$	Coordinates in the Fourier domain	$1/m$
f_0	Fringe modulation frequency in the FFA technique	$1/m$
F_1, F_2	Filter functions in the PSI evaluation	
f_{3dB}	3dB closed-loop servo cut-off frequency	Hz
f_G	Greenwood frequency	Hz
$FT\{x\}$	Fourier transform	
f_{T_G}	Tilt Greenwood frequency	Hz
g	Gradient (slopes) of a wavefront	
G	Fourier transform of the gradient g	
G_0, G_X, G_Y	Amplitude spatial filter functions for the effective atmospheric spectrum (combined, large-scale, small-scale)	
$G_x(\bar{\kappa}),$ $G_y(\bar{\kappa})$	Two-dimensional Fourier transforms of the slope components g_x and g_y	

$H(f,f_{3dB})$	Closed-loop servo response	
$H_{dot}(\vec{q})$	Transfer function of the CPI filter dot	
H_{sat}	Satellite altitude above ground	m
I	Intensity of Irradiance	W/m^2
I_F	Fourier transform of the intensity signal	Ws/m^2
I_L	Intensity of the local oscillator	W/m^2
I_0	Intensity distribution of the interferometer object beam	W/m^2
I_{P0}	Intensity distribution in the entrance pupil of the curvature sensor	W/m^2
I_R	Intensity distribution of the interferometer reference beam	W/m^2
I_S	Intensity of the received signal	W/m^2
I_T	Threshold intensity (normalized) of a cumulative distribution function (CDF)	
J	Performance metric in model-free optimization techniques	
$J_n(\text{x})$	Bessel function of the first kind.	
J_{QWP}, J_P	Jones matrix of a quarter-wave plate and a polarizer	
k	Wave number $k = 2\pi/\lambda$	$1/m$
$K_p(\text{x})$	Modified Bessel function of the second kind	
L	Path length	m
l_0	Atmospheric inner scale	m
L_0	Atmospheric outer scale	m
n	Refractive index	
N	Number of samples/coefficients	
P	Pressure	$Pascal$
$p(I)$	Probability density function of the intensity	
$P(z)$	Characteristic polynomial in the PSI evaluation	
p_j	Availability of ground station j	
p_M	Combined availability of M ground stations	
$PV\{x\}$	Principal value operator	
$\vec{q} = (q_x, q_y)$	Spatial coordinate in the Fourier plane	m
q_0	Filter-dot radius	m
(r, ϕ)	Polar coordinates with radius and azimuth angle.	m, rad
r_0	Atmospheric coherence length, Fried parameter	m
r_d	Radius of the (circular) detector	m
R_e	Earth radius (spherical model), $R_e \sim 6370\text{km}$	m
S	Strehl ratio	

s_v	Integrated vibration sensitivity value for a phase-shifting interferometer.	
t	Time	s
T	Temperature	K
u,v	Normalized Cartesian coordinates	
U	Complex electric field	V
$u_l^{(m)}$	Position of actuator l at the iteration m	
U_L	Electric field of the local oscillator	V
U_0, U_R	Complex electric field of the object/reference wave	V
U_S	Electric field of the received signal	V
$v_\perp$	Transversal wind velocity	m/s
v_0	Wind velocity on ground	m/s
V_{Hz}	Hertz potential	
V	Visibility of fringes	
V_f	Fiber normalized frequency	
V_{sat}	Satellite speed	m/s
v_v	Vibration frequency	Hz
w_0	Waist radius of a Gaussian beam (1/e for the amplitude and 1/e² for the intensity)	m
W_0	Aperture transmittance function	
$w_G(z)$	Beam radius of a Gaussian beam at distance z	m
w	Beam radius	m
(x,y)	Cartesian coordinates	m
$\triangle x_a, \triangle x_f$	Sampling interval in the spatial/frequency domain	$m, 1/m$
z	Distance from the ground station	m
z_R	Rayleigh range	m
$Z_j(\rho,\psi)$	Zernike polynomial of order j	

D References

[AND95]   C. Anderson, "Fringe visibility, irradiance, and accuracy in common path interferometers for visualization of phase disturbances," Appl. Opt. **34**, 7474-7485 (1995).

[AND00]   L. Andrews, R. Philips, and C. Hopen, "Scintillation model for a satellite communication link at large zenith angles," Opt. Eng. **39**, 3272-3280 (2000).

[AND01]   L. Andrews, R. Philips, and C. Hopen, *Laser Beam Scintillation with Applications* (SPIE Press, Bellingham, 2001).

[AND03]   L. Andrews and R. Philips, *Mathematical Techniques for Engineers and Scientists* (SPIE Press, Bellingham, 2003).

[AND05]   L. C. Andrews and R. L. Philips, *Laser Beam Propagation through Random Media* (SPIE Press, Bellingham 2005).

[BAR81]   N. Baranova and B. Zeldovich, "Dislocations of the wave-front surface and zeros of the amplitude," Sov. Phys. JETP **53** (1961).

[BAR83]   N. Baranova, A. Mamaev, N. Pilipetsky, V. Shkunov, and B. Zeldovich, "Wave-front dislocations: topological limitations for adaptive systems with phase conjugation," J. Opt. Soc. Am. **73**, No. 5 (1983).

[BAR90]   J. Barry and E. Lee, "Performance of coherent optical receivers", Proc. of the IEEE **78**, No.8 (1990).

[BAR02a]   J. Barchers, D. Fried, and D. Link, "Evaluation of the performance of Hartmann sensors in strong scintillation," Appl. Opt. **41**, No. 6 (2002).

[BAR02b]   J. Barchers, D. Fried, and D. Link, "Evaluation of the performance of a shearing interferometer in strong scintillation in the absence of additive measurement noise," Appl. Opt. **41**, No. 18 (2002).

[BAT82]   R. Bates, "Fourier phase problems are uniquely soluble in more than one dimension. I: underlying theory," Optik (Stuttgart) **61**, 247-262 (1982).

[BOR99]   M. Born and E. Wolf, *Principles of Optics* (Cambridge University Press, 7th edition, 1999).

[BRI74]   W. B. Bridges, P. T. Brunner, S. P. Lazzara, T. A. Nussmeier, T. R. O'Meara, J. A. Sanguinet, and W. P. Brown, Jr. "Coherent optical adaptive techniques", Appl. Opt. **13** (2), 291-300 (1974).

[BRO93]   I. Bronstein, K. Semendjajew, G. Musiol, and H. Mühlig, *Taschenbuch der Mathematik* (Verlag Harri Deutsch, 1993).

[BRU74]   J. Bruning, D. Herriott, J. Gallagher, D. Rosenfeld, A. White, and D. Brangaccio, "Digital wavefront measuring interferometer for testing optical surfaces and lenses," Appl. Opt. **13**, 2693-2703 (1974).

[BRU05]   H. W. Brüsselbach, S. Wang, M. Minden, D. Jones, and M. Mangir, 'Powerscalable phase compensating fiber-array transceiver for laser communications through the atmosphere", J. Opt. Soc. Am. B **22** (2), 347-353, (2005).

[CAC87]   J. L. Caccia, M. Azouit, and J. Vernin "Wind and C_n^2 profiling by single-star scintillation analysis", Appl. Opt. **26**, No 7, 1288-1294 (1987).

[CIA09]   E. Ciaramella, Y. Arimoto, G. Contestabile, M. Presi, A. D'Errico, V. Guarino, and M. Matsumoto, "1.28 Terabit/s (32x40 Gbit/s) WDM transmission system

References

for free space optical communications," IEEE Journal on Selected Areas in Communications **27**, No.9 (2009).

[COH75]   S. Cohen, "Heterodyne detection: phase front alignment, beam spot size, and detector uniformity," Appl. Opt. **14**, 1953-1959 (1975).

[CRE88]   K. Creath, "Phase-measurement interferometry techniques," Prog. Opt., E. Wolf, ed., XXVI (1988).

[DAI07]   G. Dai and V. Mahajan, "Zernike annular polynomials and atmospheric turbulence," J. Opt. Soc. Am. A **24**, No. 1 (2007).

[DAL05]   E. Dalimier and C. Dainty, "Comparative analysis of deformable mirrors for ocular adaptive optics," Opt. Express **13** (2005).

[DAM02]   M. van Dam and R. Lane, "Extended analysis of curvature sensing," J. Opt. Soc. Am. A **19**, No. 7 (2002).

[DAV04]   F. David, D. Giggenbach, H. Henniger, J. Horwath, M. Knapek, R. Landrock, and N. Perlot, *Coherent Transmission Feasibility Report*, Project Report for the ESA (2004).

[DAV04b]   F. David, *Neue Verfahren zur Phasensynchronisation in kohärent-optischen PSK-Homodynsystemen*, Ph.D. Thesis (Christian-Albrechts-Universität zu Kiel, 2004).

[DEV08]   N. Devaney, E. Dalimier, T. Farrell, D. Coburn, R. Mackey, D. Mackey, F. Laurent, E. Daly, and J. C. Dainty, "Correction of ocular and atmospheric wave-fronts: a comparison of the performance of various deformable mirrors", Appl. Opt. **47** (35), 6550-6562 (2008).

[DUN03]   C. Dunsby, Y. Gu, and P. French, "Single-shot phase-stepped wide-field coherence-gated imaging," Opt. Express **11,** No.2 (2003).

[FAN61]   W. Fante, "Wave propagation in random media: systems approach;" Progress in Optics, E. Wolf, ed. **22**, 343-398 (1961).

[FID10]   F. Fidler, M. Knapek, J. Horwath, and W. R. Leeb, "Optical communications for high altitude platforms," IEEE J. Sel. Top. Quantum Electron. (accepted 2010).

[FIE82]   J. Fienup, "Phase retrieval algorithms: a comparison," Appl. Opt. **21**, No. 15, (1982).

[FIE87]   J. Fienup, "Reconstruction of a complex-valued object from the modulus of its Fourier transform using a support constraint," J. Opt. Soc. Am. A. **4**, No.1 (1987).

[FOL81]   J. Foley and R. Butts, "Uniqueness of phase retrieval from intensity measurements," J. Opt. Soc. Am. A. **71**, No.8 (1981).

[FRE90]   K. Freischlad and C. Koliopoulos, "Fourier description of digital phase-measuring interferometry," J. Opt. Soc. Am. A, **7**, No. 4 (1990).

[FRI65]   D. Fried, "Statistics of a geometric representation of wave-front distortion," J. Opt. Soc. Am. **55**, No.11 (1965).

[FRI92]   D. Fried and J. Vaughn, "Branch cuts in the phase function," Appl. Opt. **31** (1992).

[FRI98]   D. Fried, "Branch point problem in adaptive optics," J. Opt. Soc. Am. A **15** (1998).

[FRI01]   D. Fried, "Adaptive optics wave function reconstruction and phase unwrapping when branch points are present," Opt. Commun. **200**, Issues 1-6 (2001).

[GAV03]   D. Gavel, "Suppressing anomalous localized waffle behaviour in least-squares wavefront reconstructors," in *Proc. SPIE: Adaptive Optical System Technologies II*, P. Wizinowich, ed., 4839 (2003).

[GER72]   R. Gerchberg and W. Saxton, "A practical algorithm for the determination of phase from image and diffraction plane pictures" Optik **35**, No.2, 237-246 (1972).

[GHI98]   D. Ghiglia and M. Pritt, *Two-Dimensional Phase Unwrapping – Theory, Algorithms, and Software* (John Wiley & Sons, 1998).

[GIG04]   D. Giggenbach, *Optimierung der optischen Freiraumkommunikation durch die turbulente Atmosphäre – Focal Array Receiver*, (PhD Thesis, Shaker Verlag, 2004).

[GIG09]   D. Giggenbach, J. Horwath, and M. Knapek, "Optical data downlinks from earth observation platforms," *SPIE Free-Space Laser Communications XXI*, San Jose, (2009).

[GLI97]   A. Glindemann, *Beating the Seeing Limit- Adaptive Optics on Large Telescopes*, Habilitationsschrift (1997).

[GLU98]   J. Glückstad, "Graphic method for analyzing common path interferometers," Appl. Opt. **37**, 8151-8152 (1998).

[GLU01]   J. Glückstad and P. Mogensen, "Optimal phase contrast in common-path interferometry;" Appl. Opt. **40**, No. 2 (2001).

[GOO96]   J. Goodman, *Introduction to Fourier Optics* (McGraw-Hill, New York, 1996).

[GRA81]   I. Gradstein and I. Ryshik, *Tables of Series, Products, and Integrals*, Vol. 1&2, (Verlag Hari Deutsch, Thun 1981).

[GRE76]   D.P. Greenwood and D. Fried, "Power spectra requirements for wave-front-compensative systems," J. Opt. Soc. Am. A **66**, No. 3 (1976).

[GRE77]   D.P. Greenwood, "Bandwidth specification for adaptive optics systems," J. Opt. Soc. Am. A **67**, No. 3 (1977).

[GRO96]   P. J. de Groot and L. L. Deck, "Numerical simulations of vibration in phase-shifting interferometry," Appl. Opt. **35**, 2172-2178 (1996).

[HAR98]   J. Hardy, *Adaptive Optics for Astronomical Telescopes* (Oxford University Press, 1998).

[HEN74]   H. Henning, "A new scheme for viewing phase contrast images," Electro-Optical Systems Design (1974).

[HET00]   A. Hettwer, J. Kranz, and J. Schwider, "Three channel phase-shifting interferometer using polarization-optics and a diffraction grating," Opt. Eng. **39** (2000).

[HIB95]   K. Hibino, B. F. Oreb, D. I. Farrant, and K. G. Larkin, "Phase shifting for nonsinusoidal waveforms with phase-shift errors," J. Opt. Soc. Am. A **12**, 761-768 (1995).

[HOR04]   J. Horwath, N. Perlot, D. Giggenbach, and R. Jüngling, "Numerical simulations of beam propagation through optical turbulence for high-altitude platform crosslinks," LASE 2004 **5338**, 243-248 (2004).

[HOR06]   J. Horwath, M. Knapek, B. Epple, and M. Brechtelsbauer, "Broadband backhaul communication for stratospheric platforms: results of the stratospheric optical payload experiment," SPIE Free-Space Laser Communications VI (San Diego, 2006).

References

[HUD77]   R. Hudgin, "Wave-front compensation error due to finite corrector-element size," J. Opt. Soc. Am. A **67**, No. 3 (1977).

[ICH88]   K. Ichikawa, A. Lohmann, and M. Takeda, "Phase retrieval based on the irradiance transport equation and the Fourier transform method: experiments," Appl. Opt. **27** (1988).

[JOL06]   L. Jolissaint, "Optical turbulence generators for testing astronomical adaptive optics systems: a review and designer guide," The Publications of the Astronomical Society of the Pacific. **118**, 1205-1224 (2006).

[JON07]   T. Jono, Y. Takayama, K. Shiratamab, I. Maseb, B. Demelennec, Z. Sodnik, A. Bird, M. Toyoshima, H. Kunimori, D. Giggenbach, N. Perlot, M. Knapek, and K. Arai, "Overview of the inter-orbit and orbit-to-ground laser communication demonstration by OICETS," SPIE Free-Space Laser Communication Technologies XIX and Atmospheric Propagation of Electromagnetic Waves (2007).

[JUS01]   E. Justh, M. Vorontsov, G, Carhart, L. Beresnev, and P. Krishnaprasad, "Adaptive optics with advanced phase-contrast techniques. II. High-resolution wave-front control," J. Opt. Soc. Am. A. **18**, No.6 (2001).

[KNA06]   M. Knapek, J. Horwath, N. Perlot, and B. Wilkerson, "The DLR ground station in the optical payload experiment (STROPEX) – results of the atmospheric measurements instruments," SPIE Free-Space Laser Communications VI, San Diego (2006).

[KNA09]   M. Knapek, "Conditions for adaptive optics in LEO satellite-to-ground links," 7th Workshop on Adaptive Optics for Industry and Medicine (Shatura 2009).

[KNA10]   M. Knapek and R. Mackey, "Adaptive Optics" in *High Altitude Platforms and Their Applications,* Springer Verlag, Editor T. Tozer, Sub-Editor M. Knapek (to be published 2010).

[KOE02]   G. Koepf, R. Marshalek, and D. Begley, "Space laser communications: A review of major programs in the United States," Int. J. Electron. Commun. **56**, No. 4 (2002).

[KOS93]   S. Kostianovski, S. G. Lipson, and E. N. Ribak, "Interference microscopy and Fourier fringe analysis applied to measuring the spatial refractive-index distribution," Appl. Opt. **32**, 4744-4750 (1993).

[KUD94]   K. H. Kudielka, W. M. Neubert, A. L. Scholtz, and W. R. Leeb, "Adaptive optical multiaperture receive antenna for coherent intersatellite communications", Proc. SPIE **2210**, 61-70 (1994).

[KWO87]   O. Kwon, D. Shough, and R. Williams, "Stroboscopic phase-shifting interferometry, " Opt. Lett. **12**, No. 11 (1987).

[LAN05]   R. Lange, "Optical inter-satellite links based on homodyne BPSK modulation: Heritage, status and outlook," SPIE Free-Space Laser Communication Technologies XVII **5712** (2005).

[LAN06]   R. Lange, B. Smutny, B. Wandernoth, R. Czichy, and D. Giggenbach, "142km, 5.625 Gbps free-space optical link based on homodyne BPSK modulation," SPIE **6105** (2006).

[LAR92]   K. Larkin and B. Oreb, "Design and assessment of symmetrical phase-shifting algorithms," J. Opt. Soc. Am. A **9**, 1740-1748 (1992).

[LUT97]   H.P. Lutz, "Optical communications in space – twenty years of ESA effort, " ESA Bulletin 91, **25** (1997).

[MAH81]   V. N. Mahajan, "Zernike annular polynomials for imaging systems with annular pupils," J. Opt. Soc. Am. **71**, 75–86 (1981).

[MAH83]   V. Mahajan, "Strehl ratio for primary aberrations in terms of their aberration variance," J. Opt. Soc. Am. A. Vol. **73**, No.6 (1983).

[MAJ08]   A. Majumdar and J. Ricklin, *Free-Space Laser Communications - Principles and Advances* (Springer, 2008)

[MAL07]   D. Malacara, *Optical Shop Testing* (Wiley Series in Pure and Applied Optics, 2007).

[MAT08]   R. Mata Calvo, Free-Space Optical Transmission Systems (PhD Thesis, Politecnico die Torino, 2008).

[MIA98]   J. Miao, D. Sayre, and H. Chapman, "Phase retrieval from the magnitude of the Fourier transforms of nonperiodic objects," J. Opt. Soc. Am. A **15**, No. 6 (1998).

[MIL05]   J. Millerd, N. Brock, J. Hayes, B. Kimbrough, M. Novak, M. North-Morris, and J. Wyant, "Modern approach in phase measuring metrology," Proc. SPIE, Optical Measurement Systems for Industrial Inspection IV **5856** (2005).

[MOL07]   F. Moll and M. Knapek, "Wavelength selection criteria and link availability due to cloud coverage statistics and attenuation affecting satellite, aerial, and downlink scenarios," SPIE - Free-Space Laser Communications VII **6709** (2007).

[MOL09]   F. Moll, *Conception and Development of an Adaptive Optics Test-bed for Free-Space Optical Communication* (Master Thesis, Supervisor M. Knapek, A. Koch, Munich, 2009).

[MUR08]   K. Murphy, R. Mackey, and C. Dainty, "Branch point detection and correction using the branch point potential method." SPIE Defence and Security: Atmospheric Propagation V, Orlando, Florida, USA (2008).

[NEU88]   E.-G. Neumann, *Single-Mode Fibers* (Springer-Verlag, 1988).

[NOL76]   R. Noll, "Zernike polynomials and atmospheric turbulence," J. Opt. Soc. Am. A. **66**, No.3 (1976).

[NOT07]   J. Notaras and C. Paterson, "Demonstration of closed-loop adaptive optics with a point-diffraction interferometer in strong scintillation with optical vortices, " Opt. Express **15**, No. 21 (2007).

[NOT08]   J. Notaras and C. Paterson, "Point-diffraction interferometer for atmospheric adaptive optics in strong scintillation, " Opt. Commun. **281** (2008).

[OME77]   T. O'Meara, "The multidither principle in adaptive optics," J. Opt. Soc. Am. A. **67**, No.3 (1977).

[PAX88]   R. Paxman and J. Fienup, "Optical misalignment sensing and image reconstruction using phase diversity," J. Opt. Soc. Am. A. **5**, No.6 (1988).

[PER05]   N. Perlot, J. Horwath, and R. Jüngling, "Modelling wind in simulations of atmospheric optical propagation," SPIE Free-Space Laser Communication Technologies XVII. Edited by Mecherle, G. Stephen **5712**, 140-150 (2005).

[PER06]   N. Perlot, *Characterization of Signal Fluctuations in Optical Communications with Intensity Modulation and Direct Detection through the Turbulent Atmospheric Channel* (PhD Thesis, Shaker Verlag, 2006).

[PER07]   N. Perlot, M. Knapek, D. Giggenbach, J. Horwath, M. Brechtelsbauer, Y. Takayama, and T. Jono, "Results of the optical downlink experiment KIODO from OICETS satellite to optical ground station Oberpfaffenhofen (OGS-OP),"

References

SPIE Photonics West, Free-Space Laser Communication Technologies XIX, San Jose (2007).

[PLA04]   G. Planche and V. Chorvalli, "SILEX in-orbit performances," Intl. Conf. on Space Optics, Toulouse (2004).

[PRE92]   W. Press, S. Teukolsky, W. Vetterlin, and B. Flannery, *Numerical Recipes in C – The Art of Scientific Computing* (Cambridge University Press, 1992).

[ROD87]   C. Roddier and F. Roddier, "Interferogram analysis using Fourier transform techniques," Appl. Opt. **26**, 1668-1673 (1987).

[ROD88]   F. Roddier, "Curvature sensing and compensation: A new concept in adaptive optics," Appl. Opt. **27**, No. 7 (1988).

[ROD90]   R. Roddier, "Wave-front sensing and the irradiance transport," Appl. Opt. **29**, No.10 (1990).

[ROD99]   F. Roddier, *Adaptive Optics in Astronomy* (Cambridge University Press, 1999).

[RUI98]   C. Ruilier, "A study of degraded light coupling into single-mode fibers," SPIE Astronomical Interferometry **3350**, 319-329 (1998).

[RUI01]   C. Ruilier and F. Cassaing, "Coupling of large telescopes and single-mode waveguides: application to stellar interferometry," J. Opt. Soc. Am. A. **18**, No.1 (2001).

[RYU94]   S. Ryu, *Coherent Lightwave Communication Systems* (Artech House, 1994).

[SAL91]   B. Saleh and M. Teich, *Fundamentals of Photonics* (A Wiley-Interscience Publication, 1991).

[SAR90]   M. Sarazin and F. Roddier, "The ESO differential image motion monitor," Astron. Astrophys. **227**, 294-300 (1990).

[SCH83]   J. Schwider, R. Burow, K.-E. Elssner, J. Grzanna, R. Spolaczyk, and K. Merkel, "Digital wave-front measuring interferometry: some systematic error sources," Appl. Opt. **22** (1983).

[SCH92]   E. Schrüfer, *Signalverarbeitung – Numerische Verarbeitung digitaler Signale* (Carl Hanser Verlag, 1992).

[SCH93]   J. Schwider, O. Falkenstoerfer, H. Schreiber, A. Zoeller, and N. Streibl, " New compensating four-phase algorithm for phase-shift interferometry," Opt. Eng. **32**, No. 8 (1993).

[SCH95]   J. Schmit and K. Creath, "Extended averaging technique for derivation of error-comprensating algorithms in phase-shifting interferometry," Appl. Opt. **34**, No. 19 (1995).

[SIV03]   N. Sivakumar, W. Hui, K. Venkatakrishnan, and B. Ngoi, "Large surface profile measurement with instantaneous phase-shifting interferometry," Opt. Eng. **42**, (2003).

[SMA75]   R. Smartt and W. Steel, "Theory and application of point-diffraction interferometers," Jpn. J. Appl. Phys. **14**, 351-356 (1975).

[SMI93]   F. G. Smith, *Atmospheric Propagation of Radiation - The Infrared and Electro-Optical Systems Handbook* (Bellingham: SPIE Optical Engineering Press, 1993).

[SMI99]   C. Smith, R. McDuff, N. Heckenberg, M. Soskin, and M. Vasnetsov "Experimental realisation and detection of optical vortices," in *Optical Vortices, Horizons in World Physics* **228**, M. Vasnetsov and K. Staliunas, ed. (Nova Science Publishers, 1999).

[SOD06]   Z. Sodnik, B. Furch, and H. Lutz, "Free-space laser communication activities in Europe: SILEX and beyond," Lasers and Electro-Optics Society LEOS, (2006).

[SOS99]   M. Soskin and M. Vasnetsov, "Linear theory of optical vortices," in *Optical Vortices, Horizons in World Physics* **228**, M. Vasnetsov and K. Staliunas, ed. (Nova Science Publishers, 1999).

[SOS01]   M. Soskin and M. Vasnetsov, "Singular optics," in *Progress in Optics* **42**, E. Wolf, ed. (Elsevier Science, 2001).

[SOU77]   W. Southwell, "Wave-front analyzer using a maximum likelihood algorithm," J. Opt. Soc. Am. **67**, No.3 (1977).

[STR84]   N. Streibl, "Phase imaging by the transport equation of intensity," Opt. Commun. **49**, No.1 (1984).

[SUR93]   Y. Surrel, "Phase stepping: a new self-calibrating algorithm," Appl. Opt. **32**, No. 19 (1993).

[SUR96]   Y. Surrel, "Design of algorithms for phase measurements by the use of phase stepping," Appl. Opt. **35** (1996).

[SUR97]   Y. Surrel, "Additive noise effect in digital phase detection," Appl. Opt. **36** (1997).

[TAK82]   M. Takeda, H. Ina, and S. Kobayashi, "Fourier-transform method of fringe-pattern analysis for computer topography and interferometry," J. Opt. Soc. Am. **72**, No. 1 (1982).

[TAK07]   Y. Takayama, T. Jono, M. Toyoshima, H. Kunimori, D. Giggenbach, N. Perlot, M. Knapek, K. Shiratama, J. Abe, and K. Arai, "Tracking and pointing characteristics of OICETS optical terminal in communication demonstrations with ground stations," SPIE Photonics West, Free-Space Laser Communication Technologies XIX, San Jose (2007).

[TAT67]   В. И. Татарский, *Распространение Волн в Турбулентной Атмосфере* (Наука, Москва, 1967).

            V. I. Tatarski, *Wave Propagation in the Turbulent Atmosphere* (Publisher Nauka, Moscow, 1967).

[TEA83]   M. Teague, "Deterministic phase retrieval: a Green's function solution," J. Opt. Soc. Am. **73**, No.11 (1983).

[THI04]   S. Thibault and J. Lacoursiere, "Advanced fiber coupling technology," Technical Report, INO for ESA (2004).

[TOK00]   A. Tokovinin and V. Kornilov, "Measuring turbulence profile from scintillations of single stars," In: *Astronomical Site Evaluation in the Visible and Radio Range,* Benkhaldoun Z., Munoz-Tunon C., Vernin J., ed., ASP Conf. Ser. **266**, 104-112 (2000).

[TOK02a]   A. Tokovinin, V. Kornilov, N. Shatsky, and O. Voziakova, "Restoration of turbulence profile from scintillation indices," Mon. Not. R. Astron. Soc. (2002).

[TOK02b]   A. Tokovinin, "From differential image motion to seeing", Publications of the Astronomical Society of the Pacific **114**, 1156–1166 (2002).

[TOY09]   M. Toyoshima, H. Takenaka, Y. Shoji, Y. Takayama, Y. Koyama, and H. Kunimori, "Polarization measurements through space-to-ground atmospheric propagation paths by using a highly polarized laser source in space," Opt. Express **17**, 22333-22340 (2009).

References

[TYL94]   G. Tyler, "Bandwidth considerations for tracking through turbulence," J. Opt. Soc. Am. A **11**, No. 1 (1994).

[TYL00]   G. Tyler, "Reconstruction and assessment of the least-squares and slope discrepancy components of the phase," J. Opt. Soc. Am. **17**, No.10 (2000).

[TYS98]   R. K. Tyson, *Principles of Adaptive Optics* (2nd Edition, Academic Press, 1998).

[TYS00]   R. K. Tyson, *Introduction to Adaptive Optics* (Bellingham, SPIE Press, 2000).

[VAN03]   R. Vander, S. Lipson, and I. Leizerson, "Fourier fringe analysis with improved spatial resolution," Appl. Opt. **42**, No. 34 (2003).

[VAS99]   M. Vasnetsov and K. Staliunas, *Optical Vortices* (Nova Science Publishers, 1999).

[VOI98]   V. Voitsekhovich, D. Kouznetsov, and D. Morozov, "Density of turbulence-induced phase dislocations," Appl. Opt. **37** (1998).

[VOI03]   V. Voitsekhovich and L. Sanchez, "Effect of scintillations in curvature sensing," Astronomy & Astrophysics **399** (2003).

[VOR98]   M. Vorontsov and V. Sivokon, "Stochastic parallel-gradient-descent technique for high-resolution wave-front phase-distortion correction," J. Opt. Soc. Am. A. **15**, No.10 (1998).

[VOR00]   M. Vorontsov, G. Carhart, M. Cohen, and G. Cauwenberghs, "Adaptive optics based on analog parallel stochastic optimization: analysis and experimental demonstration," J. Opt. Soc. Am. A. **17**, No.8 (2000).

[VOR01]   M. Vorontsov, E. Justh, and L. Beresnev, "Adaptive optics with advanced phase-contrast techniques. I. High-resolution wave-front sensing," J. Opt. Soc. Am. A. **18**, No.6 (2001).

[VOR02]   M. Vorontsov, "Decoupled stochastic parallel gradient descent optimization for adaptive optics: integrated approach for wave-front sensor information fusion," J. Opt. Soc. Am. A. **19**, No.2 (2002).

[VOR09]   M. A. Vorontsov, T. Weyrauch, L. A. Beresnev, G. W. Carhart, L. Liu, and K. Aschenbach, "Adaptive array of phase-locked fiber collimators: analysis and experimental demonstration", IEEE J. Sel. Top. Quantum Electron **15**, 269-280 (2009).

[WAG82]   R. Wagner and W. Tomlinson, "Coupling efficiency of optics in single-mode fiber components," Appl. Opt. **21**, No. 15 (1982).

[WAN78]   J. Wang and J. Markey, "Modal compensation of atmospheric turbulence phase distortion," J. Opt. Soc. Am. **68** (1978).

[WIL99]   W. Wild and E. Le Bigot, "Rapid and robust detection of branch points from wave-front gradients," Opt. Lett. **24**, 190-192 (1999).

[WIN91]   J. van Wingerden, H. Frankena, and C. Smorenburg, "Linear approximation for measurement errors in phase shifting interferometry," Appl. Opt. **30**, 2718-2729 (1991).

[WYA84]   J. Wyant, C. Koliopoulos, B. Bhushnan, and O. George, "An optical profilometer for surface characterization of magnetic media," ASLE Transactions **27** (1984).

E Index

Z